UTS UNIVERSITY OF TECHNOLOGY SYDNEY

Assessing Impacts of Soil Constitutive Behavior and Water Pressure on Seismic Performance of Buildings on Shallow Foundations

by Navid Yeganeh

Thesis submitted in fulfilment of the requirements for the degree of

Doctor of Philosophy

under the supervision of A/Prof. Behzad Fatahi
A/Prof. Hadi Khabbaz

University of Technology Sydney
Faculty of Engineering and Information Technology (FEIT)

September 2020

Certificate of Original Authorship Template

Graduate research students are required to make a declaration of original authorship when they submit the thesis for examination and in the final bound copies. Please note, the Research Training Program (RTP) statement is for all students. The Certificate of Original Authorship must be placed within the thesis, immediately after the thesis title page.

Required wording for the certificate of original authorship

CERTIFICATE OF ORIGINAL AUTHORSHIP

I, *Navid Yeganeh* declare that this thesis, is submitted in fulfilment of the requirements for the award of *Doctor of Philosophy*, in the *School of Civil and Environmental Engineering (Faculty of Engineering and Information Technology, FEIT)* at the University of Technology Sydney.

This thesis is wholly my own work unless otherwise referenced or acknowledged. In addition, I certify that all information sources and literature used are indicated in the thesis.

This document has not been submitted for qualifications at any other academic institution.

This research is supported by the Australian Government Research Training Program.

Signature:

Production Note:
Signature removed prior to publication.

Date:
1/09/2020

Sincerely Dedicated to

My Father and Mother

Reza and *Akram*

ACKNOWLEDGEMENT

First and foremost, I, Navid Yeganeh, would like to express my sincere gratitude to my principal supervisor, Associate Professor Behzad Fatahi, for the continuous support of my PhD study and related research, for his patience, motivation, and immense knowledge. His guidance helped me in all the time of research and writing of this thesis. I could not have imagined having a better advisor and mentor for my PhD study. I would also appreciate my alternative supervisor, Associate Professor Hadi Khabbaz, for his presence and willingness to help during this research work.

I am appreciative of all my friends, and colleagues, as well as the academic and non-academic staffs at the Centre for Built Infrastructure Research (CBIR) of the Faculty of Engineering and Information Technology (FEIT), based in UTS. It was an honor for me to walk through this PhD journey with my comrades, Yang (Alex) Dong, Piyush Punetha, and John Phung.

My appreciation is extended to the High-Performance Computer (HPC) team, Anselm Motha and Matt Gaston, at UTS for their commitment, and extensive assistance. Special thanks to the IT office of FEIT and particularly Jason Chan for providing this research study with the prompt and technical IT support. I also deeply appreciate UTS thanks to conferring the UTS President's Scholarship upon me, without which this research work could have not been possible.

Seizing the moment, I wish to express my heartfelt gratitude to my parents in light of the fact that I owe it all to them.

LIST OF PUBLICATIONS RELATED TO THIS RESEARCH

Journal Articles

Yeganeh, N. & Fatahi, B. 2019, 'Effects of choice of soil constitutive model on seismic performance of moment-resisting frames experiencing foundation rocking subjected to near-field earthquakes', *Soil Dynamics and Earthquake Engineering*, vol. 121, pp. 442-459.

Fatahi, B., Huang, B., **Yeganeh, N.**, Terzaghi, S. & Banerjee, S. 2020, 'Three-dimensional simulation of seismic slope-foundation-structure interaction for buildings near shallow slopes', *International Journal of Geomechanics*, vol. 20(1), pp. 04019140:1-20.

Yeganeh, N., Fatahi, B. & Taciroglu, E. 2020, 'Effects of pore water pressure on seismic performance of buildings resting on saturated clayey deposits considering soil-structure interaction', *Computers and Geotechnics*. (Under Review)

Peer-Reviewed Conference Papers

Yeganeh, N., Fatahi, B. & Terzaghi, S. 2017, 'Effects of shear wave velocity profile of soil on seismic response of high rise buildings', *15th International Conference of the International Association for Computer Methods and Advances in Geomechanics (15thIACMAG), Wuhan, China*.

Yeganeh, N. & Fatahi, B. 2018, 'Seasonal effects on seismic performance of high rise buildings considering soil-structure interaction', *16th European Conference on Earthquake Engineering (16ECEE), Thessaloniki, Greece*.

Yeganeh, N., Fatahi, B. & Mirlatifi, S. 2019, 'Effects of hyperbolic hardening parameters on seismic response of high rise buildings considering soil-structure interaction', *7th International Conference on Earthquake Geotechnical Engineering (VII ICEGE), Roma, Italy*.

TABLE OF CONTENTS

LIST OF FIGURES

LIST OF TABLES

LIST OF NOTATIONS

A	Acceleration coefficient of earthquake
A_0	Reference area in soil-structure relative rigidity
A_f	Area of load-carrying foundation
A_g	Gross cross-sectional area of column
A_s	Cross-sectional area of shear reinforcement
A_t	Cross-sectional area of longitudinal tensile reinforcement
A_v	Effective peak velocity-related acceleration coefficient
a	Representative of maximum value of modulus reduction factor
a_h	Earthquake horizontal peak base acceleration
B	Foundation width
b	Representative of optimum degree of saturation
b_e	Effective foundation size
C	Soil cementation
$\bar{C}$	Viscous damping of building
$C_h(T)$	Spectral shape factor
$C_h(\tilde{T}_{eff})$	Effective spectral shape factor
C_p	P-wave velocity
C_s	S-wave velocity
$\bar{C}_s$	Seismic response coefficient for fixed-base structure
$\tilde{C}_s$	Seismic response coefficient for flexible base structure
c^{mob}	Mobilized cohesion
c_{sd}	Soil dependent parameter

c'	Ultimate effective cohesion
c'_{int}	Effective cohesion of interface element
D	Damping ratio
D_{10}	Effective grain size
D_e	Depth of embedment of foundation
$D_{f=0.1}$	Damping ratio at frequency of 0.1 Hz
D_r	Relative density
D_s	Thickness of relatively uniform soil layer under foundation
D_{sd}	Shortest distance from construction site to nearest fault
DR_{tt}	Total inter-story drift ratio
d	Thickness of any soil layers from 0 to 30 m depth below foundation
d_0	Distance from extreme compressive fibre of concrete cross-section to centroid of outermost layer of tensile reinforcement
d_i	Deflection at $(i)^{th}$ building story
d_{i+1}	Deflection at $(i+1)^{th}$ building story
d_n^{int}	Interface normal displacement
d_s^{int}	Previous shear displacement of interface element
$dp'/d\varepsilon_v$	Loading tangent modulus
E_c	Modulus of elasticity of concrete
E_s	Modulus of elasticity of steel reinforcement
E_{str}	Modulus of elasticity of structural material
e	Soil void ratio
e_b	Basement embedment or foundation embedment
e_b/r_x	Embedment ratio

F_a	Axial compressive force on cross-section of column
f	Loading frequency
f_p	Volumetric yield function
f_q	Shear yield function
f_{fb}	Fundamental frequency of fixed-base building
f_{sy}	Characteristic yield strength of steel reinforcement
f_{su}	Ultimate stress of steel reinforcement
f_{cmi}	Mean in-situ compressive strength of concrete
f_c'	Concrete characteristic compressive strength
G	Soil shear modulus
G_0 or (G_{max})	Small-strain shear modulus or maximum shear modulus
$G_{0(dry)}$	Low-amplitude shear modulus for completely dry condition
G_c	elastic tangent shear modulus
G_{c_i}	Initial elastic tangent shear modulus
G_c^{ref}	Elastic tangent shear modulus at reference mean effective stress
G_d	Dashpot constant
G_i^p	Initial tangent plastic shear modulus
G_m^p	Mobilized plastic shear modulus
G_s	Specific gravity of soil solids
G_{sd}	Strain-degraded shear modulus
G_{sp}	Spring constant
G/G_0	Shear modulus reduction factor
g	Acceleration of gravity
g_p	Volumetric potential function

g_q	Shear potential function
H	Building height
H_s	Soil thickness
h	Story height in building
$\bar{h}$	Effective height of building
h_{bd}	Bedrock depth
H/r_θ	Structure aspect ratio
I	Static moment of inertia of load carrying foundation
I_g	Moment of inertia of uncracked structural section
I_p	Soil plasticity index
J_2	Second deviatoric stress invariant
K	Soil bulk modulus
K_0	At-rest earth pressure coefficient
$K_{0(OC)}$	At-rest earth pressure coefficient for overconsolidated soil
$k(\gamma)$	Decreasing function of cyclic shear strain amplitude
K_θ	Rocking stiffness of foundation
K'	Effective bulk modulus
$\bar{K}$	Initial stiffness of building
K_c	Elastic tangent bulk modulus
K_{cc}	Bulk modulus of concrete
K_{ci}	Initial elastic bulk modulus
K^*_{fixed}	Effective stiffness of Single-Degree-Of-Freedom (SDOF) oscillator
K_l	Lateral stiffness of foundation
K_M	Elasto-plastic bulk multiplier

K_n	Normal spring stiffness
K_p	Plastic bulk modulus
K^{ref}	Slope of laboratory curve in isotropic consolidation test
K_{e-p}^{ref}	Elasto-plastic bulk modulus at reference mean effective stress
K_s	Shear spring stiffness
K_{ss}	Soil-structure relative rigidity
K_t	Translational stiffness of foundation
K_u	Undrained bulk modulus
K_w	Water bulk modulus
k	Material constant from regression analysis
k_h	Horizontal seismic coefficient
k_h^*	Critical acceleration
k_p	Probability factor
L	Logarithmic strain
L_0	Foundation length in direction of analysis
L_1 & L_2	Calibrated parameters for hysteretic damping
l	Height of cross-section of structural element
M	Total mass of building
M^*	Effective mass of building for first mode of vibration
M_e	Mass of fixed-based building
M^p	Limiting plastic moment
M_s	Normalized secant modulus
M_t	Normalized tangent modulus
$m(\gamma)$	Increasing function of cyclic shear strain amplitude

N	Number of loading cycles
N_{cE}, N_{qE}, & $N_{\gamma E}$	Seismic bearing capacity factors
N_{cS}, N_{qS}, & $N_{\gamma S}$	Static bearing capacity factors
N_{bl}	Number of building spans in longitudinal direction
N_{bt}	Number of building spans in transversal direction
N_{max}	Maximum near-fault factor
N_s	Number of stories
n	Soil porosity
$\bar{n}$	Shear wave velocity reduction factor
n_c	Number of columns at story under analysis
OCR	Overconsolidation ratio
p'	Mean effective stress
p_{atm}	Atmospheric pressure
p^{cap}	Cap pressure
p_i^{cap}	Initial cap pressure
p^{ref}	Reference mean effective stress
q	Deviator stress
R	Response modification factor
R_F	SDOF strength reduction factor
R_f	Failure ratio
R_M	Practical site and interaction-dependent MDOF modification factor
R_p	Return period factor
RRS_{bsa}	Base-slab averaging effect
RRS_e	Ratio of response spectra for embedment

r, r_a & r_m	Characteristic foundation lengths
r_{eq}	Radius of equivalent circular foundation
r_f	Radius of foundation
r_x	Equivalent foundation radius for translation
r_θ	Equivalent foundation radius for rotation
S	coefficient related to soil profile characteristics of site
S_a	Spectral acceleration
$S_{a_{max}}$	Maximum response acceleration
$\bar{S}_a$	Mean spectral acceleration
$\tilde{S}_a$	SSI adjusted spectral response acceleration
S_{D1}	Design earthquake spectral response acceleration at 1-s period
S_{DS}	Design earthquake spectral response acceleration at short period
S_r	Degree of saturation
$S_{r(opt)}$	Optimum degree of saturation
S_s	Center-to-center spacing of shear reinforcement
S_u	Undrained shear strength of soil
$\bar{S}_v$	Mean spectral velocity
s	Slenderness ratio of building
T	Structural period
T_2	Second mode period of soil-structure system
$\tilde{T}$ & $\tilde{T}_{eff}$	Effective period of flexible base building
T_h	Natural period of rigid-body translation of structure
T_{int}	Limiting tensile strength of interface element
T_L	Long-period transition period

T_n	Total normal boundary traction
T_n^{ab}	Resistant traction of dashpot in normal direction
T_n^{ff}	Normal component of free field traction
T_r	Natural period of rocking of structure
T_s	Total shear boundary traction
$\bar{T}_s$	Characteristic site period
T_s^{ab}	Resistant traction of dashpot in shear direction
T_s^{ff}	Shear component of free field traction
T_{SSI}	Fundamental period of soil-structure system
$\tilde{T}_{eff}/T_{eff}$	Effective period-lengthening ratio
t_g	Geologic age
t_n	Normal resistant traction of viscous dashpot
t_s	Shear resistant traction of viscous dashpot
u	Pore water pressure
u_{dyn}/σ_v'	Excess pore water pressure ratio
V	Fixed-base structure's seismic base shear
$\tilde{V}$	Adjusted base shear for soil-structure interaction
V_c	Velocity coefficient of earthquake
V_i	Vector component of velocity
V_u	Story shear capacity
V_{MDOF}	Base shear demand of inelastic flexible base MDOF system
V_s	Soil shear wave velocity
$V_{s,30}$	Average shear wave velocity of top 30 m of soil deposit
$V_{s_{@b_e}}$	Weighted average shear wave velocity within depth of b_e

$\bar{V}_{s,i}$	Weighted average of in-situ shear wave velocity
V_{SDOF}	Base shear demand of fixed-base SDOF system
v_n	Normal component of velocity at lateral boundary
v_n^{ff}	Normal component of velocity of grid point in side free field
v_s	Shear component of velocity at lateral boundary
v_s^{ff}	Shear component of velocity of grid point in side free field
$\bar{W}$	Effective seismic weight of building
W_l	Dissipated energy in cycle of loading
W_{ms}	Stored maximum strain energy during one cycle
W_t	Total weight of building
W_i/g	Mass assigned to $(i)^{th}$ building story
Z	Earthquake hazard factor
α_0	Structure-to-soil stiffness ratio
$\alpha_1, \alpha_2, \& \alpha_3$	Calibrated parameters for hysteretic damping
$\bar{\alpha}$	Relative weight density of structure and underlying soil
α_L	Local damping coefficient
α_y	Dynamic foundation stiffness modifier for translation
α_θ	Dynamic foundation stiffness modifier for rocking
β	Elastic-plastic coupling coefficient
β_0	Effective damping ratio of soil-structure interaction
$\tilde{\beta}$	Fraction of critical damping for structure-foundation system
β_f	Foundation damping factor
β_{f_H}	Soil hysteretic damping ratio
β_{f_R}	Radiation damping-induced foundation damping

β_i	Fixed-base damping ratio
Γ_{tm}	Normalized tangent modulus
γ	Cyclic shear strain amplitude
$\dot{\gamma}$	Cyclic shear strain rate
$\gamma_{dyn_{min}}$	Minimum cyclic shear strain amplitude
γ_s	Unit weight of soil
γ_{SA}	Single-amplitude cyclic shear strain
γ_{td}	Degradation strain threshold
γ_{tf}	Flow threshold
γ_{tl}	Linear threshold shear strain
γ_{tv}	Volumetric cyclic threshold strain
Δd_s^{int}	Incremental shear displacement of soil-foundation interface
ΔT	Additional period due to soil-structure interaction
Δt	Time interval
Δu	Excess pore water pressure build-up
ΔV	Base shear reduction due to soil-structure interaction
Δz_{min}	Smallest width of adjoining zone to soil-foundation interface
$\Delta\varepsilon$	Strain increment
$\Delta\varpi$	Dissipated energy per oscillation cycle
δ	Lateral story deflection in fixed-based building
$\tilde{\delta}$	Lateral story deflection under influence of soil-structure interaction
δ_{ij}	Kronecker delta
ε_s^p	Plastic shear strain
$\dot{\varepsilon}_s^p$	Rate of plastic shear strain

ε_{su}	Ultimate strain of steel reinforcement
ε_v	Volumetric strain
ε_v^p	Irrecoverable volumetric strain
$\dot{\varepsilon}_v^p$	Rate of plastic volumetric strain
ζ	Critical damping
ζ_h	Soil damping ratio for translational mode of foundation
ζ_r	Soil damping ratio for rocking mode of foundation
η_f	Failure stress ratio
η^{mob}	Mobilized stress ratio
η_{ult}	Ultimate stress ratio
θ	Inter-story drift coefficient
θ_l	Lode's angle
κ	Recompression Index
κ_1	Stress dependency exponent
κ_2	Plasticity index-dependent exponent
Λ_i	Numerical grid point location in soil medium
λ	Compression index
$\bar{\lambda}$	User-defined analysis type factor
μ	Ductility demand
μ_s	Ductility demand of soil-structure system
μ_t	Predefined target ductility demand
$\tilde{\mu}_u$	Global ductility of equivalent oscillator of actual structure
ν	Soil Poisson's ratio
ν'	Effective Poisson's ratio

ν_c	Poisson's ratio of concrete
ν_u	Undrained Poisson's ratio
ρ	Soil mass density
ρ_c	Concrete density
ρ_{eff}	Soil effective density
ρ_s	Steel reinforcement density
ρ_w	Water density
σ^{ff}	Free field normal stress
σ_y	Yield stress of concrete material
$\sigma'_{n,int}$	Effective normal stress at foundation-soil interface
σ'_{pc}	Vertical preconsolidation pressure
σ'_v	In-situ effective overburden stress
τ	Shear stress
$\bar{\tau}$	Normalized shear stress
τ^{ff}	Free field shear stress
$\tau_{f,int}$	Interface shear strength
τ_{int}	Shear stress at foundation-soil interface
τ/τ_f	Cyclic shear stress ratio
φ^{mob}	Mobilized friction angle
φ'	Soil effective friction angle
φ'_f	Failure effective friction angle
φ'_{int}	Effective friction angle of foundation-soil interface
$\emptyset_i$	Amplitude of first mode of vibration at $(i)^{th}$ building story
χ	Threshold cyclic shear stress ratio

ψ	Dilatancy
ψ_f	Failure dilation angle
ψ^{mob}	Mobilized dilation angle
Ω	Active Coulomb wedge angle
ω	Width of cross-section of structural element
ϖ	Maximum strain energy

ABSTRACT

The growing need for the high rise buildings in the megalopolises necessitates the reliable predictions of the buildings' performance amidst the earthquakes with the aim of curtailing the severe damage and probable partial or the total collapse of the superstructures. The seismic excitation, experienced by the superstructures, is a function of the seismic source, travel path and local site effects, as well as the Soil-Structure Interaction (SSI) influences. Thus, the undeniable paramountcy of the dynamic soil-structure interaction is evident.

This thesis conducts the three-dimensional elasto-plastic-based coupled SSI numerical simulations in FLAC3D using the direct method with the help of the High-Performance Computer (HPC) at University of Technology Sydney (UTS), taking averagely a few days to a month. The 15-story and 20-story reinforced concrete moment-resisting buildings, as the examples of the typical high rise buildings in the relatively high-risk earthquake-prone zones, are designed considering the relevant Australian codes and in line with the constructability and norms. The plastic moment concept is employed to assign the elastic-perfectly plastic model to the superstructures and their mat foundations. The geometric nonlinearity of the adopted superstructures, capturing the $P-\Delta$ effect, is accommodated by the use of the large-strain solution mode. The dependency of the soil shear modulus and corresponding damping ratio on the seismically-induced shear strains is also captured. The interaction between the soil mass and building foundation is simulated by the use of the advanced interface element, mimicking the possible sliding, separation, and gapping. The cherry-picked near-field earthquake excitations are scaled by means of the response spectrum matching method.

The medium, underneath the engineering superstructures, influences their dynamic responses. An investigation on the impact of the soil dynamic properties, including the shear wave velocity and small-strain shear modulus, on the seismic performance of the

superstructures, supported by a shallow foundation, is conducted. The outcomes show that these soil properties ought to be served with the acute care in any seismic soil-foundation-structure interaction simulation so as to obtain the reliable results. Taking a step further, the variations of the degree of saturation, stemming from the extensive dry climate and floods, could impair the seismic performance of the mat-supported buildings due to exceeding the life safety drift limit, hinging around the post-earthquake damage state. The damp soils are basically softer and so absorb more energy than the dry, stiff soils. After a dry season, during a seismic event, the selected building in this study will experience more load, will move more, will crack more and ultimately will be unsafe whether it remains standing or collapses.

This thesis conducts a host of seismic SSI analyses with the consideration of the hardening hyperbolic concept. It is concluded that incorporating more advanced soil plasticity models, suitable for the seismic analyses of the soil-structure systems, could predict the foundation rocking and structural lateral deflections more accurately, both of which must be strictly overseen in the application of the foundation rocking isolation technique. Examining the geotechnical and structural objectives in this study exhibits that the presence of the water table at the construction site had better not be dismissed in any case as the generation of the excess pore water pressure could markedly weaken the seismic performance of the superstructures by pushing it from the life safety state to the near collapse damage level or even the collapse state. In practice, however, the consideration of the presence of the water table at the construction site is only limited to the drained analysis and undrained shear strength analysis.

The design and practicing engineers, stakeholders, and practitioners are meant to consider the Performance-Based Seismic Design (PBSD) approach as an indicator of the buildings' performance, subjected to the different levels of the earthquakes. This thesis is devoted to provide them with a clear understanding on the key factors, affecting the relations between SSI, PBSD, and the foundation rocking since an ounce of prevention is worth a pound of cure.

CHAPTER 1

INTRODUCTION

1.1 General

The earthquakes are a natural hazard, causing an average of 13,000 fatalities each year. It appears that in spite of the advancements in the design techniques and, generally speaking, in the construction practices, as well as the availability of the more stringent building codes and regulations, the improvements in our understanding of how the geotechnical and structural earthquake engineering aspects should be integrated are still required. Indeed, the engineers need to look at the more comprehensive design and construction practices to resourcefully respond to the rapid urbanization growth over the world and creation of the densely populated cities.

According to the previous studies (e.g., Rodriguez and Montes, 2000; Dutta et al., 2004; Wang et al., 2013), the seismic responses of the structures are believed to be dominated by the role of the Dynamic Soil-Structure Interaction (DSSI) in each case of construction. In that regard, according to Wolf and Song (2002), the practitioners must first be convinced that DSSI is an essential part of the design process. Note that DSSI is referred to the process in which the soil response is affected by the structure motion whereas the latter is influenced by the soil motion. As a result of DSSI, the seismic response of a flexibly-supported structure differs from that of the fixed-base structure in terms of the foundation motion, contribution of the foundation rocking component to the overall lateral deflection of the superstructure, fundamental period of the vibration, mode shapes, and modal participation factors, in addition to the damping rate.

DSSI comprises the kinematic interaction and inertial interaction, covering the linear to nonlinear structures and soils. The material nonlinearity stems from yielding of the soils and/or structures whereas the geometric nonlinearity is due to the foundation gapping or separation and pounding of the adjacent structures. Moreover, the analysis methods, involved in the soil-structure interaction, can be divided into the two principal categories, viz, the direct and multi-step/substructure methods. In the former, which is mightily advantaged with the possibility of assuming the nonlinear behavior for the soil and structure materials along with the possibility of modeling the complex geometries, the entire system of the soil-foundation-structure is modeled and analyzed in one single step. As emphasized by Chu (2006) and Abate et al. (2010), carrying out the time domain-based response history analyses is essential for the computation of the aforementioned nonlinear effects.

In the wake of the development attributed to the computer analysis tools, the Soil-Structure Interaction (SSI) throughout the agitation, i.e., the earthquakes, has moved to the center stage for the earthquake engineering community. Nonetheless, a myriad of suppositions would give rise to diminishing the quality of the results associated with the numerical simulations of the SSI problems. Additionally, Yegian et al. (2001) underscored that the inclusion of the soil-foundation-structure system in the seismic analysis is yet to receive the due attention. From these considerations, this study aims to numerically scrutinize the seismic performance of the high rise buildings by means of the incorporation of SSI in the Performance-Based Seismic Design (PBSD) framework. Leelataviwat et al. (1999) mentioned that the goal of a PBSD procedure is to accurately predict the performance of a structure, subjected to the different intensity levels of the seismic excitations. The research in this thesis is an attempt to donate insight into the extent to which the dynamic soil properties (e.g., the shear wave velocity and small-strain shear modulus) and soil plasticity plus the excess pore water pressure build-up

could affect the performance of the shallow-founded buildings, meant to withstand the shuddering and shaking from the earthquakes.

1.2 Research Significance

Australia's near neighbors (i.e., New Zealand, Indonesia, and Papua New Guinea) and further afield in the Asia Pacific and beyond, experience the seismic activities with the potential to cause the massive destruction to the infrastructure, and major fatalities. That can impact on the Australian businesses, working in or servicing the aforesaid areas. Indeed, the earthquakes have been reported in Australia since the British settlement in 1788. By way of illustration, the 1979 Cadoux, 1988 Tennant Creek, 1997 Collier Bay, and 2016 Petermann Ranges seismic events are some of the most severe earthquakes in Australia. The scarcity of the land in conjunction with the rapid urbanization growth compel the engineers to accept the risk of the construction in such seismically active regions. Some of the common impacts of the earthquakes are as follows: (i) damage to the buildings and infrastructure; (ii) fires; (iii) initiation of the slope failures; (iv) liquefaction; and (v) tsunami.

14th of October 1968 was meant to bring the calmness of a public holiday in Meckering, Australia; ending up, however, with a catastrophe in only 40 seconds. Johnston and White (2018) reported that 59 buildings were destroyed or rendered uninhabitable and 20 people were injured. According to Conacher and Murray (1969), the State government immediately announced Meckering as a disaster area. The extent of earthquake-induced damage was then thoroughly assessed. In spite of the fact that there were no deaths probably due to the outdoor activities, related to the public holiday, the earthquake-induced damage to the infrastructure was intensive. The water supply line was concertinaed and ruptured. In addition, buckling and fracturing the railroads were observed in the affected zone whilst the telephone network became unavailable. Some of the highways, as another vital communication link, were not

accessible. The destructive consequences of the 1968 Meckering earthquake gave rise to issuing the Australia's first earthquake code.

According to Rynn et al. (1992), the 1989 Newcastle earthquake claimed 13 lives and injured over 150 people. It damaged more than 70,000 properties and left an estimated total loss of about $AU (1991) 4 billion. A study of the psychosocial sequelae of the 1989 Newcastle earthquake, conducted by Carr et al. (1995), demonstrated that the high levels of disruption or threat were imposed on 14.8% of the population. About 25% of the said group encountered the high level of the psychological distress. The risk of developing post-traumatic stress disorder was also reported as a direct consequence of experiencing such severe levels of threat. On the same topic worldwide, referring to Raviola et al. (2013), in 2010, Port-au-Prince, the capital of Haiti was shaken by a major seismic event, triggering over 150,000 fatalities. Over 10 million folks became homeless in a fraction of a minute in the capital and main part of the southern Haiti.

Mccue et al. (2001) pointed out that the 100-year history of the Australian earthquakes suggested that Australia will experience on average two large earthquakes, which could cause the structural and non-structural damage. Indeed, the change in the seismicity pattern has been observed. In that regard, referring to Polcari et al. (2018), the 2016 Petermann Ranges earthquake was a tangible sample of the ongoing seismicity pattern changes in view of the fact that the affected area used to be considered as the low seismicity region.

It is reasoned to mention that establishing an approach, connecting the assorted fields together is required such that the governments and emergency management services could prepare themselves to cope with such hazardous events. In that respect, the geology, structural and geotechnical engineering should be joined the seismology. Therefore, updating the current codes and regulations as well as developing the more rigorous methods for designing the superstructures in the earthquake-prone zones are of vital importance. This is where the

Dynamic Soil-Structure Interaction (DSSI), as an interdisciplinary field of science, must be taken into account so as to assess the seismic performance of the structures.

1.3 Research Gap and Objectives

The research study, presented in this thesis, strives to address the challenges, which the design and practicing engineers encounter on a day-to-day basis, in the assessment of the seismic performance of the high rise buildings considering the soil-structure interaction under the framework of the performance-based seismic design. The key challenges are summarized as below:

(i) Lack of understanding of the appropriate methods to accurately estimate the small-strain shear moduli of the soil deposits in-situ.

(ii) Pathless land within the concept of the seasonality of the earthquakes, meaning the variations of the degree of saturation at the effective vadose zone, i.e., in the vicinity of the ground surface.

(iii) State of neglect for the application of the advanced soil constitutive models in the numerical simulations.

(iv) Dismissal of the simulation of the excess pore water pressure build-up in the non-liquefiable soils under the undrained condition.

(v) Lack of the clear methodology for assessing the performance of the foundation rocking isolation technique.

In line with the research significance and above-mentioned challenges, the present research aims to contribute to the body of knowledge through the following objectives:

- Developing an enhanced nonlinear three-dimensional coupled soil-structure numerical model.

- Investigating the suitable application of the shear wave velocity profile of the soil deposit in the calculation of the small-strain soil stiffness for the evaluation of the seismic performance of the high rise buildings.
- Scrutinizing the extent to which the variations of the degree of saturation of the soil could affect the performance of the high rise buildings, subjected to the earthquake excitations.
- Studying the effects of soil hardening plasticity behavior from the onset of the virgin loading in the assessment of the high rise buildings' seismic performance.
- Proposing the suitable analysis type when dealing with the assessment of the high rise buildings' seismic performance, resting on a saturated soil deposit, under the undrained loading condition.
- Providing the design and practicing engineers with a clear insight on the key factors, influencing the assessment of the buildings, experiencing the foundation rocking.

1.4 Thesis Organization

This thesis is organized into the six chapters. The introduction, as well as the significance, objectives, and scope of this study are presented in the current chapter.

Chapter 2, entitled "Literature Review", presents a comprehensive survey of the literature associated with the dynamic soil-structure interaction. The soil properties, which characterize the dynamic soil behavior, are reviewed, in conjunction with taking an excursion in the realm of the soil constitutive models, simulating the soil behaviors under the cyclic loading or the random loading conditions (e.g., an earthquake excitation). The incorporation of SSI in the PBSD is explained subsequent to delivering a presentation on the concepts of both the aforesaid topics. The knowledge on the assessment of the performance associated with the foundation rocking isolation technique forms the last section of Chapter 2.

Chapters 3 is devoted to the contemporary seismic soil-foundation-structure interaction problems. The effects of the changes in the small-strain shear modulus of the soil deposits on the seismic performance of the shallow-founded buildings are investigated. The aforesaid changes stem from the application of the in-situ shear wave velocity profile or the weighted average shear wave velocity, as well as the variations of the degree of saturation. So long as studying the effects of the soil parameters in the seismic SSI are on the line, the extent to which the hyperbolic hardening parameters, including the failure ratio and elastic-plastic coupling coefficient, are comprehensively elucidated. The said parameters influence the stress increment-strain increment relationship, affecting the induced plastic shear strains considerably.

Chapter 4 probes whether the hardening plasticity-based soil constitutive models could be replaced by the simpler soil models when dealing with the seismic SSI applications. The soil models, adopted in this study, are the isotropic Elastic with Hysteretic Damping (E-HD), elastic-perfectly plastic Mohr-Coulomb with Hysteretic Damping (MC-HD), and Hyperbolic Hardening with Hysteretic Damping (H2-HD) models. The seismic performance of the moment-resisting superstructures, resting on a mat foundation, experiencing the significant foundation rocking, is targeted.

Chapter 5 evaluates the seismic performance of the superstructures, resting on the non-liquefiable soils, in the presence of the excess pore water pressure build-up. Three approaches, including the drained effective stress response analysis, undrained effective stress response analysis, and undrained total stress response analysis, titled “DES analysis case”, “UES analysis case”, and “UTS analysis case”, respectively, are employed in the numerical simulations. The generation of the excess pore water pressure is considered in the UES analysis case while the UTS analysis case is built based on the undrained shear strength of the soil. The excess pore water pressure dissipates in the DES analysis case.

Chapter 6 presents the conclusions of the current research and some recommendations for the further research, followed by the Bibliography.

CHAPTER 2

LITERATURE REVIEW

2.1 General

Referring to Fajfar (2018), the genesis of the structural seismic design in the field of civil engineering was applying the lateral loading on the building frames, whose value was one tenth of the building's total wieght. What is more, the superstructure in reality is a part of the network, called "soil-structure system". As to Eurocode 8 – Part 5 (2004), even granting that the same excitation, recorded at the free field, is applied to the fixed-base and flexible base superstructures, their responses will not be the same. The dissimilarity stems from the differences in the fundamental and higher mode periods of the considered buildings in conjunction with the different mode shapes, and also factors of the modal participation. It should be noted that the seismic responses of the flexibly-supported and fixed-base structures are highly affected by the damping. In a soil-structure system, the damping associated with the superstructure and damping, generated at the soil-foundation interface, form the overall damping. Note that the radiation and internal damping would take place only for a flexible base building. According to Kausel (2010), the seismic Soil-Structure Interaction (SSI) is an interdisciplinary field of science, encompassing the soil and structural mechanics and dynamics, earthquake engineering, geophysics, geomechanics, mathematical-numerical methods, and so on.

The most focal simplifications in the adopted seismic demand in the code provisions with reference to the seismic SSI, reported by Mylonakis and Gazetas (2000), are as follows: (i) acceleration design spectra decrease monotonically usually in proportion to T^{-1} or $T^{-\frac{2}{3}}$ with

increasing the structural period (T); (ii) soil is considered as the homogeneous halfspace medium when estimating the impedances of the foundation, which might result in the overprediction of the structural damping; and (iii) design forces are calculated as per the behavior factor, aka "response modification coefficient", which is either period-independent or has the direct relationship with the structural period. It is well-known that the rise of the performance-based seismic design (i.e., the explicit demonstration of the displacement-based performance beyond the force-based and no-collapse philosophies, that are the traditional focus of the seismic codes and standards, pointed out by Priestley (2000)), offers the potential for the increased resilience in the built environment. Overseeing the structures' responses during the seismic analyses to check out whether they have achieved the desirable performance targets under the different intensity levels of the earthquake excitations is the Performance-Based Design (PBD) framework.

The geotechnical and structural earthquake engineering has been gradually moving towards the performance-based seismic design. It is of interest to note that the PBD approach yields a bit more general design philosophy so as to achieve a specified performance target under a stated level of the seismic hazard. It follows that the Dynamic Soil-Structure Interaction (DSSI) is correspondingly needed to shift from imposing a batch of limits on the structural forces to employing the PBD approach due to the fact that the cost-effective design could be resourcefully achieved via applying the acceptable yardsticks on the transient and residual structural deflections as well as the maximum and permanent foundation rocking.

As time goes by, the quality of design in the structural and geotechnical applications has been excelled in light of considering SSI and PBD in the seismic analyses. The design optimization was adopted with a view to enhancing the merits of the incorporation of SSI in PBD throughout the inherent concepts, one of which is the rocking isolation technique, proposed to optimize the design of the superstructures via letting the seismic energy

enormously get dissipated by the soil plasticity. The energy dissipative capability of the foundation rotation isolation thanks to the inelastic behavior of the soil medium could induce the more economic design; yet, the superstructures would collapse or will become unsafe for the residents owing to the excessive rocking and residual lateral displacements of the buildings.

In this chapter, the dynamic behavior of soils will be explained in addition to the major soil dynamic properties followed by reviewing a handful of common dynamic soil constitutive models. Then, a travel will be made in the realm of the dynamic soil-structure interaction so as to comprehend whether or not the consideration of SSI is essential. The performance-based design concept will be explained, introducing a class of targets for the seismic performance of a structure, whilst the transient and residual structural deflections and rocking rotations must meet some allowable limits. Besides, a summary of design codes in the context of PBD will be presented. The last section of the current chapter appertains to the novel technique of the foundation rocking for performing the seismic isolation. Like all the new methodologies, when being in their infancy, the inviting-plastic-hinging-into-soil isolation technique could put the safety of the structures in jeopardy if the value of the rocking rotation, highly relying on the dynamic properties of the soil deposit, is not predicted precisely. It will be illustrated what ought to be done in order to thoroughly benefit from the said technique in default of making any risk. The next section revolves around the soil properties under the dynamic loadings, inclined to break down the soil structure, implying the changes in the properties of the soil, as Andersen (2015) stated.

2.2 Dynamic Soil Behavior

The combination of the applied mechanics and soil physics delineates one of the civil engineering's branches, called "soil mechanics", investigating the soil behaviors under the sizeable amount of deformations. Moreover, in the static problems, a major concern, from a

safety standpoint, is to evaluate the degree of stability for the entire system of the soil medium, foundation, and superstructure against the possible failure scenarios. The shear strain level under the aforesaid conditions, i.e., the significant deformation and failure event, is in the order of 10^{-3} or greater, referring to Ishihara (1996). One of the branches of soil mechanics, dealing with the behavior of the soils, subjected to the motion and vibration, is the soil dynamics. According to Prakash (1981), the dynamic loading would be generated by the seismic excitations, wind and wave actions, traffic vibrations (including landing aircraft), bomb explosions, and operation of machinery. Such loads are imposed on the soil layers and superstructures plus the subterranean structures. Figure 2.1 graphically represents the different types of dynamic loading and corresponding sources. When the soil deposit is in motion, the inertia force plays a paramount role, relying on the frequency at which the soil is deformed (Whitman and Liao, 1988). The shorter the time interval of the deformation, the more effect of the inertia force according to Das and Ramana (2011). Furthermore, the existence of the infinitesimal strain does not necessarily occasion lessening the effect of the inertia force due to the fact that increasing the rapidity in motion could potentially boost the level of the inertia force. Hence, a cyclic test is not demanded to be always considered as dynamic when the frequency of the loading is too small that the inertia of the soil does not influence the results. In other words, according to Wichtmann (2005), the inertia forces are negligible or relevant when the cycles are applied with a low or large loading frequency, consecutively. If the latter takes place, the loading is dynamic. To give an idea, the load frequencies for the earthquake on the structures and foundations for machinery are 0.1-10 Hz and up to 100 Hz, respectively, as reported by Head (1986).

Another factor, which characterizes the dynamic behavior, is the duration of load application. The static problems involve the much longer time of loading compared to the dynamic problems (Ishihara, 1996). The speed effect or strain rate effect also expresses the

time of the load application. It is noteworthy to state that a monotonic load is the static load, incrementally or decrementally building up over time without being cycled, as stated by O'Reilly and Brown (1991). The monotonic load, aka “slow static loading”, could become the rapid or transient loading when the loading to the failure is executed in a very short time.

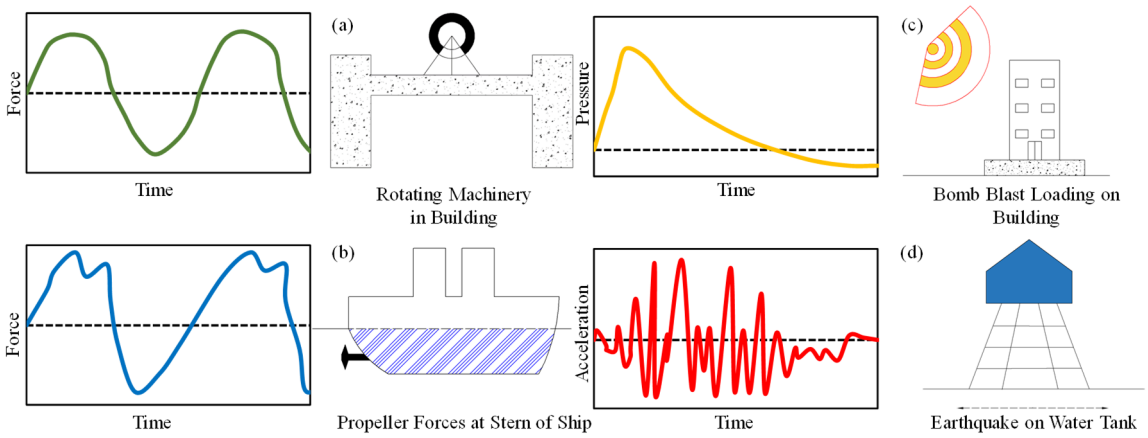

Figure 2.1 Characteristics and sources of common dynamic loads: a) harmonic loading, b) complex periodic loading, c) transient or impulsive loading, and d) earthquake loading (modified after Clough and Penzien, 1975).

The loads could technically be classified as dynamic or static on the basis of whether or not a load is time-varying. In that regard, the magnitude, direction, and action point of the static loads do not change with time, as pointed out by Bai and Xu (2019). In the realm of soil dynamics, Lamb (1904) set the ball rolling via studying the vibration of the elastic ground. The dynamic problems can be classified by the repetitiveness in the loading. The regularity in the frequency and magnitude of the repetitive loading define the cyclic load, meaning the uniform changes in the states of the stress and strain over the course of time. On the other hand, the seismic loading, which is categorized under the dynamic loading application, involves 10-20 times repetition of the loads with the differing amplitudes, mentioned by Ishihara (1996). It is noteworthy to mention that the earthquake-induced load is considered as a random load owing to the highly irregular fashion. According to Stafford and Bommer (2009), the liquefaction hazard assessment demands the number of the equivalent cycles, occurring amidst a seismic excitation. The use of the equivalent cycles could help overcome the complexity of the

problem, stemming from the complicated nature of an earthquake. Beyond of that, investigating the behaviors of a soil sample under the real format of an earthquake load in the laboratory via the available apparatus is a daunting task, the number of the equivalent cycles is employed to carry out the experiments. As a result, the term “cyclic shear strain” is common to be used in the dynamic context whether the type of the loading is technically cyclic or inherently cyclic, i.e., the seismic excitations.

2.2.1 Properties of Dynamically Loaded Soils

As stated by Ishihara (1996), the body waves form the main part of a seismic shaking, which are propagating upwardly whilst traveling from the seismic bedrock towards the ground surface. The two wave types, which construct the body waves, are the transverse and longitudinal waves. The former and latter are also called the shear and compressional waves, respectively. In the idealized level ground condition, the core cyclic deformations and stresses, induced in the soil elements, resulted from the shear waves, propagating upward from the seismic bedrock. Insofar as the soil-structure interaction is concerned, which is the subject of the following sections in this chapter, the above-mentioned cyclic deformations could affect the seismic performance and dynamic responses of the superstructures as well as inducing the damage. The seismic soil-structure interaction is concerned with the shear waves in preference to the longitudinal waves on account of a prevalent greater energy content in the former. It is, indeed, not surprising that the evaluation and analysis of the cyclic behavior of the soils have attracted the attention from the geotechnical engineering communities.

During an earthquake, the seismically-induced damage, imposed on a superstructure, is substantially affected by the response of the supporting soil deposit, governed by the dynamic soil properties, previously reported by Das and Ramana (2011). The commonplace dynamic properties of a soil are the shear modulus, related to the shear wave velocity, and corresponding

damping ratio. A cluster of factors affect the aforesaid parameters during a seismic event. Referring to Hardin and Black (1968) and Kramer (1996), such factors could be summarized as follows: (i) soil type; (ii) relative density; (iii) plasticity index; (iv) degree of saturation; (v) effective confining stress; (vi) overconsolidation ratio (OCR); (vii) amplitude of the cyclic strain; and (viii) number of the loading cycles. Ishibashi and Zhang (1993) reanalyzed the available data for the sands and clays with a view to establishing the unified formulae for the dynamic shear moduli and damping ratios to cover the wide variety of soils from the non-plastic sands to the highly plastic clays. The work of Ishibashi and Zhang (1993) outperformed the attempt, made by Vucetic and Dobry (1991), wherein the effective mean pressure was dismissed notwithstanding its considerable role, emphasized by Ishibashi (1992).

Since the response of the soils to the cyclic loading governs the level of the earthquake-induced damage (Kramer, 1996), Prakash (1981) stated that the stiffness degradation, and hysteretic damping as well as the plastic deformation during the unloading ought to be considered in mimicking the dynamic behavior of a soil medium. The shear modulus reduction curve could be graphically visualized via Equation (2.1) (Ishibashi and Zhang, 1993). Figure 2.2 depicts the variations of the $k(\gamma)$ and $m(\gamma) - m_0$ with γ for the sandy soils based on the analyzed available experimental data, done by Khouri (1984), proposing the Equations (2.2) and (2.3), best fitting the data points.

$$\log\frac{G}{G_0} = \log k(\gamma) + [m(\gamma) - m_0]\log p' \tag{2.1}$$

$$k(\gamma) = 0.5\left[1 + tanh\left\{ln\left(\frac{0.000102}{\gamma}\right)^{0.492}\right\}\right] \tag{2.2}$$

$$m(\gamma) - m_0 = 0.272\left[1 - tanh\left\{\ln\left(\frac{0.000556}{\gamma}\right)^{0.4}\right\}\right] \tag{2.3}$$

where, G is the shear modulus, G_0 is the maximum shear modulus, $k(\gamma)$ is a decreasing function of the cyclic shear strain amplitude γ, the power $m(\gamma)$ is an increasing function of γ, and p' is

the mean effective stress. It shall be noted that $k(\gamma)$ becomes unity, 0.5, and zero at the very small cyclic shear strain ($\leq 10^{-6}$), $\gamma = 10^{-4}$, and $\gamma = 10^{-2}$, in the order given. On the same token, $m(\gamma) - m_0$ changes between zero and 0.544 from the very small strain to $\gamma \geq 10^{-1}$. m_0 is equal to $m(\gamma \leq 10^{-6})$.

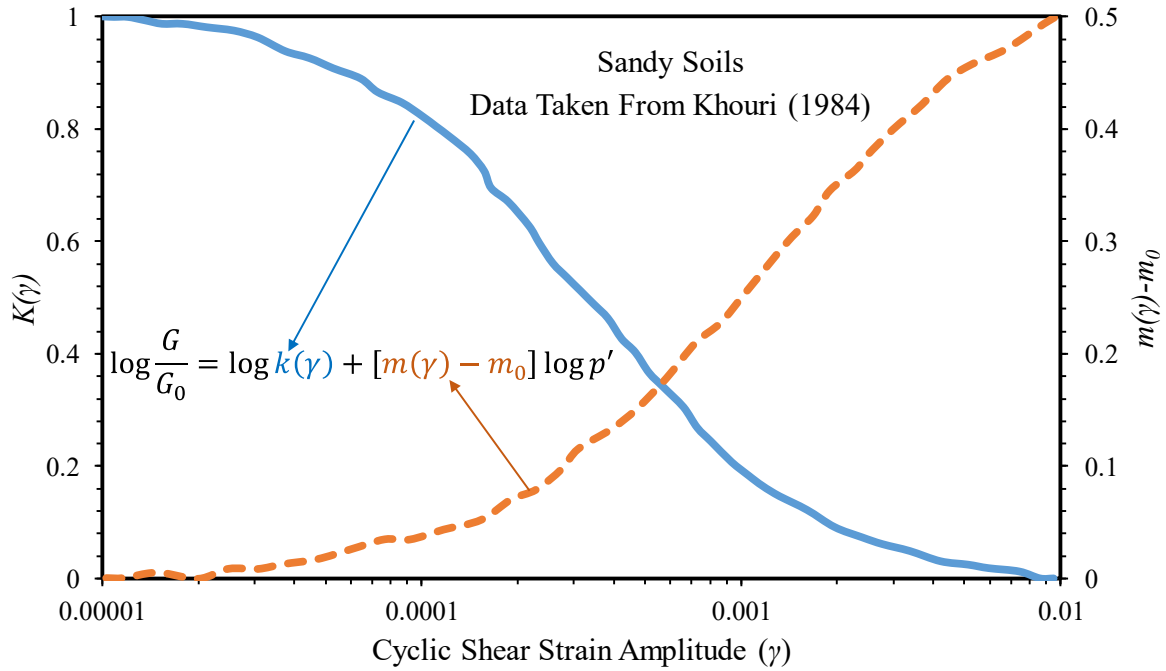

Figure 2.2 Variations of $k(\gamma)$ and $m(\gamma) - m_0$ versus γ for sands

It is known that the soils dissipate energy when subjected to the cyclic loading. $D = \frac{W_l}{(4\pi W_{ms})}$ (Kumar, 2008), wherein W_l is the dissipated energy in a cycle of loading (i.e., the area inside the hysteresis loop, shown in Figure 2.3), and W_{ms} is the stored maximum strain energy during a cycle (i.e., the area of the triangle, shown in the same figure as W_l), quantifies the so-called damping ratio under the concept of the stress-strain hysteresis loop. This energy dissipation behavior of a soil, commonly termed as "damping", significantly affects the soil-structure interaction phenomenon as well as the site effects and ground response analyses during the earthquakes, as mentioned by Lin et al. (1996). Forasmuch as the damping ratio is a function of $\frac{G}{G_0}$, the damping of the sands could be estimated using Equation (2.4) (Ishibashi and Zhang, 1993), denoting that the maximum damping ratio is 33.3% at the very high shear strain level,

which is in line with the previous studies on the sands (e.g., Sherif et al., 1977; Tatsuoka et al., 1978).

$$D = 0.333\left\{0.586\left(\frac{G}{G_0}\right)^2 - 1.547\frac{G}{G_0} + 1\right\} \tag{2.4}$$

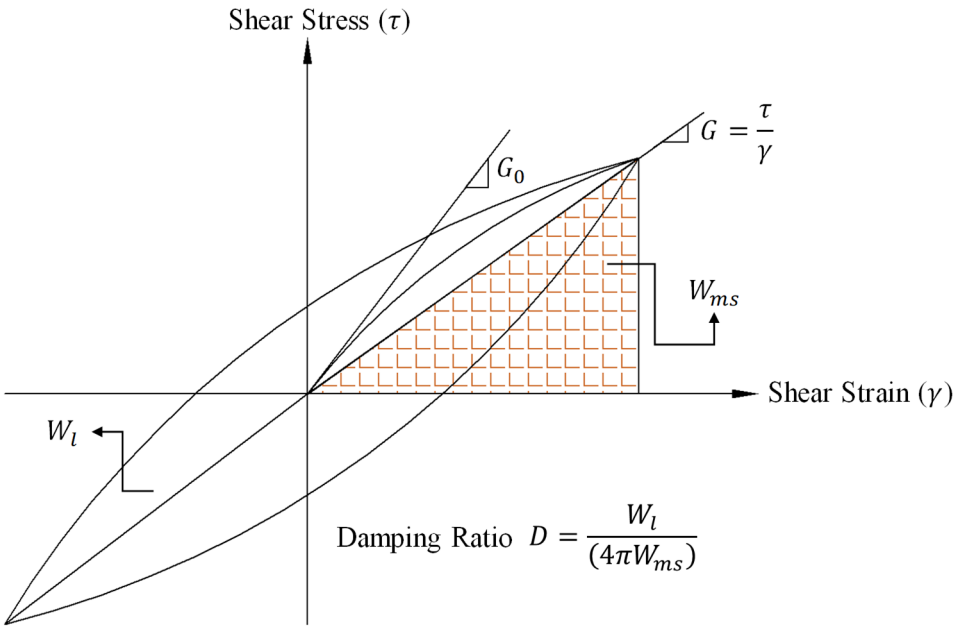

Figure 2.3 Presentation of hysteresis loop for one cycle of loading, exhibiting G_0, G, and D

A series of cyclic triaxial tests was conducted by Kokusho (1980) with the purpose of scrutinizing the possible impacts that the confining stress might have on the dynamic soil properties, which are strain-dependent. Figure 2.4a illustrates that the shear modulus reduction's rate of the Toyoura sand is on the increase while the confining stress is on the decrease. The research works of Hardin and Drnevich (1972), and Tatsuoka et al. (1978) cast light on the parameters, influencing the damping property of a soil, announcing that the damping ratio is on the increase so long as the shear strain amplitude and effective stresses increases and decrease, respectively, while the other parameters such as the void ratio and number of cycles do not have the significant effects. The damping characteristics of Toyoura sand are displayed in Figure 2.4b.

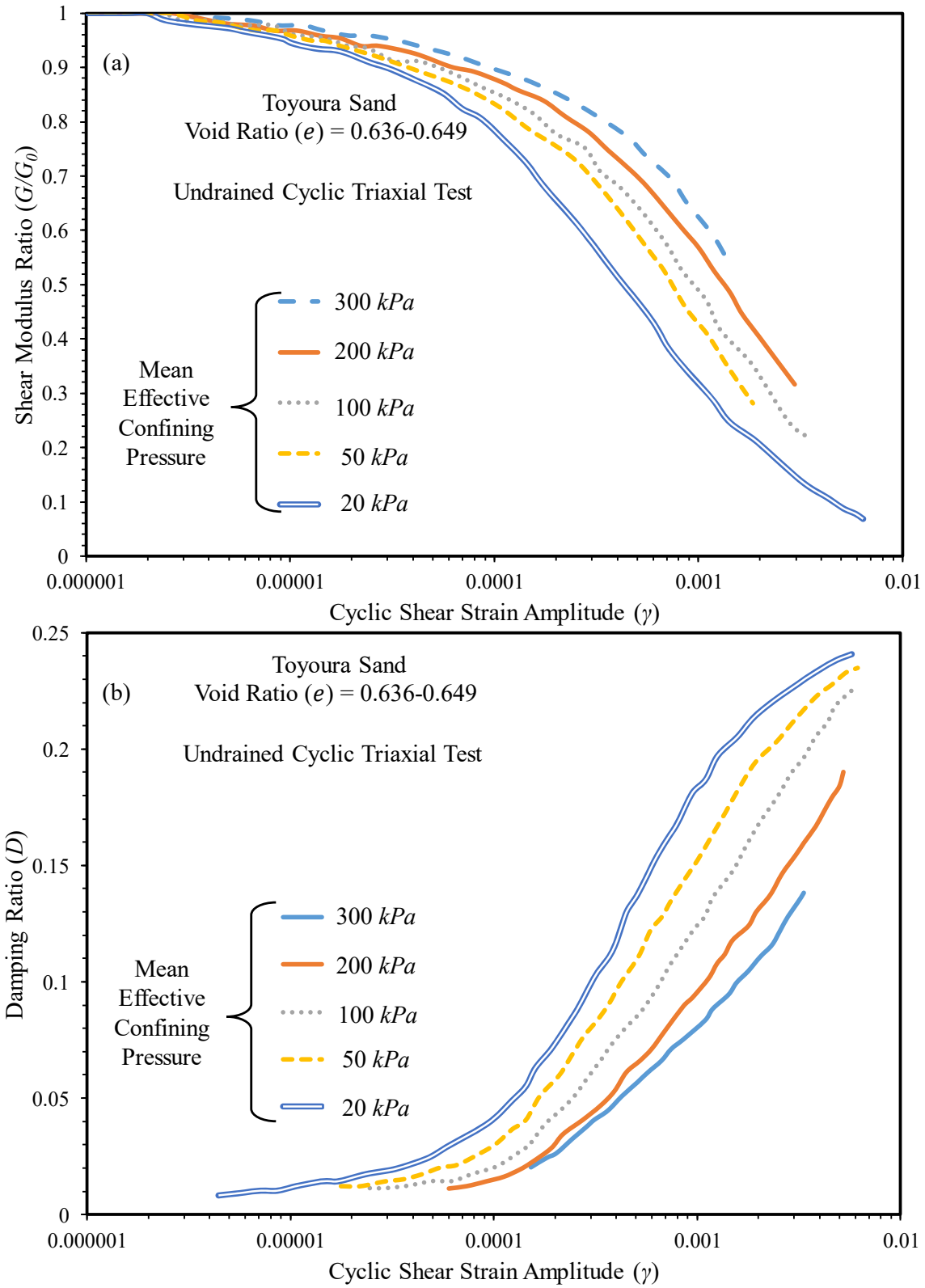

Figure 2.4 Effects of confining pressure (p') on: (a) strain-dependent shear modulus, and (b) strain-dependent damping ratio of Toyoura sand (after Kokusho, 1980)

The buildings might experience the loss of the bearing capacity in the seismic-prone zones as a result of the excess pore water pressure build-up. It is of note that such an incident could

take place owing to the stress-strain loops, which are not completely closed. Such non-closed loops under the cyclic loading with the large amplitude and limited number of cycles give rise to the generation of the excess pore water pressure and strain accumulation, as mentioned by Wichtmann et al. (2005). By way of illustration, the serviceability of the superstructures would be in peril because of the dramatic increase in the settlement when the number of loading cycles is large while the shear strain amplitude is small (i.e., $<10^{-3}$) for the drained behavior. In this light, the extent of damage was categorized in the three classes, i.e., the no damage to light damage, medium damage, and extensive damage, in accordance with the settlements of 0-100 mm, 100-300 mm, and 300-700 mm, respectively (Ishihara and Yoshimine, 1992). Not to mention, the settlements (particularly the differential settlements) could impair the functionality of the structures after the earthquake events. Considering the findings, announced by Wichtmann et al. (2005), the next paragraph explains the stress-independent modulus reduction and damping curves to be utilized in the undrained effective stress analysis with the excess pore water pressure build-up.

The different types of laboratory tests have been conducted so as to introduce the curves of the modulus reduction and damping ratio, basically characterizing the behavior of a soil under the cyclic loading. For instance, Doroudian and Vucetic (1995), Menq (2003), and Kishida et al. (2009) carried out the simple shear, resonant column, and triaxial compression tests for the aforesaid purpose. It is interesting to note that the reference shear strain, symbolized by γ_r, proposed by Hardin and Drnevich (1972), depends on the effective stress by reason of the fact that the shear strength and maximum shear modulus are scaled differently with the effective stress. Moreover, the modulus reduction and damping curves are commonly plotted against the cyclic shear strain amplitude; consequently, the dependency of the said curves on the mean effective stress potentially could be a problem when the excess pore water pressure develops during loading in the undrained effective stress analysis. In reply, Yniesta and Brandenberg

(2017) posited that the normalized shear modulus reduction and damping should be plotted against the stress ratio (η) in place of the cyclic shear strain, resulting in the practical pressure-independent curves. The ratio of the deviator stress (q) and mean effective stress (p') defines the stress ratio. Such a replacement would be beneficial for implementation in the drained and undrained effective stress analyses, wherein the water table exists and the excess pore water pressure could be generated.

Considering the fact that Kokusho et al. (1982) put particular emphasis on the influence of the soil plasticity index (I_p) on the shear modulus reduction and damping ratio, Ishibashi and Zhang (1993) modified Equations (2.2) and (2.3) so as to take into account the soil plasticity index in modeling the dynamic soil behavior. In that respect, $K(\gamma, I_p)$ and $m(\gamma, I_p) - m_0$, presented in Equations (2.5) and (2.6), consecutively, should be placed in the above-mentioned equations. Thanks to satisfying the continuity of the material properties from the sands to the clays, Equations (2.5) and (2.6) reduce to Equations (2.2) and (2.3) when I_p equals zero. The new parameter is $n(I_p)$, which is 0.0, $3.37\times10^{-6}{I_p}^{1.404}$, $7.0\times10^{-7}{I_p}^{1.976}$, and $2.7\times10^{-5}{I_p}^{1.115}$ for the sandy soils ($I_p = 0$), low plastic soils ($0 < I_p \leq 15$), medium plastic soils ($15 < I_p \leq 70$), and high plastic soils ($I_p > 70$), respectively. Figure 2.5 displays the relation between $k(\gamma = 0.1\%, I_p)$ and I_p for a range of the soil plasticity index values. Besides, Equation (2.7) (Ishibashi and Zhang, 1993) makes a connection between I_p and the damping ratio.

$$k(\gamma, I_p) = 0.5\left[1 + tanh\left\{ln\left(\frac{0.000102 + n(I_p)}{\gamma}\right)^{0.492}\right\}\right] \tag{2.5}$$

$$m(\gamma, I_p) - m_0 = 0.272\left[1 - tanh\left\{\ln\left(\frac{0.000556}{\gamma}\right)^{0.4}\right\}\right]e^{-0.0145{I_p}^{1.3}} \tag{2.6}$$

$$D = 0.333\frac{1 + e^{-0.0145{I_p}^{1.3}}}{2}\left\{0.586\left(\frac{G}{G_0}\right)^2 - 1.547\frac{G}{G_0} + 1\right\} \tag{2.7}$$

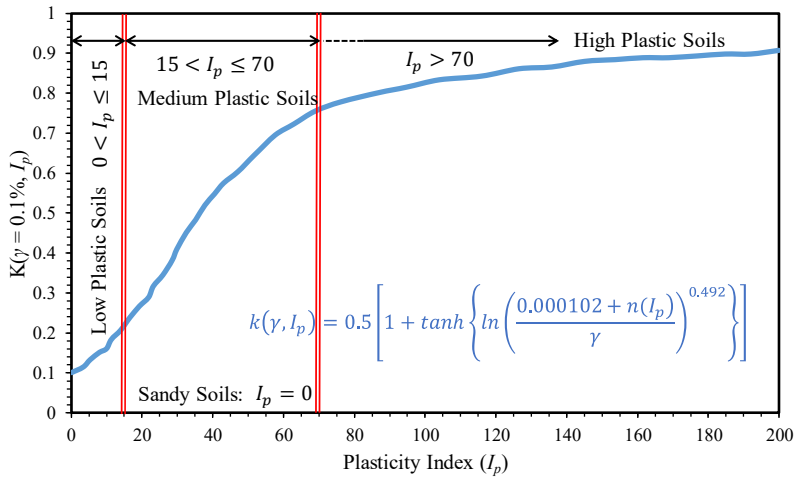

Figure 2.5 Relationships between $k(\gamma = 0.1\%, I_p)$ and plasticity index (I_p) (modified after Ishibashi and Zhang, 1993)

The demand for the small-strain and large-strain dynamic soil properties in the nonlinear numerical analyses, e.g., the seismic soil-structure interaction simulations, have been dramatically augmented, underlined by Kokusho (1980). To graphically follow the previous statement, Figure 2.6 summarizes the dependency of the shear modulus and damping ratio on the cyclic shear strain, soil plasticity index, and mean effective confining stress, as highlighted by Srbulov (2011). More comprehensively, all the important factors, which are known to be able to have some influences on the $\frac{G}{G_0}$ and D, are listed in Table 2.1.

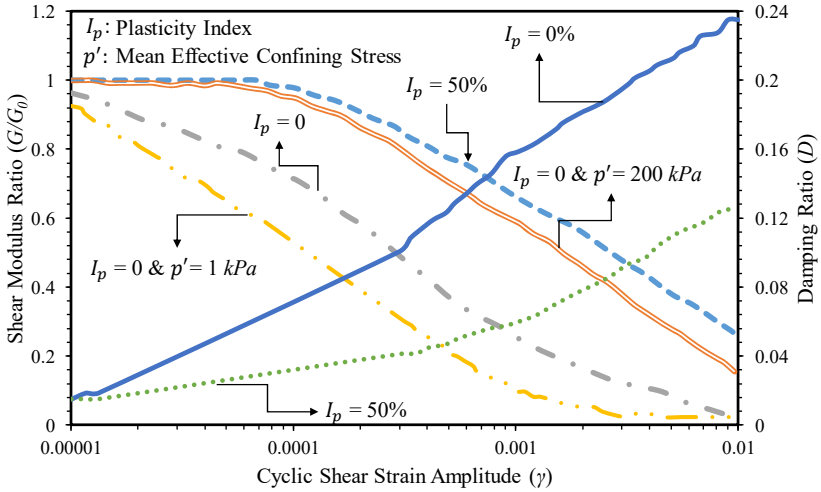

Figure 2.6 Dependence of shear modulus and damping ratio on shear strain, soil plasticity index (I_p) (modified after Vucetic and Dobry, 1991) and mean effective confining stress (p') for non-plastic soil (modified after Ishibashi, 1992)

Table 2.1 List of influential factors in estimation of shear modulus ratio and damping ratio

Factors	Symbol	$\frac{G}{G_0}$	D	References
Mean Effective Stress	p'	DR[1]	IR[3]	Dobry and Vucetic (1987) and Kramer (1996)
Void Ratio	e	DR	IR	
Geologic Age	t_g	DR	IR	
Cementation	C	DR	IR	
Overconsolidation Ratio	OCR	NE[2]	NE	
Plasticity Index	I_p	DR	IR	
Cyclic Shear Strain	γ	IR	DR	
Cyclic Shear Strain Rate	$\dot{\gamma}$	NE	IR	
Number of Loading Cycles	N	ID for Clays DR for Sands (Drained Condition) ID for Sands (Undrained Condition)	NS[4] (for Moderate γ and N)	

[1]DR: Direct Relationship.
[2]NE: No Effect.
[3]IR: Inverse Relationship.
[4]NS: Not Significant.

Subsequent to taking the effects of the confining stress, excess pore water pressure, and plasticity index on the modulus reduction and damping ratio curves into consideration, Zhang et al. (2005) claimed that the geologic age must be taken into consideration in the determination of the soil stiffness and damping, i.e., the energy dissipation for the seismic analysis. Comparing the obtained trends together in Figure 2.7 exemplified that the highest acceleration occurred, considering both the age and mean effective stress. The two spectra, including the mean effective stress effects, exhibited the peak accelerations, which are 2 to 4 times higher than the other two spectra. Making use of the developed trend by Vucetic and Dobry (1991) in the comparison casts light on the influential parameter of the geologic age as they did not consider the confining stress or age.

The seismic loading rate, as to Park and Hashash (2008), does not have any specific effect on the dynamic soil behavior. On the same topic, Matešić and Vucetic (2003) found that the shear strain rate has no particular impact on the shape of the $\frac{G}{G_0} - \log\gamma$ curve. Their

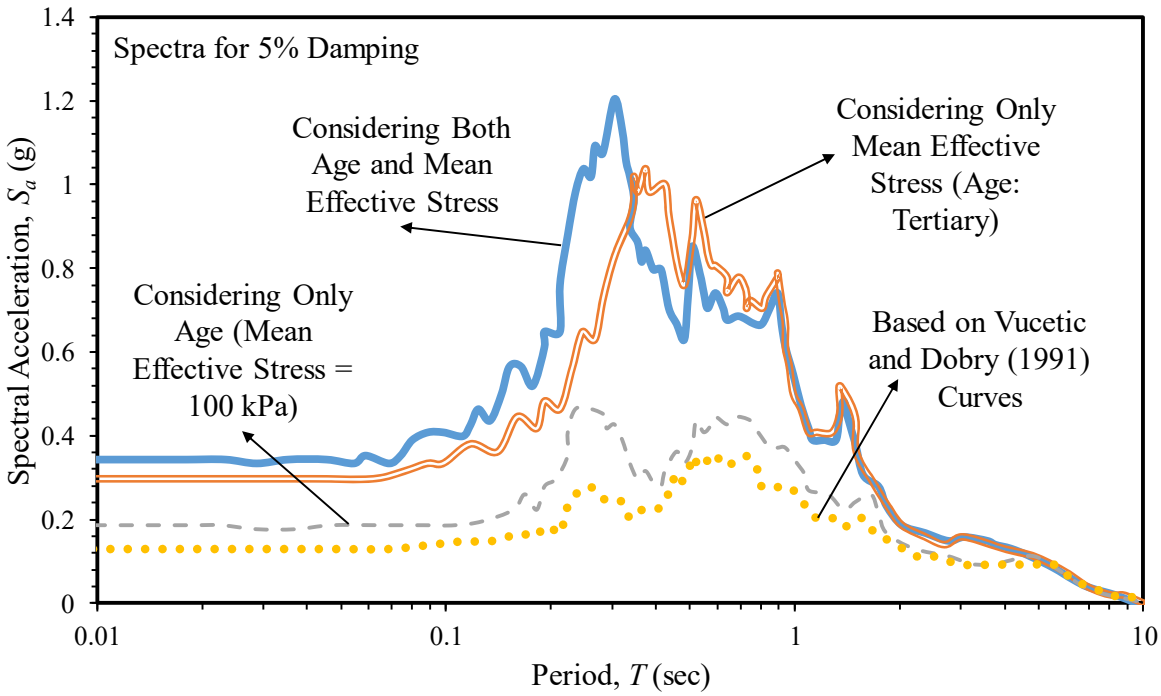

Figure 2.7 Comparing effects of geologic age and mean effective stress on spectral accelerations (modified after Zhang et al., 2005)

study revealed the coincided normalized shear modulus curves of the two clays (Augusta and La Cienega) and two sands (Nevada and Toyoura) under the different values of the shear strain rate ($\dot{\gamma}$). The research work of Shibuya et al. (1995), using the undrained cyclic torsion shear test on the normally consolidated clayey samples, revealed that the damping ratio exhibited the significant dependence on the loading frequency (f). The $D = D_{f=0.1} - 0.02(1 + \log f)$ was proposed by Shibuya et al. (1995) to account for the effects of the shear strain rate on the damping ratio, implying the inverse relationship as shown in Figure 2.8. $D_{f=0.1}$ is the damping ratio at the frequency of 0.1 Hz. Note that the shear strain rate escalates proportionally with the increase in the frequency of the loading.

Another aspect of the soil dynamics is the generation of the excess pore water pressure in a saturated soil, as a two-phase medium, during the cyclic loading. The coupled and uncoupled analyses are the two approaches to be employed to model such a behavior. The effect of the soil-water interaction is ignored in the uncoupled analysis, implying that the excess pore water

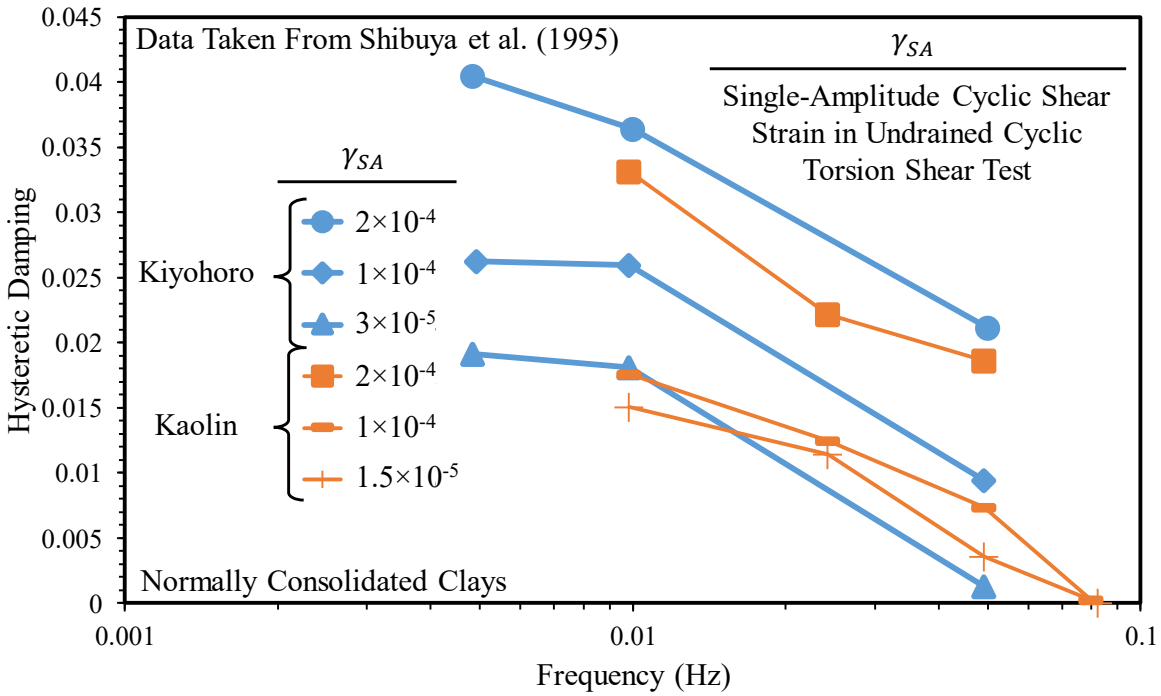

Figure 2.8 Effect of frequency of loading on hysteretic damping

pressure has to be separately included using a pore pressure generation model. Calculating all the unknowns in the problem of interest at once at each single time step engenders the formulation of the coupled analysis, providing a more realistic representation of the physical phenomena in a saturated soil under the dynamic load. The relative displacements of the solid and fluid phases, as well as the pressure of the fluid phase are the unknowns in this complete set of equations. As Taiebat et al. (2007) pointed out, the fully coupled analysis ought to possess the momentum balance not only for the fluid phase but also for the mixture of the solid particles and fluid. They finally stated that the soil-fluid system must reach the mass balance. Under the earthquake action, as an example of the dynamic problems, the high-frequency oscillation is not considered as an important element. In that connection, the fluid phase's relative velocity is believed to have the little influence on the system in the dynamic problems. Thus, Zienkiewicz et al. (1999) stated that such a factor can be eliminated in the geotechnical earthquake engineering.

It was reported by Ohara and Matsuda (1988) in accord with the results, presented in Figure

2.9, that the minimum shear strain amplitude ($\gamma_{dyn_{min}}$), producing the excess pore water pressure, has the direct relationship with the overconsolidation ratio. $\gamma_{dyn_{min}}$ was 0.05%, 0.12%, 0.22%, and 0.29% for 1, 2, 4, and 6 as OCR, respectively, in the undrained two-way strain controlled cyclic simple shear tests. The Kaolinite clays under examination were in the range of NC to OC. It was accordingly concluded that the cyclic shear-induced excess pore water pressure depends on OCR and the number of cycles as well as the shear strain amplitude. The increase in the excess pore water pressure was captured in the dynamic triaxial test device, carried out by Koutsoftas (1978), in connnection with the escalation in the amplitude of the axial strain.

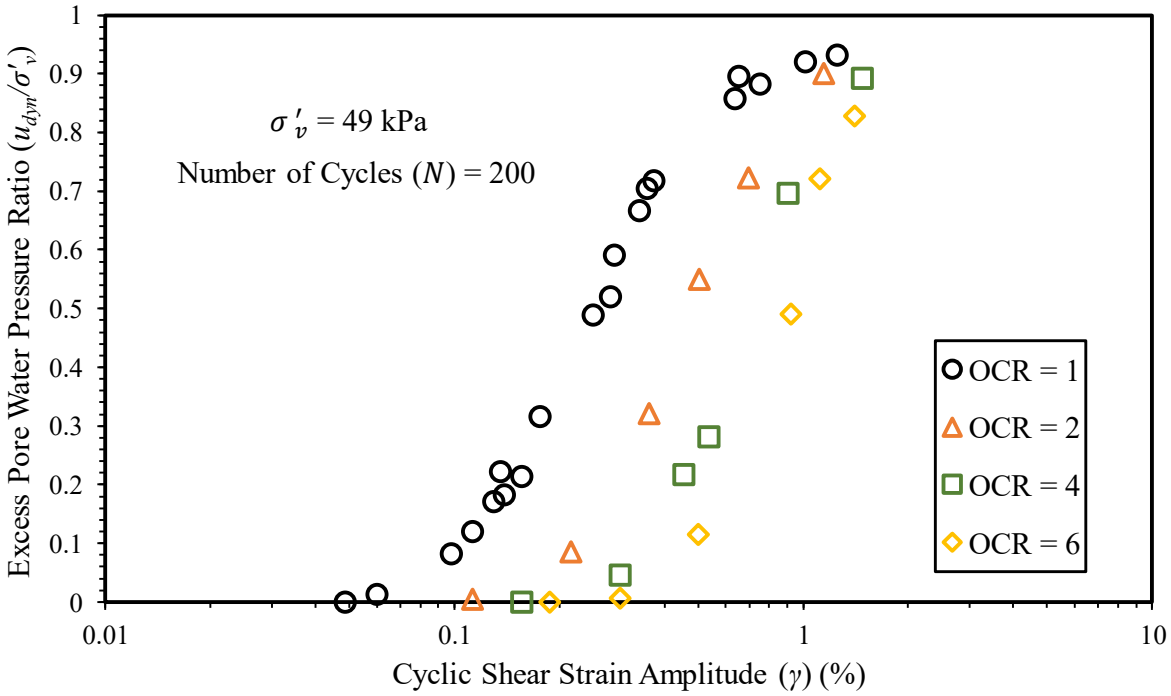

Figure 2.9 Relationships between cyclic shear strain (γ_{dyn}) and excess pore water pressure ratio (u_{dyn}/σ'_v) for OCR = 1, 2, 4, and 6 (modified after Ohara and Matsuda, 1988)

A threshold cyclic shear stress ratio was reported by Ansal and Erken (1989) for the dynamic analysis of the saturated soils. It was mentioned that the excess pore water pressure will not be generated if the shear stress under the cyclic loading does not surpass the proposed threshold, derived from the clayey samples using the cyclic simple shear test. In that regard,

the magnitude of the excess pore water pressure build-up is $\Delta u = (k + \log N)\left[\frac{\tau}{\tau_f} - \chi\right]$, wherein k is the material constant (obtained from the regression analysis), N is the number of cycles, $\frac{\tau}{\tau_f}$ is the cyclic shear stress ratio, and χ is the threshold cyclic shear stress ratio. The lines on Figure 2.10 present the relationships between the pore water pressure ratio and cyclic stress ratio whilst considering the different numbers of cycles. All the lines met the vertical axis at one single point, exhibiting the threshold cyclic shear stress ratio. The saturated sands also showed such a behavior under the cyclic strains, reported by Dobry et al. (1982).

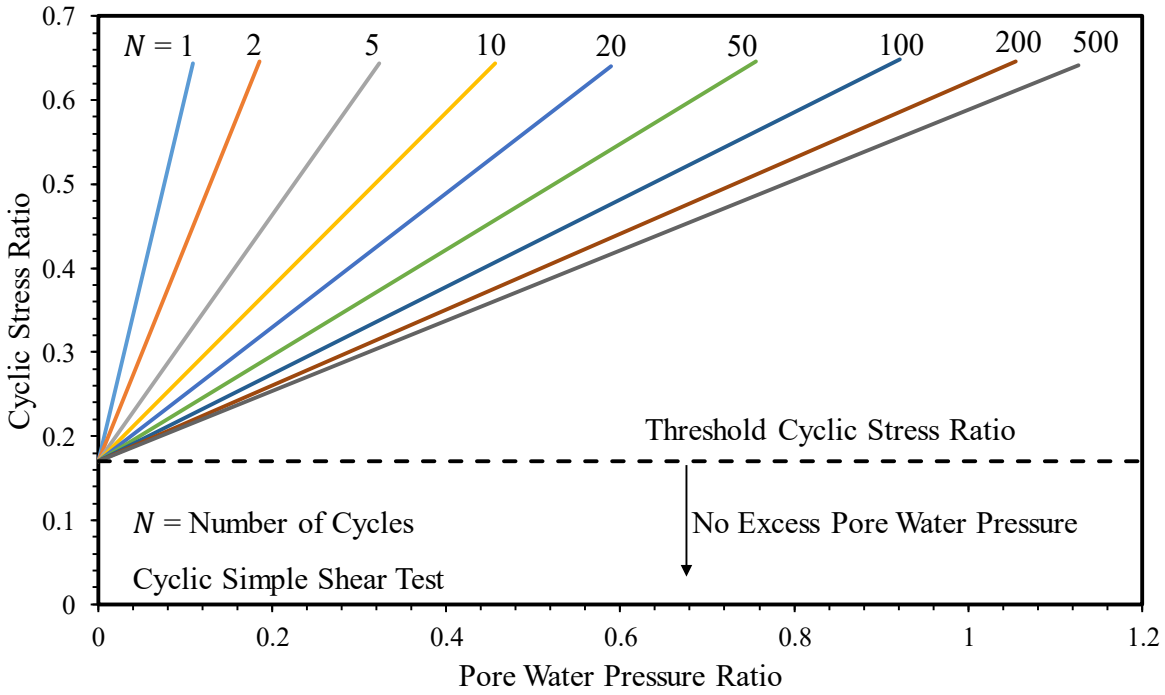

Figure 2.10 Cyclic stress ratio-pore pressure relationship for different number of cycles (modified after Ansal and Erken, 1989)

As per the literature, the strain-dependent nature of the generation of the excess pore pressure is well-established. The excess pore pressure is typically generated once the shear strain breaches a threshold value of 0.01% and 0.1% for the saturated sands and clays, respectively, triggering the degradation of the soil stiffness and strength. Hsu and Vucetic (2006) admittedly reported that the said threshold for the saturated cohesive soils outnumbers the counterpart for the cohesionless soils. Ladd et al. (1989) reported the threshold cyclic shear

strain of 0.01% for the normally consolidated dry and saturated clean sands from the strain-controlled tests below which there is neither densification nor prestraining of the dry sands whilst there is no pore-water pressure build-up for the saturated sands. According to Vucetic (1994), exceeding the threshold shear strain in terms of the volumetric cyclic leads to the nonlinear-inelastic behavior with the significant permanent microstructural changes. Such a condition induces the hardening behavior and excess pore water pressure build-up for the drained and undrained conditions, respectively. In such strain ranges, the shear strains are accompanied by the volumetric strains, demonstrated in Figure 2.11, signifying that coupling between the volumetric and shear responses in the constitutive modeling is an essential feature (Seidalinov, 2018). For the repeated loading cycles, the volumetric deformations commence to accumulate whilst the hysteresis loops begin to become more inclined with a smaller area according to Chitas (2008).

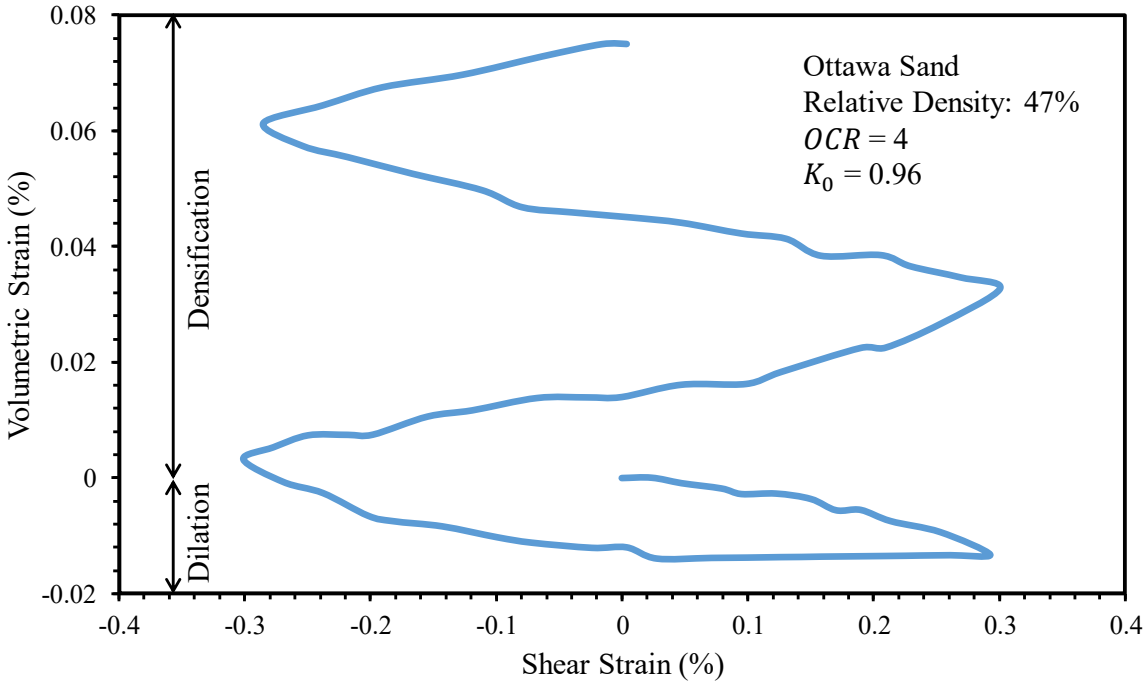

Figure 2.11 Relation of volumetric strains and shear strains under cyclic loading (modified after Pecker, 2008)

The boundaries, shown on Figure 2.12, were presented by Díaz-Rodríguez and López-Molina (2008), summarizing the strain regimes and thresholds for the saturated clays under the

undrained cyclic loading. There are four boundaries, viz, the linear threshold (γ_{tl}), volumetric cyclic threshold (γ_{tv}), degradation strain threshold (γ_{td}), and flow threshold (γ_{tf}). Such thresholds provide the information on the type of the stress-strain, level of degradation, and possibility of the excess pore water pressure build-up.

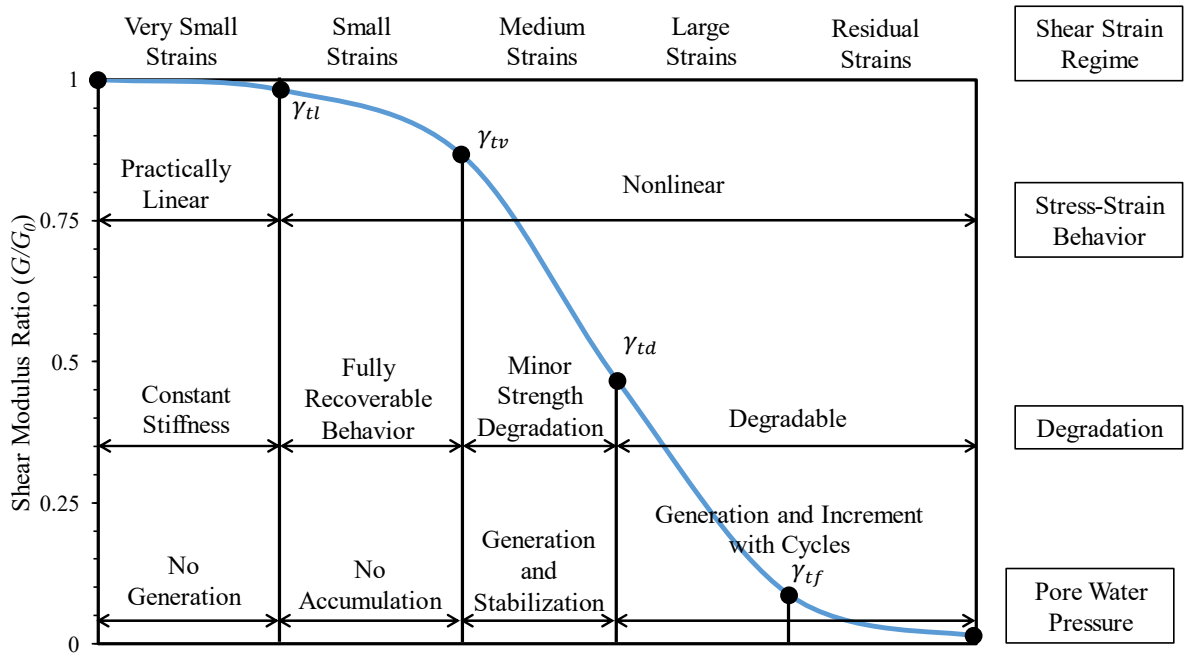

Figure 2.12 Cyclic shear strain thresholds: linear threshold shear strain (γ_{tl}), volumetric cyclic threshold strain (γ_{tv}), degradation strain threshold (γ_{td}), and flow threshold (γ_{tf}) (after Díaz-Rodríguez and López-Molina, 2008)

Subsequent to going through the major properties of a soil in the soil dynamics field, it is worth studying the soil constitutive models, capturing the different behaviors a soil. Puzrin (2012) stated that compared to the other natural and man-made materials, soils are mayhap the most complex materials in the four corners of the world in terms of the mathematical description of their mechanical behavior due to the nonlinearity in the initial loading, unloading and reloading, stress path dependency (reaching the different strains at the same stress), stress level dependency (changing the properties with the confinement stress), irreversibility (producing the residual strains in a closed stress cycle), material memory (remembering the highest stress before the unloading and following the initial loading curve after reaching it in reloading), dilatancy (changing in the volume during the shearing), hardening (changing in the

yield stress with the plastic straining), and rate dependency (the different stress-strain curves at the various strain rates), plus the time dependency (the creep, aging, and relaxation).

In fact, soil is a multi-phase material incorporating the soil skeleton, pore water and/or pore air. Potts (2002) indicated that, amongst the above-mentioned phases, mimicking and capturing the soil skeleton behavior is not only the hardest but also the most crucial one forasmuch as the total deformation of the entire medium, consisting of the soil skeleton, pore water and/or pore air, is governed by the soil skeleton phase. The generalized relationship between the stress (stress increment) and strain (strain increment), linking the equations of the equilibrium and compatibility, is termed "soil constitutive model", consisting of the mathematical expressions, which model the behavior of a soil in a single element. For the sake of practicality, the soil model should be able to make statements for the soil behavior under all the stress and strain paths, as underscored by Prevost and Popescu (1996). Since soils are, by and large, the weakest materials involved in the common geotechnical problems according to Lade (2005), the deformation and possibility of the failure of the structure are unquestionably determined by them; in consequence, it is focal to characterize the material properties accurately over the entire ranges of the stresses and strains to which the soils will become exposed.

Conducting the numerical simulations has become increasingly popular amongst the design engineers thanks to the availability of the powerful computers and also wider applicability of the numerical methods (e.g., the finite difference, and finite element). Nonetheless, such numerical solutions are only valid if the materials behaviors, represented by the material constitutive models, are realistically mimicked. Since becoming familiar with the main dynamic soil properties, a succinct summary of the soil constitutive models in the land of the dynamic loads is presented hereinafter.

According to Potts (2002), the analytical solutions associated with the conventional geotechnical problems (e.g., the soil deformation and failure stage) inherently required a class of oversimplifications contributed to the geometries of the problems as well as the artificial boundary conditions. Potts (2002) stated that the work of Coulomb in 1773 is the starting point for the generation of the soil constitutive relationships. Indeed, the development of the numerical methods should not be overlooked. For decades, a large number of advanced constitutive soil models have been developed on the basis of the different concepts. Needless to say, some models proclaimed their superiority over the others. Nevertheless, the reality is that no universal constitutive model has yet been resourceful in predicting all the possible behaviors of a soil under the general loading conditions referring to Prevost and Popescu (1996) and Muravskii and Frydman (1998).

The consistency of the soil models must be evaluated in respect to the basic theoretical requirements of the continuity and stability. What is more, the soil models parameters should be determined easily using the standard tests whilst the implementation convenience of the soil models into computer calculations is essential, as pointed out by Bazant (1985). The accuracy of the simplest models, named “elastic soil models”, relies on the evaluation of the soil elastic parameters, i.e., the elastic shear and bulk moduli. The elastic continuum analytical method is based on the closed form solution, proposed by Mindlin (1936), for the application of the point loads to a semi-infinite media. The soil stress-strain behavior is highly non-linear (Atkinson, 2000), though. As an example, presented by Gazetas and Apostolou (2004), the seismic loading, transmitted onto the foundations, caused the considerable nonlinear inelastic actions in the soils and soil-structure interfaces in the 1994 Northridge earthquake (USA) and 1995 Kobe earthquake (Japan). On the same topic, Zolghadr Zadeh Jahromi (2009) postulated that the above-mentioned method cannot deal with the geometric and material nonlinearities. Henceforth, modeling the soil-structure system’s nonlinear responses demand to make use of

the more advanced modeling techniques. To do so, the bi-linear and Dancan-Chang hyperbolic models (David and Zdravkovic, 1999) were established to model the nonlinear elastic behavior. The shortcoming of the nonlinear elastic soil model is the lack of reproducing the volume change when the soil is sheared. Despite the fact that the nonlinear hysteretic behavior could be simulated by an equivalent linear approach referring to Schnabel et al. (1972), Idriss and Sun (1992), and Kramer (1996), the use of such a method can be misleading for the problems concerning the permanent ground deformation and failure as it is assumed that the shear strain at the end of the cyclic loading ends up with zero. In spite of that, it is a possibility to make use of the equivalent linear soil model particularly in the geotechnical earthquake engineering applications, involving the low strain levels. Reaching a higher level of mimicking the dynamic soil behavior is feasible by means of the cyclic nonlinear models, characterizing by a backbone curve, the unloading-reloading excursions, and stiffness degradation. The superiority of the cyclic nonlinear models compared to the equivalent linear models is the capability of capturing the non-zero shear strain for the large shear strains, greater than 10^{-2}, or when the non-zero shear strain/zero shear stress happens as to Jia (2018). Beyond of that, the cyclic nonlinear models are capable of capturing the changes in the effective stresses because of the generation of the excess pore pressures. Such a condition diminishes the soil stiffness and shear strength at the low and high strains, respectively, changing the shape of the soil skeleton curve. The elastic-perfectly plastic Mohr-Coulomb yardstick was employed by Mroueh and Shahrour (2003) in the study of the tunneling-adjacent linear elastic structure interaction via the finite element program PECPLAS. It was, then, highlighted that the soil hardening and stress-dependent elastic properties should be taken into account so as to achieve the more reliable results from the numerical analyses. The detailed tales of the soil constitutive models, which have been proposed for the capturing the soil behaviors under the dynamic loads, are accommodated in the next subsection.

2.2.2 Representation of Stress-Strain Relations in Dynamic Loading

Simulating the soil behavior under the cyclic loading or the random loading conditions, e.g., an earthquake excitation, had better be done by means of the soil constitutive models, able to duplicate the deformation characteristics in the broad range of the strains, from the very small to large shear strains, as highlighted by Ishihara (1996). The changes in the cyclic soil behavior are commonly delimited by a class of cyclic threshold shear strains, introduced in Subsection 2.2.1. Under the strain level as small as 10^{-5}, the soil elastic properties do not experience any change, meaning that the hysteretic damping does not emerge during the cyclic loading. Therefore, the simple linear elastic soil constitutive models seem to be suitable. It is of note that the linear elastic model does not support the dependency on the loading/straining rate.

Table 2.2 categorizes the soil constitutive models into the three main groups based on the level of nonlinearity, viz, the linear, simplified nonlinear, and nonlinear soil models. The elasto-plastic behavior of a soil appertains to the shear strains, greater than roughly 10^{-3}. The higher the shear strain, the more profound the effects of the soil plasticity. If the level of strain is small (i.e., 10^{-5} to 10^{-3}), the stress-strain relation could be still presumed to be linear; nonetheless, the soil damping characteristics ought to be considered. The reason for that is the seismic waves are significantly affected by the dissipation of the energy, provided by the soil deposit. Such a condition belongs to the propagation of the weak ground motions through the soils, as explained by Groholski (2012). The strain-dependent soil properties, which are not cyclic-dependent, could be accommodated by the viscoelastic-based equivalent linear method, according to Assimaki (1999). The energy dissipation in the linear viscoelastic model is considered by dint of the spring (representing the elastic properties)-dashpot (representing the damping characteristics) system. The spring and dashpot are connected in series or in parallel, as illustrated in Figure 2.13. In the said figure, G_{sp} and G_d are the spring and dashpot constants,

respectively, whilst τ and γ are the shear stress and shear strain, in the order given. The stress-strain relations for the Kelvin and Maxwell models are evaluated as to Equations (2.8) and (2.9), respectively, wherein t is for the time. The dashpot herein is the representative of the rate-dependent damping, depending on the deformation's time rate. The deformation depends on the frequency in case of the cyclic loading. Ishihara (1996) uttered that the applications of the spring-dashpot models are totally restricted to the cases, wherein the load frequency varies infinitesimally. The said claim has been approved by the damping properties, shown by the soils in the seismic loading environments, which are practically independent of the frequency according to Park and Hashash (2004).

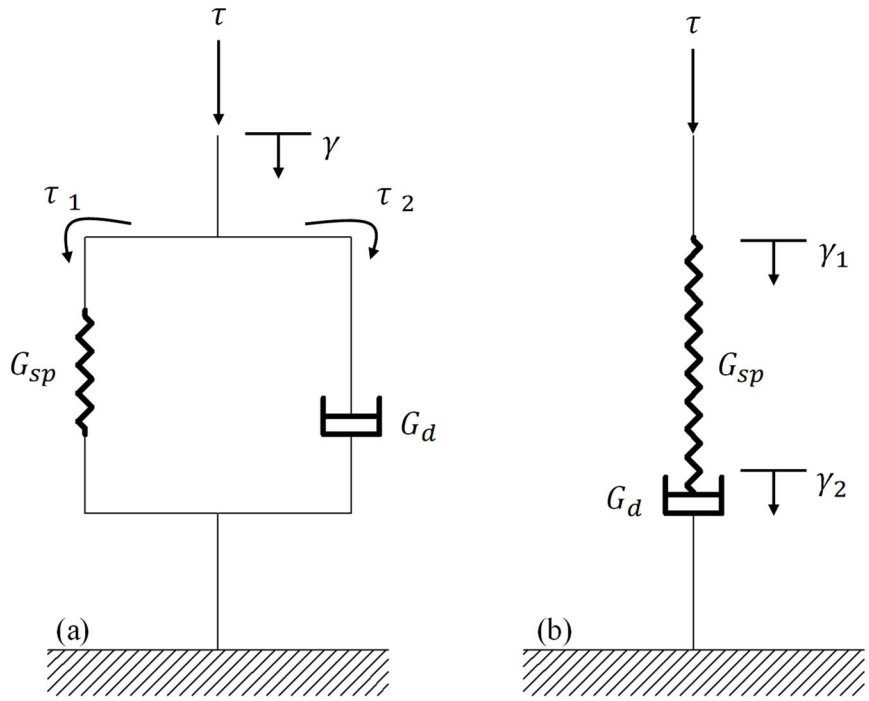

Figure 2.13 Typical viscoelastic models: (a) Kelvin model, and (b) Maxwell model (after Ishihara, 1996)

$$\tau = G_{sp}\,\gamma + G_d \frac{d\gamma}{d\tau} \tag{2.8}$$

$$\frac{\tau}{G_d} + \frac{1}{G_{sp}} \frac{d\tau}{dt} = \frac{d\gamma}{dt} \tag{2.9}$$

One step further under the simplified nonlinear behavior framework, the soil nonlinearity is taken into consideration in conjunction with the energy dissipation, occurring amidst the cycles of the load application for the shear strain in the vicinity of 10^{-3} and less than approximately 10^{-2}. The progression of the cycles in the load application is not followed by any progressive change in the soil properties, which is classified as the non-degraded hysteresis behavior. The nonlinear cycle-independent models, e.g., the Ramberg-Osgood model (proposed by Ramberg and Osgood, 1943) and hyperbolic model (proposed by Kondnor and Zelasko, 1963) could capture the said characteristic of a soil to a reasonable degree of accuracy. The nonlinear cycle-independent models deliver a speech on the fact that the response of the soil does not change with repeating loading cycles while not behaving like a linear elastic material anymore. As regards the soil nonlinearity, Darve (1990) proposed the incrementally nonlinear concept based on which a nonlinear relationship between stress and strain should be utilized, implying that there is no need for the decomposition of the incremental strain.

Concerning the stress-strain nonlinear soil behavior, the backbone curve or the skeleton curve and the hysteresis loop need to be specified. The former indicates the elastic property whilst the latter shows the characteristics of the energy dissipation. The initial (virgin) loading phase could be treated by the hyperbolic relation between the shear stress and strain. The hyperbola is formulated via $\tau = f(\gamma) = \frac{G_0\gamma}{1+(G_0|\gamma|/\tau_{max})}$, wherein τ_{max} is the shear strength. The unloading-reloading should be modeled by means of the Masing criterion (Masing, 1926), based on which Equation (2.10) is in charge of producing the unloading curve from the point of reversal (τ_r, γ_r) in Figure 2.14. Pyke (1979) proposed the rules for extending the Masing concept to the area of the irregular loading, e.g., the seismic excitations. Stated briefly, once the prior maximum shear strain is surpassed, the unloading-reloading curve will follow the backbone curve. Additionally, as reported by Kramer (1996), if the intersection of the current and previous unloading/reloading curves takes place, the stress-strain curve associated with the

preceding cycle will be followed. The nonlinearity casts light on the fact that the backbone curve does not follow a linear path. Additionally, the hysteresis loop is not a perfectly ellipse-shaped loop.

$$\frac{\tau - \tau_f}{2} = \frac{G_0(\gamma - \gamma_r)/2}{1 + (G_0|\gamma - \gamma_r|/2\tau_{max})} \tag{2.10}$$

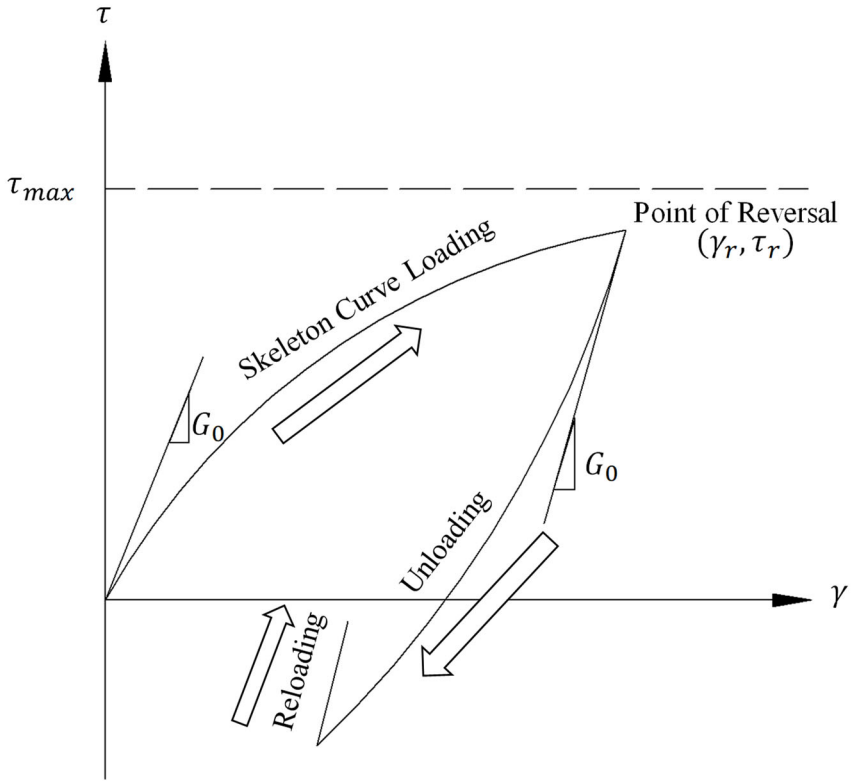

Figure 2.14 Initial loading curve , aka “backbone curve”, and Masing stress-strain curve for unloading and reloading (modified after Finn et al., 1986)

Prior to moving to the higher range of the cyclic shear strain, another practical soil constitutive model should be introduced. The combination of the Hooke’s law and Coulomb’s law makes the foundation of this soil constitutive model, named “elastic-perfectly plastic Mohr-Coulomb model”. The linear elasticity and perfect plasticity are captured by the Hooke’s law and Coulomb’s law, consecutively. The model is called “MC-HD” by benefiting from the Hysteretic Damping feature. The MC-HD model, used by Yeganeh and Fatahi (2019), is able to take into account the effects of the soil plasticity whenever the stress state reaches the yield surface, technically capturing the residual deformation, and excess pore water pressure build-

up. As soon as the shear strain level reaches 10^{-2}, the shear strain and progression of the cycles simultaneously begin affecting the soil properties, classified as the degraded hysteresis behavior according to Choobbasti et al. (2014). Figure 2.15 graphically illustrates the degraded hysteresis attitude, whereby the (secant) shear modulus and hysteretic behavior are on the decrease and increase, in the order given, with the number of cycles. In that regard, the numerical simulation is required to accommodate such stress-strain relations in a step-by-step manner during the loading phases and unloading-reloading excursions, as underscored by Assimaki (1999). This is the place where the plasticity concept ought to be considered properly when dealing with modeling and the simulation of the soil dynamics applications. Note that the nonlinearity, hardening, softening, and anisotropy are included to some level in the soil plasticity-based constitutive models. Generally speaking, the plasticity models inquire a yield surface, a hardening rule, and a flow rule. The yield surface and a hardening rule represent the stress state, beyond which the soil behave plastically, and non-fixed yield surface in terms of its size and shape, respectively. The incremental relation between plastic shear strain and shear stress is rendered by the flow rule.

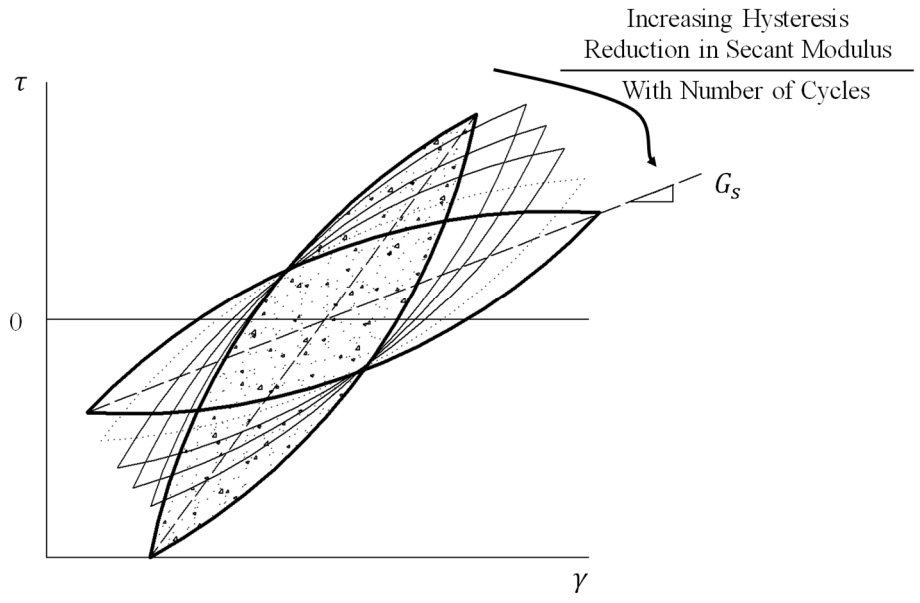

Figure 2.15 Degraded hysteresis behavior of soil in cyclic shearing (modified after Naesgaard, 2011)

In the field of the plasticity-based soil constitutive models under the cyclic loading, two general categories could be set, namely, the empirical models, and theoretical models. The former are proposed based on the data, recorded from one or a group of common laboratory tests, e.g., the cyclic shear test. However, it should be borne in mind that the loading paths in the lab tests and in the field are considerably different. Tsai and Hashash (2008) commented that the tests, conducted in the lab, cannot necessarily capture the soil behaviors under the various loading types. The simplest soil constitutive models herein are the plane strain models. A group of soil models have been presented throughout the plane strain cyclic loading tests, i.e., the Plane Strain Compression (PSC) tests, and Plane Strain Extension (PSE) tests. Some of such soil models are UBCSAND (Beaty and Byrne, 2011), UBCHYST (Naesgaard, 2011), PM4Sand (Boulanger and Ziotopoulou, 2013), and SimpleDSS (Pestana and Biscontin, 2000).

Some of the soil constitutive models are purely empirical, e.g., the multi-axial constitutive models, whereas the others are developed on the basis of certain theoretical frameworks, such as the classical elastoplasticity, hypoplasticity, or endochronic plasticity. As Seidalinov (2018) explained, the seismic loading has the true multi-directional nature, necessitating the use of the multi-axial constitutive models. The aforesaid model was underpinned by the physical bases from the multi-directional cyclic shear tests. For instance, SANICLAY and SANISAND, proposed by Yang et al. (2019), soil constitutive models were developed in the framework of the critical state soil mechanics and bounding surface plasticity for the simulation of the monotonic and cyclic responses of the clays and sands. Contrary to the classical plasticity theory, the bounding surface plasticity, according to Dafalias (1986), permits the plastic deformation even if the stress state has not reached the yield surface. As a tangible sample, the existence and direction of the irreversible strain increment is considered via one surface in the bounding surface plastic theory whereas such a strain increment needs the non-associative flow rule in the conventional plasticity theory, pointed out by Bardet (1987). Consequently, it will

simulate the stress-strain response under both the monotonic and cyclic loading conditions realistically. The major deficiency of this concept is that it cannot describe the unloading-reloading excursion. Continuing on that line, if the stress path undertakes a sudden change, this concept cannot capture it. Several attempts were made to overcome the said shortcoming by introducing the elastic hysteretic formulation referring to Hueckel and Nova (1979) or the recent stress history according to Atkinson et al. (1990). On a side note, the Cam-Clay model and modified Cam-Clay model were proposed in accord with the concept of the critical state mechanics framework, introduced by Schofield and Wroth (1968) and Roscoe and Burland (1968). Although the modified Cam-Clay soil constitutive model considered both the plastic shear and volumetric strains in the energy dissipation, inside the yield surface only accommodates the elastic behavior, which is a notably drawback.

As opposed to the conventional elastoplasticity models, within the theoretically-based hypoplasticity models, the direction of the plastic strain rate relies on the stress rate, first provided by Wu and Kolymbas (1990). There is neither the yield function nor the elastic domain. Aside from being complicated, the major drawback of the hypoplasticity framework is that there is no physical meaning in deriving the formulations. Besides, the overprediction of the dilation necessitated the use of the non-associated form of plasticity. To address that, the plastic potential functions must be defined separately from the flow surface.

Another plasticity framework is the endochronic theory, introduced by Valanis (1971). Unlike the classical plasticity theory, the yield surfaces or flow rules are not accommodated in the endochronic approach. Yet, the plastic strain is allowed to accumulate in a gradual continuous manner inasmuch as the plasticity-induced damping and nonlinear soil behavior are developed from the onset of loading. As an example, Wu and Sheu (1983) put forward the soil constitutive model, utilizing the endochronic theory to forecast the hysteretic shear response of the sands under the cyclic simple shearing.

Prevost and Popescu (1996) stated that the basic cap models are not applicable to the cyclic loading conditions. Nonetheless, there has been a development in this field as the clays and rocks could now be assigned the cap constitutive models like the sandy soils. Taking a step further, DiMaggio and Sandler (1971) and later by Baladi and Rohani (1979) presented the modified cap models as to the state boundary surface concept.

To summarize, numerous advanced soil constitutive models have been developed based on the different concepts, some of which are discussed herein, tabulated in Table 2.2. Each model has its own advantages and disadvantages. To date, no universal constitutive model has yet been developed that can be capitalized on for the all geological materials under the all known, possible loading conditions. Since this thesis is rooted in the interaction amongst the superstructure, foundation, and soil medium, the next section covers the importance of the dynamic soil-structure interaction followed by casting light on the design approach of the performance-based method as well as introducing the assessment of the novel isolation technique, i.e., the foundation rocking isolation.

Table 2.2 Review of soil constitutive models in realm of soil dynamics

Soil Behavior	Cyclic Shear Strain Range		Linearity, Nonlinearity	Damping	Model Type	General Framework	Plastic/Residual Deformation	Excess Pore Water Pressure Build-up	Examples
Elastic	$< 10^{-5}$		Linear	Dismissed	Linear Elastic	Constant Elastic Properties	×	×	---
Elasto-Plastic	$> 10^{-3}$	10^{-5}-10^{-3}	Linear	Viscoelastic Dashpot	Linear & Equivalent Linear Viscoelastic	Spring-Dashpot	×	×	Kelvin & Maxwell models (Ishihara, 1996)
		10^{-3}-10^{-2}	Simplified Nonlinear	Masing Rule (Hysteresis Loop)	Nonlinear Cycle-Independent	Non-Degraded Hysteresis	×	×	Hyperbolic Model (Kondnor and Zelasko, 1963)
				Masing Rule & Soil Plasticity-Induced Damping	Featured by Yield Surface	Classical Elastoplasticity	×	✓ (Disregarding Cyclic Shear Strain-Induced Volumetric Strain)	MC-HD (Yeganeh and Fatahi, 2019)
		$> 10^{-2}$	Nonlinear	Masing Rule & Soil Plasticity-Induced Damping	Empirical-Based	Plane Strain; Multi-Axial; Critical State	✓	✓ (Cyclic Shear Strain-Induced Volumetric Strain in Liquefaction Analysis)	Modified Cam-Clay Model (Roscoe and Burland, 1968); SANISAND (Yang et al., 2019)
					Theoretical-Based	Classical Elastoplasticity; Hypoplasticity; Endochronic Plasticity; Bounding Surface Plasticity	✓	✓ (Cyclic Shear Strain-Induced Volumetric Strain in Liquefaction Analysis)	Wu and Kolymbas (1990); Valanis (1971); DiMaggio and Sandler (1971)

2.3 Realm of Dynamic Soil-Structure Interaction (DSSI)

The late 19th century is believed to be the starting point of the soil-structure interaction topic as mentioned by Lou et al. (2011). It was evolving with the help of the analytical methods particularly for the first few decades. Indeed, there was a surge in the application of the soil-structure interaction concept for the seismic analyses in the 20th century in light of the debut of the numerical computation tools, followed by the emergence of the numerical methods. As stated by Datta (2010), the structure interacts with the surrounding soil, imposing the soil deformations amidst an earthquake excitation. Such deformations, in turn, give rise to the differences in the motion of the contact interface between the soil and superstructure and that of the free field ground motion.

Various procedures have been put forth so as to consider the soil-structure interaction effects in the seismic analyses of the structures. One of the common simplifications is to replace a Multi-Degree-Of-Freedom (MDOF) structure with an Equivalent Single-Degree-Of-Freedom (ESDOF) structure, assuming that the higher modes are not affected by DSSI according to Raychowdhury (2011). Contrariwise, the needfulness of considering the interaction effects via the direct method must be emphasized, particularly for the moment-resisting frames, once the shear wave velocity of the supporting soil is less than 600 m/s referring to Tabatabaiefar and Fatahi (2014). Bielak and Christiano (1984) presented the direct method as an approach wherein the motion in the structure and entire soil medium, truncated by the artificial absorbing boundaries, is determined simultaneously. According to Carr (2008), the multiplex geometries of the analyzed problems as well as the possible nonlinearity could be properly treated by the direct approach. The main demerit of the aforesaid approach is the requirement of modeling the whole system of the soil-foundation-structure at once, skyrocketing the cost of the analysis and assigned time, as highlighted by Datta (2010). It also

should be noticed that the dimensions of the soil domain considerably outweighs that of the superstructure and its foundation, making, thus, the method computationally expensive. The other method, termed "substructure approach" as to Gutierrez and Chopra (1978), is computationally more efficient thanks to dividing the entire system into the subsystems; however, it is limited to the linear or equivalent linear problems as the principle of the superposition is assumed in the analysis, stated by Halabian and El Naggar (2002). Within the substructure method of analysis, the impedance functions are introduced with the intent of presenting the dynamic characteristics of the foundation soil in terms of the damping in addition to the stiffness according to Datta (2010). Such impedance functions are commonly determined using the formulas, presented by Gazetas (1991), based on the ratio of the forces (or moments) and displacements at the foundation base, applying the massless assumption. Furthermore, the centrifuge and shaking table tests are adopted (e.g., Rayhani and El Naggar, 2008; Turan et al., 2013) for the DSSI problems, classified as a physical model testing approach. Given the circumstance, the use of the numerical simulation has become more popular in analyzing such a complex interactive behavior by the increasing availability of the high-performance computers and wider applicability of the numerical methods in contrast to the analytical approaches. Far (2019) pointed out that the outstanding capabilities of the direct method, despite the above-mentioned disadvantage, introduce it as the most suitable technique for DSSI.

The seismic soil-structure interaction is certainly a complex phenomenon with the significant amount of uncertainties, making the codes and standards, as well as the design engineers show a reluctance to cope with it. However, Ghiocel and Ghanem (2002) stated that the ability to rationally account for such uncertainties whilst distributing the same level of accuracy amongst the predictions of the behaviors associated with the components, involved in the soil-structure system, might possibly reduce the imposed cost as well as sharpening the

results' reliability. It is perceived that the DSSI analysis inquires the preparation for the complexity whilst the soil modeling often requires the non-routine soil testing. The resulted optimization can bring the economic, elegant, and delightful solutions. Quite differently, the pseudo-static analyses and simplified methods, in general, deter the optimization.

Conceding the fact that the tremendous development in computing software programs and numerical methods has taken place, the knowledge about the ground motions, structural behavior, and soil-structure interaction has not kept up the same speed, as brought out by Fajfar (2018). Another issue, which has come into picture, is on account of the rapid development of the societies and global explosion of the population. On that basis, the structures are built closely to each other. Jiang and Yan (1998) presented that the neighboring buildings with the distance less than 2.5 times of the foundation width are interacting with each other. It was shown that the structures' responses might increase or decrease tens of percent when the above-mentioned distance is less than one time of the foundation width. It should be noticed that SSI, technically escalating the structural damping, might have a detrimental effect by reason of the resonance and amplified the $P-\Delta$ effect, resulting in the structural instability, highlighted by Wolf (1985). In the following sectors, the readers will be served by the information in regard to the dynamic soil-structure interaction concept and performance-based design procedure.

2.3.1 DSSI: To Be Considered or Not?

The point of departure for the soil-structure interaction studies is traced back to the foundation vibration theory, introduced by Reissner (1936). It is noteworthy to mention that the phenomenon associated with the soil-structure interaction was indentified for the first time in early 1930s. Another state-of-the-art work on SSI was presented by Hadjian et al. (1974). Wolf (1985) extensively elaborated on the principles of SSI, modeling of the soil-foundation-structure system, and equations of the motions as well as the analysis methods. It is worth

mentioning that the seismic waves, generated by the seismic fault, pinpoint the superstructure, divided to the two sets of waves, viz, the reflection waves and transmission waves. The radiation waves are induced by the transmission waves, travelling within the superstructure while being able to enter back to the soil mass. The damping, resulting from the radiation waves, is referred as the radiation damping, implying that the higher damping for the soil-structure system than that of the structure itself. In summary, the soil-structure interaction gives rise to increasing the system damping; therefore, the role of DSSI is usually assumed to be beneficial. Bhattacharya and Dutta (2004) assessed the extent to which the natural periods of the isolated foundation-supported superstructures are influenced by SSI. It was pointed out that the evaluation of the lateral natural periods of any buildings, particularly the ones on the soft soils, must be seriously considered. Clearly, the fundamental period of a flexible base building is greater than its counterpart in a fixed-base building. Moreover, Gazetas and Mylonakis (1998) proclaimed that the increment of the fundamental natural period of a superstructure in a soil-foundation-structure system could spark off the unsafe design, especially for the buildings, founded on a soft soil deposit. Considering that, ASCE-41-17 (2017) suggested the evaluation of SSI for the buildings, wherein an increase in the fundamental period, resulting from the SSI effects, leads to the spectral acceleration increment. On the same topic, the research works of Goel and Chopra (1998) and Ghrib and Mamedov (2004) demonstrated the inadequacy of the proposed fundamental period formulae by the building codes without the consideration of the foundation flexibility. In that regard, the SSI's effects on the fundamental periods of the buildings were investigated by Khalil et al. (2007), showing that such an effect mainly depends on the soil-structure relative rigidity, denoted by K_{ss}. In Equation (2.11), K_{ss} is expressed in terms of the number of spans in both the transversal and longitudinal directions (N_{bt} and N_{bl}, respectively), soil mass density (ρ), soil shear wave velocity (V_s), story height (h), foundation area (A_f), reference area (A_0), number of stories (N_s), and flexural rigidity of

the building columns (E_c and I_c). A practical chart was put forward to figure out whether the consideration of SSI in the determination of the fundamental frequency of a building is essential. Figure 2.16 shows the variations of the ratio $\frac{f}{f_{fb}}$ (f is the fundamental frequency and f_{fb} is the fundamental frequency of a fixed-base building) with K_{ss}, signifying that the influence of SSI on the building fundamental frequency could be dismissed once the logarithm of the soil-structure relative rigidity (i.e., $\log K_{ss}$) is greater than 1.5. Conversely, ignoring SSI for the lower values of K_{ss} could trigger a considerable misestimation of f.

$$K_{ss} = \frac{N_{bt} N_{bl} \rho {V_s}^2 h^3 \sqrt{\frac{A_f}{A_0}}}{N_s E_c {I_c}^{\frac{3}{4}}} \tag{2.11}$$

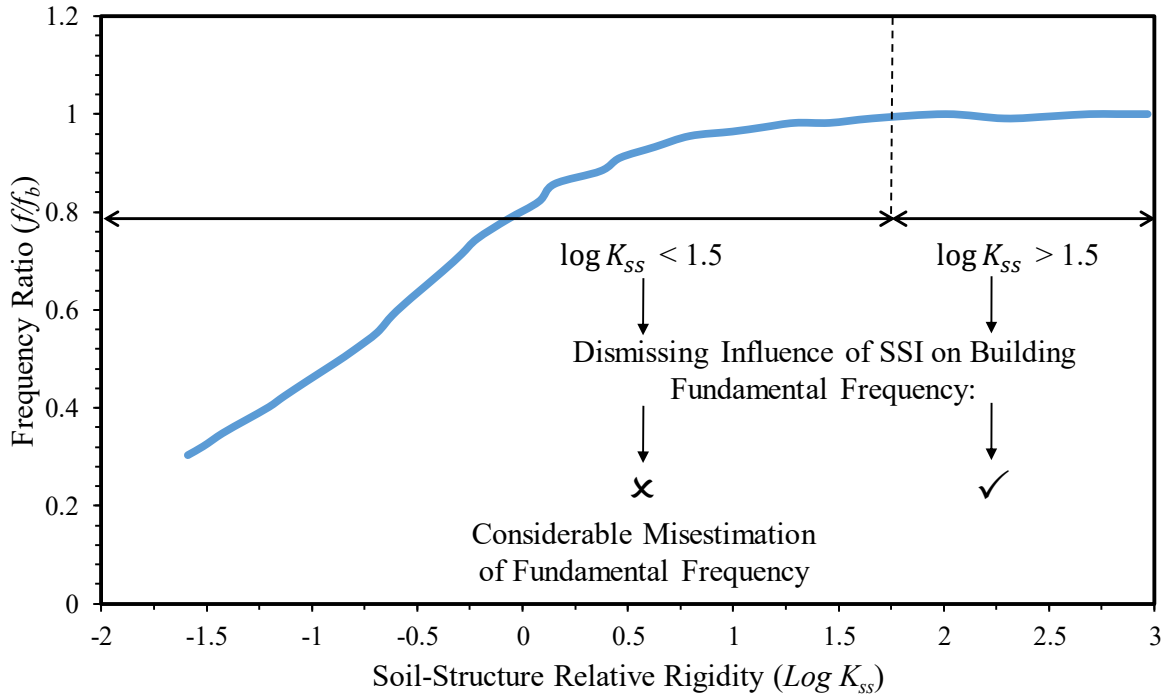

Figure 2.16 Effects of SSI on fundamental frequency of building (modified after Khalil et al., 2007)

The 1977 Vrancea earthquake (Romania), M_s = 7.1, reported by Hartzell (1979), was one of the global catastrophes, occurring in the 1970's. On March 4, it was the culprit

Figure 2.17 Buildings damage in Bucharest courtesy of 1977 Vrancea earthquake (Bery et al., 1980)

of claiming the 1,578 lives and 11,321 injured individuals while Bucharest, the capital of Romania, was compelled to accommodate 90% of the fatalities, as reported by Georgescu and Pomonis (2008). Figure 2.17 exhibits the seismically-induced damage to the buildings in Bucharest during the 1977 Vrancea earthquake. The said earthquake in Romania was reported by Mylonakis and Gazetas (2000) as a seismic event, wherein SSI aroused a surge in the seismic responses of the structures in spite of a possible elevation in the system damping. To elucidate that, the normalized acceleration response spectrum of 1977 Vrancea earthquake was compared graphically against the design response spectrum of the soft deep soil based on Eurocode 8 – Part 1 (2004) in Figure 2.18. The peak acceleration values were used to derive the normalized spectral accelerations, sketching out the spectra in their general forms, as recommended by Seed et al. (1976). Although the code-based response spectrum presented the maximum normalized spectral acceleration of 2.5 at the period of 0.8 s, the recorded response spectrum experienced the maximum around 3 at the period of 1.5 s. In a broad look, the code-based response spectrum could not precisely predict the actual forces, imposed on the structures by the earthquake of interest, at the different fundamental periods. In this example, the long-period superstructures, whose period was higher than that of the 10-story buildings (approximately 1 s), encountered the higher earthquake-induced shear forces during the 1977

Vrancea earthquake. It is evident that the SSI-induced fundamental period increment would beget the boosted response of a structure in spite of the ascent in the damping. In retrospect, the evidence of the damage associated with the SSI effects was highlighted by Celebi (1998) in the 1998 Adana-Ceyhan (Turkey) seismic event. It was concluded that the soil-structure interaction might have contributed to lengthening the buildings' periods, triggering the hazardous resonance phenomenon, due to coinciding with the characteristic site period.

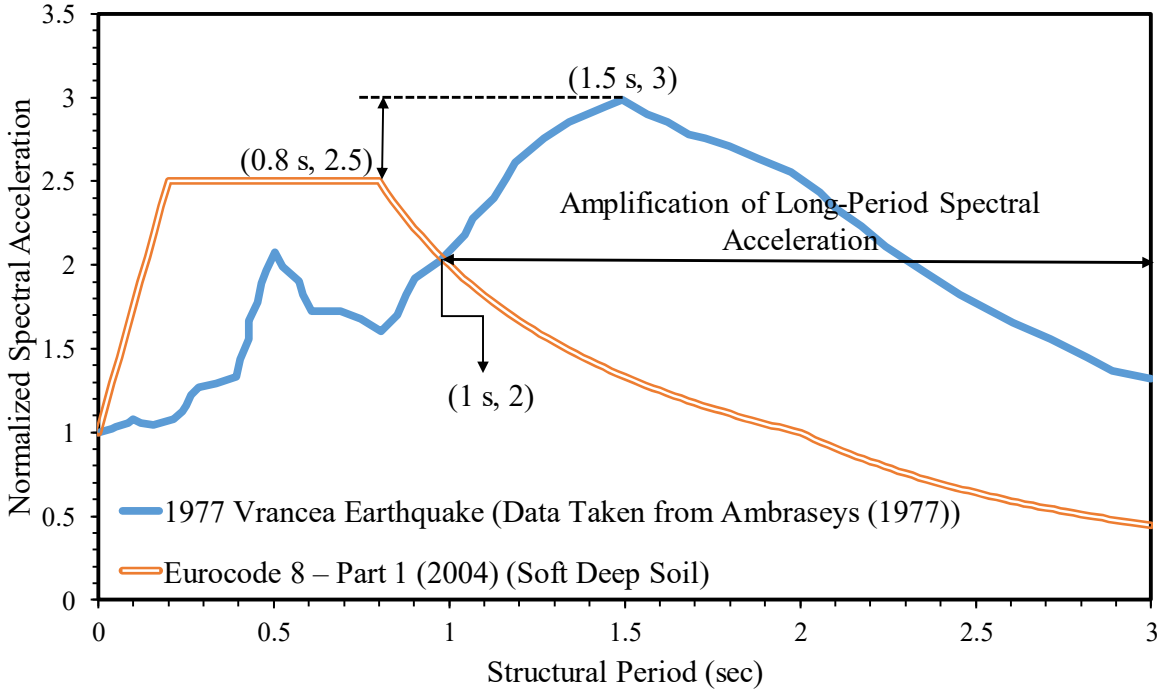

Figure 2.18 Acceleration response spectra of 1977 Vrancea earthquake, obtained from Ambraseys (1977), and soft deep soil according to Eurocode 8 – Part 1 (2004)

The 1985 Mexico earthquake on 19th of September and its strong aftershock 36 hours later caused the intensive damage and even collapse of hundreds of the engineered multi-story buildings while thousands of lives were lost, reported by Dobry and Vucetic (1987). The aforesaid seismic event in Mexico City is another tangible example for the amplification phenomenon of the earthquake waves by the soft clay. Borcherdt (1970) and Shearer and Orcutt (1987) documented that the unconsolidated sedimentary deposits could amplify the seismic waves, in charge of boosting the damage, experienced by the structures during an earthquake. As it can be discerned in Figure 2.19, the shear wave velocity profile of the Mexico City clay

deposit was far smaller than those of the other major cities (San Francisco, Tokyo, Boston, and Salt Lake City). The basic expression of $G_0 = \rho V_s^2$, according to Zhang et al. (2005), is the relation between the maximum shear modulus (G_0) and shear wave velocity (V_s) via the soil mass density (ρ). Thus, the initial shear modulus was significantly low for the Mexico City clay deposit. The intense damage was concentrated in the downtown of the city, resting on the ancient Texcoco Lake, known as the Lake Zone. Dobry and Vucetic (1987) reported 75 m/s as the average shear wave velocity of the 37-m deep Lake Zone. The fundamental resonance frequency was 0.5 Hz, denoting 2 s as the resonance period of the soil site (Figure 2.20). It was reported that the measured ground motion's predominant period in the heavy damaged area was also around 2 s.

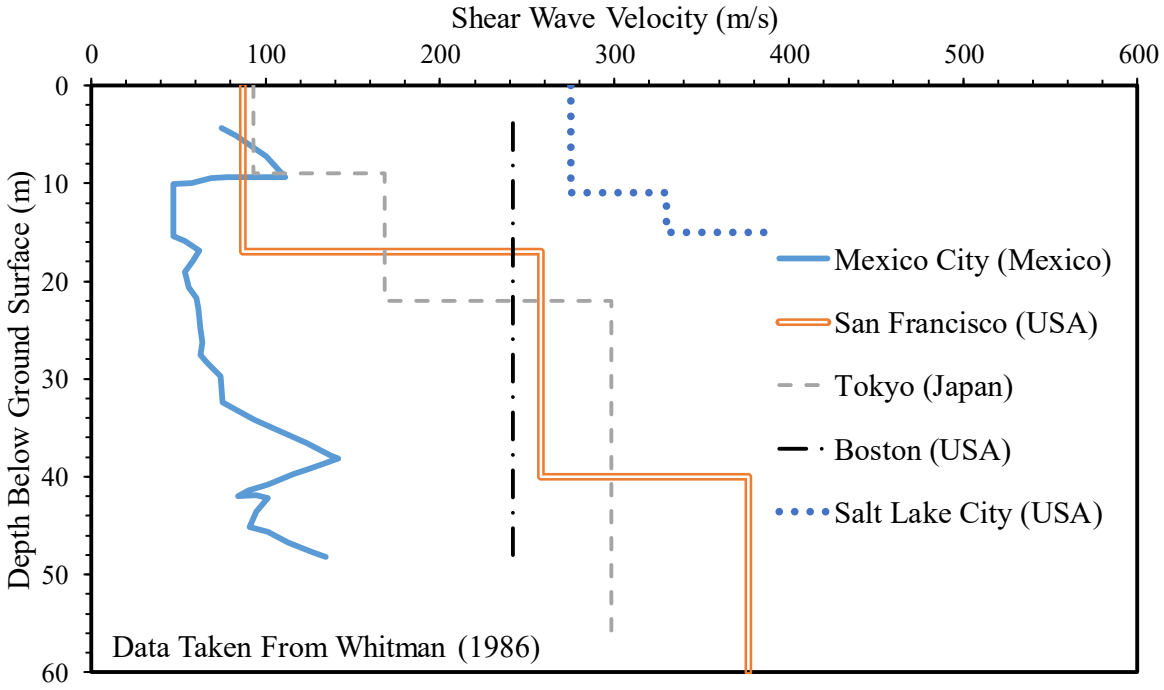

Figure 2.19 Variations of shear wave velocity with depth for clay deposits in several cities

In addition to the resonance owing to the coincidence of the periods associated with the soil deposit and incident seismic waves, the double resonance phenomenon, as pointed out by Housner (1986), transpired in light of the increased periods of the 6 to 15 stories, stemming from the nonlinear response of the buildings in the soil-structure system. Much less damage

occurred in the other zones of the city, wherein the hard soil resided or the clay layer was markedly thinner. Figure 2.20 illustrates the mentioned double resonance through the response spectra of the two sites, viz, the National University (UNAM) and Secretory of Communications and Transportation (SCT). The latter was located on the soft clay in the heavy damaged zone whereas the former was placed on the cemented, compact sand and gravel. Comparing the trends in Figure 2.20 exhibits that the peak ground accelerations were amplified four times higher on the surface of the soft clay medium from 0.03g to 0.14g. Beyond of that, the seismic load, acting on the structures, having the period of 2 s, was amplified seven times since the response accelerations were 0.1g and 0.75g at UNAM and SCT, respectively. The said observations were in line with the results, reported by Aki (1993), based on which the amplifications of the ground motions in the stiff and old soil deposits are outnumbered by those, happening in the medium of the soft and young soils.

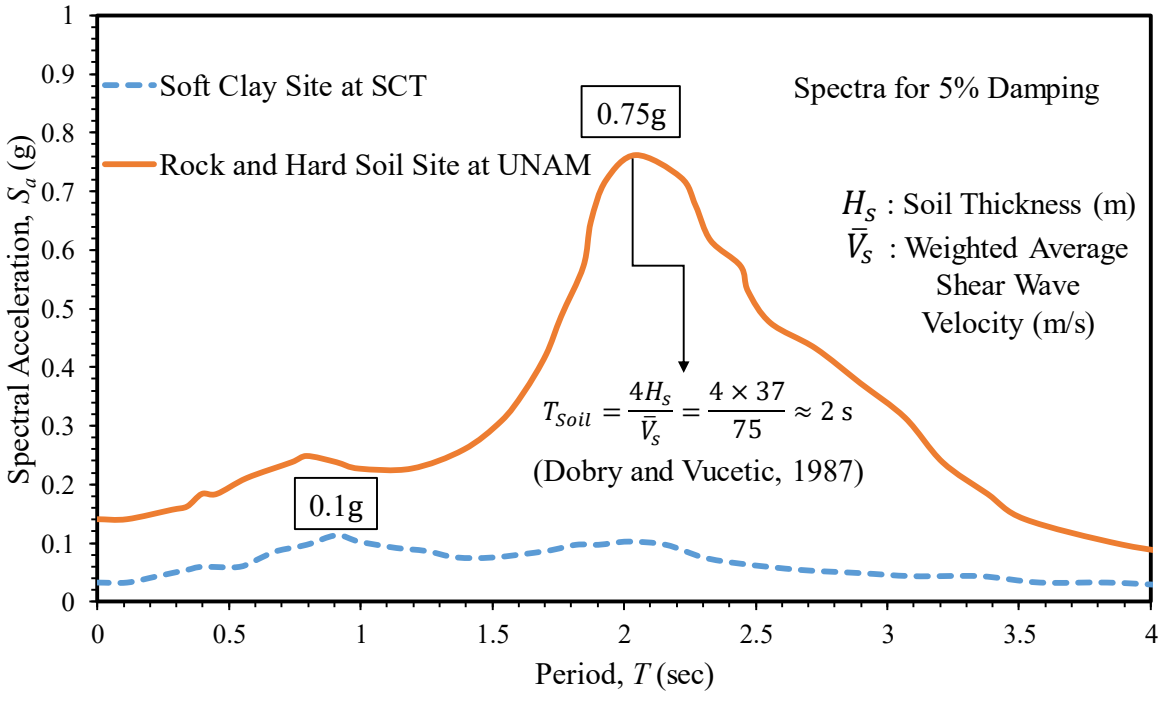

Figure 2.20 Double resonance and earthquake amplification on Mexico City soft clay (modified after Dobry, 2014)

The majority of civil engineering structures are dictated to be considered in conjunction with the surrounding soil medium so as to precisely forecast their responses to the dynamic design loads, as concluded by Wolf and Deeks (2004), Snieder and Safak (2006), and Galal and Naimi (2008). The topic of their research studies was about the effects of SSI on the seismic responses of the superstructures, including the braced frames and unbraced buildings. In this firmament, Ghannad and Ahmadnia (2006) reported that SSI could conspicuously alter the structural demands, i.e., the strength and ductility. Besides, the hysteretic damping feature of the superstructures might also be changed by the seismic SSI. Hence, the different levels of damage may be undertaken by the buildings considering the seismic soil-foundation-structure interaction.

2.3.2 Performance-Based Seismic Design (PBSD) Concept

The design objectives in the current building codes demand the twofold targets under the different intensity levels of the earthquakes. According to Ghobarah (2001), the collapse prevention is to be met under the major ground motions whilst the minor to moderate earthquake excitations are employed to predict and control the level of damage. The said damage is defined in line with the serviceability and life safety drift limits. Ghobarah (2001), questioning the reliability of the current design approaches, emphasized that there is no guarentee that such design objectives will be thoroughly met. The recent earthquakes have clearly supported the statement, made by Ghobarah (2001), via exhibitting the extensive level of damage to the structural elements and also non-structural components, reported by Eguchi et al. (1998). Taking two major California earthquakes as tangible samples, the 1989 Loma Prieta and 1994 Northridge events (USA) begot fewer than 100 fatalities; however, the economic losses were approximately 7-30 billion US dollars, reported by Hamburger (1996). As to FEMA283 (1996), it is attested that the critical or economically important buildings

might suffer the large losses since the designs are not properly related to the performance needs and expectations. Henceforth, it is safe to say that the Performance-Based Design (PBD) sharpens the lifelong performance of the buildings, gifting the engineers and construction industry with the cost-effective design methodologies.

The Vision 2000 report (SEAOC, 1995) technically pioneered the performance-based seismic engineering as a process, including a class of the performance levels, which were coined in terms of the two main concepts, viz, the damage level and building's post-earthquake functionality. It should be borne in mind that the damage to the nonstructural elements, e.g., see Figure 2.21, cannot be overlooked from an economical standpoint as they could happen even in the minor seismic excitations.

Figure 2.21 Fallen concrete curtain wall panels in 1978 Miyagi earthquake (Ishiyama, 2011)

The performance levels, introduced by SEAOC (1995), are fully operational, functional (operational), life safe, and near collapse, which are called differently in other codes. For example, FEMA-P-750 (2009) announced the corresponding performance levels to those of SEAOC (1995) as operational, immediate occupancy, life safety, and collapse prevention, respectively. The performance levels according to Bertero et al. (1996) are fully operational or serviceable, operational or functional, life safety, and near collapse or impending collapse. The level of damage is on the increase from the fully operational to near collapse performance levels. Note that the life safety is in absolute jeopardy whilst the structural collapse is shunned

at the near collapse/impending collapse performance level. Table 2.3 describes the performance levels, showcased in SEAOC (1995), in terms of the damage level and reparability.

Table 2.3 Performance levels descriptions as to SEAOC (1995)

Performance Level	Structural & Non-Structural Damage	Loss of Stiffness and Strength	Repair	Risk of Life Threatening Injury
Fully Operational	Very minor	Insignificant	Not required	Negligible
Functional/Operational	Minor	Insignificant	Minor	Very low
Life Safe	Significant	Significant	Necessary	Low
Near Collapse	Severe	Substantial	Not practical	Possible

SEAOC (1995) announced the four ground motion hazard levels with the specified probabilities of occurrence for the aforesaid discrete performance levels. The frequent and occasional hazard levels have the 43-year return period with 50% exceedance probability in 30 years and 72-year return period with 50% exceedance probability in 50 years, respectively. The 475-year return period with 10% exceedance probability in 50 years defines the rare level. The very rare hazard level is the 970-year return period with 10% exceedance probability in 100 years. Priestley (2000) pointed out the seismic performance objectives are defined with the help of the two expected levels, including the performance level and intensity level of the seismic motions, which need to be coupled. A group of performance objectives are shown in Table 2.4, i.e., the basic objective, essential/hazardous objective, and safety critical objective in line with the importance levels of the structures. To give a general idea herein, it could be mentioned that the typical buildings, hospitals, and nuclear containment facilities are requisite to meet the minimum objectives as follows: (i) basic; (ii) essential/hazardous; and (iii) safety critical, respectively. Another factors in Table 2.4, presented by the Vision 2000 report (SEAOC, 1995), are the performance and earthquake hazard levels. Looking back to the first edition of SEAOC (1959), the structure must be demanded to resist the three different levels of shakings whilst Kramer (2008) placed emphasis on the vagueness of the damage definitions in that standard. Stated briefly, during a minor level of shaking, the damage of the structural and non-structural elements is not permitted. Some non-structural damage is possible in a

moderate level of shaking; however, both the non-structural and structural damage might take place without collapse for a strong level shaking.

It is of note that utilizing multiple seismic demand levels are common in PBD (Liu et al., 2005). Klemencic et al. (2012) listed the seismic design levels into the three general groups, viz, frequent (approximately 50-year return period), intermediate/rare (around 500-year return period), and extremely rare/severe (1000 to 2500-year return period). The basic safety earthquake 1 (BSE-1, which is the 10%/50-year event) and basic safety earthquake 2 (BSE-2, which is the 2%/50-year event) were introduced by FEMA273 (1997). The return periods of the BSE-1 and BSE-2 earthquakes are 475 years and 2475 years, respectively. Further, PEER-TBI (2017) introduced the Service-Level Earthquake (SLE) for the operational level and Maximum Considered Earthquake (MCE) for the collapse-resistance level of the tall buildings. As a matter of fact, SLE (43-year return period), and MCE (2475-year return period) are the counterparts of the frequent, and extremely rare/severe hazard levels, respectively.

Table 2.4 Recommended seismic performance objectives for buildings along with earthquake hazard and performance levels, proposed by SEAOC (1995)

Earthquake Design Level	Return Period	Earthquake Performance Level			
		Fully Operational	Operational	Life Safe	Near Collapse
Very Rare	975 years	NR[1]	SC-PO	E-PO	B-PO
Rare	475 years	SC-PO[2]	E-PO	B-PO	NR
Occasional	72 years	E-PO[3]	B-PO	NR	NR
Frequent	43 years	B-PO[4]	NR	NR	NR

[1]NR: Not Recommended.
[2]SC-PO: Safety Critical Performance Objective.
[3]E-PO: Essential Performance Objective.
[4]B-PO: Basic Performance Objective.

ATC3-06 (1978) only introduced a 475-year-return-period ground shaking level, categorized as the Design Level Earthquake (DLE), along with three seismic hazard exposure groups I, II, III, classified in the performance objectives of basic, essential/hazardous, and safety critical, displayed in Table 2.4, respectively. As an example, the post-earthquake recovery is the core of the above-mentioned group III, necessitating the safety of the buildings, providing the vital services after the earthquake events and also the aftershocks. UBC (1997)

defined the Design Level Earthquake (DLE), which is the two-thirds of the corresponding risk-targeted maximum considered earthquake with the 2475-year return period, usually considered as a 475-year-ruturn-period earthquake. Indeed, it is desirable to design the structures so that they behave in a predetermined manner amidst DLE according to Goel and Leelataviwat (1998). Taking Eurocode 8 – Part 1 (2004) into consideration, the two design levels of ground motion, namely, a Damage Limitation Level Earthquake (DLLE) with a return period of 95 years and a No-Collapse Level Earthquake (NCLE) with a return period of 475 years, are presented referring to the serviceability and ultimate limit states, respectively, under the seismic loading.

In Asia, Building Standard Law of Japan (BSLJ, 2013) is believed to be a futuristic standard, revised in 2000 towards the performance-based structural engineering according to Midorikawa et al. (2004). There are two kinds of the performance requirements for the seismic provisions corresponding to the two earthquake motion levels. The life safety requirement accentuates that the whole building and also each single story should not encounter any failure/collapse. The purpose of the damage limitation is to limit and preclude the damage of a building, including the structural frames and interior/exterior finishing materials. In that connection, the levels of the Maximum Earthquake (ME) motions and Once-In-A-Lifetime Earthquake (OIALE) events correspond to the categories of the life safety and damage limitation, consecutively. The return periods of the seismic ground motions are 500 years and 50 years for ME and OIALE, in the order given. Note that the performance-based design is required as per BSLJ (2013) for the buildings, greater than 60 m in height.

In Australia, a return period of between 500 and 2500 years (10%/50–2%/50), depending on the conditions of the soils and buildings, is typically associated with the Ultimate Limit State (ULS) earthquake event, as mentioned by Wilson and Lam (2006). Additionally, preventing the collapse of the buildings must be ensured. The Serviceability Limit State (SLS),

having the 50-year return period, does not need to be considered since SLS is deemed to be automatically satisfied so long as the design of the building of interest is done in full compliance with the Australian Seismic Design Code AS1170.4 (2007). Unlike the Australian code, the New Zealand code NZS1170.5 (2004) spelled out the necessity of the consideration of SLS and ULS in the design stage. The Serviceability Limit State 1 (SLS-1) and SLS-2 define the limits at which the structural and non-structural components do not require any repair and the structure maintains the operational continuity, respectively. The Serviceability Limit State 2 has to be only applied to the buildings with the special post-earthquake functions. The return periods for SLS-1 and SLS-2 are 25 (90% in 50 years) and 500 (10% in 50 years) years, respectively. The seismic demand level of the ULS design varies from the 100-year return period to the 2500-year return period as per the importance levels. The importance level 1 is for the minor structures with the low consequence of the failure (the return period of 100 years). The normal structures with the medium consequence for the loss of the human life is classified under the importance level 2 (the return period of 500 years). The major structures (highly affecting the crowds) and post-disaster buildings are listed under the importance levels of 3 and 4, consecutively. A 1000-year-ruturn-period earthquake is considered for the importance level 3 whereas the return period for the importance level 4 is 2500 years for a structure with a critical post-earthquake designation.

The performance indicator, which is meant to be self-explanatory to the public, is the deformation, e.g., the displacements and drifts. The horizontal displacement at the highest point of the story of interest relative to that of its lowest point is the inter-story drift ratio once it is divided by the height of the story. The upper limits for the inter-story drift ratios (0.2%, 0.5%, 1.5%, and 2.5%) are shown, taken from SEAOC (1995), corresponding to the fourfold performance levels, i.e., the fully operational, functional (operational), life safe, near collapse, respectively. According to FEMA273 (1997), the performance levels are employed to preclude

the damage level not only for the structural elements but also for the non-structural components. The overall levels of damage for the operation, immediate occupancy, life safety, and collapse prevention performance levels are very light, light, moderate, and severe, in the order given. Since the operation level and immediate occupancy level share the same structural performance level, the same limiting drift ratio, i.e., 1%, is assigned to them. The transient drift ratios of 2% and 4% are for the performance measures of the life safety and collapse prevention performance levels, respectively.

The performance of the structural components and non-structural elements in a building could be utterly affected by the permanent deflection of the building due to a seismic shaking, as pointed out by Ruiz-Garcia and Miranda (2005). The significant residual displacements have been observed in the previous earthquakes, reported by Mahin and Bertero (1981), put on view in Figure 2.22. By way of illustration, the technical difficulties and enormous cost attributed to repairing and straightening the structures, experiencing the seismically-induced permanent deformations after the 1985 Michoacán earthquake (Mexico) gave rise to demolishing a large number of the reinforced concrete buildings as reported by Rosenblueth and Meli (1986). The same story took place in the 1995 Kobe earthquake by reason of the tilted bridges, meeting the collapse prevention performance level thanks to remaining standing; yet, the demolition and reconstruction resulted in the large economic losses and the loss of use in Japan. It was previously reported by Muto et al. (1960) the importance of the lateral drifts as a basis for the design. FEMA273 (1997) suggested 1% and 4% for the residual drift ratios of the life safety and collapse prevention performance levels, consecutively, whereas the negligible permanent drift must be met for the operational and immediate occupancy performance levels.

Figure 2.22 Examples of buildings with considerable residual displacements, leading to demolition (Ramirez and Miranda, 2012)

The transient story drift limit of 0.5% in PEER-TBI (2017) is for the SLE shaking, ensuring the negligible permanent lateral displacement of the structure as well as protecting the non-structural components. Protecting against the global instability under the MCE shaking could be guaranteed by capping the transient drift ratio to 3%, including the drift from the rigid-body rotation. The residual story drift ratio of 1% intends to protect a tall building against the excessive post-earthquake deformations, causing the condemnation or excessive downtime because of performing the repairs.

ATC3-06 (1978) announced the allowable drift ratios of 1.5%, 1.5%, and 1% for the life safety level, immediate occupancy level, and operational level, consecutively. In UBC (1997), the maximum inelastic drift ratio is limited to 2.5% and 2% when the fundamental period of the building is less than 0.7 s or greater than that, respectively, covering the life safety level towards the collapse level. The inter-story drift ratio limits in the serviceability state, i.e., the damage limitation level earthquake in Eurocode 8 – Part 1 (2004), are 0.5% for the brittle non-structural elements, 0.75% for the ductile non-structural elements, and 1% when the non-structural components do not interfere with the structural deformations. In case of the operational and immediate occupancy levels, the general requirements are announced to be no

permanent deformations as well as no stiffness and strength degradation referring to Soós and Vigh (2012). Interestingly enough, the European code defined the inter-story drift coefficient, taking into account the second-order effects, for the ultimate limit state instead of the inter-story drift ratio. It was emphasized that the inter-story drift coefficient must not surpass 0.3.

In Japan, as mentioned by Otani (2004), the linear structural response is imposed on the high rise superstructures. The aim is to achieve the reasonable performance response for the non-structural elements. Note that the applied seimsic motion is characterized by 0.25 m/s as the peak ground velocity. In addition, the acceptable inter-story drift ratios for the demand levels of damage limit and safety limit are 0.5% and 1.5%, respectively. BSLJ (2013) remained silent as regards the acceptable permanent drift ratio.

In the Australian code AS1170.4 (2007), as a force-based/displacement-check design standard according to Priestley (2000), three Earthquake Design Category (EDC) are introduced based on a three-tiered approach. The simple static analysis (i.e., the 10% weight of the building) is for EDC I. The tall buildings with the higher mode effects are to be designed in consistent with EDC III, representing the full dynamic earthquake analysis. The static earthquake analysis is for EDC II. The maximum inter-story drift ratio at the ultimate limit state, which could be interpreted as the life safety performance level, shall not surpass 1.5% in each single level. There is no specific clause in AS1170.4 (2007) as regards the acceptable limit for the permanent drift ratio. Staying with the Meganesia, NZS1170.5 (2004) suggested the maximum allowable inter-story drift of 2.5% for the ULS design when conducting the inelastic time history analyses. However, the modification/scaling factors are for simulating the inter-story drifts in the post-elastic range, corresponding to ULS. The deflection scale factors in NZS1170.5 (2004), ranging from 0.85 to 1.0 on the basis of the number of stories, shall be used as the equivalent static method over-predicts the deflections in the structure compared to the modal response spectrum method. Given the circumstance, the drift modification factors, i.e.,

1.2-1.5, depending on the building height, are responsible for ascending the estimated drifts when using the elastic methods in lieu of the inelastic time history analytical methods. King and Shelton (2004) underlined that the maximum permitted inter-story drift of 2.5% for the inelastic analyses under the ultimate limit state design should be reduced to 2% when calculating the drifts via magnifying the deflection profile, derived from the elastic analysis techniques. The allowable inter-story drift ratio is not specified for SLS. To close up this subsection, a summary of the reviewed codes and standards in the field of the performance-based seismic design is provided in Table 2.5. It is apparent that the PBSD approach is gaining the international acceptance. Nonetheless, the majority of the codes are required to be updated so as to cover PBSD more comprehensively for all the fourfold performance levels. From all accounts, FEMA273 (1997) was chosen to define the required yardsticks for assessing the performance of the adopted superstructures in the three-dimensional coupled numerical simulations of the seismic soil-structure interaction in this study using FLAC3D software.

Table 2.5 Summary of reviewed performance-based seismic design building codes

Design Code	Earthquake Performance Level															
	Operational				Immediate Occupancy				Life Safety				Collapse Prevention			
	SDL[1]	RP[2]	ATDR[3]	ARDR[4]	SDL	RP	ATDR	ARDR	SDL	RP	ATDR	ARDR	SDL	RP	ATDR	ARDR
ATC3-06 (1978)	DLE[5]	475 years	1%	---	DLE[5]	475 years	1.5%	---	DLE[5]	475 years	1.5%	---	---	---	---	---
SEAOC (1995)	FHL[6]	43 years	0.2%	---	OHL[7]	72 years	0.5%	---	RHL[8]	475 years	1.5%	---	VRHL[9]	970 years	2.5%	---
UBC (1997)	---	---	---	---	---	---	---	---	DLE[5]	475 years	2-2.5%	---	---	---	---	---
FEMA273 (1997)	BSE-1[10]	475 years	1%	N*	BSE-1[10]	475 years	1%	N*	BSE-1[10]	475 years	2%	1%	BSE-2[10]	2475 years	4%	4%
Eurocode 8 – Part 1 (2004)	DLLE[11]	95 years	0.5%, 0.75 %, & 1%	---	DLLE[11]	95 years	0.5%, 0.75%, & 1%	---	NCLE[12]	475 years	$\theta^{**} <$ 0.3	---	---	---	---	---
NZS1170. 5 (2004)	SLS-1&2[13]	25 & 500 years	---	---	SLS-1&2[13]	25 & 500 years	---	---	ULS[14]	100, 500, 1000, 2500 years	2.5%	---	---	---	---	---
AS1170.4 (2007)	---	---	---	---	---	---	---	---	ULS[14]	500 & 2500 years	1.5%	---	---	---	---	---
BSLJ (2013)	OIALE[15]	50 years	0.5%	---	OIALE[15]	50 years	0.5%	---	ME[16]	500 years	1.5%	---	---	---	---	---
PEER-TBI (2017)	SLE[17]	43 years	0.5%	N*	SLE[17]	43 years	0.5%	N*	---	---	---	---	MCE[18]	2475 years	3%	1%

[1]SDL: Seismic Demand Level, [2]RP: Return Period, [3]ATDR: Allowable Transient Drift Ratio, [4]ARDR: Allowable Residual Drift Ratio, [5]DLE: Design Level Earthquake, [6]FHL: Frequent Hazard Level, [7]OHL: Occasional Hazard Level, [8]RHL: Rare Hazard Level, [9]VRHL: Very Rare Hazard Level, [10]BSE-1&2: Basic Safety Earthquake 1&2, [11]DLLE: Damage Limitation Level Earthquake, [12]NCLE: No-Collapse Level Earthquake, [13]SLS-1&2: Serviceability Limit State 1&2, [14]ULS: Ultimate Limit State, [15]OIALE: Once-In-A-Lifetime Earthquake, [16]ME: Maximum Earthquake, [17]SLE: Service-Level Earthquake, and [18]MCE: Maximum Considered Earthquake.
*N: Negligible. **θ: Inter-story drift coefficient.

2.3.3 DSSI in Eyes of Seismic Design Codes

To say nothing of the types of the superstructures and foundations, the amplification or the de-amplification of the seismic waves might occur owing to the characteristics of the ground motion and soil conditions. As Wong (1984) pointed out that the uncertainties in the dynamic soil-structure interaction are rooted in the model and parameters, the codes and regulations are often reluctant to strongly suggest carrying out the seismic SSI design, which is obviously a complex procedure. The research work, carried out by Tabatabaiefar et al. (2012), indicated the unsafe design when neglecting the effects associated with the seismic soil-structure interaction even though the majority of the current cods and standards leaned towards that. The considerable inter-story drift ratios were observed for a shallow-founded 10-story moment resisting frame once considering the soil flexibility in a site-dependent dynamic numerical simulation using FLAC2D.

Some of the codes such as the Turkish Earthquake Code TEC (2007) and Australian Seismic Design Code AS1170.4 (2007) did not cover the topic of the soil-structure interaction. FEMA356 (2000) underscored that the effects of the soil-structure interaction shall be evaluated with the provision that the SSI-induced increase in the fundamental period results in an increase in the spectral accelerations, e.g., the near-field and soft soil sites. Dismissing SSI was permitted by the Indian Standard IS-1893 (2002) for the rock-supported buildings. It was not only limited to rock since the rock-like soils were also mentioned in the above-mentioned cluase by the Indian Standard IS-1893 (2002). NZS1170.5 (2004) appreciated the momentousness of the soil-structure interaction in the analyses, but did not provide the practical methods in order to consider such a phenomenon. The Iranian Standard 2800 (2017) permitted to disregard the effect of SSI as long as the building has the maximum of two levels as the basement; otherwise, the SSI effects could be taken into account via the procedures in its appendix 5, entirely inspired by the chapter 19 of ASCE7-16 (2016), explained in the

following pages. In Part 1 of Eurocode 8 (2004), it was stated that the foundation deformability, including the soil-structure interaction, shall be considered whenever it might have an adverse overall influence on the structural responses. Indeed, the beneficial effects of the soil-structure interaction were highlighted as the reductions in the internal forces and moments of the buildings.

Eurocode 8 – Part 5 (2004) took a step further, mentioning the cases wherein the effects of the soil-structure interaction could be detrimental. The said cases are bullet-pointed below while the concepts and details of the computation methods of SSI were abandoned by Eurocode 8 – Part 5 (2004).

- Structures with the significant $P - \Delta$ effect as a destabilizing second-order effect.
- Deep-seated foundations as well as the massive foundations.
- Tall buildings and slender structures.
- Low shear wave velocity of the soil (i.e., less than 100 m/s).

Referring to FEMA-P-750 (2009), the response of a building to an earthquake shaking is significantly influenced by: (i) foundation stiffness and the damping; (ii) incompatibility of motions at the free field ground and foundation level; and (iii) foundation deformations. The second factor has been proved by the previous studies. For example, Yamahara (1970) presented that the recorded motions for the instrumented Hachinohe Technical College building on the foundation and adjacent to the superstructure were conspicuously different. Taking into account the last factor (i.e., the foundation deformations), FEMA440 (2005) elucidated the soil-structure interaction throughout the three key effects, i.e., the flexible foundation, kinematic, and foundation damping effects. The middle effect describes the motions, which the superstructures experience, subsequent to the local soil-induced filtration. The last effect describes the hysteretic damping and soil radiation damping. The interface between the foundation and soil deposit hosts not only the displacements but also the rotations,

both of which stem from the developed inertia in a building, subjected to an earthquake. The structural flexibility is elevated by such displacements and rotations, leading to lengthening the building period. Additionally, the total damping of the flexible soil-structure system increases in view of the presence of the hysteretic damping and soil radiation damping. To sum, the inertial interaction effects in a soil-foundation-structure system consist of the above-mentioned first and last effects. Kramer (1996) declared that the kinematic and inertial interactions are the two important mechanisms during the seismic analysis of a soil-foundation-structure system.

The soil-structure interaction for the buildings was presented in the ATC3-06 report (1978) as the first official standard, showcasing the said topic in the force-based design approach. Diminishing the story shear forces and overturning moments as well as elevating the structural lateral deflections were reported. In that regard, the base shear in the equivalent lateral force procedure is computed via $\tilde{V} = V - \Delta V$. The said reduction (ΔV) is defined based on Equation (2.12) (ATC3-06, 1978). FEMA273 (1997) underlined that the effects of the soil-structure interaction should not be employed in the project, wherein the elements and components actions are diminished by more than 25%. The Iranian Standard 2800 (2017) limited ΔV to 85% of the seismic base shear (V) for a fixed-base building.

$$\Delta V = \left(\frac{1.2A_v S}{R}\right)\left[\frac{1}{T^{2/3}} - \frac{1}{\tilde{T}^{2/3}}\left(\frac{1}{0.05\beta_f + \frac{1}{\left(\tilde{T}/T\right)^3}}\right)^{0.4}\right]\bar{W} \tag{2.12}$$

where, A_v is the coefficient, representing the effective peak velocity-related acceleration, S is the coefficient for the soil profile characteristics of the site, R is the response modification factor, T is the fundamental period of the building, $\tilde{T}$ is the effective building period, and $\bar{W}$ is the 70% of the total gravity load of the building. In line with Eurocode 8 – Part 5 (2004), hinging around the consideration of the damping as an additional ground property in the SSI analysis, β_f is the foundation damping factor as specified in ATC3-06 (1978). Figure 2.23

presents the trends for estimating β_f on the basis of $\tilde{T}/T$, value of A_v, and $\bar{h}/r$. $\bar{h}$ is the effective height of the building, taken a 0.7 times the total height whilst r is a characteristic foundation length, determined in accordance with $\sqrt{A_f/\pi}$ for $\bar{h}/L_0 \leq 0.5$ or $\sqrt[4]{4I/\pi}$ if $\bar{h}/L_0 \geq 1.0$, where A_f, L_0, and I are the area of the foundation, foundation length in the direction of analysis, and static moment of inertia of the foundation, respectively.

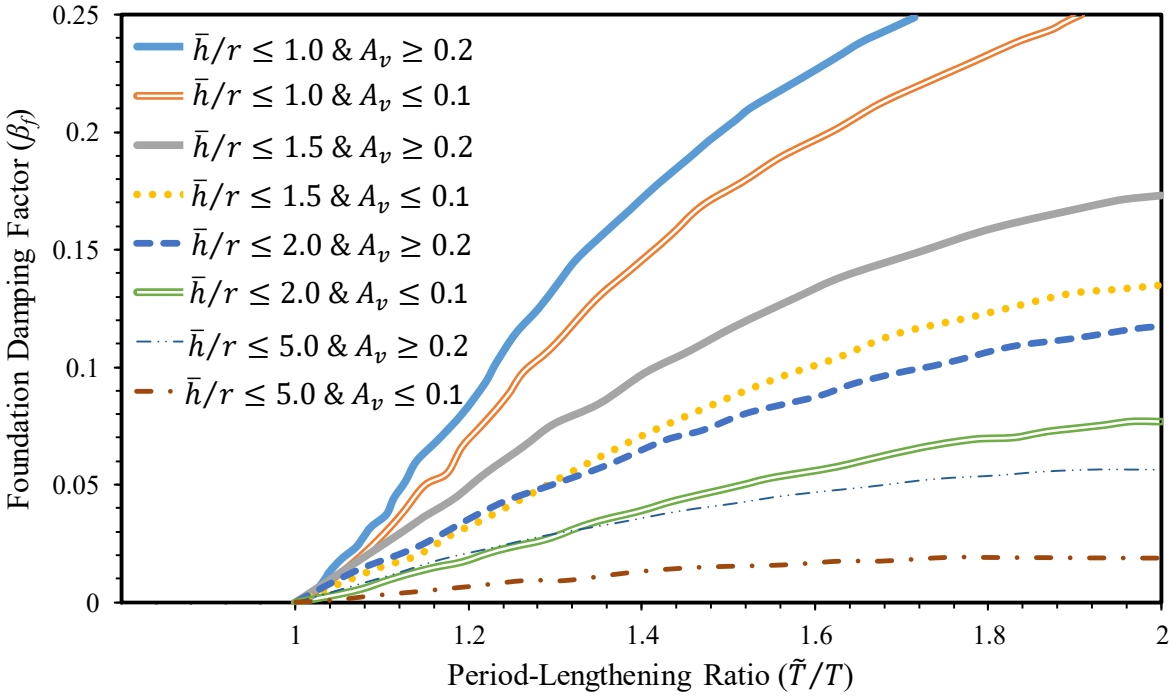

Figure 2.23 Determination of foundation damping factor (β_f) based on $\tilde{T}/T$, $\bar{h}/r$, and A_v (after ATC3-06, 1978)

The Chinese Standard GB50011 (2010) put forward the force reduction factor when considering the subsoil-structure interaction for a building, having the height-width ratio less than 3. The reduction factor of the horizontal seismic shear of each floor is $\left(\frac{T}{T+\Delta T}\right)^{0.9}$. ΔT is the additional period after taking into account SSI, which could be picked from Table 2.6. The site class III ($V_s \leq 140\ m/s$ with $H_s = 15\sim80\ m$ and $140 < V_s \leq 500\ m/s$ with $H_s > 50\ m$) and site class IV ($V_s \leq 140\ m/s$ with $H_s > 80\ m$) represent the medium to soft soils and very soft soils, consecutively. Note that H_s is the thickness of the soil site of interest.

Table 2.6 Additional period (ΔT) (after GB50011, 2010)

Design Acceleration of Ground Motion	Site Class III	Site Class IV
0.2g (0.3g)	0.08 sec	0.20 sec
0.4g	0.10 sec	0.25 sec

Referring to Stewart et al. (1999), the fixed-base damping ratio (β_i), i.e., the structural viscous damping, as well as the hysteretic damping and soil radiation damping associated with the foundation grant the flexible base damping ratio to the soil-foundation-structure system. The latter ones (i.e., the hysteretic damping and soil radiation damping) are the results of the inertial soil-structure interaction, entitled the foundation damping. The former (i.e., β_i) is by and large equal to 5%, recommended by FEMA-P-1050-1 (2015). The foundation damping only due to the radiation damping ($\beta_{f_R} = \left[\left(1.5\left(\frac{e_b}{r_x}\right)+1\right)\left(e^{4.7-1.6H/r_\theta}\right)\right]\left(\frac{\tilde{T}_{eff}}{T_{eff}}-1\right)+\left[\left(1.5\left(\frac{e_b}{r_x}\right)+1\right)\left(25\ln\left(\frac{H}{r_\theta}\right)-16\right)\right]\left(\frac{\tilde{T}_{eff}}{T_{eff}}-1\right)^2$) based on $\tilde{T}_{eff}/T_{eff}$, e_b/r_x, and H/r_θ are plotted in Figure 2.24. Note that r_θ ($=\left[\frac{3(1-\nu)K_\theta}{8G}\right]^{\frac{1}{3}}$) is the equivalent foundation radius for the rotation and r_x ($=\sqrt{\frac{A_f}{\pi}}$) is the equivalent foundation radius for the translation. A_f is the foundation area. It was emphasized in FEMA440 (2005) that the foundation damping, β_{f_R}, is underestimated for $\tilde{T}_{eff}/T_{eff} > 1.5$. The effective period-lengthening ratio ($\tilde{T}_{eff}/T_{eff}$) is calculated by means of Equation (2.13), presented by ASCE7-16 (2016), accounting for the ductility demand of the system (μ_s), including the structural ductility and also soil ductility. The soil hysteretic damping ratio (β_{f_H}) in Table 2.7 is approximately determined based on the effective peak acceleration (S_{DS}) and site classes C, D, and E, representing the very dense soil and soft rock, stiff soil, and soft clay soil, in the order given, in ASCE7-16 (2016). There is a modification for β_{f_H}, presented in ASCE-41-17 (2017), if a site within the depth of half the smaller dimension of the base of the structure meet the following criteria: (i) existence of the relatively uniform layer, whose thickness is shown by D_s; (ii) presence of the stiff layer under

the uniform layer while its shear wave velocity must be two times larger than the of the surface layer; and (iii) $4D_s/V_s\tilde{T} < 1$. In that case, β'_{fH} is equal to $\left(4D_s/V_s\tilde{T}\right)^4\beta_{f_H}$. Finally, the flexible base damping ratio (β_0), named the modified system-damping ratio, is determined using Equation (2.14), taken from Veletsos and Nair (1975), utilizing β_i and β_f (Equation (2.15)). It is now attempted to alter the SSI adjusted spectral response accelerations ($\tilde{S}_a$) to the appropriate level of β_0 as the flexible base damping ratio via $\frac{\tilde{S}_a}{\left[\frac{4}{5.6-\ln\beta_0}\right]}$.

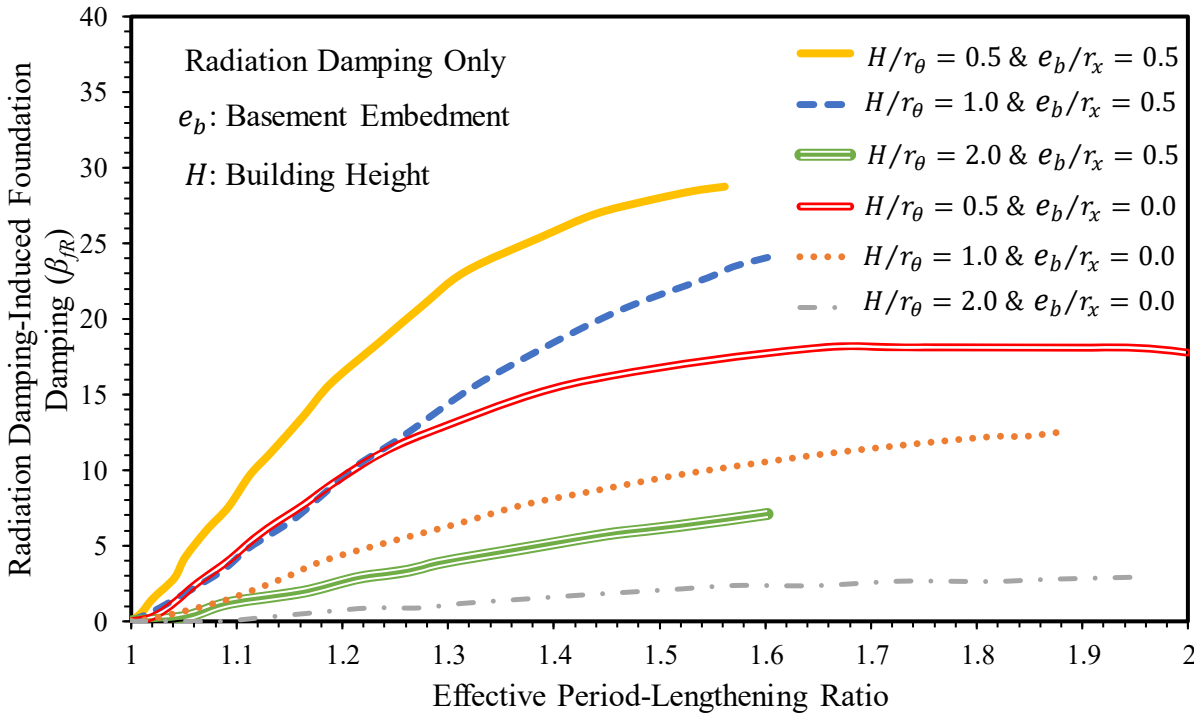

Figure 2.24 Determination of foundation damping due to radiation damping (β_{f_R}) as function of effective period-lengthening ratio ($\tilde{T}_{eff}/T_{eff}$), embedment ratio (e_b/r_x), and structure aspect ratio (H/r_θ) (after FEMA440, 2005)

Table 2.7 Soil hysteretic damping ratio (β_{f_H}) (after ASCE7-16, 2016)

Site Class	Description	Effective Peak Acceleration (S_{DS})		
		0.0	0.25	1.0
C	Very Dense Soil and Soft Rock	0.01	0.01	0.03
D	Stiff Soil	0.01	0.02	0.07
E	Soft Clay Soil	0.01	0.05	0.20

$$\frac{\tilde{T}_{eff}}{T_{eff}} = \left\{1 + \frac{1}{\mu_s}\left[\left(\frac{\tilde{T}}{T}\right)^2 - 1\right]\right\}^{0.5} \tag{2.13}$$

$$\beta_0 = \beta_f + \frac{\beta_i}{\left(\frac{\tilde{T}_{eff}}{T_{eff}}\right)^3} \tag{2.14}$$

$$\beta f = \left(\frac{\left(\frac{\tilde{T}}{\overline{T}}\right)^2 - 1}{\left(\frac{\tilde{T}}{\overline{T}}\right)^2}\right)\beta_{f_H} + \beta_{f_R} \tag{2.15}$$

The effective building period is determined in accordance with Equation (2.16), presented in ATC3-06 (1978), wherein g is the acceleration of gravity, K_l and K_θ are the lateral and rocking stiffness parameters of the foundation, respectively. The foundation stiffnesses are presented in Equations (2.17) and (2.18) for a circular mat foundation at a surface of the homogeneous halfspace as per FEMA450 – Part 2 (2003). Some research studies (e.g., Balkaya et al., 2012) have forewarned the design and practice engineers that the code-based methods for the estimation of the periods could be misleading.

$$\tilde{T} = T\sqrt{1 + \frac{4\pi^2\overline{W}}{gT^2}\left(\frac{1}{K_l} + \frac{(0.7H)^2}{K_\theta}\right)} \tag{2.16}$$

$$K_l = \frac{8\alpha_y}{2-\nu}Gr_f \tag{2.17}$$

$$K_\theta = \frac{8\alpha_\theta}{3(1-\nu)}Gr_f{}^3 \tag{2.18}$$

where, α_y and α_θ are the dynamic foundation stiffness modifiers for the translation and rocking, respectively, ν is the soil Poisson's ratio, G is the soil shear modulus, and r_f is the radius of the foundation.

FEMA440 (2005) suggested that the linear period of a flexible base building ($\tilde{T}$) is

calculated using Equation (2.16), employing Equations (2.19) and (2.20) for evaluating the translational stiffness of the foundation (K_t) and foundation rotational stiffness (K_θ). For information, K_l in Equation (2.16) is replaced by K_t.

$$K_t = \frac{8G_{sd}}{2-\upsilon}\sqrt{\frac{A_f}{\pi}} \tag{2.19}$$

$$K_\theta = \frac{K^*_{fixed}(\bar{h})^2}{\left(\frac{\tilde{T}}{\bar{T}}\right)^2 - 1 - \frac{K^*_{fixed}}{K_x}} \approx \frac{K^*_{fixed}\left(\bar{h}\right)^2}{\left(\frac{\tilde{T}}{\bar{T}}\right)^2 - 1} \; as \; K_x \gg K^*_{fixed} \tag{2.20}$$

where, G_{sd} is the strain-degraded shear modulus, A_f is the area of the foundation footprint, K^*_{fixed} is the effective structural stiffness of the Single-Degree-Of-Freedom (SDOF) oscillator for the fixed-base condition, and $\bar{h}$ is the effective structure height, well-approximated as 70% of the total structure height.

ATC3-06 (1978) suggested $0.81G_0$, $0.64G_0$, $0.49G_0$, and $0.42G_0$ for the strain-degraded shear modulus (G_{sd}), corresponding to the ground acceleration coefficient (A_v) of ≤0.1, 0.15, 0.2, and ≥0.3, in the order given. Referring back to Equation (2.20), K^*_{fixed} equals $M^*\left(\frac{2\pi}{T}\right)^2$, wherein M^* is the effective mass for the first mode, calculated from Equation (2.21).

$$M^* = \frac{\left[\sum_{i=1}^{N_s}(W_i\emptyset_i)/g\right]^2}{\left[\sum_{i=1}^{N_s}W_i/g\right]\sum_{i=1}^{N_s}\left(W_i{\emptyset_i}^2\right)/g}M \tag{2.21}$$

where, N_s is the number of the stories, W_i/g is the mass, which is assigned to the level i, $\emptyset_i$ is the amplitude of the first mode at the level i, and M is the total mass of the structure.

Whittaker et al. (2011) pointed out that the seismic design codes and standards took into account the soil-structure interaction effects through the reduction in the seismic base shear, implying that neglecting the SSI concept in the seismic analyses will give rise to the conservative design. The equivalent lateral force procedure was also suggested by ASCE7-16 (2016) with some modifications (see Equation (2.12)) so as to take into account the effects of

SSI. $\tilde{V}$, which is the base shear, adjusted for SSI, is estimated by modifying the fixed-base structure base shear (V) from the linear static procedure. Equation (2.22) from ASCE7-16 (2016) incorporates the minimum limits for $\tilde{V}$.

$$\tilde{V} = V - \left[\left(\bar{C}_s - \frac{\tilde{C}_s}{4/(5.6 - \ln(100\beta_0))}\right)\bar{W}\right] \geq \begin{cases} 0.7V & for\ R \leq 3 \\ (0.5 + R/15)V & for\ 3 < R < 6 \\ 0.9V & for\ R \geq 6 \end{cases} \quad (2.22)$$

where, $\bar{C}_s$ is the seismic response coefficient for a fixed-base building, $\tilde{C}_s$ is the same as C_s whilst assuming the flexibility of the structural base, β_0 is the effective damping ratio of the soil-structure interaction, and R is the response modification factor.

As regards the SSI analysis, ASCE7-16 (2016) allowed the design engineers to make use of the equivalent lateral force and a linear dynamic analysis. The linear dynamic analysis could be performed using the SSI modified design response spectrum, formulated via $\tilde{S}_a = \left[\left(\frac{5}{4/(5.6-\ln(100\beta_0))} - 2\right)(T/T_s) + 0.4\right]S_{DS}$ for $0 < T < T_0$, $\tilde{S}_a = \frac{S_{DS}}{4/(5.6-\ln(100\beta_0))}$ for $T_0 \leq T \leq T_s$, $\tilde{S}_a = \frac{S_{D1}}{4/(5.6-\ln(100\beta_0))}$ for $T_s \leq T \leq T_L$, and $\tilde{S}_a = \frac{S_{D1}T_L}{4T^2/(5.6-\ln(100\beta_0))}$ for $T > T_L$. The descriptions of the parameters in the said figure are as follows: (i) $\tilde{S}_a$ is the SSI adjusted spectral response acceleration; (ii) S_{DS} and S_{D1} are the design earthquake spectral response acceleration parameters at the short period and at the 1-s period, respectively; (iii) T_L is the long-period transition period, and (iv) T_0 and T_s are equal to 0.2 $\frac{S_{D1}}{S_{DS}}$ and $\frac{S_{D1}}{S_{DS}}$, respectively.

The provisions, presented in the two well-known codes, i.e., ATC3-06 (1978) and FEMA356 (2000), were capable of considering the inertial SSI effect according to the seismic demand (i.e., the free field motion) and assigned 5% damping to the building. However, the kinematic interaction effect was not addressed in the above-mentioned procedures. The kinematic interaction effect induces some level of diminishment in the seismic demand of the building compared to the free field motion. The concrete foundation is much stiffer than the

soil mass, leading to the differences between the free field motion and foundation motion, generating the kinematic interaction. As concerns the kinematic interaction, Aldea et al. (2007) reported that the instrumented high rise building in Bucharest, Romania, cast light on the significant difference between the recorded motions at the adjacent free field ground surface and instrumented building basement.

The most comprehensive method of considering SSI is the nonlinear response history procedure by means of the acceleration histories. The acceleration records should be scaled to a response spectrum, representing the site, and also should have the kinematic interaction modification. The base-slab averaging and embedment effects are classified under the kinematic interaction. The short-period components (or the high-frequency components) are affected by the aforesaid effects, acting as a filter for the free field motion. Continuing on this line, the kinematic interaction effects can be represented by the Ratio of Response Spectra (RRS), which is the ratio of the foundation input motion spectral ordinates to the free field spectral ordinates. In the first instance, the base-slab averaging effect, named RRS_{bsa}, is computed via Equation (2.23) (FEMA440, 2005), which ought to be greater than the corresponding value for the period of 0.2 s. In the said equation, b_e is the effective foundation size ($= \sqrt{A_f}$, wherein A_f is the area of the load-carrying foundation (ft^2)). The variations of RRS_{bsa} with the period and effective foundation size are put on view in Figure 2.25. A couple of years later, ASCE7-16 (2016) introduced b_0 ($= 0.0023 b_e/T$) when $b_e \leq 80\ m$, $T \geq 0.2\ s$, and $200 \leq V_s \leq 500\ m/s$ for the calculation of RRS_{bsa} via Equation (2.24) since the effective foundation size plays a key role herein.

$$RRS_{bsa} = 1 - \frac{1}{14{,}100}\left(\frac{b_e}{T}\right)^{1.2} \geq (RRS_{bsa})_{@T=0.2\ s} \tag{2.23}$$

$$RRS_{bsa} = \begin{cases} 0.25 + 0.75\left\{\frac{1}{b_0^2}\left[1 - exp(-2b_0^2)\left(1 + b_0^2 + b_0^4 + \frac{b_0^6}{2} + \frac{b_0^8}{4} + \frac{b_0^{10}}{12}\right)\right]\right\}^{0.5} \\ for\ b_o \le 1 \\ 0.25 + 0.75\left\{\frac{1}{b_0^2}\left[1 - exp(-2b_0^2)\left(exp(2b_0^2)\left(\frac{1}{\sqrt{\pi}b_0}\left(1 - \frac{1}{16b_0^2}\right)\right)\right)\right]\right\}^{0.5} \\ for\ b_o > 1 \end{cases} \quad (2.24)$$

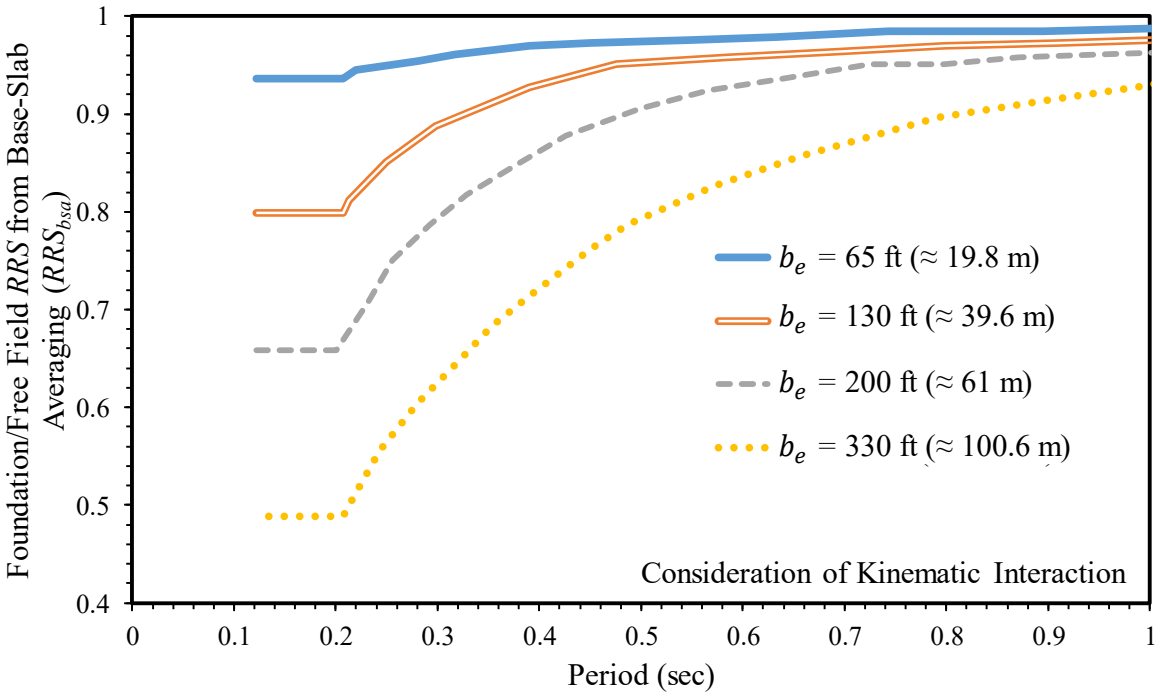

Figure 2.25 Ratio of response spectra for base-slab averaging (RRS_{bsa}) as function of period (T) and effective foundation size (b_e) (after FEMA440, 2005)

The additional RRS from the embedment, RRS_e, plotted in Figure 2.26 for an embedment of 30 ft, is based on Equation (2.25), presented in FEMA440 (2005). The foundation embedment effects could be dismissed, provided that the building of interest does not have a basement even granting that the footing is embedded. By referring to Figures 2.25 and 2.26, it is manifest that such effects are strongly period-dependent, being significantly influential at the relatively short periods (e.g., < 0.5 s). In 2016, Equation (2.26) was proposed by ASCE7-16 (2016), determining the modification factor for the embedment, providing that the foundation

embedment depth is not greater than 6.1 m whilst must have the interface surface with at least 75% of the foundation area.

$$RRS_e = \cos\left(\frac{2\pi e_b}{T\bar{n}V_{s_{@b_e}}}\right) \geq Max\{0.453, RRS_{e_{@T=0.2\ s}}\} \tag{2.25}$$

$$RRS_e = 0.25 + 0.75\cos\left(\frac{2\pi e_b}{TV_{s_{@b_e}}}\right) \ for\ V_{s_{@b_e}} \geq 200\ m/s \tag{2.26}$$

where, e_b is the foundation embedment (ft), $V_{s_{@b_e}}$ is the weighted average shear wave velocity within the depth of b_e below the foundation, and $\bar{n}$ is the shear wave velocity reduction factor, depending on the Peak Ground Acceleration (PGA), listed in Table 2.8.

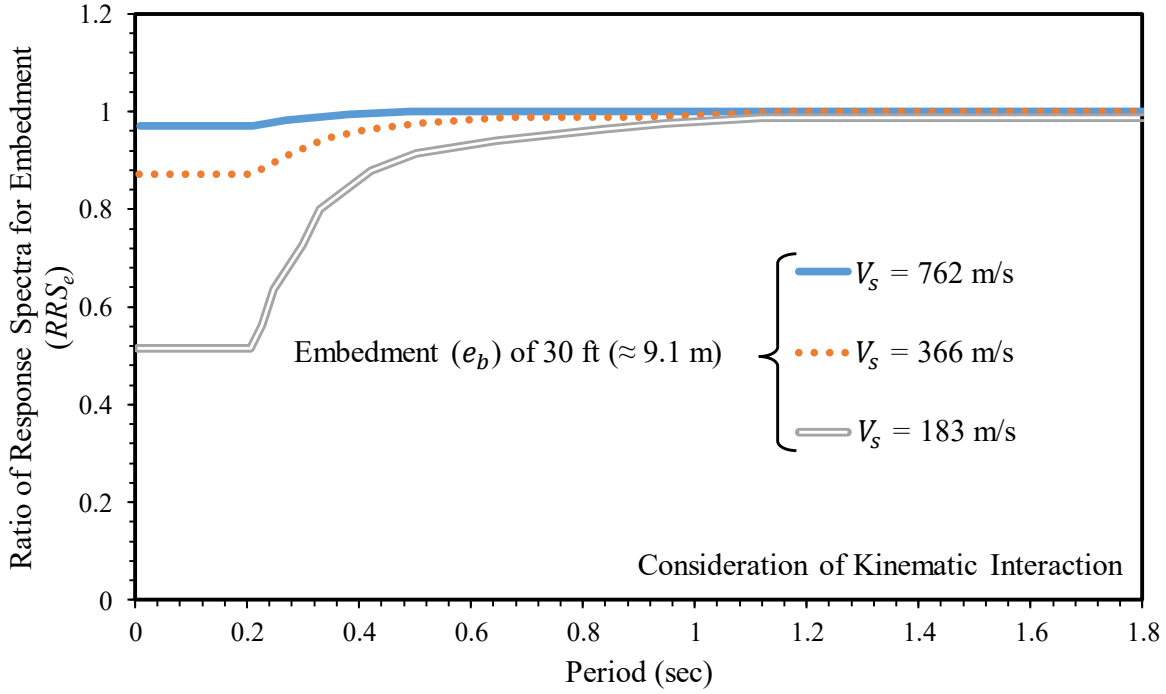

Figure 2.26 Ratio of response spectra for embedment (RRS_e) as function of period (T) and shear wave velocity (V_s) (after FEMA440, 2005)

Table 2.8 Approximate values of shear wave velocity reduction factor ($\bar{n}$) (after FEMA440, 2005)

Peak Ground Acceleration (PGA)	0.1g	0.15g	0.2g	0.3g
$\bar{n}$	0.90	0.80	0.70	0.65

For generating a complete spectrum of the foundation input motion, the product of the total RRS $(= RRS_{bsa}.RRS_e)$ times the free field spectrum should be carried out at each period.

According to ASCE7-16 (2016), the total RRS shall not be less than 0.7. The limitations of the above-mentioned procedure for the consideration of the kinematic interaction are mentioned herein. The embedment and kinematic interaction effects should not be considered for the foundations, resting in/on the strong rocks and soft clayey soils, respectively. The underestimation of reducing the ground motions happens when utilizing the base-slab averaging model for the strong rock sites. Another drawback of the base-slab averaging model is that there has been no comprehensive study for expanding its application to the structures with a mat foundation and pile-supported buildings as well as the massive superstructures in terms of the plan dimensions.

It should be brought up here that the modal response spectrum analysis could be used in conjunction with the implementation of SSI in the seismic design, which is similar to the implementation for the equivalent lateral force analysis, explained above. Indeed, the modal response spectrum analysis follows one controversial assumption, revolving around the consideration of the damping modification and period lengthening only for the fundamental vibration mode inasmuch as it is believed that the periods and damping ratios of the higher modes are not meant to be modified due to SSI according to Veletsos and Meek (1974) and Bielak (1976). However, in the following sections, the results of this thesis will demonstrate the effects of the higher modes on the seismic responses of the soil-structure systems.

The modification of period (i.e., the effective period) and damping (i.e., the equivalent damping ratio) so as to consider the effects of SSI was underscored by the Building Standard Law of Japan BSLJ (2013) in the event of the severe ground shakings. Besides, the excessive reduction of the structural actions is not permitted when considering the effects of SSI. In that regard, FEMA273 (1997) limited the maximum amount of the said reduction to 25%. With that being said, some of the codes and regulations still remained silent as regards the soil-structure interaction analyses. By all accounts, the methods, found in the standards, are either overly

simplified and limited to some specific problems or too vague to be used in the real projects. The modified fixed-base approach is the most common approach according to Veletsos (1977). It involves the adjustment of the damping ratio of the structure and its fundamental period of the first mode of the vibration in order to account for the soil-structure interaction effects. It could be finally uttered that the nonlinear dynamic procedure outshines the linear static and dynamic methods, as well as the nonlinear static procedure whilst its application is not strongly recommended by the codes. For instance, the nonlinear time history analysis should only be conducted for the buildings, between 200 and 300 meters high as per the Chinese Standard GB50011 (2010). FEMA273 (1997) emphasized that the analysis and design based on the nonlinear dynamic procedure must be subjected to the stringent review by the independent, well-experienced design engineers in the field of the nonlinear seismic analysis and design. The past research works (e.g., Barcena and Esteva, 2007; Renzi et al., 2013) have delivered the knowledge that the reliability of dynamic soil-structure interaction analyses depends on the representativeness of the subsoil and geotechnical aspects. In sum, the current methods and procedures in the standards and codes for the consideration of the soil-structure interaction phenomena are not only unclear to a large extent, but also overlooking the crucial topics, such as the soil plasticity, generation of excess pore water pressure, and other types of the foundations rather than the circular and square footing, mat foundations and conventional pile foundations. Having utterly perused the concepts of the dynamic soil-structure interaction and performance-based seismic design, the next step should be relating the aforesaid topics together with the intention of excelling the quality of the analyses and outcomes thereof.

2.3.4 Incorporation of SSI in PBSD

The past experiences and observations (e.g., Maheshwari et al., 2004; Jayalekshmi and Chinmayi, 2016) have indicated the fact that the presence of a building could change the

characteristics of the free field ground motion whilst the flexibility of the supporting soil is altering the structural dynamic response against the earthquake motion. The damage cost and death toll, befalling in the several recent earthquakes, e.g., the 1994 Northridge earthquake (USA), 1995 Kobe earthquake (Japan), 1999 Kocaeli earthquake (Turkey), 2009 L'Aquila earthquake (Italy), and 2017 Chiapas earthquake (Mexico), are the examples of such a claim, revolving around the unsafe or extravagant design, resulting from excluding the dynamic soil-structure interaction. Besides, building the superstructures on the completely favorable geotechnical conditions in the earthquake-prone zones seems unrealistic. That is why the problem of the soil-structure interaction has received the growing attention from the structural and geotechnical societies, as mentioned by Gazetas and Mylonakis (1998). According to Kraus and Džakić (2013), it suffices to say that the fixed base analysis is valid only if the soil stiffness is relatively higher than that of the structure on the grounds that the interface between the soil and superstructure undertakes the negligible deformations.

The goal line in the PBD approach is satisfying a cluster of specific performance targets. To achieve that, all the crucial factors, one of which is the soil-structure interaction phenomenon, must be taken into account. It is also necessary to consider the soil shear velocity, building height, and its natural period under the fixed-base condition when dealing with the effects of SSI, emphasized by Veletsos and Meek (1974). In line with the preceding notions, Tabatabaiefar et al. (2014) proposed an empirical relationship for the estimation of the maximum lateral displacement of a story ($\tilde{\delta} = \delta\left(1 + \frac{H^2 h_{bd} E_{str}}{\bar{\lambda}\rho {V_s}^2 B^2}\right)$) under the influence of the soil-structure interaction. δ is the corresponding lateral displacement at the same level under the fixed-base condition. The other parameters are as follows: (i) H is the building height; (ii) h_{bd} is the bedrock depth; (iii) E_{str} is the modulus of elasticity of the structural material; (iv) $\bar{\lambda}$ is the analysis type factor, which is 33800 and 44700 for the elastic analysis and inelastic analysis, respectively; (v) V_s is the shear wave velocity of the subsoil; and (vi) B is the

foundation width. Then, the inter-story drifts under the influence of the soil-structure interaction for each two adjacent stories can be determined so as to be checked against the limiting values, reported in Section 2.3.2. As a result, the seismic performance of the building could be predicted to ensure that the design is safe and reliable. With due consideration of the previous sectors of Section 2.3 in conjunction with the observations from the recent earthquake events, performing a realistic SSI analysis, taking into account the stiffness and damping of the soil, surrounding the foundation and superstructure, is inevitable. Continuing on this line, SSI could conspicuously alter the structural demands, i.e., the strength and ductility, as underscored by Ghannad and Ahmadnia (2006). Another effect, related to the consideration of SSI is the modification of the damping. Referring to Nakhaei and Ghannad (2008), the soil-foundation-building interaction would be in charge of imposing the considerable changes on the dissipation of the seismic energy under the name of the hysteretic damping amidst the earthquake events. Therefore, the damage level, imposed on a building due to an earthquake, will be expected to be significantly different between the two scenarios, namely, the fixed-base structure and flexible base structure. Moreover, the variables, including the Intensity Measure (IM), Engineering Demand Parameter (EDP), Damage Measure (DM), and Decision Variable (DV), were introduced by Kramer (2008). The aim was fomalizing the PBD methodology in accordance with the probabilistic framework. EDP represents the geotechnical aspects. Moehle and Deierlein (2004) mentioned that the analysis of the soil-structure system via the direct one-step approach should be placed in EDP. For information, the direct method means that there is no need to separately analyze each part of the SSI domain. In the context of the performance-based design, the soil-structure interaction is an integral part of the seismic evaluation of the buildings even though the effects of SSI were observed to be reduced with increasing the number of underground stories in the study, conducted by El Ganainy and El Naggar (2009).

Ac concerns the application of SSI in the performance-based design method, the Chilean Seismic Code (NCh433.Of96, 1996) did not cover neither the performance-based design nor the soil-structure interaction concept although Chile is one of the world's most earthquake-prone countries. On the other hand, the Korean Building Code (KBC, 2009) considers the foundation interaction via assigning the stiffness to the springs at the foundation level for the overly soft soil condition. But, it did not allow to bypass the prescriptive code restrictions, e.g., the height and location of the seismic force-resisting system, by means of the outcomes of the performance-based design. ASEP (2010) from the Philippines allowed the performance-based design method as an alternative design approach whilst referring to PEER-TBI (2017) for more details. Speaking of PEER-TBI (2017), providing the guidelines for PBSD of the tall buildings, it was reported that the soil-structure interaction has little effects on the seismic performance of such buildings at the SLE demand level, referring back to Section 2.3.2.

In the Winkler's idealization (Winkler, 1867), a group of the independent, linear elastic springs represent the soil mass under the foundation. It is of note that the deformation of the foundation of interest is limited to the loaded area in the Winkler model. As an improvement, Lysmer and Richart (1966) presented the six spring stiffness values for the point, wherein the soil is lumped, including the vertical spring, two horizontal springs, two rocking springs, and twisting spring. The said spring stiffnesses are tabulated in Table 2.9. Finn (2005) stated that the idealization of the soil continuum with the discrete soil reactions, working in a decoupled way, is the main drawbacks of the static Beam-on-Nonlinear-Winkler-Foundation (BNWF) approach. Additionally, the shear transfer between the springs is another vivid missing fundamental mechanism in the Winkler model. Anent the soil-pile-structure interaction problems, which are of the direct concern to the performance-based design of the superstructures, Allotey and El Naggar (2008) developed a model, within the framework of BNWF, with the considerations from both the structural and geotechnical engineering

perspectives, facilitating the incorporation of the SSI in the PBSD. The chief features of the aforesaid model are presented hereinafter: (i) stiffness degradation due to the irregular cyclic loading; (ii) nonlinearity of the soil; (iii) advanced interface between the soil and pile, capable of considering of the gap and discontinuity; and (iv) radiation damping reduction owing to the generation of the nonlinearity.

Table 2.9 Soil spring stiffness values according to Lysmer and Richart (1966)

Type of Behavior	Spring Stiffness	Equivalent Radius
Vertical	$K_z = \frac{4Gr_z}{1-\upsilon}$	$r_z = r_x = \sqrt{\frac{LB}{\pi}}$
Horizontal	$K_x = K_y = \frac{32Gr_x(1-\upsilon)}{(7-8\nu)}$	
Rocking	$K_{\phi_x} = \frac{8G{r_{\phi_x}}^3}{3(1-\nu)}$	$r_{\phi_x} = r_{\phi_y} = \sqrt[4]{\frac{LB^3}{3\pi}}$
	$K_{\phi_y} = \frac{8G{r_{\phi_y}}^3}{3(1-\nu)}$	
Twisting	$K_{\phi_z} = \frac{16G{r_{\phi_z}}^3}{3}$	$r_{\phi_z} = \sqrt[4]{\frac{LB^3 + BL^3}{6\pi}}$

Considering the most promising approach for incorporating SSI, an equivalent fixed-base oscillator could be introduced. Avilés and Pérez-Rocha (2003) posited a method for replacing the flexible-base structure by an equivalent fixed-base oscillator. If the foundation's mass and moment of inertia are disregarded, the relationships of the system's period ($\tilde{T}_e$) and damping ($\tilde{\zeta}_e$) based on the natural period (T_e) and damping ratio (ζ_e) of the single structure are given by Equations (2.27) and (2.28). The expression of $\tilde{\mu}_u = 1 + (\mu - 1)\left(\frac{T_e}{\tilde{T}_e}\right)^2$ represents the global ductility of an equivalent oscillator with the same capacity for the plastic deformation and strength as the actual structure. Referring to Avilés and Pérez-Rocha (2003), it is to assume the elasto-plastic and elastic behaviors for the structure and soil mass, respectively. It eventually results in the same foundation rocking and translation of the foundation for the ultimate stage and yielding condition.

$$\tilde{T}_e = \sqrt{{T_e}^2 + {T_h}^2 + {T_r}^2} \tag{2.27}$$

$$\tilde{\zeta}_e = \zeta_e \left(\frac{T_e}{\tilde{T}_e}\right)^3 + \frac{\zeta_h}{1 + 2{\zeta_h}^2}\left(\frac{T_h}{\tilde{T}_e}\right)^2 + \frac{\zeta_r}{1 + 2{\zeta_r}^2}\left(\frac{T_r}{\tilde{T}_e}\right)^2 \tag{2.28}$$

where, $T_h = 2\pi(M_e/\bar{K}_h)^{0.5}$ and $T_r = 2\pi[M_e(H + D_e)^2/\bar{K}_r]^{0.5}$ are the natural periods associated with the rigid-body translation and rocking of the structure, respectively, plus $\zeta_h = \pi\bar{C}_h/\tilde{T}_e\bar{K}_h$ and $\zeta_r = \pi\bar{C}_r/\tilde{T}_e\bar{K}_r$ are the damping ratios of the soil for the horizontal and rocking modes of the foundation, in the order given. H and M_e are the height and mass of the structure in the fixed-base condition, respectively. D_e is the depth of embedment for a circular mat whilst $\bar{C}$ and $\bar{K}$ are, consecutively, the viscous damping and initial stiffness of the structure.

Lu et al. (2016) rendered a series of comprehensive parametric study to investigate the seismic performance of the multi-story shear buildings on the shallow foundations considering the soil-structure interaction. The cone model was adopted in their study in order to mimic the dynamic behavior of an elastic homogeneous soil half-space. The following design procedure was proposed for the PBSD of the flexible base structures. Designing the Multi-Degree-Of-Freedom (MDOF) should be done initially under the gravity and seismic loads by ignoring the effects of SSI. Next, the fundamental period (T) and slenderness ratio (s) are calculated via $T = C_t H^x$ and $s = \bar{h}/r$, respectively. H and $\bar{h}$ are the total height and effective height of the structures, respectively. According to ATC-40 (1996), $\bar{h}$ can be approximated as 0.7 times the building height. C_t and x are both related to the structural system type, that could be chosen from ASCE7-16 (2016). $\alpha_0 = 2\pi\bar{h}/TV_{s,30}$ is the structure-to-soil stiffness ratio as to the average shear wave velocity of the top 30 m of the soil deposit ($V_{s,30}$). Now, the base shear demand of the fixed-base elastic SDOF structure $V_{SDOF}(T, \alpha_0 = 0, \mu = 1)$ should be computed from the elastic design spectrum via T as the fundamental period. μ, as the ductility demand,

shows the utterly elastic behavior when equaling unity. In this step, the design base shear of the inelastic flexible base MDOF structure (V_{MDOF}) is derived using Equation (2.29).

$$V_{MDOF}(T, \alpha_0, s, \mu_t) = \frac{V_{SDOF}(T_n, \alpha_0=0, \mu=1)}{R_M R_F} \quad (2.29)$$

where, μ_t is the predefined target ductility demand, R_M is the practical site and interaction-dependent MDOF modification factor (Equation (2.30)), and R_F ($= \frac{V_{SDOF}(T, \alpha_0=0, \mu=1)}{V_{SDOF}(T, \alpha_0, s, \mu=\mu_t)}$) is the SDOF strength reduction factor, suggested by Lu et al. (2016). At this juncture, the MDOF structure could be analyzed and designed against the calculated base shear strength, acted as the design lateral load pattern.

$$\frac{1}{R_M} = 1 + (N_s - 1) ln\left(c_{sd} \mu_t^{(0.05-N_s)/1000}\right) \quad (2.30)$$

where, N_s is the number of stories, and c_{sd} is the soil dependent parameter, equal to 1.040 (Site Class C), 1.027 (Site Class D), and 0.982 (Site Class E).

The seismic SSI is potentially a highly nonlinear phenomenon according to Reséndiz and Roesset (1985) and Ghalibafian et al. (2008). As a result, Allotey and El Naggar (2005) underlined the importance of the nonlinear analysis of the entire soil-structure system. In this way, the performance-based design approach could lead to the more accurate predictions of the seismic performance of the buildings incorporating SSI. At this juncture, Dutta and Roy (2002) claimed that the numerical techniques are able to duly accommodate the material nonlinearity, geometrical complexity, and intricate seismic wave propagations of a soil-structure system.

One of the efficient domain-based computing method in the civil engineering projects is the Finite Element Method (FEM). In the said method, the continuum is discretized into a large number of the elements (or zones), computationally governing the overall behavior of the continuum according to Lou et al. (2011). FEM is used frequently in the study of the seismic soil-structure system. In that regard, the effects of distance, direction of alignment, embedment and structural inertia were considered in the parametric study on the dynamic interaction

between the adjacent structures, harnessing the hybrid method, dealing with a near-field (FEM) and a far-field (the unbounded region), carried out by Lin et al. (1987). A novel procedure, presented by Ghiocel and Ghanem (2002), accounted for the uncertainty in the free field input motion and local site conditions, plus the structural parameters for the probabilistic analysis of the seismic SSI problems. The techniques from the stochastic finite element were applied to the probabilistic characterization and probabilistic risk assessment under the dynamic loading. Hatzigeorgiou and Beskos (2010) assigned the inelastic behavior to the concrete liner of a tunnel as well as the soft rock type of soil with the intent of investigating the necessity of the seismic SSI for the fiber-reinforced concrete lined tunnels, constructed in the earthquake-prone zones, through FEM in the time domain. Celebi et al. (2012) concluded that the constitutive material models, employed for the underlying soil, particularly the soft deposit, play an important role on the seismic performance of the buildings, derived from the two-dimensional finite element simulations in PLAXIS. In 2013, a host of two- and three-dimensional finite element analyses was conducted via ABAQUS to study the responses of the foundations to the marked overturning moments, resting on the inelastic homogeneous deposit of the medium plasticity clay under the undrained condition. Based on the said research work, Gazetas et al. (2013) developed a class of formula and charts for the determination of the rotational stiffness of the different types of the shallow foundations in the nonlinear effective manner.

A numerous researchers (e.g., Gutierrez and Chopra, 1978) have appreciated the performance and level of accuracy of the numerical simulations. One of the numerical discretization schemes, which is oftentimes employed in the study of the seismic SSI, is the Finite Difference Method (FDM). Three types of the reinforced concrete moment-resisting mid-rise buildings, consisting of 5, 10, and 15 stories, on a cluster of soft soils, were analyzed via FLAC2D throughout FDM by Tabatabaiefar et al. (2013). The adopted shear wave velocity was less than 600 m/s. It was shown that DSSI had better not be dismissed for the mid-rise

buildings on the soft soil deposits since the inter-story drift ratios, calculated based on the structural lateral displacements, pushed the performance level towards the collapse state. Hokmabadi et al. (2014) developed a three-dimensional finite difference model in FLAC3D utilizing the fully nonlinear hysteretic damping algorithm. Such an algorithm captured the changes in the shear modulus in accord with the variations of the cyclic shear strain. Then, the corresponding damping ratio was calculated. A conventional 15-story reinforced concrete moment-resisting building was adopted. The derived numerical results for the adopted soil-pile-building system were verified by the results of the shaking table tests, carried out by Hokmabadi et al. (2014). It was concluded that the floating pile foundations are able to improve the seismic performance of the superstructures by lessening the structural lateral deflections. It was, then, illustrated that the rocking rotations are on the decrease when utilizing the pile foundations compared to the shallow foundations.

The use of the finite element and finite difference techniques for the soil-structure interaction effects on the seismic responses of the structures began in the 1970s according to Krishna et al. (2018). The nonlinear properties of the continuum require the employment of the finite difference technique, as a popular numerical method, once conducting the analysis of the wave propagation in the continuous media.

The finite element method is the unquestionable choice for analyzing the structures without doubt. As, however, the resulting equations are the same in the above-mentioned methods, arguing as regards the superiority is pointless, as pointed out by Cundall (1976). Stevens and Krauthammer (1988) proposed to make use of the analysis technique, based on the combined finite difference-finite element code so as to achieve the efficiency enhancement in the numerical modeling. The said combined code is capable of capturing the actual dynamic behavior of the soil, including the radiation damping, material damping and hysteresis, arching, nonlinear elasticity, plasticity, and rate effects. The combined finite difference-finite element

approach in conjunction with the substructuring method also represent an attractive and effective technique for the SSI analyses as Chen and Krauthammer (1989) announced. In that context, the pure FE technique was harnessed in their study of a soil-lifeline interaction, triggering the costly analyses whilst the pure FD approach ended up with the very small solution time-step.

In a nutshell, the numerical analysis of the soil-structure interaction could be done via the domain type methods, such as FEM and FDM, or the boundary type methods, e.g., the Boundary Element Method (BEM). Dominguez and Roesset (1978) pioneered the use of BEM for the SSI problems. The boundary element method has been employed in the various SSI applications, such as, the surface foundations (e.g., Wolf and Obernhuber, 1985), embedded foundations (e.g., Wolf and Darbre, 1986), and wavefield excited soil-structure interaction (e.g., Auersch and Schmid, 1990). In the case of the isotropic and homogeneous materials in the bounded or unbounded domains, BEM performs well whilst not requiring the domain discretization, underlined by Mansur (1983). Yazdchi et al. (1999), on the other hand, shed light on the disadvantages of BEM, pointing out that the boundary element method is not suitable for the anisotropic domains, material and geometrical nonlinearities and complex geometries. To tackle the aforesaid drawbacks, the FEM or FDM would be utilized for the near-field discretization while the boundary element method will be employed to simulate the semi-infinite far-field. The coupling should be done by means of the equilibrium and compatibility conditions at the soil-structure interfaces. The research works of von Estorff and Kausel (1989) and Genes and Kocak (2005) are the examples of coupling the boundary type and domain type frameworks for the investigations of the complex soil-structure interaction problems. As a kind reminder, BEM, which was first introduced by Cruse and Rizzo (1968), is per se not practical for the nonlinear SSI problems according to Chen and Krauthammer (1989).

The advent of the powerful computers has considerably altered the computational aspects in all engineering fields. Taking into account all the merits and demerits of the numerical frameworks, briefly explained above, the finite difference method was picked as the main numerical technique in this thesis by means of FLAC3D (Itasca, 2012), which is the explicit finite difference program, being used in the engineering mechanics computation. The next section is garnished by the novel isolation technique, named "foundation rocking", in the fields of DSSI and PBSD. Prior to cascading to Section 2.4, it is to remind that Table 2.5 gathers a summary of the main codes and standards, concerning the performance-based seismic design concept.

2.4 Inviting Plastic Hinging Into Soil

The base isolation is the widely adopted seismic protection strategy for the infrastructures in the relatively high-risk earthquake-prone zones, as pointed out by Jangid and Londhe (1998). In the past few decades, the implementation of the base isolation devices in the superstructures, such as, the bridges and buildings, e.g., Nagarajaiah and Sun (2001) and Moroni et al. (2012), has provided the safe margins by the elongation of the system's natural frequency, placed far from the seismic period range, having the largest amplitudes of the earthquakes. It, however, should be asserted that fewer than 5% of the buildings in the United States are constructed with the base isolators according to Liu (2014) due to either the large construction cost or a life-cycle maintenance cost. In spite of the fact that the concept of the base isolation technique was established on the basis of decoupling the two main components of the soil-structure system, i.e., the building and soil medium, once the earthquake strikes the entire system according to Jangid (2007), the soil beneath the superstructure plays the main role in another isolation technique (i.e., the rocking isolation approach) referring to Makris (2014). Hung et al. (2011) stated that when the rocking mode is engaged for a foundation, subjected to the horizontal

loading above the base of the foundation, the ductility demand of the superstructure will be reduced. It intimates that the rocking isolation technique aims to protect the superstructure from the earthquake-induced damage. Housner (1963) and Meek (1975) pointed out that the seismic performance of the buildings could be enhanced by the above-mentioned role of the foundation rocking. It was demonstrated that the moment-rotation hysteresis could dissipate the seismic energy thanks to the highly nonlinear behavior once the moment capacity of the foundation is mobilized. Such a framework was observed in the 1960 Valdivia earthquake (Chile), reporting the survival of several tall slender rocking blocks, such as, the water tank structures, whilst some modern structures were severely damaged. Since then, many researchers have conducted experiments and numerical simulations so as to study the foundation rocking mechanism under various foundation types and soil conditions (e.g., Yim et al., 1980; Paolucci et al., 2008; Hakhamaneshi et al., 2012; Xu and Fatahi, 2018).

Seeking an inexpensive way in order to reduce the cost of the civil engineering projects is of interest to the design and practicing engineers, stakeholders, and practitioners. One of the recent approaches in that field is called “rocking isolation”, which is based on the foundation plastic hinging, mainly in the forms of the uplifting (according to Ganev et al. (1997)) and soil yielding (referring to Gazetas et al. (2013)). In the said emerging seismic design concept, allowing the uplift/soil yielding could lead to reducing the structural demand, as mentioned by Kourkoulis et al. (2012). Beyond of that, the role of the soil-structure interaction whilst employing the rocking isolation concept had better be thoroughly comprehended. In reply, the nonlinear soil-structure interaction analysis for the seismic retrofit of an eight-story shear wall-frame building on the spread footings, carried out by Comartin et al. (1996), evinced that 75% of the inelastic demand on the shear walls was absorbed by the soil deformation, technically acting as an energy dissipater. Additionally, the concept of the foundation rocking isolation was under experimentally scrutiny by Hutchinson et al. (2006) and Chang et al. (2006)

throughout a centrifuge model, taking account of the nonlinear foundation response. Furthermore, the more a foundation is permitted to rock, the lesser the damage, imposed on the superstructure (Pelekis et al., 2017). It could also be voiced that the permanent rotations can conspicuously affect the soil-foundation-building interaction responses referring to Zeng and Steedma (1998) and Maugeri et al. (2000). On that basis, the soil plasticity must be scrutinized as the rocking isolation method comes at the expense of the significant rocking-induced structural lateral deflection plus the large residual differential settlement, possibly breaching the performance-based seismic design yardsticks, presented in Subsection 2.3.2. The last but not the least, the generation of the excess pore water pressure amidst a seismic excitation is another challenging element in the geotechnical and structural earthquake engineering fields, which could shift the merits of harnessing the foundation rocking isolation approach to a nightmare of the rocking-isolated structures courtesy of impairing their seismic performance. Yu and Zeng (2013) reported that the softened soil owing to the excess pore water pressure build-up intends to trigger the larger structural settlement and tilt courtesy of the reduction of the foundation bearing capacity and consequent stability failure in addition to the effects of the soil-structure interaction. To make all the preceding forewarnings crystal clear, three tilted buildings from the 1999 İzmit earthquake (Turkey) are exhibited in Figure 2.27, demonstrating the real examples of the unintended plastic hinging in the soil deposits, beneath the foundations, acting as a shield for their superstructures. Notwithstanding, such excessive rotations are the culprits of jeopardizing the seismic performance of the superstructures, possibly triggering the collapse, so that they are completely unsafe for the human occupancy in spite of the fact that the superstructures remained totally unscathed in the wake of the foundation failure (see Figure 2.27).

Figure 2.27 Unintended plastic hinging in soil foundations and intact tilted buildings in 1999 İzmit earthquake (Turkey) (Yılmaz et al., 2004; Bird and Bommer, 2004; Anastasopoulos et al., 2010)

2.4.1 Foundation Rocking Isolation Technique: Residing on Razor's Edge!

Everything started from the fail-safe system concept, proposed by Frangopol and Curley (1987). This concept educates the design and practicing engineers that the collapse will not take place due to the failure of some elements or even subsystems since some alternative load paths will take the responsibility on behalf of their weakened comrades. Assuming that there is a pier of a bridge, going to be designed against the earthquake action. It could be done twofold. In the first case scenario, the plastic hinging only occurs in the superstructure, meaning the totally elastic behavior of the soil foundation in line with the conventional code-based design. Note that the notable foundation uplifting and sliding, plus the soil-bearing capacity mobilization are forbidden or strictly limited by the current codes and regulations, e.g., Eurocode 8 – Part 5 (2004) and AS2870 (2011). For the second case scenario, the soil is permitted to enjoy the plastic deformation, implying the intact superstructure under the seismic excitation. The question is which of the aforesaid scenarios could guarantee the safety of the superstructure whilst being cost-effective? To answer that, Anastasopoulos et al. (2010) conducted the nonlinear finite element seismic time history analyses, investigating the seismic performance of the cases, portrayed in Figure 2.28. In that study, the conventional system

undertook only the structural distortion, supported by the square footing, free to rotate on a homogenous stiff clay deposit. For the foundation rocking case, the foundation dimensions were reduced to one-half of the values, required by Eurocode 8 – Part 5 (2004). It was shown that the new design concept appeared to provide much larger safety margins as it did not come close to the displacement ductility capacity. Contrariwise, for the strong earthquake shaking, the failure of the conventional system was unavoidable. On the same topic, the in-ground seismic isolation, i.e., the so-called rocking isolation method, has been proven to be quite effective in reducing the inertia forces, transmitted onto the superstructures as to Palmeri and Makris (2008). It is noteworthy to mention that the foundation rocking isolation, wherein the intentionally under-designed foundation acts as a safety valve, could give rise to descending the cost of the construction and consumption of the material resources, provided that the structure and its foundation were designed such that the inelastic behavior definitely occurs in the superstructure under the conventional capacity design procedure.

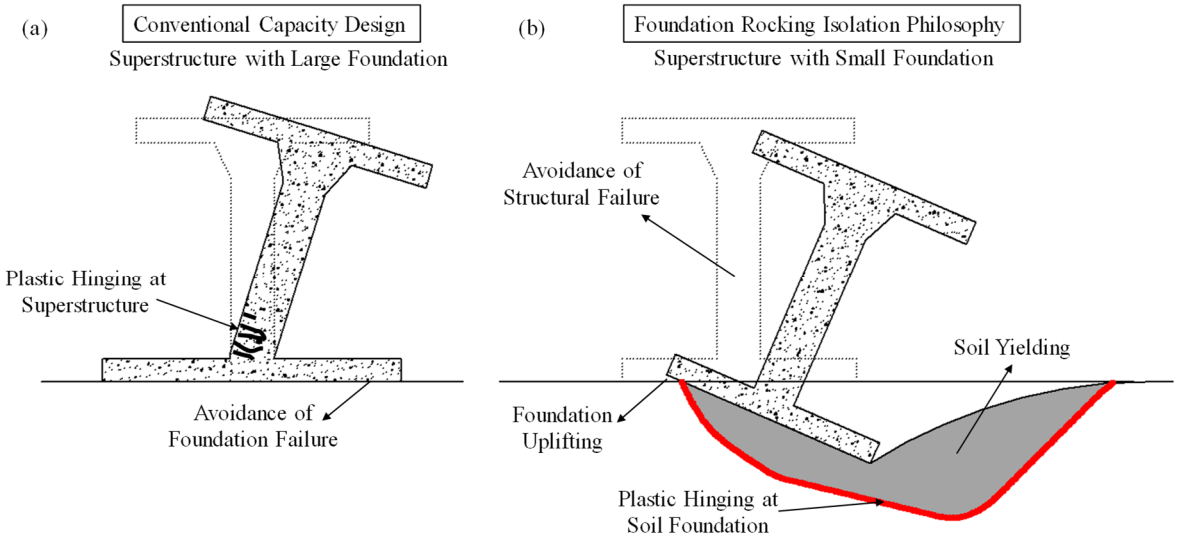

Figure 2.28 (a) Conventional code-based design with plastic hinging in superstructure, and (b) foundation rocking isolation with plastic hinging in soil medium (modified after Gazetas, 2015)

In reference to the use of the rocking isolation for the buildings, it was documented by Chang et al. (2007) that 90% of the total system dissipated energy resulted from the rocking footings of the two reduced-scale 2D frame-wall reinforced concrete building models. The said

percentage did not go below 65% despite increasing the drift demand (≥ 2%). The soil was dry dense sand, on which the one-bay and two-bay building models rested, supported on the surface shallow footings. Note that the beam nonlinearity was accounted by the replaceable ductile fuses at the ends of the beams. The mobilization of the capacity associated with the shallow foundation as a design concept was supported by such results. Moreover, the merits of the intentionally under-designed foundation, guiding the plastic hinging into the soil deposit, were shown by the reduced-scaled shaking table tests, performed by Drosos et al. (2012). A 13-m bridge pier, represented by a single degree-of-freedom structure, was constructed on a surface foundation, resting on a sandy soil. Evidently, the under-designed foundations drastically alleviated the maximum acceleration, pinpointing the deck of the bridge pier for all the adopted earthquake records in their study. Here is an interesting point that the foundation rocking isolation mechanism becomes more pronounced under the biaxial excitation compared to the uniaxial excitation whilst the said isolation effect is negligible under a vertical motion excitation, as highlighted by Mergos and Kawashima (2005).

It could be proclaimed that the foundation rocking system is the most economical solution in light of the reduced foundation size as well as not requiring any supplementary components for the energy dissipation while the overstrength concept is undesirable according to Liu (2014). The undue foundation rocking is the flip side of the foundation rotation isolation framework, though. A series of large-scale 1-g shaking table tests was conducted on the shallow foundation behavior during the earthquakes, shown in Figure 2.29, at the Public Works Research Institute in Japan. Paolucci et al. (2008) presented that the foundation tipped over eventually courtesy of the excessive foundation rocking, considering the uplifting, becoming as predominant as the soil-yielding-induced plastic component of the displacement (Shirato et al., 2008). Anastasopoulos et al. (2013) also stated that producing the hazardous residual settlements and rotations when harnessing the rocking isolation method is the only price to pay,

which ought to be properly assessed in the design stage. On the same line, Saad et al. (2012) reported that the large-scale shaking table tests of a horizontally curved bridge, taking into account the foundation rocking isolation, in conjunction with the numerical models in SAP2000 revealed that the force demands, transmitted to the substructure, were alleviated whereas the amplification of the drift demands attributed to the bridge deck transpired.

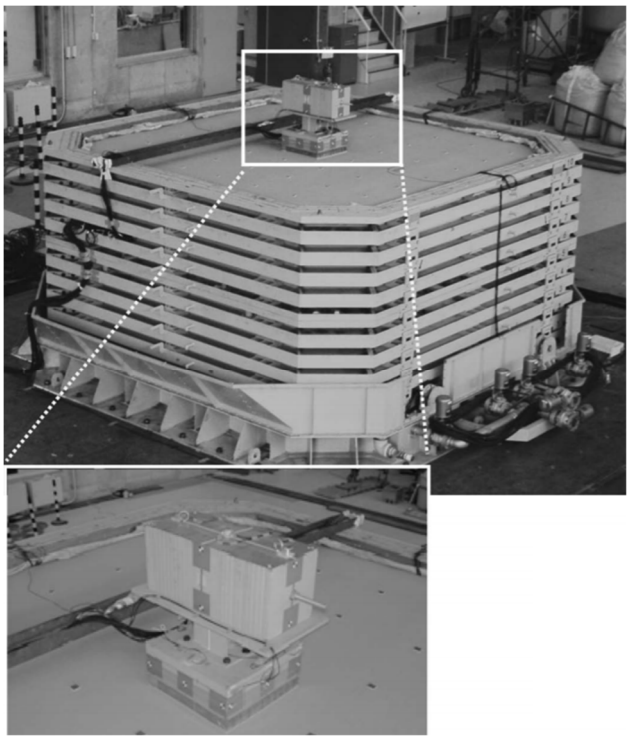

Figure 2.29 Experimental set-up and foundation rocking model (Shirato et al., 2008)

The large-scale cyclic testing on a rocking shallow foundation, resting on the loose and dense sands, was run considering the soil-structure interaction. Negro et al. (2000) pinpointed the top of the foundation during the seismic loading as the place at which the cyclic horizontal force was applied so as to replicate the inertial force, transmitted from the superstructure. The significant residual deformations, i.e., the settlement and rotation, were captured at the end of the test, affecting significantly the serviceability of the superstructure. It is then reasoned to conclude that the rocking-isolated structures must be carefully designed whilst comprehensively considering the soil-structure interaction concept. Admittedly, Coleman et al.

(2016) emphasized that the soil-structure interaction analysis in the nonlinear form is required for scrutinizing the seismic isolation systems.

2.4.2 Performance Assessment of Foundation Rocking Isolation Technique

As aforementioned, the permanent foundation rotation and corresponding accumulated settlement delimit the application of the rocking isolation technique in practice, as reported by Anastasopoulos (2010). Nonetheless, the advantages of the said method outweigh its demerits so long as the soil deformation during and at the end of an earthquake excitation is predicted precisely. To do so, the interaction between the soil and superstructure ought to be analyzed under the seismic loads. For information, the combined phenomena, modifying the response of a structure due to the foundation flexibility as well as the supporting foundation response because of the structure vibration, define the dynamic soil-structure interaction. Referring back to Section 2.3, DSSI encompasses the kinematic interaction and inertial interaction.

It is noteworthy to mention that the building and its foundation types could change the effects of SSI during the earthquake excitations. Van Nguyen et al. (2016) studied the extent to which the dimentions of a shallow foundation might alter the seismic response of the buidlings. In that regard, a regular building frame, categorized as a mid-rise structure with the moment-resisiting system, was adopted. The evaluation and quantification of such influences were investigated using ABAQUS. According to the obtained results from the fully coupled nonlinear time history analysis, the larger shallow foundations moderated the amplifications of the structural lateral deflection and inter-story drift ratios, resulted from SSI, potentially acting as a cost-effective alternative in order to control the seismic performance level of the shallow-founded buildings. As compared to the larger foundation, the building on the smaller shallow foundation attracted the less inertial forces. Their numerical research project revealed that the fundamental period of the entire soil-structure system was altered markedly by the size of a

shallow foundation whereas its influence on the higher natural modes was insignificant. Insofar as the deep foundations are concerned, the design engineers have leaned towards the pile foundations more than the shallow foundations referring to Yegian et al. (2001). Thus, the research studies in the field of the seismic soil-structure interaction have also been directed towards the deep foundations so as to provide the design engineers with a clear insight into the dynamic responses and behaviors of the pile foundations. The key factors in the seismic analyses of the soil-deep foundation-building systems were listed by Kavitha et al. (2016), presenting the two governing groups, viz, the soil and piles. The latter group includes the geometry and arrangement of the piles. The properties of the soil profile and ground surface gradient belong to the former.

The seismic performance of the rocking soil-structure system with due attention to the soil plasticity and foundation uplifting, which are the bases of the rocking isolation technique as a new seismic protection approach, was probed by Masaeli et al. (2015). The three different boundary conditions, i.e., the fixed-base, linear SSI, and nonlinear SSI, were assigned to the soil-structure system. The foundation type was the shallow raft whilst the superstructures were in the range of the mid-rise to high rise buildings to make the study's outcomes more comprehensive. The results disclosed that the more slender superstructures considerably benefited from the soil yielding and uplifting in comparison to the short and massive structures, signifying that the SSI-induced nonlinearities could substantially diminish the structural demands. Masaeli et al. (2015) put forth that the residual foundation tilting should be practically limited to 0.015 rad. El Naggar (2012) classified the nonlinearity into the two classes, namely, the material and geometric nonlinearities. The soil yielding and yielding of the structure could trigger the material nonlinearity. On the other hand, the geometric nonlinearity is more about the separation of the foundation from the soil surface (i.e., gapping) as well as the buildings pounding. Gajan et al. (2008)'s study also admitted that the geometric

and material nonlinearities in the soil could enhance the seismic performance of a building. In this context, Beresnev et al. (1998) pointed out that the nonlinearity could reduce the wave velocity and resonance frequency. Figure 2.30 details that the Mexico City clay, taken into consideration in Subsection 2.3.1, behaved almost linearly with the insignificant modulus reduction and small damping, postulating that the resonance period would have been increased, inducing the smaller dynamic forces on the 6-15-story buildings if that case had happened in Mexico City in 1985.

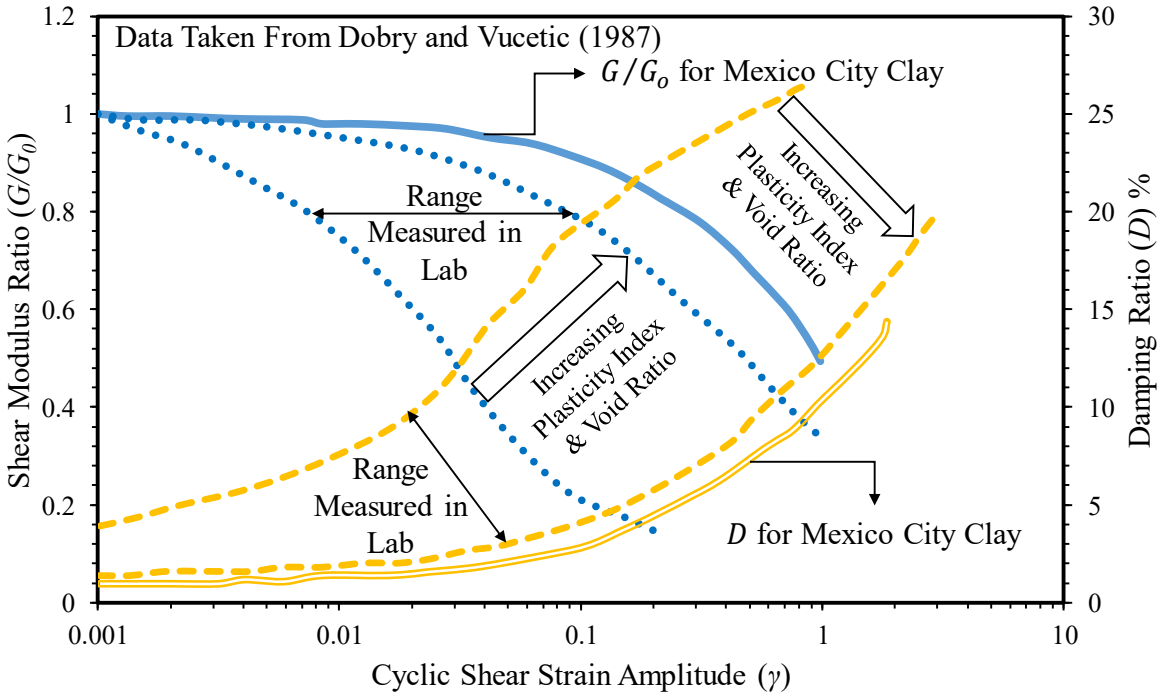

Figure 2.30 Modulus reduction and damping ratio trends of Mexico City clay along with corresponding ranges, measured in laboratory

The progressive permanent settlements were observed in the experiments, carried out at University of Auckland by Bartlett (1976) and Wiessing and Taylor (1979), on the shallow foundation rocking for the clay and dry sand deposits. Thereupon, the soil deformation, and not to mention the permanent foundation rotation, are conspicuously affected by the soil plasticity. After conducting a critical review of the existing literature (Kausel, 2010; Lou et al., 2011), it is crystal clear that the common uncertainties in the DSSI area are linked mainly with the lack of the implementation associated with the recently developed, plasticity-based soil

constitutive equations into the commercial numerical codes. In this connection, the research work, conducted by Rayhani and El Naggar (2012) in FLAC3D, illustrated that the foundation input motion could be modified by the stiffness and stratification of the soil profiles. They chose the Mohr-Coulomb failure criterion with the hysteretic damping as the soil model. Tabatabaiefar and Fatahi (2014) and Hokmabadi et al. (2014) scrutinized the effects of the soil-structure interaction on the seismic response of the mid-rise building frames with the shallow and deep foundations, employing the elastic-perfectly plastic Mohr-Coulomb yardstick plus the hysteretic damping. The modified equivalent linear method for the DSSI analysis, proposed by Ghandil and Behnamfar (2015), could put a further reduction of the soil shear modulus into active in the near-field of a foundation as a result of the large strains. Yeganeh et al. (2015) addressed the seismic interaction between a high rise building and the adjacent deep excavation on the basis of the finite difference method using FLAC2D. Taking a step further, the modified constitutive model with the Mohr-Coulomb failure criterion was utilized for the soil medium, allowing the implementation of the dependency of the stiffness on the stress as well as the unloading behavior. Thereafter, the equivalent linear soil model with the adopted Rayleigh damping was used in the seismic soil-pile-structure interaction phenomena with the use of ABAQUS (Fatahi et al., 2018). Raj et al. (2018) examined the response of the soil slopes under the single and multiple adjacent irregular (step-back) configuration reinforced concrete frame buildings with the varying height (i.e., 2- and 4-story) in the finite element limit analysis. The elasto-plastic constitutive model was based on the Mohr-Coulomb failure criterion. Forasmuch as the period of the SSI system is affected extremely by the soil nonlinearity in preference to the nonlinearity of the structure, as underscored by Trifunac et al. (2001), bypassing the advanced concepts in the employed soil constitutive models, accounting for the nonlinearity and pre-failure yielding of a soil deposit, for performing the DSSI numerical simulations whilst considering the rocking rotation isolation, is dictated to be stopped. As well, it was underlined

by Sáez et al. (2013) that the soil would reach its limit of elasticity even under the weak to moderate shaking, implying the paramountcy of the soil plasticity from the onset of the virgin loading. Given the circumstance, the risk of the excessive transient and residual foundation rotations makes running the nonlinear soil-structure interaction simulations with the advanced plasticity-based soil constitutive models undoubtedly essential when employing the foundation rocking isolation concept.

Another concern in the numerical simulation of SSI for the foundation rocking isolation design is the level of accuracy in modeling the superstructures since the primary challenge in the seismic SSI problems is holding the knowledge of both the structural and geotechnical engineering disciplines, underlined by Trombetta et al. (2013). First and foremost, the surface buildings on the soil deposit do not generally behave in a plane strain manner referring to Mirhabibi and Soroush (2013), implying the supremacy of the three-dimensional numerical analysis over the two-dimensional counterpart. Besides, the nonlinear interaction between the superstructure and substructure must be taken into account in SSI, as underlined by Meymand (1998). It, furthermore, should be noticed that the structure-foundation system's seismic performance could be excelled as long as the stable balance between the rocking of the foundation and inelastic behavior of the structure is achieved. As mentioned earlier, the foundation rocking could lead to the beneficial contributions only if it is under the strict control. Note that the inelastic structural behavior acts as a structural fuse in the seismic soil-structure interaction analyses. In this respect, Liu (2014) announced that the balanced design system is able to offer the acceptable residual deformations as well as the well-distributed dissipated energy amongst the rocking foundations and structural fuses in contradiction to the structural hinging dominated and foundation rocking dominated cases. Some examples are provided hereinafter to elucidate the simple assumptions, made in the numerical modeling of the structures, whilst utilizing a group of so-called advanced soil constitutive models. The

nonlinear, plane-strain finite element analysis was employed by Gelagoti et al. (2012) with a view to studying the seismic performance of the rocking-isolated structure that was an idealized 5 m wide and 7 m high 2-story reinforced concrete frame. In that project, the nonlinear soil behavior was modeled through a simple kinematic hardening model with the Von Mises failure criterion. A linear elastic SDOF structure in OpenSees accompanying the nonlinear elasto-plastic constitutive model, called "multi-yield-surface J2 plasticity (Von Mises)", for the saturated soft clay, formed a study in 2014, carried out by Torabi and Rayhani (2014). A year later, the dynamic performance of a geosynthetics-reinforced pile foundation system was simulated in PLAXIS3D followed by the verification of the numerical results against the reduced-scale model test (Taha et al., 2015). In the said project, the superstructure was not modeled either as a frame or a surcharge. Indeed, the Hardening Soil model with small-strain stiffness (HSsmall) was assigned to the top soil layers in the three-dimensional numerical model. Amorosi et al. (2017) executed a three-dimensional finite element approach to analyze the dynamic soil-structure interaction phenomena, observed at the Lotung Large-Scale Seismic Test (LSST). The soil response was simulated by the HSsmall model in PLAXIS3D. The downsides of their project were modeling the nuclear power plant containment structure by the linear visco-elastic plates together with neglecting the application of the interface elements. Karimi et al. (2018) performed the three-dimensional numerical analysis of the liquefaction-induced building settlement in OpenSees with the multi-yield-surface soil constitutive model whilst assigning the elastic material behavior to the foundation and a one-story structure.

It is a well-established fact in the soil mechanics that the deformation of a soil is a function of the effective stresses in preference to the total stresses, as pointed out by Das (2015). Finn et al. (1986) highlighted the major factors, which must be considered when conducting the seismic analyses of the soil-structure systems. The said factors are as follows: (i) in-situ shear modulus; (ii) shear modulus variation in a nonlinear manner with the cyclic shear strain; (iii)

effects of the strain softening/hardening; (iv) excess pore water pressure generation; (v) excess pore pressure-induced changes in the effective stress; (vi) viscous and hysteretic damping; and (vii) volume changes in the soil skeleton. Amongst the aforesaid factors, evaluating the generation and redistribution of the excess pore water pressures seem to be challenging in both the theoretical and applied soil mechanics, let alone in the geotechnical earthquake engineering applications. On the same topic, Ma et al. (2009) proclaimed that the foundation rocking-induced excess pore water pressure has the potential for changing the rigid strip footing responses under the dynamic loading. Furthermore, the earthquake-induced excess pore water pressure build-up in the saturated soils could cause the diminishment of in the strength and stiffness till the liquefaction happens. As a consequence, the resulting outcomes of the numerical simulations of DSSI with the foundation rocking dominated behavior might become misleading if the build-up of the excess pore water pressure is ignorantly dismissed once the water table is present at the site.

Ishihara (1996) uttered that the factors of safety for the foundations under the static conditions are generally so large that the essential requirements for their dynamic performance are met accordingly. The last statement could not be applied for a liquefiable soil, though. The liquefaction, triggering the foundation failure, stems from the generation of the excess pore water pressure and corresponding diminishment that the strength of the soil experiences. Thereupon, the destructive effects of the excess pore water pressure in the realm of the soil liquefaction have been deservedly scrutinized (e.g., Tropeano et al., 2019; Franke et al., 2019). By way of illustration, the extension of the Biot's theory was introduced to the seismic interaction between the liquefying soil and a superstructure, according to Popescu et al. (2006), as a saturated porous medium. The research study of Miwa et al. (2006) demonstrated that a large bending moment beyond the ultimate plastic moment of the steel pipe pile foundation, induced mainly by the large ground displacement, caused by the liquefaction, was the major

reason behind the severe damage to the deep foundations in the event of the 1995 Kobe earthquake (Japan). Lopez-Caballero and Farahmand-Razavi (2008) carried out the 2D coupled finite element simulation with GEFDYN using an elasto-plastic multi-mechanism model to mimic the soil behavior so as to assess the influence of the liquefaction-induced soil nonlinearity on the SSI phenomena. In 2011, the method for the assessment of the lateral response of the isolated piles/drilled shafts in the fully liquefied soils, presented in Ashour and Ardalan (2011), was proposed, capable of evaluating the near-field excess pore water pressure and associated post-liquefaction soil strength. Thereafter, Chakrabortty and Popescu (2012) provided an explanation for a paramount behavior on the topic of the soil liquefaction, observed in the numerical simulations of the centrifuge tests. It was announced that the seismically-induced excess pore water pressure in a heterogeneous medium outweighed that of in the equivalent uniform soil deposit.

The assumption of neglecting the accumulation and dissipation of the excess pore water pressure has been made in the assorted seismically-based SSI research studies (e.g., Michalowski, 1998; Halabian and El Naggar, 2002; Bagheri et al., 2018; Xu and Fatahi, 2019). The stamp of approval of overlooking the excess pore water pressure build-up for the non-liquefiable soils in the seismic soil-structure interaction is a handful of studies among which Sáez et al. (2013) probed the influence of the inelastic dynamic SSI on the seismic response of the two reinforced concrete moment-resisting multi-story frames, resting on the dry and fully saturated sandy soils. They implemented a modeling approach to ensure the compatibility between a 2D model of a building and a plane-strain approach for the soil. It was concluded that the inelastic dynamic soil-structure interaction would seem to be very important if the structural behavior becomes markedly inelastic as well as coinciding the mean period of the seismic motion and characteristic soil site period takes place. Gazetas et al. (2016) presented a case study of the seismic response of a deep anchored steel sheet-pile wall, supporting 18 m of

the sandy soil, excluding any threat of the substantial excess pore water pressure. It was, indeed, underscored that if the retained soil is cohesionless and likely to be developing the excess pore water pressure, the soil improvement ought to be performed. The significant effects of the excess pore water pressure generation on a non-liquefiable soil deposit were highlighted by Hazirbaba and Rathje (2009), stating that the soil deformations and shear strength of the soil are to be notably affected by the build-up of the excess pore water pressure. It is now manifest that the equivalent linear methods work acceptably so long as the strong soil nonlinearity and/or high excess pore water pressures are not developed in the event of a seismic excitation. Such methods will become less satisfactory when the generations of the permanent deformations and excess pore water pressure occur.

In consultation with what have been presented in this section, the soil plasticity and excess pore water pressure, excluding the liquefaction occurrence, are the facets, on which the accuracy of the numerical analyses of the seismic soil-structure interaction associated with the foundation rocking isolation technique relies. In line with Section 2.3 and particularly Subsection 2.3.4, the performance-based design would be able to offer the cost-effective, safe design on the condition that the foundation rocking isolation technique is investigated within the entire soil-structure system. Thus, the current research in this thesis is an attempt to donate insight into extent to which the dynamic soil properties (e.g., the shear wave velocity and shear modulus) and soil plasticity plus the excess pore water pressure build-up could affect the performance of the shallow-founded buildings, meant to withstand the shuddering and shaking from the earthquakes.

2.5 Summary

This chapter briefly described and summarized the previous research studies related to the realm of dynamic soil-structure interaction, specifically targeting the seismic performance of

the buildings, resting on the shallow foundations. Owing to the reluctance, the majority of codes and standards, in the best case scenario, proposed a class of simplified methods for the consideration of SSI. For instance, the increased period and modified damping of the soil-structure system were presented in ASCE7-16 (2016), while ATC-40 (1996) accounted for the SSI framework by means of the elastic-plastic Winkler springs in conjunction with the spring stiffness, proposed by Gazetas (1991). However, the Performance-Based Seismic Design (PBSD) demands the design engineers to utilize the direct approach, signifying the importance of the consideration of the entire soil-structure system.

In order to achieve the precise results in the prediction of the seismic performance of the buildings under the PBSD philosophy, firstly, the behavior of the soil must be simulated properly. Developing the stress-strain relationships for the soil constitutive models has a long history. Nevertheless, the firm agreement amongst the engineers and researchers over establishing one versatile soil constitutive model has not yet been settled. This is the rationale behind why the soil models must be picked with the consideration of the type of the loading and nature of the governing aspects of the material response during that loading. For instance, the soil constitutive models for the seismic application should be able to capture the soil deformations, particularly the residual displacements, stemming from the wide range of the cyclic shear strains. If the performance of such a stress-strain-strength relationship in duplicating the behavior of a soil under the irregular or random cyclic loading is poor, the assessment of the seismic performance of the superstructures will not be able to provide the reliable results. Gundersen and Josefsen (2016) mentioned that the cyclic loading could be surged by the resonance phenomonen. The review of the dynamic soil properties and a class of soil models were drafted in Section 2.2.

The 2008 Wenchuan earthquake (China), and 2010 Baja California earthquake (Mexico) are the tangible samples, showing the overwhelming structural and nonstructural damage, and

economic and human losses, raising an increasing awareness to the design community regarding the necessity of developing the earthquake-resistant structural systems by means of the SSI analysis throughout PBSD. The performance-based approaches generally possess the different performance levels, including immediate occupancy, damage control, life safety, and collapse prevention. Whilst the level of damage is negligible for the immediate occupancy performance level, the complete property loss might occur in the collapse prevention performance level.

It is of note that the performance-based design is promoted by many professionals as a tool for the structural and geotechnical design, according to Jia (2018). Indeed, the cost of construction is the chief key in almost all the civil engineering projects. In that regard, amidst the preceding years, the base isolation devices have been implemented not only for the bridges but also for the buildings with the purpose of diminishing the superstructures damage. The analysis of the 60-story high vertically tapered pyramidal Transamerica building in San Francisco, subjected to the 1989 Loma Prieta earthquake (USA), revealed that the rocking motions could potentially pose the significant influences on the seismic performance of the superstructures, as reported by Celebi and Şafak (1991). Therefore, recently, the foundation rocking technique as a new isolation method was proposed, wherein the foundation size is reduced whilst the overstrength is undesirable, in the hope of limiting the inertia forces on the superstructure.

There have been some pros and cons regarding the rocking isolation technique since it highly relies on the residual deformations of the soil underneath the superstructure, significantly depending on the soil plasticity. Needless to say, the significant permanent lateral deflections of the buildings could put the safety of the surrounding buildings, infrastructure, and construction projects into jeopardy under the influences of the aftershocks. It is not unfair to accentuate that the application of the foundation rocking isolation technique in the realm of

DSSI with the consideration of PBSD ought to be done with caution. To address that, this thesis provides the information, excelling the trustability of the resulting outcomes from the foundation rocking approach when simulating the entire system of the soil and structure whilst putting the performance targets into practice.

CHAPTER 3

CONTEMPORARY PROBLEMS IN SEISMIC SOIL-FOUNDATION-STRUCTURE INTERACTION

3.1 General

Generally speaking, the structure is considered fixed-base in the calculation of the lateral forces, imposed on the structure by an earthquake, disregarding the flexibility of the soil foundation. Nevertheless, the past experiences and observations (e.g., Tabatabaiefar and Fatahi, 2014; Hokmabadi and Fatahi, 2016; Van Nguyen et al., 2017) have indicated the fact that the soil deformation changes the characteristics of the free field motion at the ground level in addition to altering the structure reactions against the earthquakes. As a general rule, SSI yields the certain results such as a diminishment in the base shear but an escalation in the structure period (or the reduction of the frequency), system damping, and contribution of the rocking mode to the total deflection response. Yet, it is daunting to clearly discuss as regards the $P-\Delta$ effect and lateral displacements of the structures in default of conducting the interaction analysis for each project (Yeganeh et al., 2015).

Be it geotechnical or structural design situations, the Dynamic Soil-Structure Interaction (DSSI) plays a fundamental role to the extent that the unexpected damage might befall, e.g., stemming from the resonance. In contrast, DSSI might act as a precursor to the soil-foundation relative displacement, markedly abating the energy that reaches the superstructure, reducing the expected damage accordingly.

There is, nowadays, a conspicuous demand for the high rise buildings in the high-density dwellings of the urban areas; in consequence, harnessing the rigorous numerical simulations plus conducting the experimental studies so as to design and construct such prodigious structures would be essential. In this chapter, the results, derived from the numerical investigations of the contemporary seismic soil-structure interaction problems using FLAC3D through the fully nonlinear analysis in time domain adopting the direct method of analysis, are presented and discussed. The first question, raised by the design and practicing engineers, is the possible application of the weighted average shear wave velocity, estimated from the in-situ shear wave velocity profile, in conducting the numerical simulations of SSI in addition to its common application in the seismic site classification field. Another thought-provoking topic in this study is the seasonality of the earthquakes. Forasmuch as the soil mass density, small-strain shear modulus, and shear wave velocity are affected by the change in the soil moisture content and corresponding degree of saturation, is the season, in which an earthquake befalls, potent to impact the extend of the damage in a superstructure? Moreover, the level of influence associated with employing the simply assumptive parameters, presented in the literature, for mimicking the dynamic behavior of the soil deposit in the soil-structure system is scrutinized below.

3.2 Effects of Shear Wave Velocity Profile of Soil on Seismic Performance of High Rise Buildings

It is now widely accepted that, throughout the agitation (i.e., the earthquakes), the local site conditions might strikingly affect the rock-like motions and the soil-structure interaction phenomena would, in turn, alter the free field ground motions. The most spectacular cases of the soil amplification and soil-structure interaction effects have observed in 1906 San Francisco (USA), 1985 Mexico City (Mexico), 1989 Loma Prieta (USA), 1994 Northridge (USA), 2010

Maule (Chile), and 2011 Tohoku earthquakes (Japan), reported by some researchers (e.g., Romo, 1995; Xia et al., 1999). The stiffness of the soils in the shallow depths underneath the superstructures could spark off the ground motion amplification. Note that the soil stiffness is characterized by the seismic shear wave velocity.

The current research zeroed in on the soil shear wave velocity and its influence on the superstructure performance during the earthquake shaking. Invoking the weighted average shear wave velocity with the aim of calculating the soil shear modulus, closely related to the strength and deformation characteristics of the soil medium, has been a hotly debated issue since the aforesaid parameter was only posited by a class of codes and regulations to obtain the soil site classification for the earthquake design. To that end, the numerical model, having the two profiles associated with the shear wave velocity, namely, the in-situ non-uniform profile (Case A) and equivalent uniform profile (Case B), was built in FLAC3D. The said software program is capable of analyzing the complex interaction issues via the direct method. Therefore, the entire system of the soil-foundation-structure was modeled and analyzed in one single step. In the current study, the material and geometric nonlinearities (i.e., the uplifting, gapping, and $P-\Delta$ effect) were taken into consideration in the time history analyses of the numerical models via FLAC3D. Besides, the Mohr-Coulomb soil constitutive model, accompanied by the hysteretic damping feature, covering the backbone curve and Masing rule (Masing, 1926), was assigned to the soil.

To put it in a nutshell, employing the weighted average shear wave velocity for the entire soil mass in analyzing the three-dimensional seismic soil-structure interaction problems would be accused for ending up with the unreliable results, e.g., the underestimated inter-story drift ratios, which might be the culprit of the damage to the superstructures and possibly the death of the residents, residing in the earthquake-prone zones.

3.2.1 Modeling Structural Frame and Building Foundation

A 20-story (60 m height), 3-span (12 m length) reinforced concrete moment-resisting building frame was considered, illustrated in Figure 3.1. SAP2000 was utilized for the structural design purpose in full compliance with AS/NZS1170.1 (2002), and AS3600 (2009), plus AS1170.4 (2007). It should be stated that in the final selection of the beam and column sections, the constructability and norms were taken into account. Moreover, the modulus of elasticity of the concrete and its Poisson's ratio were 3.01×10^{10} N/m^2 and 0.2, respectively. The mass density of the reinforced concrete was equal to 2400 kg/m^3. The thickness of the concrete slabs was 0.25 m. It is worth underscoring that all the structural sections of the superstructure were analyzed in FLAC3D on the basis of the inelastic method. In that regard, the elastic-perfectly plastic behavior was considered by specifying the limiting plastic moments for the structural elements, giving rise to the plastic hinge. Further, to better understand the dynamic behavior of the adopted superstructure under the lateral loading, the cracked-section flexural stiffness properties were assigned to the reinforced concrete components. Hence, the modification coefficients for the moment of inertia of the uncracked sections associated with the slabs, beams, and columns were 0.25, 0.35 and 0.7, recommended by ACI318 (2014), respectively. Besides, the building foundation had a thickness of 1 m and a width of 14 m, modeled by means of the finite difference zones. The bulk modulus, shear modulus, and mass density of the concrete foundation were 1.67×10^{10} N/m^2, 1.25×10^{10} N/m^2, and 2400 kg/m^3, in the order given.

It is manifest that the necessity of utilizing the damping in the dynamic problems is undeniable. Therefore, the local damping coefficient of 0.157, engendering 5% damping, was considered for the building and mat foundation. The local damping was meant to rationally capture the hysteretic behavior of the structural elements in the conducted seismic analyses in this study.

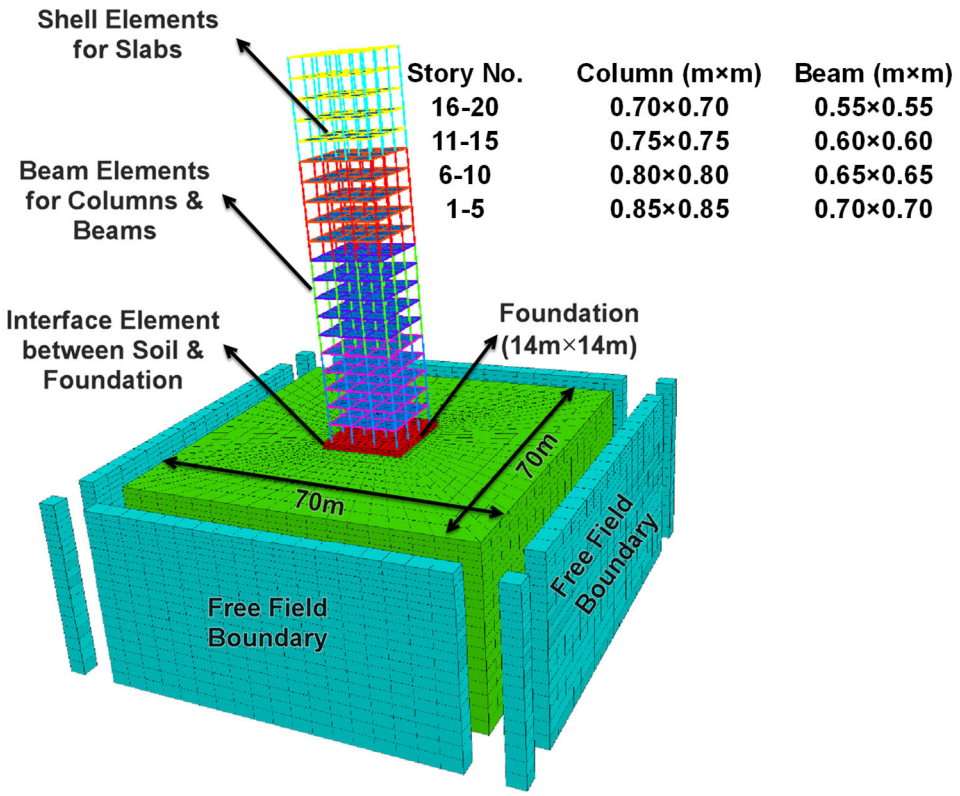

Figure 3.1 Illustration of soil-structure system in direct method

A plane between the mat foundation and underneath soil, on which the sliding and/or separation, i.e., the uplift, could take place amidst the seismic excitation, was adopted in this research work. The interface stiffness values, expressed in the stress-per-distance unit, were K_n, named the normal spring stiffness, and K_s, called the shear spring stiffness. K_n and K_s were set to ten times the equivalent stiffness of the stiffest neighboring zone on the basis of Equation (3.1), suggested by Itasca (2012).

$$K_n = K_s = 10 \times max\left[\frac{K + \left(\frac{4}{3}\right)G}{\Delta z_{min}}\right] \tag{3.1}$$

where, G and K are the shear and bulk moduli of a neighboring zone, respectively, and Δz_{min} is the smallest dimension of that zone, perpendicular to the interface.

3.2.2 Boundary Conditions and Input Earthquake Record

The free field boundaries, illustrated in Figure 3.1, were applied at the side boundaries of the soil mass. The propagation of the free field waves, i.e., in the absence of the superstructure, was generated in a one-dimensional manner. The distortion of the upwardly propagating shear waves was accordingly prohibited at the free field boundaries. In this way, the grids of the free field boundaries simulated the infinite boundary conditions. It is of note that the adopted free field boundaries encompassed the four planes of the free field grids on the side boundaries of the soil medium, matching the main grid zones, as well as the four columns of the free field grids at the corners.

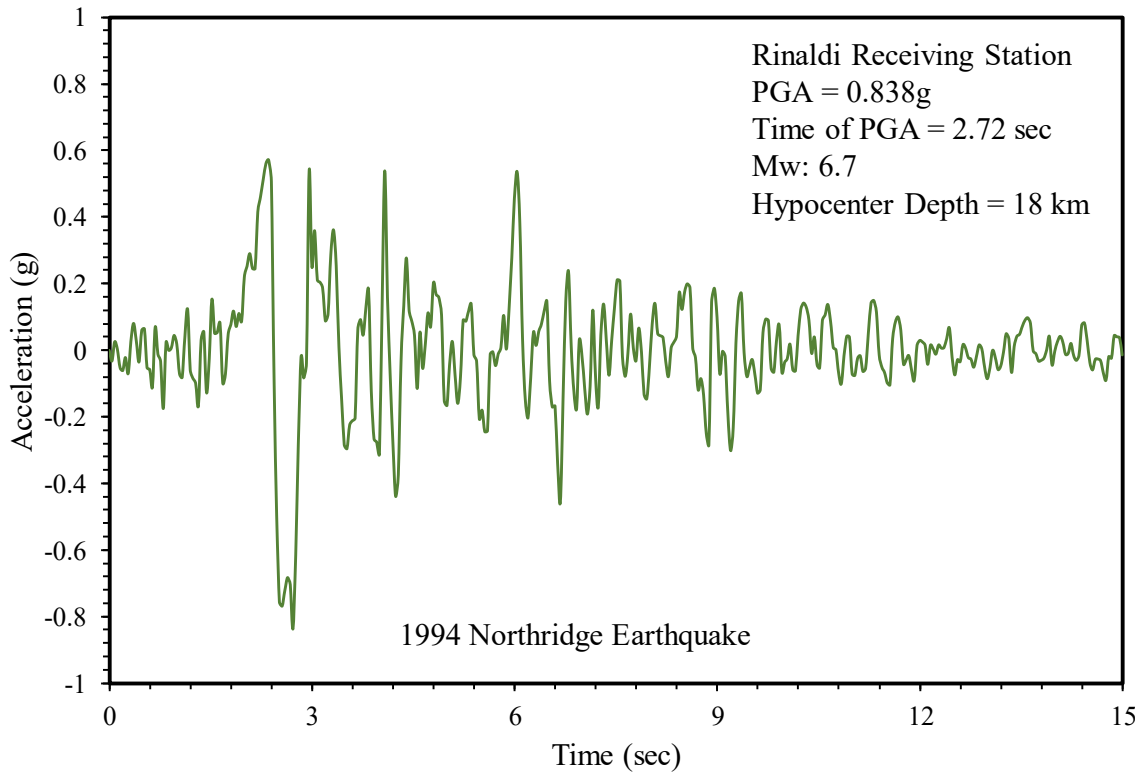

Figure 3.2 Utilized earthquake base motion

The seismic acceleration record attributed to the 1994 Northridge earthquake (USA), recorded at the Rinaldi station, was cherry-picked from the Strong-Motion Virtual Data Center (VDC). Figure 3.2 exhibits the aforesaid baseline-corrected earthquake acceleration record, which was applied at the base of the numerical model, i.e., the seismic bedrock. The majority

of the seismic codes and standards (e.g., ASCE7-10 (2010) and AS1170.4 (2007)) proposed a 30 m depth for the seismic bedrock in view of transpiring the chief part of the amplification and/or attenuation in the aforesaid depth. The large dynamic impedance, demystifying the presence of the low velocity sediment on the high velocity bedrock, was simulated via assigning the rigid boundary to the assumed seismic bedrock (i.e., 30 m below the ground surface).

3.2.3 Adopted Shear Wave Velocity Profiles

It is deemed necessary to lay emphasis on the needfulness of considering the interaction effects, particularly for the moment-resisting frames, as pointed out by Tabatabaiefar et al. (2013), once the shear wave velocity of the supporting soil is less than 600 m/s, which was the case in this study as to Figure 3.3. According to ASCE7-10 (2010), the weighted average of the in-situ shear wave velocity ($\bar{V}_{s,i}$) was formulated in Equation (3.2), which was not the arithmetic average of $V_{s,i}$ to a depth of 30 m. In order to cast light on the possibility of utilizing the weighted average of the shear wave velocity not only in the seismic site classification but also in carrying out the SSI analyses via defining the shear modulus of the soil medium, in-situ non-uniform profile (Case A) and equivalent uniform profile (Case B) were employed. The latter was obtained using Equation (3.2), wherein $\sum_{j=1}^{n}(d)_j$ was equal to 30 m. Figure 3.3 portrays the abovementioned cases, adopted in this research study. The small-strain shear modulus (G_0) is the core soil dynamic property, which is employed in the assorted seismic analyses (e.g., the hazard and site response analyses) along with the shear wave velocity of a soil. It is of note that the seismic soil-structure interaction is not the exception. The caption on Figure 3.4 states the variations of the small-strain shear moduli in the considered cases herein, i.e., Case A and Case B. G_0 was calculated based on $\rho {V_{s,i}}^2$, wherein ρ is the soil mass density (i.e., 1900 kg/m^3).

$$\bar{V}_{s,i} = \frac{\sum_{j=1}^{n}(d)_j}{\sum_{j=1}^{n}\left(\frac{d}{V_{s,i}}\right)_j} \tag{3.2}$$

where, d is the thickness of any layers from 0 to 30 m depth, and $V_{s,i}$ is the in-situ shear wave velocity of each layer between 0 and 30 m depth.

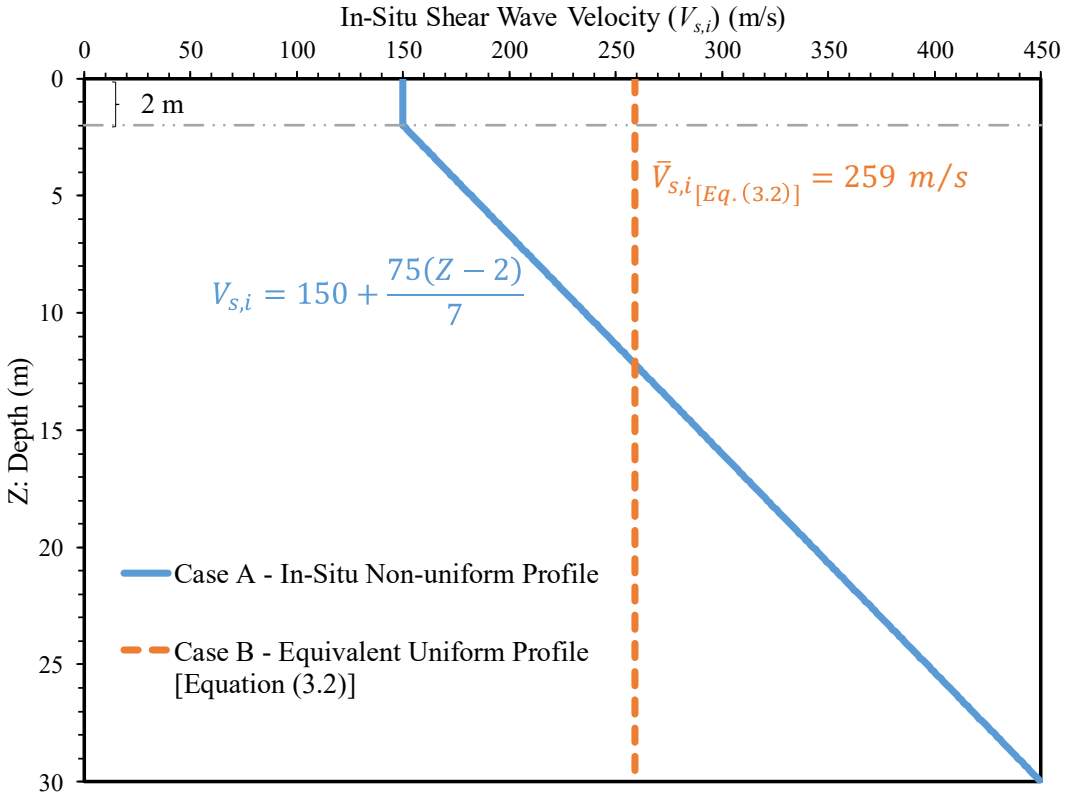

Figure 3.3 In-situ shear wave velocity profiles of Case A and Case B

The generalized relationship between stress and strain, linking the equations of equilibrium and compatibility, is termed “soil constitutive model”. The adopted nonlinear Mohr-Coulomb model was an elastic-perfectly plastic yardstick plus the hysteretic damping as a supplement, simulating the inelastic cyclic behavior. It is to be noted that, in the soils and rocks, the natural damping is believed to be mainly hysteretic, implying the independency of such a damping behavior on the frequency. The said soil constitutive model has been capitalized on in the previous research studies (e.g., Conniff and Kiousis, 2007; Rayhani and El Naggar, 2012;

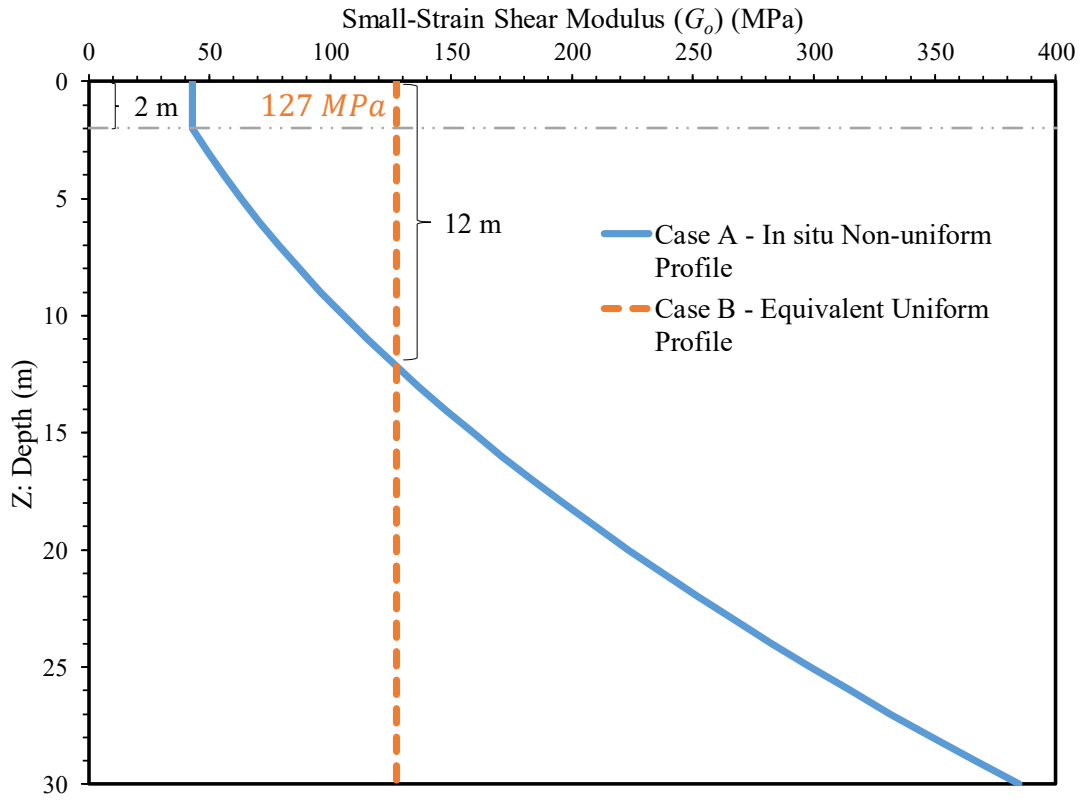

Figure 3.4 Small-strain shear modulus profiles of Case A and Case B

Walton et al., 2016) so as to mimic the soil behavior under the seismic loading in the soil-structure systems. In order to determine the hysteretic damping in the seismic analyses of the current research, the two-variable function, named "Default Model" was employed. The calibrated parameters for DM were L_1 = -3.325 and L_2 = 0.823, as suggested by Itasca (2012). The programmed hysteretic damping algorithm was able to replicate the soil stiffness degradation with the generated cyclic shear strains. Additionally, the soil parameters, involved in the said constitutive model, were as follows: (i) friction angle = 29°; (ii) cohesion = 20 kPa; (iii) dilation angle = 5°; and (iv) density = 1900 kg/m^3.

3.2.4 Results and Discussions

The structural results, embodying the base shears, distributed shear forces along the structure, maximum lateral displacements, and inter-story drift ratios, plus the response spectra, attributed to Cases A and B (referring back to Figures 3.3 and 3.4), are presented in this section.

The base shear as well as the shear force distribution along the superstructure height are per se at the forefront of designing any buildings. The shear force distributions along the building height when the summation of all the columns shear forces on a same level reached the utmost amidst the applied excitations were presented in Figure 3.5. Such generated shear forces resulted from the relative movements between the columns and slabs. As it is discerned in Figure 3.5, the distributions of the maximum story shear forces for Case A and Case B showed some level of difference. For example, the shear force on the 8th story experienced the 60%-increase from Case A to Case B.

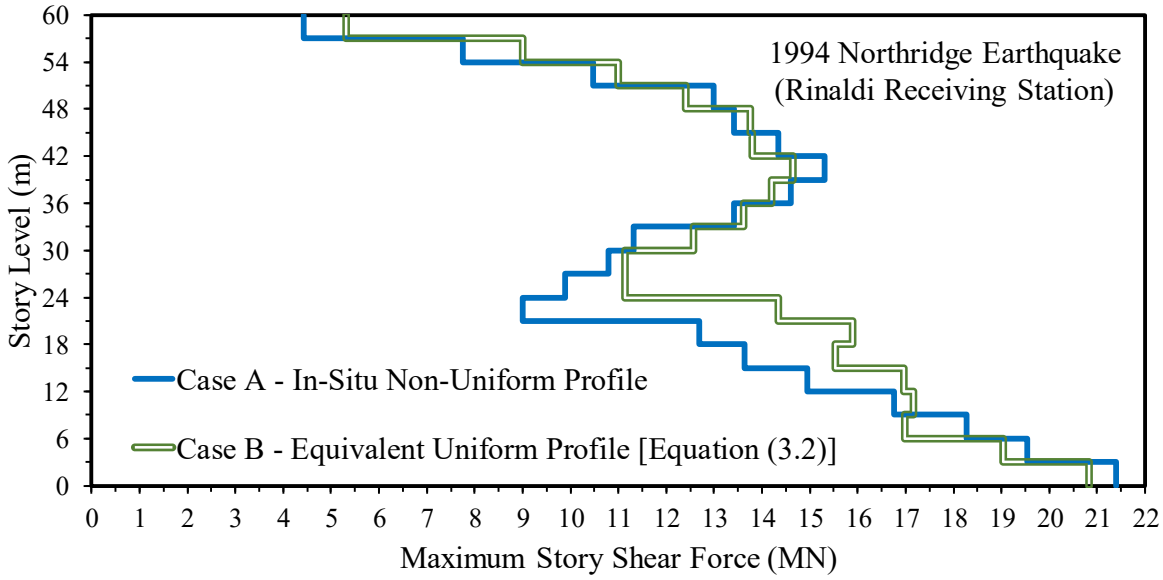

Figure 3.5 Distributions of developed story shear forces over height of 20-story structure under influence of Northridge (Rinaldi) earthquake

Investigating the response spectra of the considered cases in this study could help find out the reason for the difference in the obtained shear force distribution patterns for Cases A and B. Since $N/10$ sec is the approximate estimation of the fundamental period of an N-story fixed-base building, presented by Bungale (2016), the vibration period of the adopted soil-structure system was more than 2 s. In further detail, the characteristic site period was determined to be 0.46 s using $4H_s/\bar{V}_{s,i}$, as to Kramer (1996). The thickness of the soil deposit (H_s) was 30 m and $\bar{V}_{s,i}$ was equal to 259 m/s, referring back to Figure 3.3. The second

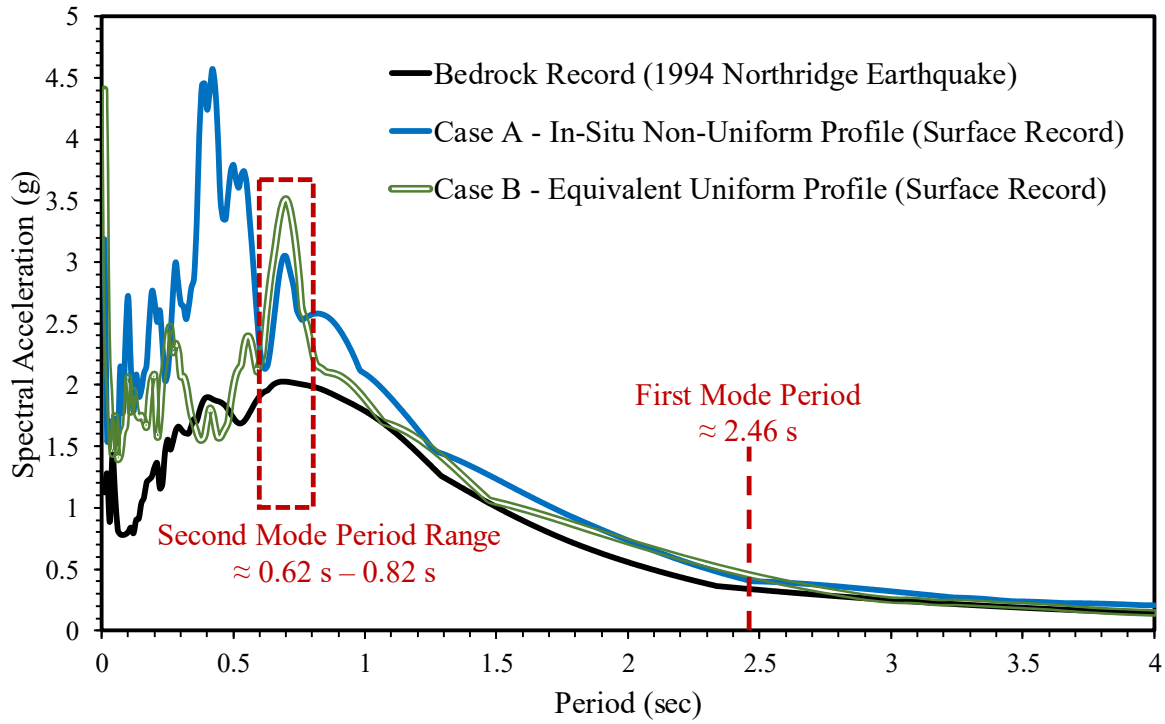

Figure 3.6 Acceleration response spectra, with 5% damping ratio for superstructure, associated with bedrock record and foundation level motions

mode period of the adopted SSI was within the range of 0.62 s to 0.82 s since NIST-GCR-11-917-15 (2011) reported that the period of the second mode is commonly bracketed by the one-quarter and one-third of the fundamental period (i.e., 2.46 s herein). The fluctuations in the distributions of the shear forces, displayed in Figure 3.5, revealed that the response of the adopted high rise building under such a strong ground shaking was heavily influenced by the complex dynamic behaviors, including the impacts of the higher modes of vibration. Whereas, only the effects of the first mode of vibration are still taken into account in the conventional structural engineering practice. Comparing the trends of Cases A and B in Figure 3.6 at the estimated fundamental period showed the more or less identical spectral accelerations, denoting the above-mentioned resemblance in the shear force distributions of the adopted cases. Indeed, the predicted maximum difference in the story shear forces of Cases A and B was 6 MN, stemming from the different values of the spectral accelerations for Cases A and B within the range of 0.62 s to 0.82 s in Figure 3.6.

There have been pros and cons regarding the most informative estimation methodology attributed to the calculation and presentation of the lateral displacements of the superstructures through the time history analyses. The lateral displacement of each story, when the maximum occurred at the top level of the designed 20-story moment-resisting building, i.e., the rooftop, was recorded in this study. Such a method, which was harnessed in this study, could be underpinned by the following reasoning. First, the lateral displacement at the rooftop level governs the minimum seismic separation gap between the neighboring structures, which was the topic of a research study, conducted by Fatahi et al. (2018). Furthermore, the implemented approach herein demonstrated a more tangible pattern of the structure's deformation by comparison with the pattern, casting light on the absolute maximum displacements of all the stories regardless of the time of occurrence. The results connected with the transient lateral displacements and transient inter-story drift ratios, graphically illustrated in Figures. 3.7 and 3.8, could be encapsulated as below.

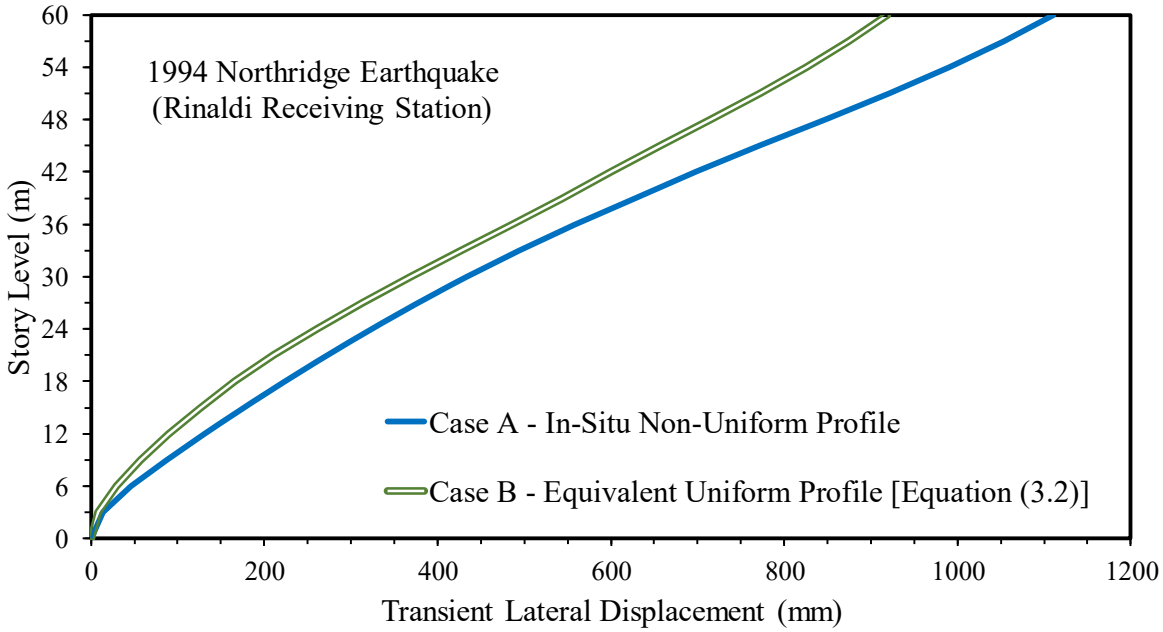

Figure 3.7 Transient lateral displacements of 20-story structure under influence of Northridge (Rinaldi) earthquake

The life safety criterion for the assessment of the seismic performance level, presented in FEMA273 (1997), ought to be met so as to avoid dealing with the severely damaged structural

and non-structural components amidst an earthquake. To satisfy the life safety performance level, the transient inter-story drift ratio must remain less than 2%, as per FEMA273 (1997). The predicted inter-story drift ratios for Case B as to Figure 3.8 misleadingly satisfied the said yardstick in all the building levels. Quite the contrary, those of Case A in the upper levels surpassed the 2% life safety drift limit such that the inter-story drift ratio of 2.5% was predicted. Figure 3.7 reveals that the transient lateral displacement at the rooftop in Case B was 918 mm whilst that of Case A was increased by 21% to 1111 mm. By all accounts, the lateral deflection of the adopted building and inter-story drift ratios in Case A outweighed those of Case B due to possessing the lower soil stiffness in the vicinity of the shallow foundation, referring back to Figure 3.4. On that basis, the small-strain shear modulus in the depth of 12 m beneath the mat foundation level imposed the considerable effect on the deformation-related results. For instance, G_0 within the 2 m depth in Case A was 43 MPa whereas Case B enjoyed the rather threefold increase in the soil stiffness on grounds of possessing 127 MPa as the assigned small-strain shear modulus to the aforesaid depth.

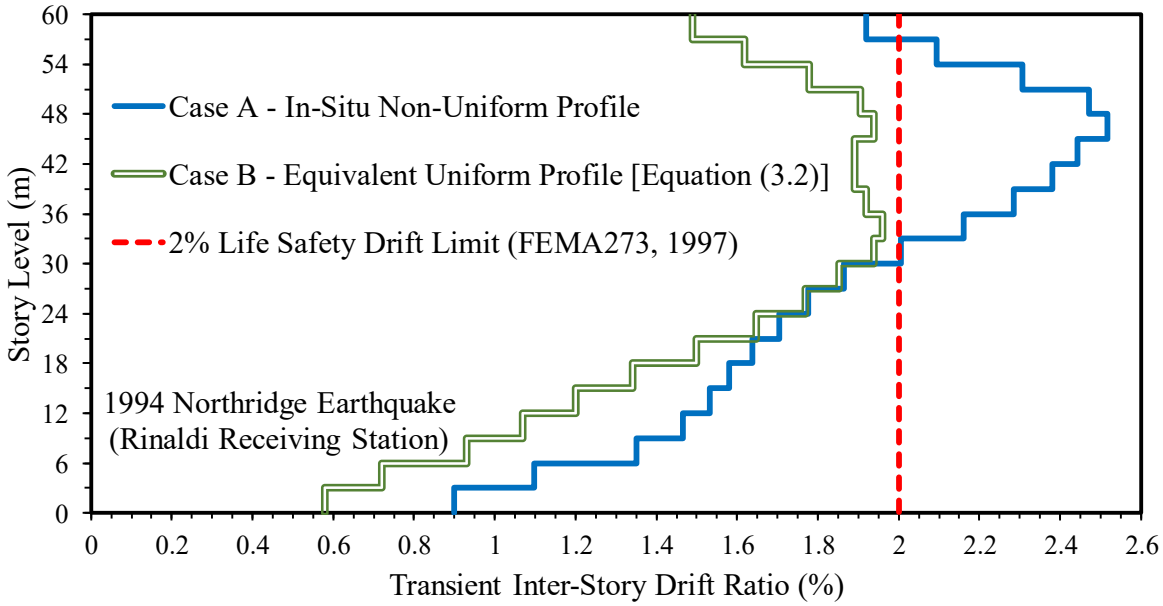

Figure 3.8 Transient inter-story drift ratios of 20-story structure under influence of Northridge (Rinaldi) earthquake

3.3 Effects of Degree of Saturation on Seismic Performance of High Rise Buildings Considering Soil-Structure Interaction

By and large, the soil is the weakest material, involved in the common geotechnical engineering projects. Georgiannou (1991) pointed out that the shear modulus at the mightily small strains (i.e., below 10^{-3}%) is the salient dynamic property of a soil, controlling the behavior of the geotechnical structures. The small-strain shear modulus (G_0) is calculated via Equation (3.3) (Bullen and Bolt, 1985). Experimentally studying the correlation between the water content and maximum soil shear modulus threw light on the key role of the degree of saturation in the estimation of G_0, as reported by Mendoza et al. (2005) and Ngoc et al. (2017). ρ, as the soil mass density, and V_s, which is the shear wave velocity of the soil mass, expectedly depend on the soil moisture content. Without regard for such a dependency, what is being done on a daily basis by the practicing engineers is directly making use of the measured shear wave velocity profiles, derived from the field tests, such as the cross-hole shooting, and shooting up/down hole.

$$G_0 = \rho {V_s}^2 \tag{3.3}$$

The three-dimensional finite difference numerical modeling was performed in FLAC3D in this study in order to scrutinize whether the ascent or descent in the degree of saturation could trigger the considerable change in the seismic performance of a high rise building. To fulfill the foregoing, the variation connected with the small-strain shear modulus, embraced by the changes in the degree of saturation, was taken into account in the effective vadose zone in the vicinity of the ground surface. Note that “vadose” is from the Latin for “shallow’. Four numerical cases were proposed herein, namely, the S_r = 5%, S_r = 17.5%, S_r = 60%, and S_r = 100% cases, introducing the term of the seasonality of the earthquakes. Finally, the results of the soil-structure system in the aforesaid cases, including the base shears, shear force

distributions along the building height, response spectra, rocking of the foundation, structural lateral deformations, and inter-story drift ratios, were explored. To give further details, the variations of the degree of saturation near the ground surface would emphatically effectuate the response of an entire soil-structure system. Thus, assigning the soil properties, e.g., the shear wave velocity, acquired from the field and/or laboratory tests, to the numerical models in compliance with the spasmodic changes, occurring in the course of the superstructures' useful life, should be taken into account in the seismic design of the high rise buildings.

3.3.1 Overview of Soil-Foundation-Structure System

Insofar as the soil-structure interaction is concerned, the direct method was adopted in this study, in which the whole system of the soil-foundation-superstructure was modeled followed by being analyzed in one single step. Additionally, the nonlinear behaviors connected with the structure and the underlying soil were taken into account herein. Stated succinctly, a three-dimensional, 20-story (60 m height), 3-span (12 m length) reinforced concrete moment-resisting building frame, designed in SAP2000, plus the 0.25-m thick concrete slabs along with a 14 m × 14 m × 1 m mat foundation, placed on a 30-m thick soil deposit, were considered in the current study. The details of the designed sections of the adopted 20-story superstructure were tabulated in Table 3.1. It should be noted that the Australian codes, viz, AS/NZS1170.1 (2002), AS1170.4 (2007), AS3600 (2009), and AS2870 (2011), were harnessed with a view to designing the superstructure and foundation. The adopted elastic-perfectly plastic model, acted as a precursor to making the concrete material behave linear-elastically, provided that the defined yield stress was not breached. In that behalf, a plastic hinge was formed when the plastic moment capacity, otherwise known as the resisting moment, was surpassed by the moments, being transmitted between the structural elements. The bulk and shear moduli, plus the mass density of the Grade 32 concrete material were 1.67×10^{10} N/m^2, 1.25×10^{10} N/m^2, and

2400 kg/m^3, respectively. It is noteworthy to state that the bearing capacity of the mat foundation satisfied the minimum required factor of safety (FOS) of 3, suggested by Das (2015), estimated based on the Meyerhof method (Meyerhof, 1963).

Table 3.1 Designed sections for structural beams and columns of concrete moment-resisting building

Story No.	Column (m×m)	Beam (m×m)
16-20	0.70×0.70	0.55×0.55
11-15	0.75×0.75	0.60×0.60
6-10	0.80×0.80	0.65×0.65
1-5	0.85×0.85	0.70×0.70

In this study, the $P-\Delta$ effect was taken into account by utilizing the large-strain mode in FLAC3D. Besides, the cracking of the structural components was covered throughout multiplying the moment of inertia of the structural sections in the uncracked mode (I_g) by the modification coefficients attributed to the slabs, beams, and columns, put forward by ACI318 (2014), i.e., 0.25, 0.35, and 0.7, consecutively. Apropos of the damping for the building and its mat foundation, the local damping coefficient (α_L) of 0.157, engendering the 5% damping (D), by the use of Equation (3.4), presented by Itasca (2012), capturing the hysteretic behavior.

$$\alpha_L = \pi D \tag{3.4}$$

Figure 3.9 depicts the schematic of the established numerical model in the current project. The free field boundary conditions, mitigating the wave reflections, were assigned to the four vertical lateral boundaries. In addition, the distance between the side boundaries, which was herein 70 m, as indicated at Part F in Figure 3.9, satisfied the minimum five times the width of the existing building (i.e., 5×12 m = 60 m), recommended by Rayhani and El Naggar (2008). Besides, the adopted interface (i.e., Part G in Figure 3.9) between the mat foundation and soil mass would have witnessed the sliding/separation during the conducted seismic analyses. The normal and shear spring stiffness values, expressed in the stress-per-distance unit, were determined to be ten times the equivalent stiffness of the stiffest neighboring zone, posited by Itasca (2012).

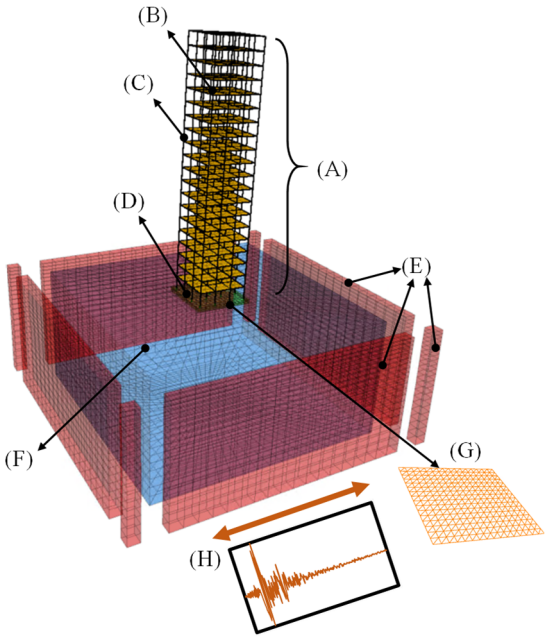

(A): 20-Story, 3-Span Reinforced Concrete Moment-Resisting Building Frame
(B): Shell Elements, Representing 0.25-m Floor Slabs
(C): Beam Elements, Representing Columns and Beams
(D): Mat Foundation (14 m × 14 m × 1 m)
(E): Free Field Boundaries
(F): Soil Medium (70 m × 70 m × 30 m)
(G): Soil-Foundation Interface Element
(H): 1994 Northridge Earthquake Excitation

Figure 3.9 Pivotal components of adopted soil-structure system in FLAC3D simulation

In this study, the adopted pre-yield hysteretic damping combined with the Mohr-Coulomb plastic criterion resulted in a nonlinear elastic-perfectly plastic constitutive model. It is of interest to notice that the tangent shear modulus was updated at each calculation step by implementing the programmed hysteretic damping algorithm in FLAC3D. The said algorithm was in charge of the simulating the variations of the soil shear modulus and corresponding damping against the seismically-induced shear strain. Equation (3.5) was programmed based on the two-variable function of the Default Model. γ is the cyclic shear strain in the equation below. L_1 and L_2, as the calibrated parameters, were -3.325 and 0.823, respectively, taken from Itasca (2012). The adopted soil medium consisted of Glacier Way Silt, as a cohesionless soil. Wu et al. (1984) reported the properties of Glacier Way Silt as follows: (i) friction angle = 29°; and (ii) dilation angle = 0°. The remainder of the required parameters are presented in the next section.

$$\frac{G}{G_0} = \left[\frac{L_2 - \log_{10}\gamma}{L_2 - L_1}\right]^2 \left(3 - \frac{2(L_2 - \log_{10}\gamma)}{L_2 - L_1}\right) \tag{3.5}$$

It is now standard practice for the seismic analyses to apply the selected acceleration record to the seismic bedrock while performing a time history analysis. The baseline-corrected near-field earthquake excitation, named "1994 Northridge earthquake (USA)", portrayed in Figure 3.10, was picked to apply at the base of all the considered numerical models in this study. Moreover, it is manifest to truncate the length of the cherry-picked excitation with the aim of surmounting the sizable effort in carrying out such nonlinear dynamic analyses.

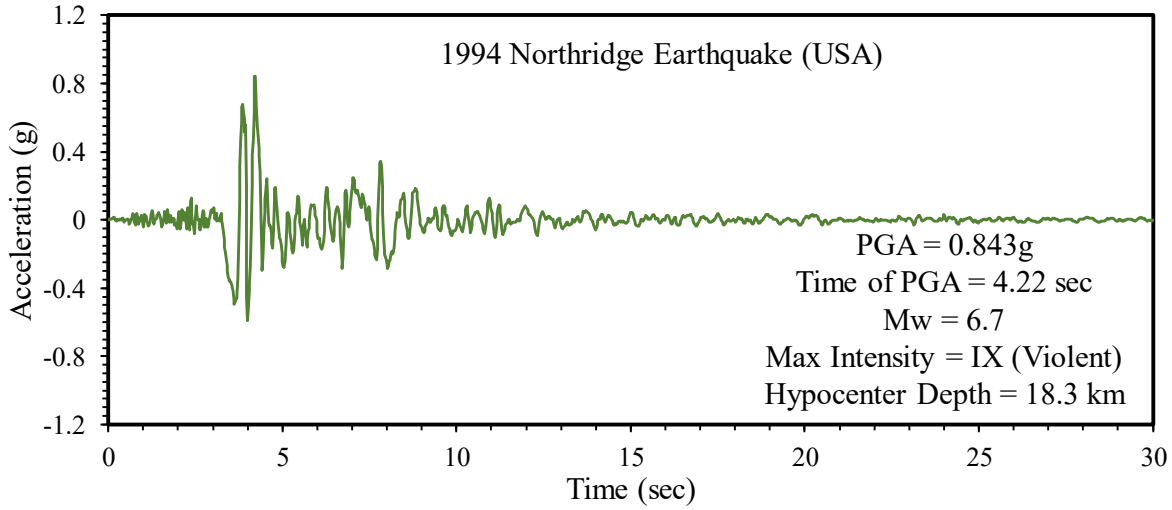

Figure 3.10 Input seismic base motion

3.3.2 Adopted Shear Wave Velocity Profiles

Qiu and Fox (2008) postulated the concept of the effective density (ρ_{eff}), controlling the velocity of a small-strain shear wave. It is to be asserted that ρ_{eff} emerges from the relative motion between the solid phase (representing the soil grains) and fluid phase (representing the pore water) amidst the passage of a shear wave in a saturated soil. In the cited paper, the determination of the momentousness attributed to the effective soil density for a given application could be done by taking account of the hydraulic conductivity, effective grain size, and wave frequency. It was shown that the clays and silts (i.e., the low permeable soils) have the same saturated density and effective density. In this study, the use of the effective density was neglected in the fully saturated mode courtesy of the type of the adopted soil, i.e., Glacier

Way Silt. Moreover, according to Santamarina et al. (2001), dismissing the effective density for the seismic waves, propagating through the saturated soil medium, is generally well-grounded. In this study, the soil mass density in Equation (3.3) was directly quantified via Equation (3.6) whilst considering the different values for the degree of saturation. G_s, S_r, e, and ρ_w in Equation (3.6) are the specific gravity of the soil solids (i.e., 2.66), degree of saturation, void ratio (i.e., 0.65), and water mass density (i.e., 1000 kg/m^3), respectively.

$$\rho = \frac{(G_s + S_r e)\rho_w}{1 + e} \tag{3.6}$$

The second parameter, introduced in Equation (3.3), is the shear wave velocity, being a requisite for rendering the seismic analyses of the soil-structure interaction problems. It is of vital importance that the field condition will not abide from the time when the in-situ tests were run at the site till the end of the building's service life. Henceforth, the modification of the measured V_s ought to be conducted. On that basis, G_0 should be modified in line with the possible range for the degree of saturation in the effective vadose zone. The variation in the soil water content or the change of the degree of saturation in the vicinity of the ground surface could be owing to the rain, drying, inundation, and loading-unloading process. Proceeding on that track, the zone of influence was assumed to be 4 m in this study with due attention to the recommended values for the effective vadose zone in AS2870 (2011).

A series of resonant column tests was conducted by Wu et al. (1984), producing a group of trends for the normalized small-strain shear modulus ($G_o/G_{0(dry)}$) versus the degree of saturation. Equation (3.7), suggested by Wu et al. (1984) throughout a curve-fitting procedure, was adopted in this study to estimate G_0 based on the selected values for S_r (i.e., 5%, 17.5%, 60%, and 100%). Equation (3.7) is supported by Equations (3.8), (3.9), and (3.10), including the S_r-related parameters, i.e., $H(S_r)$, $H_1(S_r)$, and $H_2(S_r)$.

$$\frac{G_0}{G_{0(dry)}} = 1 + H(S_r) \tag{3.7}$$

$$H(S_r) = \begin{cases} (a-1)sin\left(\frac{\pi S_r}{2b}\right), & S_r \leq b \\ (a-1)[H_1(S_r)][H_2(S_r)], & S_r > b \end{cases} \tag{3.8}$$

$$H_1(S_r) = \frac{1}{2}\left(\frac{S_r - b}{100 - b}\right)^2 \tag{3.9}$$

$$H_2(S_r) = sin\left\{\frac{\pi}{100 - b}\left[S_r + 50 - \frac{3}{2}b\right]\right\} + 1 \tag{3.10}$$

where, $G_{0(dry)}$ is the low-amplitude shear modulus for the completely dry condition, a is the maximum value of $G_o/G_{0(dry)}$, b is the optimum degree of saturation ($S_{r(opt)}$), and S_r is the degree of saturation expressed in percent.

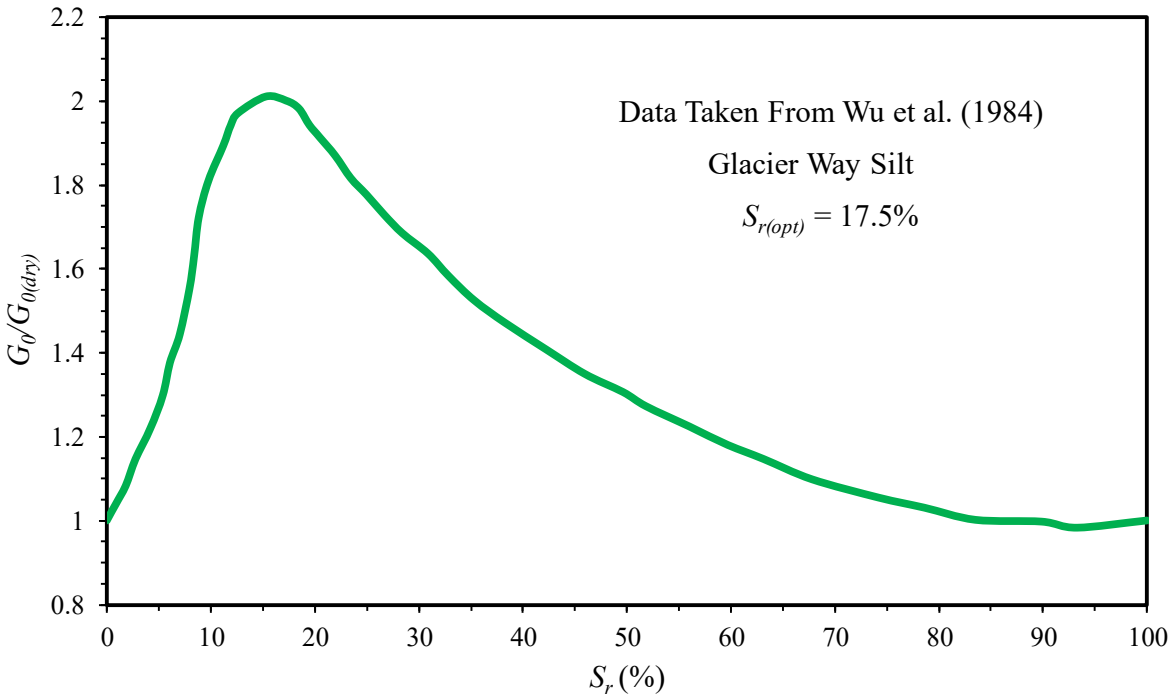

Figure 3.11 Normalized small-strain shear modulus versus degree of saturation for Glacier Way Sand

Santamarina (2003) and Dong and Lu (2016) reported that the highest value of normalized small-strain shear modulus might be observed around the dry state. However, as depicted in Figure 3.11, the corresponding $S_{r(opt)}$ of $\left(G_o/G_{0(dry)}\right)_{max}$ was not related to the fully dry state

since the clay fraction in Glacier Way Silt was infinitesimal. It is of importance to point out that four adopted values for the degree of saturation (i.e., 5%, 17.5%, 60%, and 100%) in order to calculate the small-strain shear moduli and corresponding shear wave velocities were selected such that the two ranges of S_r, smaller and greater than $S_{r(opt)}$, were covered, shown in Figure 3.11, wherein the apex of the trend corresponded to $S_{r(opt)}$.

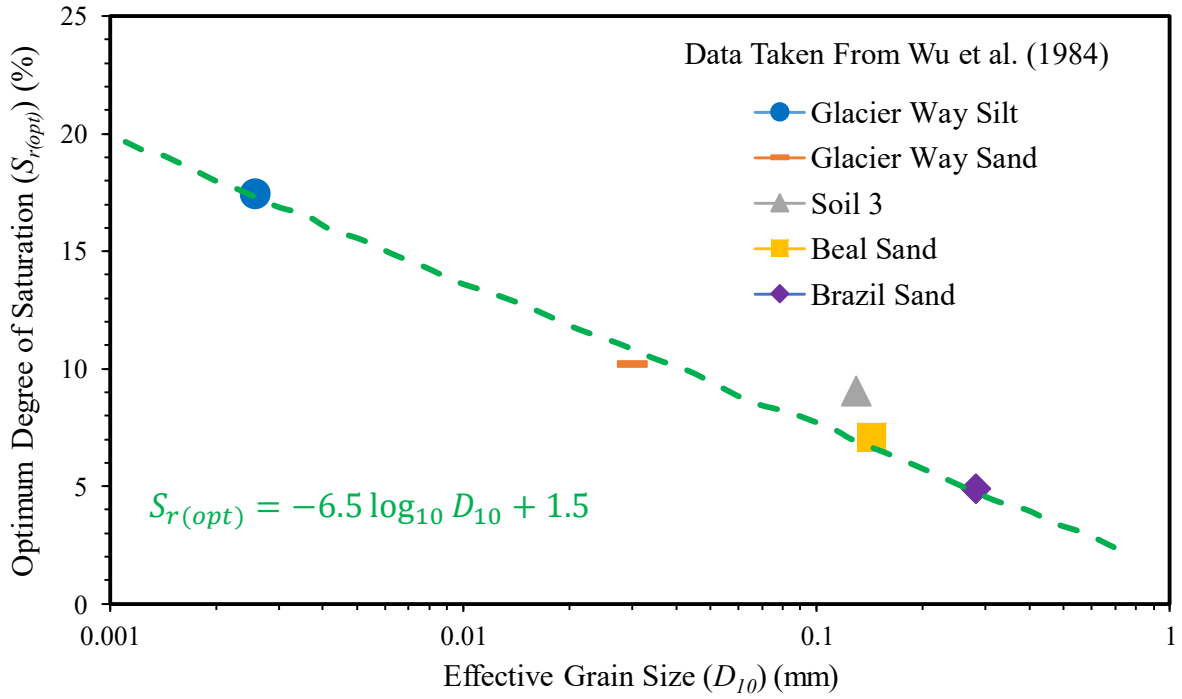

Figure 3.12 Relationship of optimum degree of saturation ($S_{r(opt)}$) and effective grain size (D_{10})

The experimental results of the five test materials, including Glacier Way Silt, Glacier Way Sand, Beal Sand, Brazil Sand, and Soil 3, which contained the appreciable amounts of shells and mica, reported by Wu et al. (1984), are portrayed in Figure 3.12. They showed the linear relation, formulated in Equation (3.11), between $S_{r(opt)}$ and the logarithm of the effective grain size (D_{10}). Referring to Wu et al. (1984), Equation (3.11) could be employed for the soils with both the rounded and angular grains. That is to say, the optimum degree of saturation for the adopted soil herein (i.e., Glacier Way Silt) was reported by Wu et al. (1984) to be hovering around 17.5%. The said value was in a good agreement with 18.5%, computed by substituting D_{10} by 0.0024 mm in Equation (3.11).

$$S_{r(opt)}(\%) = -6.5 \log_{10} D_{10} + 1.5 \quad (3.11)$$

The summary of the parameters, which were used so as to estimate V_s based on the chosen values for the degree of saturation in the shallow depth of 4 m, construed as "zone of influence", could be reviewed in the tabular form through Table 3.2. $G_{0(dry)}$ was adopted as 57.8 MPa as reported by Wu et al. (1984) for Glacier Way Silt. In addition, Figure 3.13a is a pictorial description of the established shear wave velocity profiles in the current research whilst the caption on Figure 3.13b implies the soil mass density profiles on the basis of Equation (3.6).

Table 3.2 Adopted soil parameters in top 4-m vadose zone, influenced by degree of saturation

S_r (%)	ρ (kg/m^3)	a	b	$H(S_r)$	$H_1(S_r)$	$H_2(S_r)$	$G_0/G_{0(dry)}$	$G_{0(dry)}$ (MPa)	G_0 (MPa)	V_s (m/s)
5	1630	2.05	17.5	0.456	---	---	1.456	57.8	84.2	230
17.5	1680	2.05	17.5	1.050	---	---	2.050	57.8	118.5	270
60	1850	2.05	17.5	0.133	0.133	0.952	1.133	57.8	65.5	190
100	2000	2.05	17.5	0	0.500	0	1	57.8	57.8	170

3.3.3 Results and Discussions

The most common and essential soil properties, involved in the seismic design procedures, are the shear wave velocity and small-strain shear modulus. As might be expected, both the cohesionless and cohesive soil layers in the vicinage of the ground surface for the different reasons consistently encounter the change in the degree of saturation. The small-strain shear modulus is affected by such a change; so certainly is the shear wave velocity. In that view, a series of numerical simulations, including the S_r = 5%, S_r = 17.5%, S_r = 60%, and S_r = 100% cases, was conducted via FLAC3D, followed by probing the recorded time histories of the structural and geotechnical parameters in the adopted soil-structure system.

The distributions of the shear forces on all the building levels for the four cases, i.e., S_r = 5%, S_r = 17.5%, S_r = 60%, and S_r = 100%, as displayed in Figure 3.14, exhibited some level of difference, which would be set forth throughout the response spectra, exposed in Figure 3.15, utilizing a 5% damping ratio. At this scope, the fundamental translational period of the

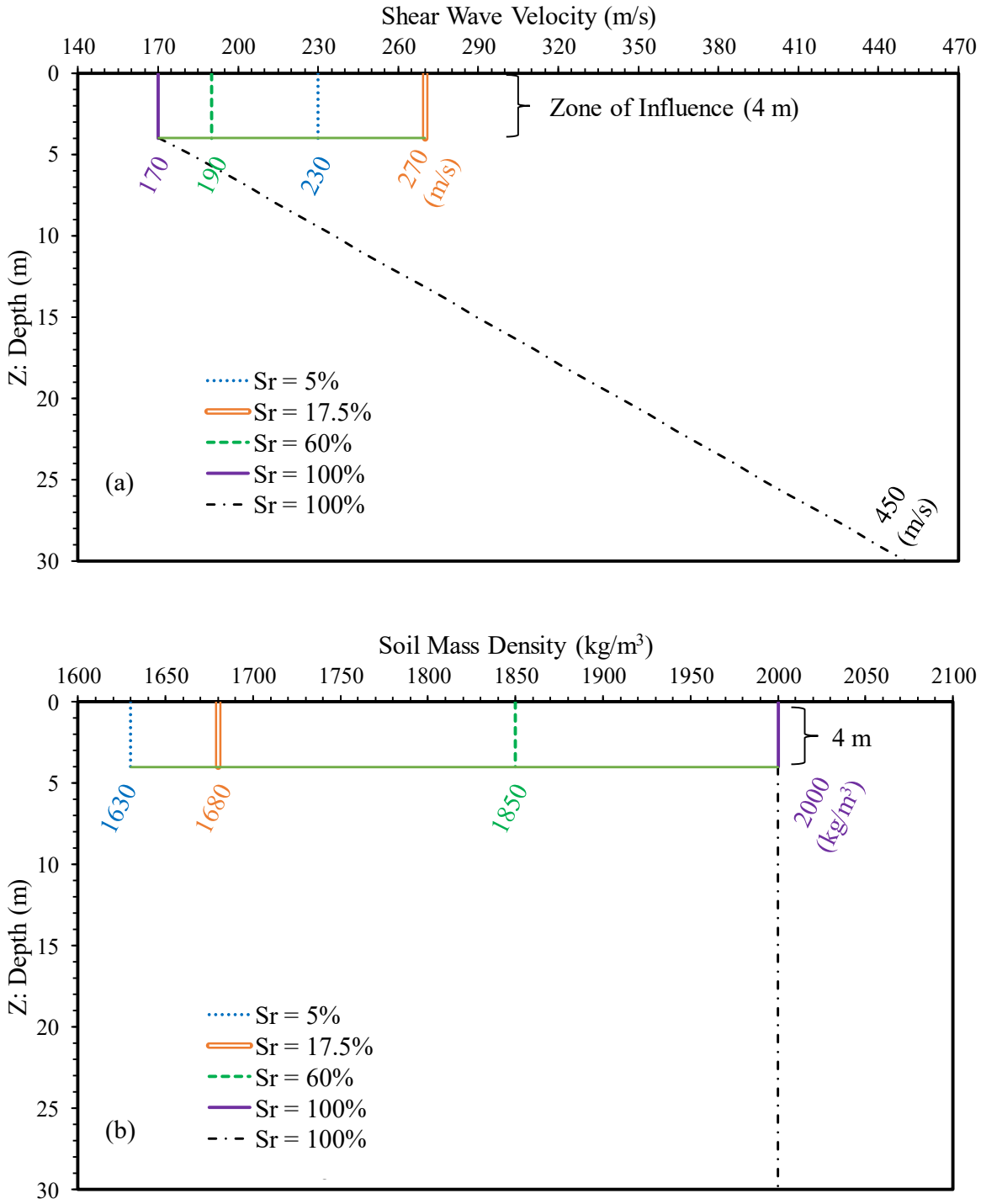

Figure 3.13 (a) Adopted shear wave velocity profiles, and (b) variations of soil mass density with depth for selected values of degree of saturation

adopted building (T), and characteristic site period ($\bar{T}_s$), as well as the second mode period of the entire soil-structure system (T_2) were estimated. Making use of $N/10$ sec, as the approximate estimation of the fundamental period of an N-story fixed-base building, suggested by Di Julio (2001), and Equation (3.12) (presented by Kramer (1996)) resulted in 2 s and 0.4 s

for T and $\bar{T}_s$, respectively. Note that the soil deposit thickness (H_s), and weighted average of the in-situ shear wave velocity ($\bar{V}_{s,i}$) were 30 m and about 300 m/s (estimated via Equation (3.2)), consecutively. As a result, the fundamental period of the SSI model (i.e., $T_{SSI} = T + \bar{T}_s$) was determined to be 2.4 s. It is previously reported by NIST-GCR-11-917-15 (2011) that the second mode period is often bracketed by the one-quarter and one-third of the fundamental period so long as the building frame is regular. Accordingly, T_2 was estimated rather 0.6 s to 0.8 s.

$$\bar{T}_s = \frac{4H_s}{\bar{V}_{s,i}} \tag{3.12}$$

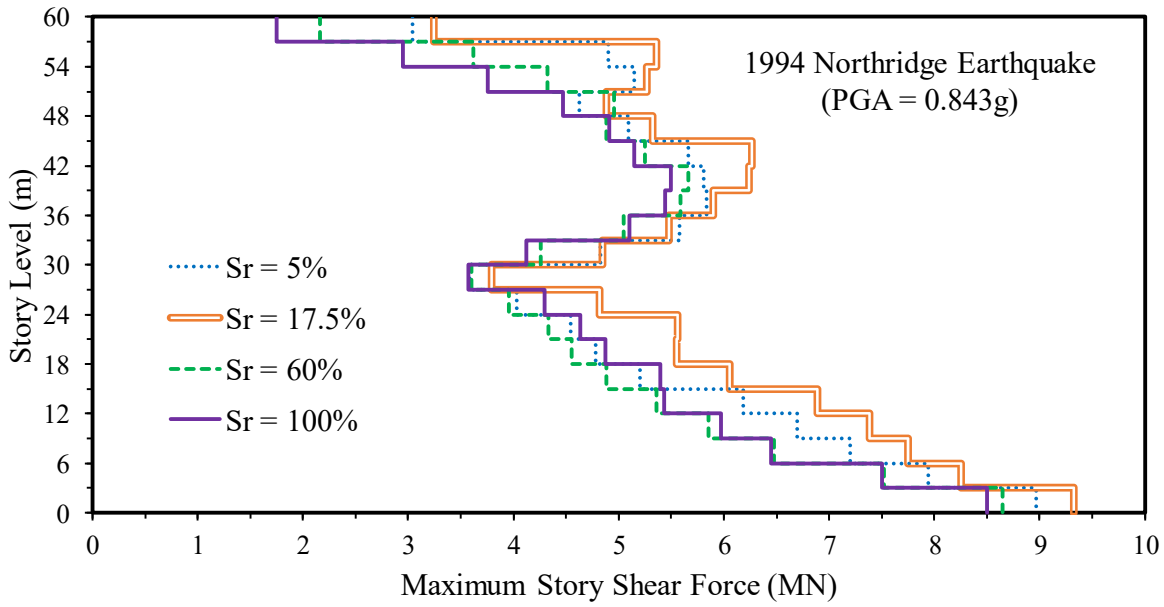

Figure 3.14 Shear force envelope distributions along height of 20-story superstructure under excitation of 1994 Northridge earthquake

The contribution of the first and second modes signposted the seismic energy towards generating the shear forces in the designed superstructure. All the trends in Figure 3.15 coincided at T_{SSI} (i.e., 2.4 s) while the S_r = 17.5% trend sat atop the others in the second mode period range, i.e., 0.6-0.8 s. By way of illustration, the highest spectral acceleration of the S_r = 17.5% case in the said period range was observed to be 1.6g whereas the S_r = 60% case

experienced only 0.8g. Therefore, the shear force envelope distribution of the S_r = 17.5% case, having the optimum degree of saturation, located on the far right side of Figure 3.14 compared to the other cases. As regards the seismic base shear, there was a 10%-increase from the S_r = 100% case to the S_r = 17.5% case (see Figure 3.14).

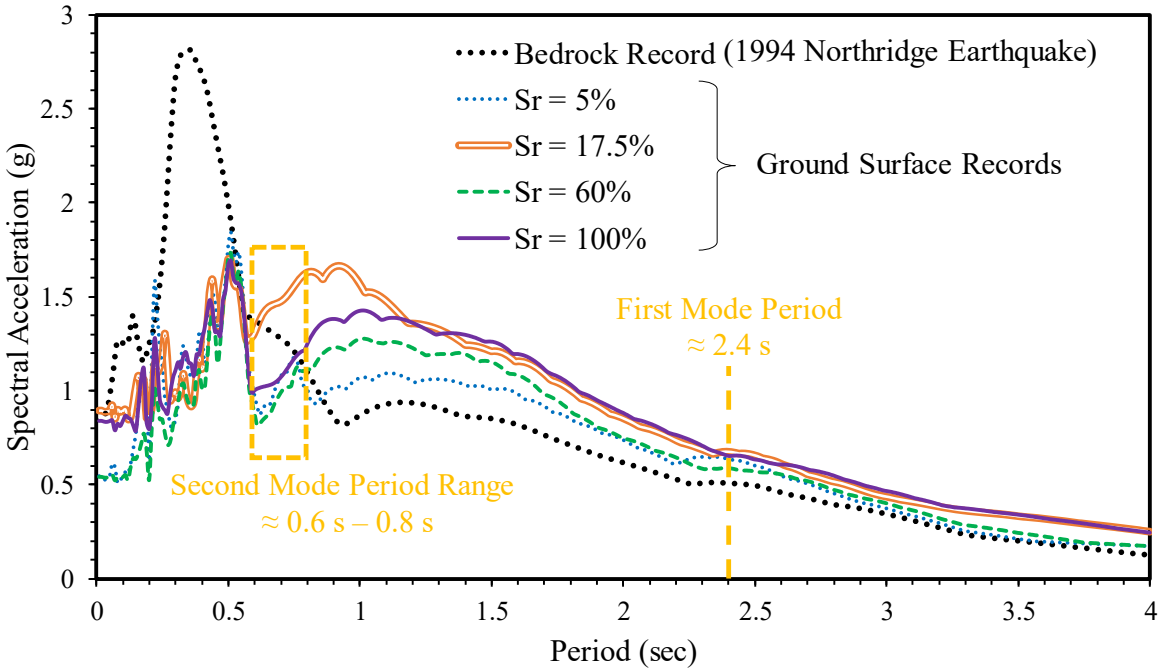

Figure 3.15 Response spectra of bedrock record and ground motions under excitation of 1994 Northridge earthquake

The upsurge in the story shear forces happened on the upper levels in Figure 3.14, signifying the irrevocable impacts of the structure's higher modes on its dynamic responses in the SSI analysis. The aforesaid outcome is of vital importance inasmuch as the conventional belief, as mentioned in Veletsos and Meek (1974) and Stewart et al. (2003), revolves around that the soil-structure system is immune to the higher modes of the vibration, denoting that only the structural parameters of the fundamental mode are basically needed for the analysis of SSI. Moreover, the lateral sliding resistance of the mat foundation under the applied earthquake was checked in this study. In that regard, the foundation-soil interface friction angle of 26 degrees, corresponding to the friction coefficient of 0.5, as recommended by FEMA273 (1997), and the total dead load of the building and foundation were considered. The sliding resistance

was well more than the generated base shear, induced by the 1994 Northridge earthquake, whose maximum value was approximately 9.5 MN (looking back to Figure 3.14). It was concluded that the factor of safety (FOS) against sliding was 2.

The foundation rocking could potentially engender a significant portion of the superstructure lateral deflection during an earthquake. Scrutiny of the time histories of the rocking rotations, presented in Figure 3.16, for the considered cases in this study revealed that the change in S_r from 5% to the fully saturated state not only resulted in the fourfold alleviation but also a nearly 25-second shift in the occurrence time of the maximum foundation rocking. In Figure 3.16, all the analyzed cases in this study showed the more or less similar foundation rotation history in the first five seconds of the 1994 Northridge earthquake, reaching approximately 0.92 degrees, which was the maximum rocking rotation for the S_r = 100% case. In line with Figure 3.15, when the top layer of the soil just below the foundation, called the effective vadose zone, was semi-dry (e.g., the S_r = 5% case), more of the earthquake load was transferred to the building due to the higher mode effects. As a result, the overturning moments, induced by the seismic shear forces in the building, boosted the foundation rocking forasmuch as, referring back to Figure 3.14, the story shear forces and base shears were on the increase when descending the degree of saturation. From all accounts, the foundation rocking was on the increase owing to the aforesaid effect of the overturning moments, mainly taking place in the last 20 s of the applied input record. For instance, 1.25 degrees and 1.10 degrees as the maximum rocking rotations were observed in the S_r = 5% and S_r = 17.5% cases, respectively, as discerned in Figure 3.16. It is important to notice that the lowest shear modulus, reported for the S_r = 100% case in Table 3.2, would have had an adverse effect on the amount of the foundation rocking in this study by elevating the total settlement of the foundation whilst diminishing the differential settlement due to the highest soil self-weight in the effective vadose zone, displayed in Figure 3.13b.

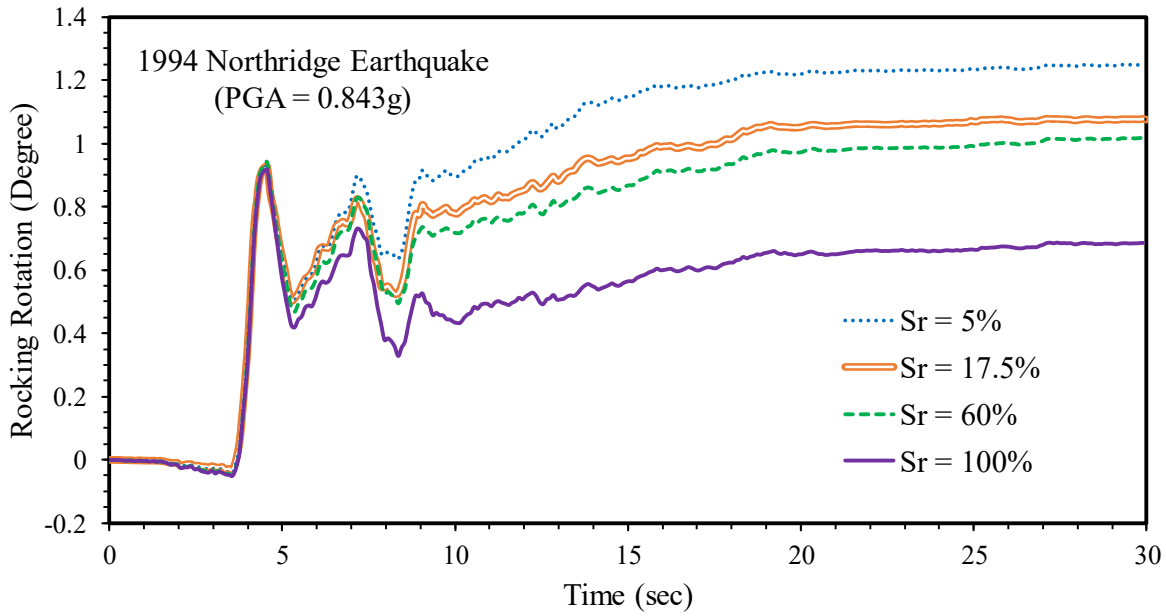

Figure 3.16 Time histories of foundation rocking under excitation of 1994 Northridge earthquake

The transient lateral displacements of the 20-story reinforced concrete moment-resisting building were sketched out in Figure 3.17 when the maxima took place at the rooftop in the considered cases. Thus, each single trend instanced the actual deformation, experienced by the high rise building, subjected to the 1994 Northridge earthquake. Figure 3.17 clearly demonstrates that the S_r = 5% case, undertook 1336 mm as the maximum lateral displacement whilst those of the S_r = 17.5%, S_r = 60%, and S_r = 100% were 1156 mm, 1087 mm, and 1070 mm, in the order given. The significant foundation rocking, predicted for the S_r = 5% case, shown in Figure 3.16, was the reason for the observed considerable transient lateral deflection of the building. Note that the lateral deflections in the models of interest were relative to the movements of the concrete foundation on the soil surface. Accordingly, the lateral displacements of the building, depicted in Figure 3.17, were the combination of the two components, viz, the foundation rocking and structural distortion. The latter was directly related to the generated shear forces in the columns of the building.

In the performance-based seismic engineering methodology, it is imperative that the inter-story drift ratio, as the most common parameter to evaluate the seismic performance of a

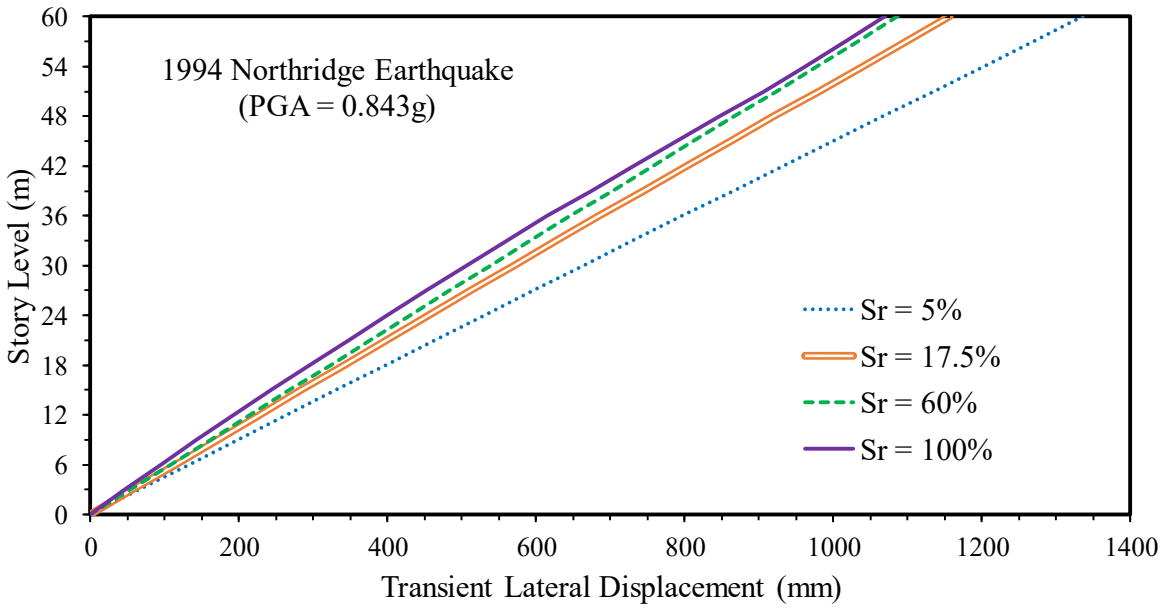

Figure 3.17 Transient lateral displacements of 20-story superstructure under excitation of 1994 Northridge earthquake

building, be compared with the 2% life safety drift limit according to FEMA273 (1997). In Figure 3.18, the inter-story drift ratios were calculated via Equation (3.13) as to AS1170.4 (2007), wherein DR_{tt} is the total inter-story drift ratio, d_i and d_{i+1} are the deflections at the $(i)^{th}$ and $(i+1)^{th}$ levels, respectively, and h is the story height (i.e., 3 m).

$$DR_{tt} = \frac{d_{i+1} - d_i}{h} \tag{3.13}$$

Comparing the results of the S_r = 17.5% and S_r = 5% cases in Figure 3.18 with the other two cases divulged the notable contribution of the foundation rocking into the transient inter-story drift ratio. In that regard, the S_r = 17.5% case ended up with the maximum transient inter-story drift ratio of 1.98%, which was about to breach the 2% life safety drift limit. The S_r = 5% case breached the said safety limit since its distribution of the transient inter-story drift ratio consisted of the minimum value of 2.2% and maximum value of 2.26%, both of which were greater than 2%. Such a seismic response triggered the partial or total loss of the structural and non-structural elements and gave rise to skyrocketing the cost of repair and possible replacement of the said components. As exemplified in Figure 3.18, the structural distortion

affected the transient inter-story drift ratios in the S_r = 100% case throughout outweighing the effect of the foundation rocking component. In point of fact, the shear force-induced building distortion in the S_r = 100% case compensated the 0.33-degree difference between the foundation rocking values of the S_r = 60% and S_r = 100% cases. Thus, the transient inter-story drift ratio in the S_r = 100% case surpassed that of the S_r = 60% case between 11th story to 19th story, hitting 1.95%.

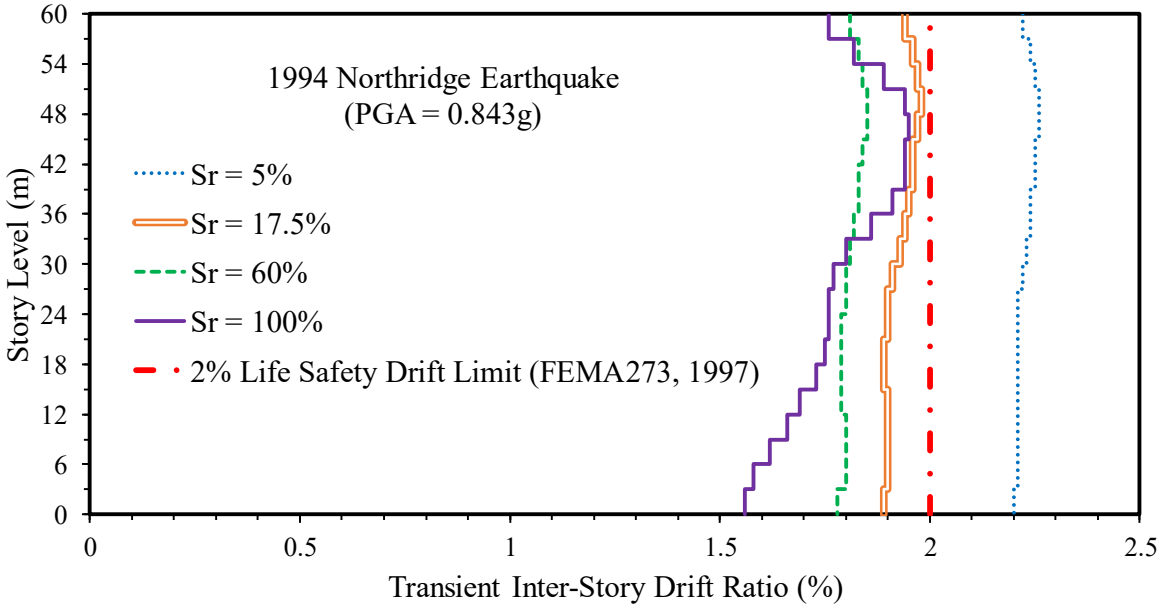

Figure 3.18 Transient inter-story drift ratios of 20-story superstructure under excitation of 1994 Northridge earthquake

3.4 Effects of Hyperbolic Hardening Parameters on Seismic Performance of High Rise Buildings Considering Soil-Structure Interaction

The recent research studies on the seismic soil-structure interaction (e.g., Gazetas, 2015; Choinière et al., 2019; Ramadan et al., 2020; Scarfone et al., 2020), have demonstrated the importance of SSI in the geotechnical earthquake engineering applications. Lade (2005) pointed out that the predictions of the structures response, subjected to the external loading,

very much depend on the stress-strain relationship, known as the constitutive model. Indeed, there are numerous plasticity-based soil constitutive models in the literature, being frequently employed in the SSI numerical simulations (e.g., Castaldo and De Iuliis, 2014; Fatahi et al., 2020), whereas the engineers might need to use some assumptive values for some of the parameters based on the reported ranges in the literature for the various soils. It has been realized that assessing the extent to which the choice of such assumptive parameters can affect the seismic response of the superstructures has not been fully scrutinized. In this study, the Hyperbolic Hardening with Hysteretic Damping (H2-HD) model was cherry-picked among the advanced hardening plasticity-based soil constitutive models. In order to investigate the above-mentioned effects, FLAC3D software and its internal programming language, named "FISH", were utilized so as to numerically analyze a fully coupled soil-structure system in the time domain. In summary, it could be deduced that precisely estimating the parameters values in a plasticity-based soil model could preclude any potential damage to the soil-structure systems due to the earthquakes or result in the optimized and more cost-effective design.

3.4.1 Adopted Soil-Structure Interaction Numerical Model

A 20-story (60 m height), 3-span (12 m length) reinforced concrete moment-resisting building was analyzed and designed using SAP2000 considering the relevant Australian codes and in line with the constructability and norms. The properties of the Grade 32 concrete material, adopted in the building (i.e., the columns, beams, and 0.25-m slabs) and foundation, are as follows: (i) modulus of elasticity, equal to 30.1 GPa; (ii) Poisson's ratio of 0.2; (iii) mass density of 2400 kg/m^3; and (iv) concrete characteristic compressive strength f_c' = 32 MPa. The possibility of forming the plastic hinges was considered in the rectangular columns and beams by specifying the limiting plastic moment (M^p) based on f_c' and the geometries of the structural elements. Consequently, the structural elements behaved elastically till breaching the limiting

plastic moment. If the limiting plastic moment was reached, the section could deform without inducing any additional resistance. The adopted sizes of the columns and beams were 0.85 m × 0.85 m and 0.70 m × 0.70 m till the fifth story, respectively, and above which the dimensions were reduced by 0.05 m every five floors. Moreover, according to ACI318 (2014), the cracked section properties for the reinforced concrete components were employed by diminishing the stiffness of the columns (to 0.70 I_g), beams (to 0.35 I_g), and slabs (to 0.25 I_g), considering I_g as the moment of inertia associated with an uncracked section. Besides, a damping ratio of 5% was adopted to consider the vibration dissipation of the superstructure and foundation. The designed mat foundation had a thickness of 1 m and a width of 14 m while the building total width was 12 m. The Meyerhof method (Meyerhof, 1963) showed the satisfaction of the minimum required factor of safety (FOS) of 3, suggested by Das (2015), for the bearing capacity of the adopted mat foundation, subjected to the building weight.

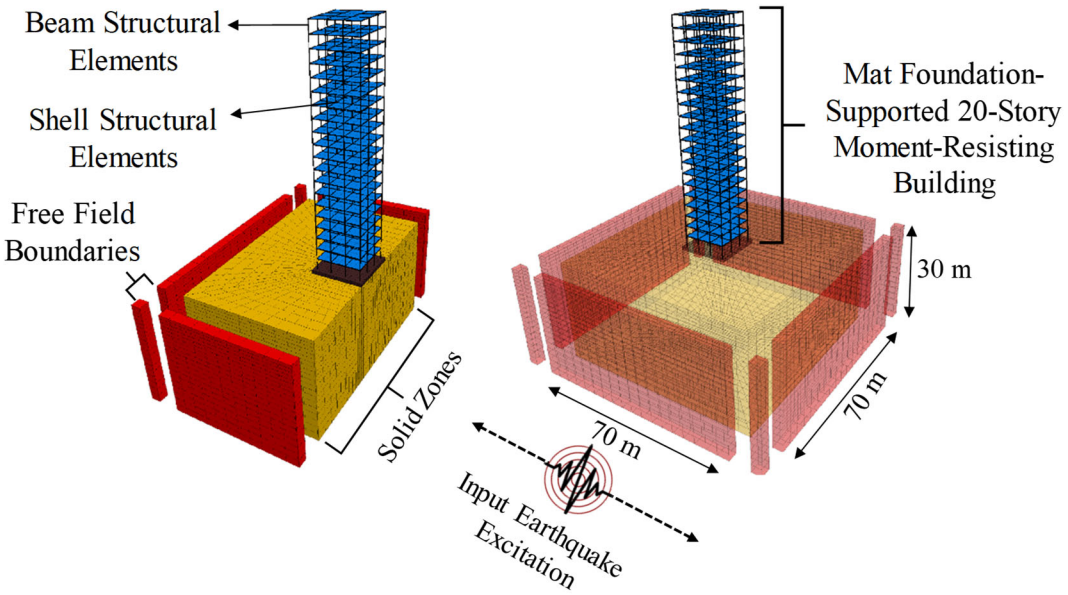

Figure 3.19 Adopted soil-structure system via direct one-step approach in FLAC3D

The adopted plan dimensions of the soil medium, shown in Figure 3.19, were 70 m × 70 m, satisfying the minimum requirement, being five times the width of the existing building, proposed by Rayhani and El Naggar (2008). The convergence analysis was also performed on

the zone sizes for rationally reducing the seismic analysis time without impacting the predictions. In addition, the free field boundary conditions were applied to the lateral boundaries of the soil deposit to simulate the seismic motions, propagating along the edges of the numerical model. Furthermore, the viscous dashpots, coupled with the said free field boundaries, were utilized so as to absorb the boundary wave reflections. Prior to applying the earthquake excitation, the base of the model was fully fixed whilst the lateral boundaries were fixed horizontally in the static analysis, subjected to the gravity loading. Furthermore, the seismic bedrock at the model base was considered as a rigid base due to the significant impedance difference between the hard rock and soil deposit. Further, the 30-m thickness of the soil deposit was selected since Maheswari et al., 2010 reported that the potential amplification/attenuation of a site during the ground shaking could be predicted throughout the properties of the top 30 m of the soil. The baseline-corrected near-field excitation of the 1994 Northridge earthquake (USA), portrayed in Figure 3.20, was imposed upon the bedrock level to carry out the time history analysis. The severity of the damage associated with the near-field ground motions, e.g. the 1994 Northridge earthquake, was outlined by Attalla et al. (1998). In this study, the mat foundation was modeled using the solid zones, capturing the shear deformations of the foundation under the applied loads. Last but foremost, the possible separation, gapping, and/or sliding at the interface between the concrete mat foundation and soil, were captured by means of the interface element, represented by the springs and sliders. The normal and shear spring stiffnesses were set to ten times the stiffness of the neighboring zone, as per Itasca (2012), while the Mohr-Coulomb yield criterion was assigned to the sliders.

3.4.2 Adopted Soil Constitutive Model

The adopted Hyperbolic Hardening with Hysteretic Damping soil model, called hereinafter H2-HD, inspired by the UBCSAND model, proposed by Puebla (1999), captured the shear

hardening, volumetric hardening, and Mohr-Coulomb failure envelope. The detailed description of the H2-HD soil constitutive model was reported by Yeganeh and Fatahi (2019). In addition to the nonlinear elasticity considering the Hook's law in the incremental manner, the two-variable hysteretic damping algorithm, stemming from the small-strain nonlinearity, was employed in this study (see Table 3.4).

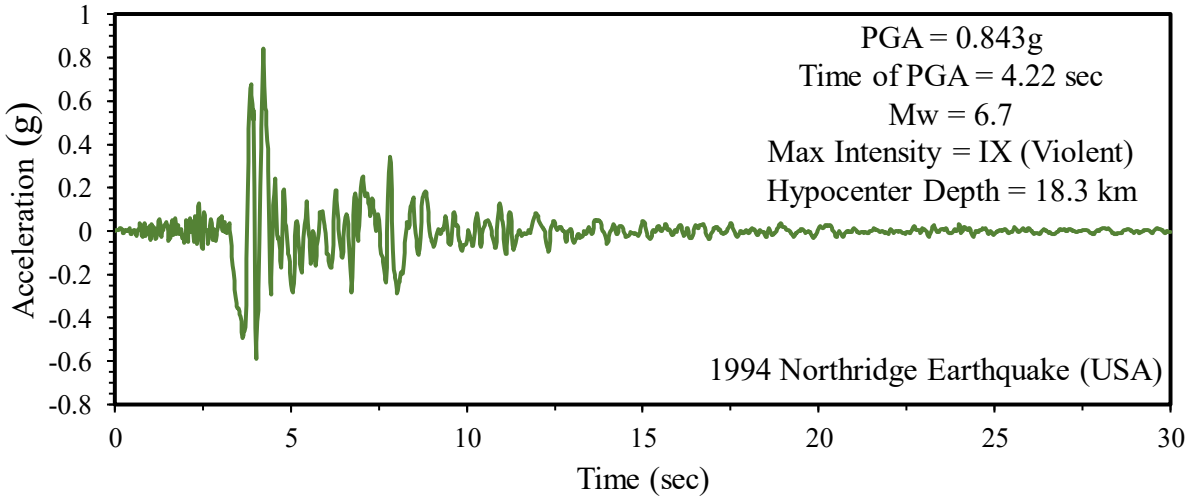

Figure 3.20 Adopted earthquake accelerogram of 1994 Northridge Earthquake as input base motion

The shear hardening law, revised from the well-known hyperbolic model, established by Duncan and Chang (1970), offered the possibility of expressing the hyperbolic behavior via the relation between the mobilized stress ratio (η^{mob}) and plastic shear strain (ε_s^p), given in Equation (3.14). η^{mob} was defined as the sine of a mobilized friction angle (φ^{mob}), whose ultimate value was the failure effective friction angle (φ_f').

$$d(\eta^{mob}) = d(sin\varphi^{mob}) = \frac{G_m^p}{P'} d(\varepsilon_s^p) = \frac{G_i^p}{P'}\left(1 - R_f \frac{sin\varphi^{mob}}{sin\varphi_f'}\right)^2 d(\varepsilon_s^p) = \frac{\beta G_c}{P'}\left(1 - R_f \frac{sin\varphi^{mob}}{sin\varphi_f'}\right)^2 d(\varepsilon_s^p) \quad (3.14)$$

where, G_i^p is the initial tangent plastic shear modulus at very low stress ratio level (i.e., η^{mob} near 0), β is the elastic-plastic coupling coefficient, G_c is the elastic tangent shear modulus,

whose initial distribution (i.e., G_o), consistent with the in-situ shear wave velocity ($V_{s,i}$) profile, is displayed in Figure 3.21, and R_f is the failure ratio.

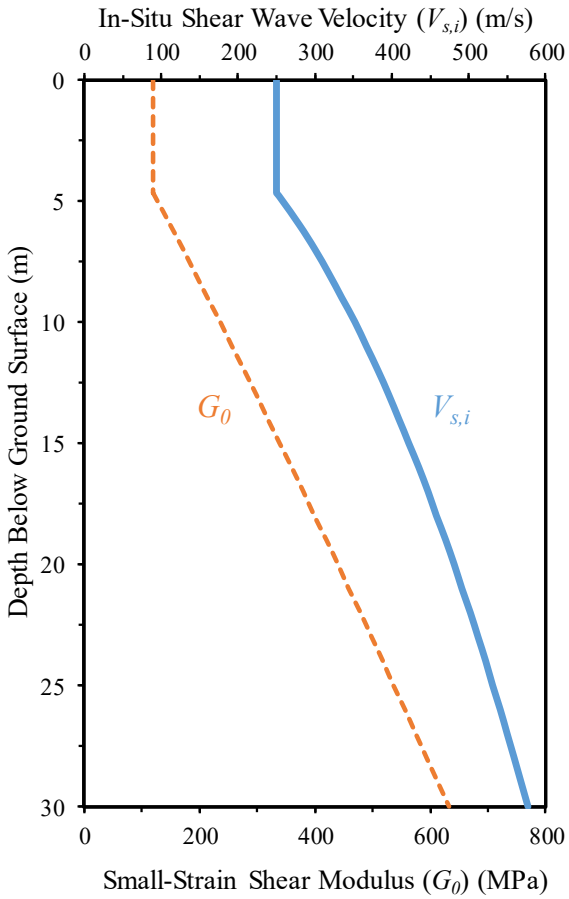

Figure 3.21 Adopted in-situ shear wave velocity and corresponding small-strain shear modulus profiles

Equation (3.15) formulates the shear yield locus, corresponding to a constant stress ratio and the mobilized intercept ($c'\left(tan\varphi^{mob}/tan\,\varphi'_f\right)$, where c' is the ultimate effective cohesion) in the $p'-q$ space. The compression yield surface was a straight line, perpendicular to the mean effective stress axis (p') and independent of the deviatoric stress (q). In the H2-HD model, the associated and non-associated flow rules were adopted for the volumetric and shear responses, in the order given.

$$f_q = p'\left(\frac{6sin\varphi^{mob}}{3-sin\varphi^{mob}}\right)+c'\left(\frac{tan\varphi^{mob}}{tan\varphi'_f}\right)\left(\frac{6cos\varphi^{mob}}{3-sin\varphi^{mob}}\right)-q \tag{3.15}$$

By means of a cap hardening power law, the nonlinear volumetric behavior was reproduced.

The cap pressure (p^{cap}) in Equation (3.16), defined the size of the compression yield surface in compliance with the irrecoverable volumetric strain (ε_v^p). Note that the in-situ stress state was simulated based on the coefficient of lateral earth pressure at rest for the overconsolidated soil deposit ($K_{0(OC)}$). As the analysis was up and running, the elastic tangent bulk (K_c) and shear (G_c) moduli were evolving as a function of p^{cap} and p', as given in Equations (3.17) and (3.18), respectively. Simply put, the stress-dependent elastic stiffness was taken into account in the H2-HD soil model.

$$p^{cap} = p^{ref}\left[0.12\varepsilon_v^p \frac{K^{ref}}{p^{ref}}\right]^{(1/0.1)} \tag{3.16}$$

$$K_c = K_{e-p}^{ref}\left(\frac{p^{cap}}{p^{ref}}\right)^{0.9} \tag{3.17}$$

$$G_c = G_c^{ref}\left(\frac{p'}{p^{ref}}\right)^{0.9} \tag{3.18}$$

where, K^{ref} is the slope of the laboratory curve in an isotropic consolidation test for the mean effective stress (p') versus the volumetric strain (ε_v) at the reference mean effective stress (p^{ref}), K_{e-p}^{ref} is the isotropic elasto-plastic bulk modulus at the reference mean effective stress, and G_c^{ref} is the elastic tangent shear modulus at p^{ref}. Theoretically, p^{ref} could be any value so long as K^{ref} and G_c^{ref} are given correspondingly referring to Sadat et al. (2018).

3.4.3 Adopted Hyperbolic Hardening Parameters

In the adopted elasto-plastic soil constitutive model, the failure ratio (R_f) and elastic-plastic coupling coefficient (β) were the key parameters, influencing the stress increment-strain increment relationship, affecting the induced plastic shear strains significantly. Through the adopted formulations, the failure ratio could affect not only the soil strength but also the soil stiffness. In the adopted soil model, the failure ratio linked the hyperbolic asymptote, i.e. the

ultimate strength (η_{ult}), aka "ultimate stress ratio", to the Mohr-Coulomb failure envelope (i.e., η_f, called "failure stress ratio") via Equation (3.19). In addition, the decremental slope of the employed hyperbola (G_m^p as the mobilized plastic shear modulus in Equation (3.14)) was altered by assigning the different values to the failure ratio, i.e. 0.7, 0.8, and 0.9, denoting the changes in the soil stiffness. It is to be noted that R_f should be always less than 1.0 and greater than 0.7, according to Wong and Broms (1989).

$$\eta_{ult} = \left(R_f\right)^{-1}\eta_f = \left(R_f\right)^{-1} sin\left(\varphi_f'\right) \tag{3.19}$$

While R_f prevented the overprediction of the ultimate shear strength in the conducted numerical simulations, the dimensionless elastic-plastic coupling coefficient supervised the initial tangent slope of the hyperbola at the very low stress ratios. Said otherwise, the initial tangent plastic shear modulus (G_i^p) in Equation (3.14) was overseen by β. Allocating three values, i.e. 0.10, 0.20, and 0.35, to β was in line with the fact that β, usually less than 1 (see Byrne et al., 2003; Sadat et al., 2018), practically depends on the relative density (D_r) as per Equation (3.20), recommended by Byrne et al. (2004). The adopted relative density for the soil of interest was assumed to be 48% (±8%) to cover the common range for a medium dense soil deposit, reported by Budhu (2010). The summary of the adopted scenarios for the various R_f and β parameters is presented in Table 3.3. The effects of the adopted values for the failure ratio and elastic-plastic coupling coefficient on the performance of the H2-HD soil constitutive model in the space of $\eta - \varepsilon_s^p$ are graphically illustrated in Figure 3.22. The rest of the parameters attributed to the H2-HD model are tabulated in Table 3.4.

$$\beta \approx 3.7(D_r)^4 \tag{3.20}$$

Table 3.3 Developed numerical models based on adopted R_f and β

Case ID	I	II	III	IV	V
R_f	0.70	0.80	0.90	0.70	0.70
β	0.35	0.35	0.35	0.20	0.10

Table 3.4 Adopted soil properties for considered soil deposit

Soil Parameter	Symbol	Value	Unit
Soil Mass Density	ρ	1900	kg/m^3
Poisson's Ratio	ν	0.3	---
Failure Effective Friction Angle	φ'_f	29	°
Dilatancy	ψ	0	°
Ultimate Effective Cohesion	c'	20	kPa
Failure Stress Ratio	η_f	0.48	---
In-Situ Shear Wave Velocity$_{@\text{depth of 6 m}}$	$V_{s,i}$	280	m/s
Small-Strain Shear Modulus$_{@\text{depth of 6 m}}$	G_0	149	MPa
Initial Elastic Bulk Modulus$_{@\text{depth of 6 m}}$	K_{ci}	323	MPa
Overconsolidated K_0 Coefficient$_{@\text{depth of 6 m}}$	$K_{0(OC)}$	0.88	---
Overconsolidation Ratio$_{@\text{depth of 6 m}}$	OCR	3.1	---
Isotropic Elasto-Plastic Bulk Modulus$_{@\text{depth of 6 m}}$	K_{e-p}^{ref}	428	MPa
p^{ref}-Related Elastic Shear Modulus$_{@\text{depth of 6 m}}$	G_c^{ref}	196	MPa
Initial Cap Pressure$_{@\text{depth of 6 m}}$	p_i^{cap}	310	MPa
Hysteretic Damping Parameters (Itasca, 2012)	L_1 & L_2	-3.325 & 0.823	---

*Reference mean effective stress (p^{ref}) at depth of 6 m equaled atmospheric pressure (p_{atm}), i.e. 100 kPa.

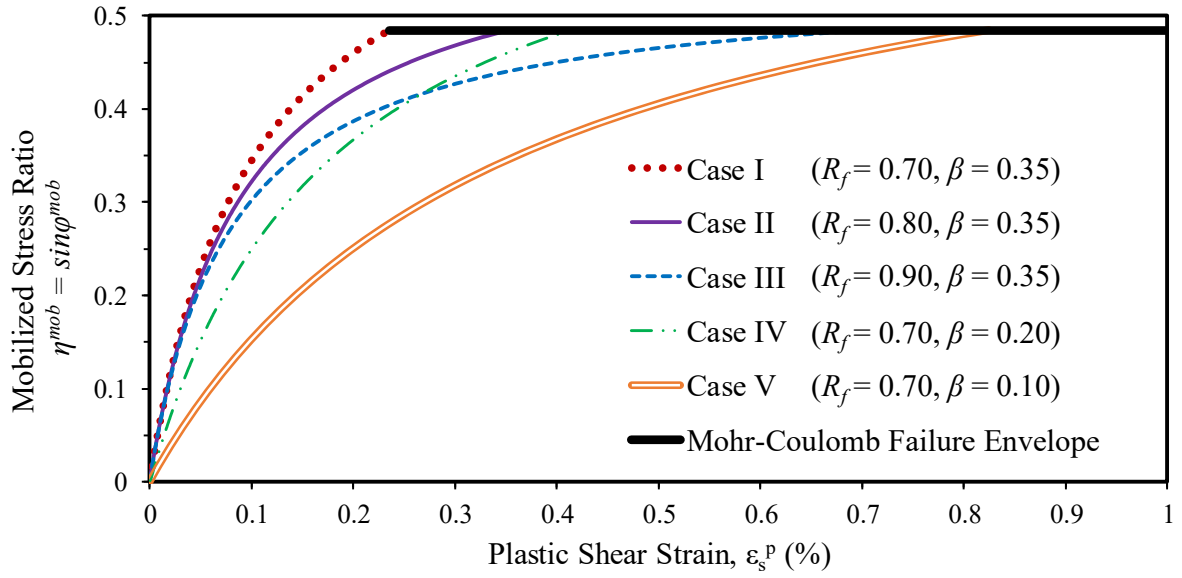

Figure 3.22 Implemented hyperbolic hardening relationships at depth of 6 m for developed numerical cases

3.4.4 Results and Discussions

Figure 3.23 displays the response spectra of the motions at the bedrock and ground surface through the Duhamel integral method, adopting 5% damping ratio. As is evident in Figure 3.23, some level of attenuation occurred almost for all the considered cases owing to the contribution

of the hardening plasticity and perfect plasticity-induced damping as well as the hysteretic damping feature. The estimated effective period range of the soil-structure system from the second mode to the fundamental/first mode was 0.48-1.90 s. Figure 3.23 reveals that decreasing the failure ratio (R_f) or increasing the elastic-plastic coupling coefficient (β) led to augmenting the inertial forces in the superstructure during the earthquake since the trend of Case I sat atop the others in the aforesaid effective period range.

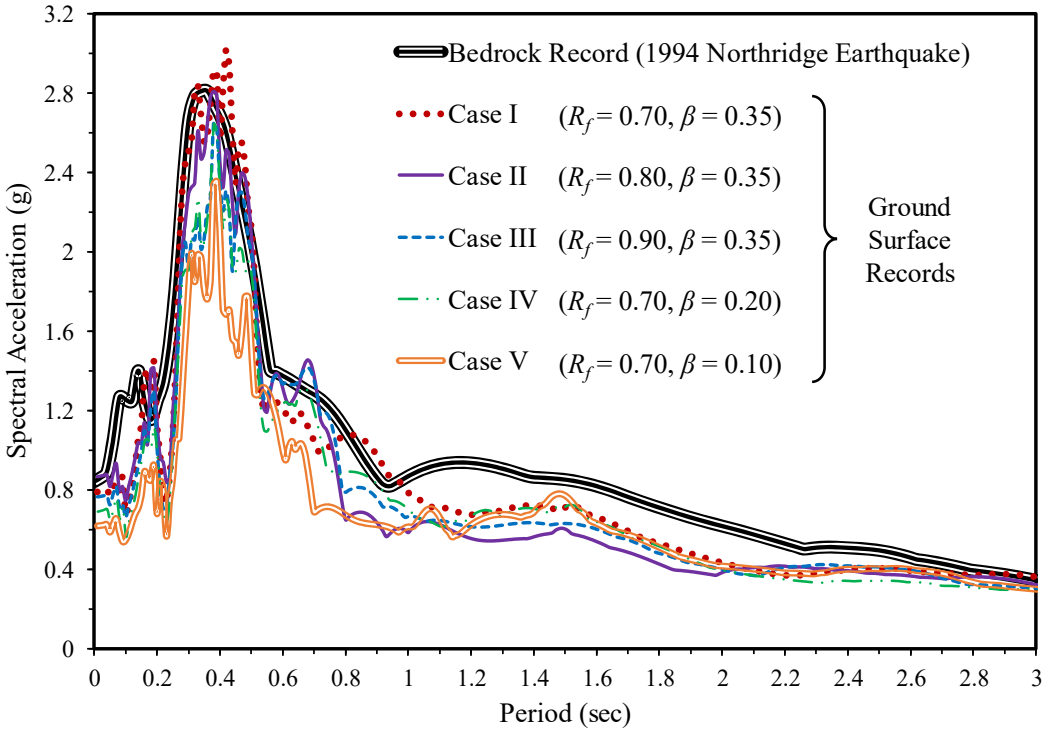

Figure 3.23 Response spectra of bedrock record and ground motions

The maximum story shear forces are shown in Figure 3.24, determined by taking the summation of all the columns shear forces on the same level once reaching the utmost during the excitation. Referring to Figure 3.24, about 30% diminishment in the story shear force on the 6th story from Case I to Case V was observed. Indeed, the effect of β on the structural demand outweighed that of R_f. Reducing the elastic-plastic coupling coefficient, whilst keeping R_f constant (i.e., comparing Cases I, IV, and V), induced the 15% reduction in the base shear, whereas the corresponding drop due to the changes in R_f was about 4% (i.e.,

comparing Cases I, II, and III). The reason was that increasing β abated the hardening plasticity-induced damping and hysteretic damping much more than decreasing R_f owing to shortening the hyperbolic path towards the Mohr-Coulomb failure envelope, referring back to Figure 3.22.

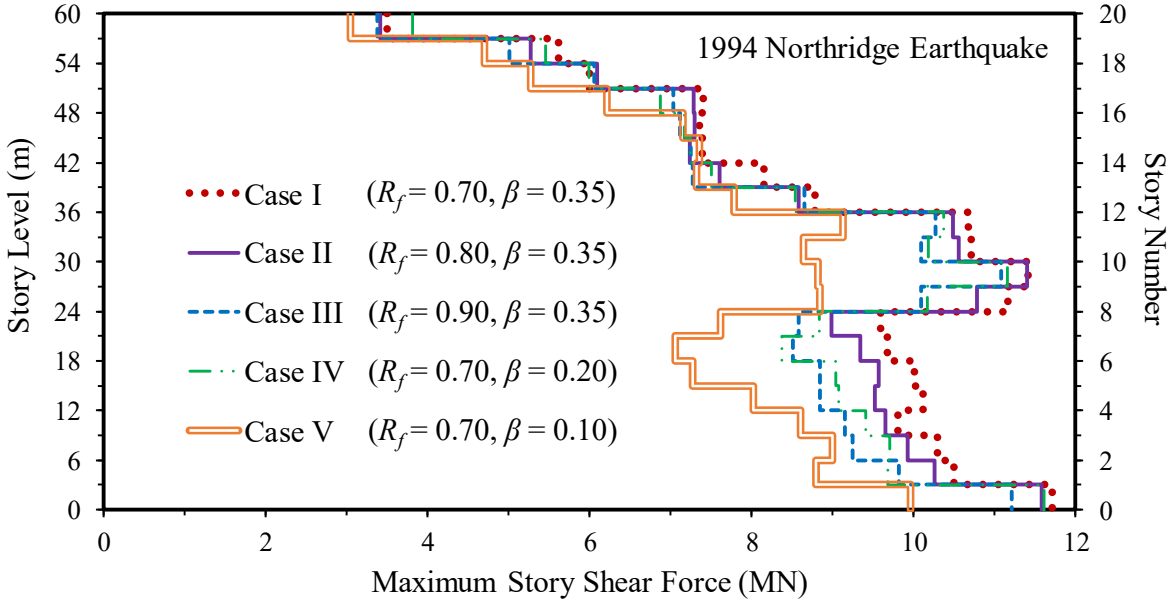

Figure 3.24 Maximum shear force distributions over height of building under 1994 Northridge earthquake

As sketched in Figure 3.25, the foundation rocking rotations were ascended by the rise in the structural forces, as previously reported in Figure 3.24. The lower the R_f value (e.g., Case I), the more contribution of the brittle manner to the soil behavior and thus giving rise to the soil perfect plasticity status at the low plastic shear strains. For instance, the permanent rotation of the foundation slab was 0.50 degrees for Case I whereas the corresponding value in Case V was declined by over 50% to 0.24 degrees. When the Mohr-Coulomb failure envelope was reached at the large plastic shear strains (see Figure 3.22), the lowest values of the transient foundation rocking were observed. It should be noted that the said values for Case III and Case V were 0.50 degrees and 0.39 degrees, consecutively.

The lateral deflections of the adopted 20-story building, stemming from the combination of the foundation rocking and structural distortion, reported in Figure 3.26, were obtained once

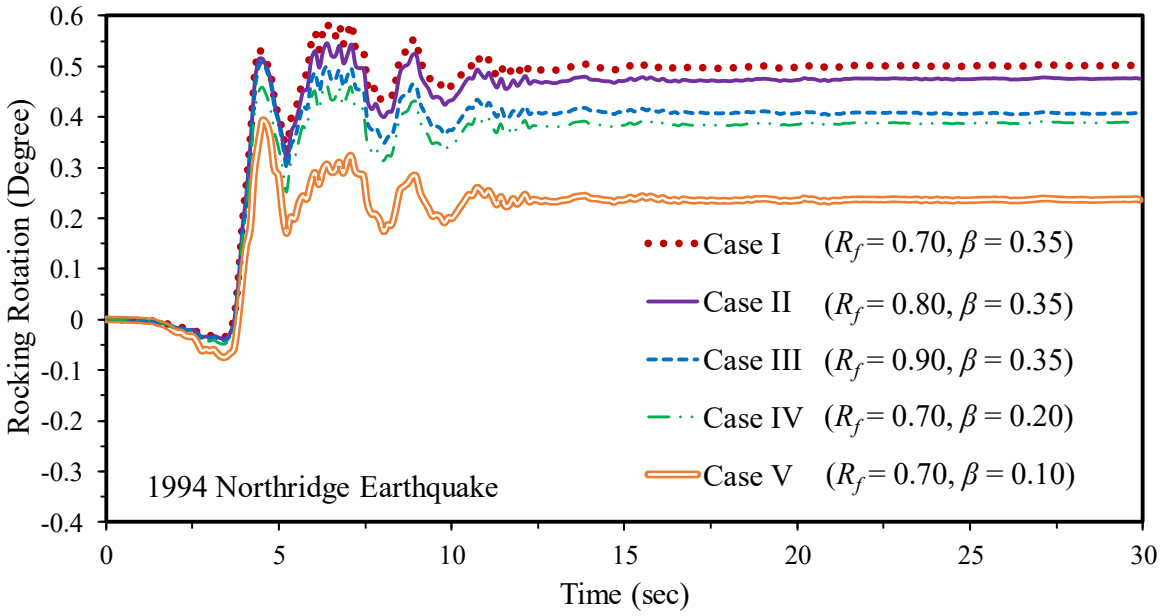

Figure 3.25 Foundation rocking histories under 1994 Northridge earthquake

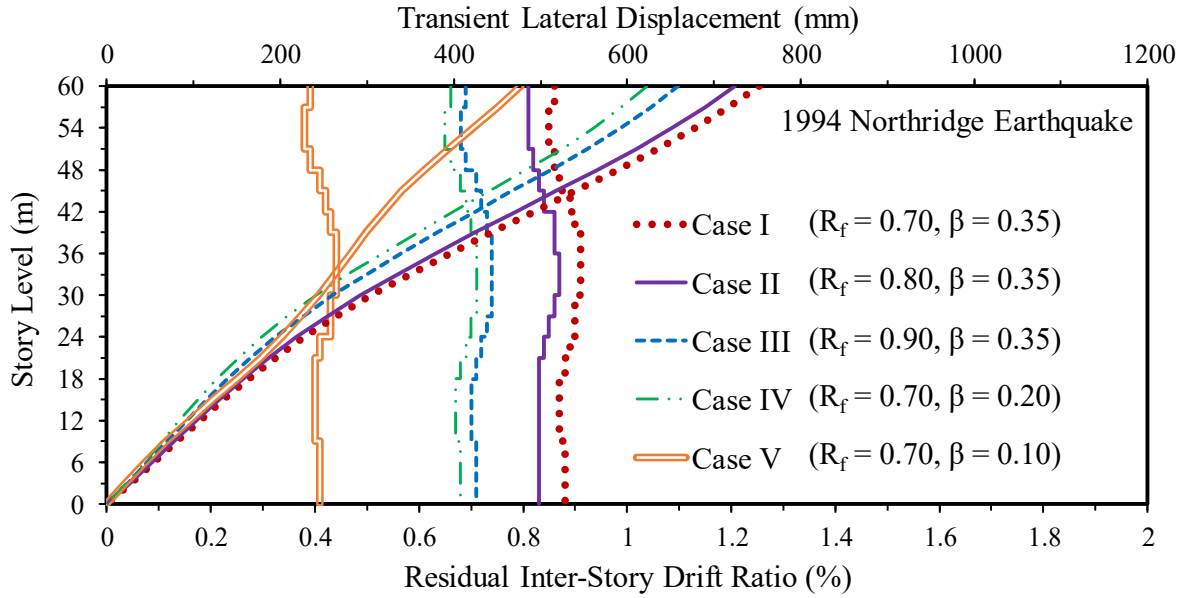

Figure 3.26 Transient lateral displacements and residual inter-story drifts of building under 1994 Northridge earthquake

the rooftop displacement reached its utmost during the seismic excitation. The notable contribution of the foundation rocking into the lateral displacement of the adopted superstructure was observed in this study. As displayed in Figure 3.26, Case I, in agreement with Figures 3.24 and 3.25, underwent the highest lateral displacements, e.g. about 750 mm at the top level (roof), compared to the rest. Sözen (1981) proclaimed that an inter-story drift of

0.5% is acceptable to almost any critic, experienced by Case V, displayed in Figure 3.26. Nonetheless, the expected percentages of the structural damage according to Equation (3.21), proposed by Sözen (1981), wherein DR_{tt} is the total inter-story drift ratio of the story level of interest in percentage, were 21%, 18%, and 12% for Case I, Case II, and Case III, respectively.

$$\%\ of\ Damage = 50DR_{tt} - 25 \tag{3.21}$$

3.5 Summary

Several numerical models were developed to probe the possible influences of the shear wave velocity of the soils on the seismic performance of the high rise superstructures. In that regard, a 20-story reinforced concrete moment-resisting building was adopted, which was an example of the typical high rise buildings in the relatively high-risk earthquake-prone zones. The soil shear wave velocity profile, derived from the field and/or laboratory tests, is commonly used to determine the weighted average shear wave velocity in order to carry out the seismic site classification as per the seismic codes and standards (e.g., AS1170.4, 2007; ASCE7-16, 2016). The design and practicing engineers also on a daily basis employ the weighted average shear wave velocity for the estimation of the small-strain shear modulus (G_0), which is the core soil dynamic property, involved in the geotechnical earthquake engineering applications. This study, however, divulged that G_0 must be estimated according to the shear wave velocity profile at the construction site. It is important to note that the 2% life safety drift limit, reported by FEMA273 (1997), was surpassed by the predicted inter-story drift ratio of 2.5% only when employing the in-situ profile of the shear wave velocity in this study for the seismic SSI analysis. Quite differently, the small-strain shear modulus, estimated as to the weighted average shear wave velocity, ignorantly predicted the safe state for the adopted high rise building herein during the applied earthquake. In reference to the inevitable role of the shear wave velocity, demonstrated by this study in the seismic SSI application, the change in

the shear wave velocity ought to be taken into account due to the variation of the soil moisture content, said otherwise, the change in the degree of saturation. This research study shed light on the term “seasonality of earthquake” since the changes in the degree of saturation of the soil owing to a sequel of the natural and artificial wetting-drying cycles could highly impact the extend of the damage on the superstructures. Note that dismissing the effect of degree of saturation on the shear wave velocity and corresponding small-strain shear modulus would potentially overlook the shift of the seismic performance level from the life safety state to the near collapse damage level or even the collapse state owing to not accurately capturing the surge in the overall lateral displacements of the superstructures on a mat foundation.

To assess the seismic response of the soil-structure systems, selecting the appropriate soil constitutive models’ parameters is of great importance. Performing the fully nonlinear analysis of the developed soil-foundation-structure models in the time domain, adopting the direct method of analysis via FLAC3D in this study, disclosed that the predictions of the seismic performance associated with the superstructures can be significantly impacted if the simply assumptive parameters, presented in the literature, are employed without due scrutiny. Taking the Hyperbolic Hardening with Hysteretic Damping (H2-HD) model, as a representative of the advanced hardening plasticity-based soil constitutive models, it was concluded that the relation between the hyperbola and Mohr-Coulomb failure criterion has a major contribution to the predictions of the seismic responses of a building, considering the soil-structure interaction.

CHAPTER 4

EFFECTS OF CHOICE OF SOIL CONSTITUTIVE MODEL ON SEISMIC PERFORMANCE OF MOMENT-RESISTING FRAMES EXPERIENCING FOUNDATION ROCKING SUBJECTED TO NEAR-FIELD EARTHQUAKES

4.1 General

The current study investigated the extent to which the choice of the soil constitutive models can impact the predicted seismic performance of a 20-story reinforced concrete moment-resisting building with a mat foundation considering the Seismic Soil-Structure Interaction (SSSI). Since the soil, in general, is the weakest material, involved in the commonplace geotechnical engineering projects, a soil constitutive model would be able to rule the dynamic response of the system. In this research, the hardening plasticity-based soil constitutive model, named "hyperbolic hardening with hysteretic damping", in conjunction with the two simple, conventional soil models, namely, the isotropic elastic with hysteretic damping model, and elastic-perfectly plastic Mohr-Coulomb with hysteretic damping model, were invoked in the three-dimensional coupled soil-structure numerical simulations using FLAC3D software. The direct method of analysis was used for analyzing the soil-foundation-structure system in one single step without a need to separately analyze each part of the domain. The cherry-picked

earthquake excitations, viz, the 1999 Chi-Chi (Taiwan) and 2011 Kohriyama (Japan) earthquakes, were scaled by means of the widely-used response spectrum matching method as per the design response spectrum of a strong rock. The plastic moment concept was employed so as to assign the elastic-perfectly plastic model to the superstructure and its foundation. Additionally, the strain-compatible shear modulus and damping dependency on the cyclic shear strain were considered via the programmed hysteretic damping algorithm. The numerical predictions included the response spectra at the seismic bedrock and ground surface, base shear forces, shear force distributions along the building height, maximum and permanent foundation displacements, and foundation rocking, plus the flooring lateral deflections and inter-story drifts. The life safety limits for the transient and residual total inter-story drift ratios were not met whilst considering the soil pre-failure plasticity. The concluded remarks herein on the significant effects of the soil hardening plasticity on the seismic performance of the adopted 20-story moment-resisting frame would be applicable to the other structures on a mat foundation, potentially experiencing the foundation rocking amidst the earthquakes.

4.2 Development of 3D Numerical Model

FLAC3D, adopted in this study, is the explicit finite difference program, being used in the engineering mechanics computation (Itasca, 2012). The details of the structural elements, adopted soil constitutive models, interface element, and boundary conditions are explained in the following sections. The last sector hinges around how the picked earthquake excitations were scaled by means of the response spectrum matching method.

4.2.1 Characteristics of Superstructure and Mat Foundation

In the current study, a three-dimensional, 20-story (60 m height), 3-span (12 m length) code-conforming (AS/NZS1170.1, 2002; AS1170.4, 2007; AS3600, 2009) reinforced concrete

moment-resisting building frame was designed in line with the construction norms using SAP2000 (CSI, 2016) through the advanced nonlinear time history analysis. The adopted building was an example of the typical high rise buildings in the relatively high-risk earthquake-prone zones. The $P-\Delta$ effect was taken into consideration in FLAC3D by activating the large-strain mode. The grid point coordinates were updated at each step, in the large-strain mode, according to the computed displacements. In addition, the cracking of the structural elements, in the design stage, should be controlled for a concrete structure to be serviceable. To build upon that, the second moment of the area associated with the uncracked sections were multiplied by the modification coefficients attributed to the slabs, beams, and columns, i.e., 0.25, 0.35, and 0.7 (taken from ACI318 (2014)), consecutively. It should be noted that the thickness of the concrete slabs was 0.25 m. Besides, the local damping coefficient ($\alpha_L = \pi D$ (Itasca, 2012)) of 0.157, engendering 5% damping (D), suggested by FEMA-P-1050-1, 2015, was herein considered for the building and foundation so as to capture the hysteretic behavior.

The elastic-perfectly plastic model was assigned to the superstructure elements in acknowledging the fact that the elastic analyses of the structures, subjected to the seismic actions, do not always predict the hierarchy of the failure mechanisms, as mentioned by Katsanos et al. (2010). In this context, the limiting plastic moment ($M^p = \sigma_y \left(\frac{\omega l^2}{4}\right)$, where ω and l are the width and height of the element cross-section, respectively, and σ_y is the yield stress of the material) allowed the possible gradual plastic deformation of the adopted structure during the applied earthquakes in the current study. As Han and Chen (1985) pointed out, the yield stress of the concrete material (σ_y) at the failure could be assumed to be equal to the compressive strength of the concrete (f_c'). Referring to AS3600 (2009), the modulus of the elasticity of the concrete was determined to be 3.01×10^{10} N/m^2 based on the concrete compressive strength of 32 MPa (i.e., Grade 32). Note that the Poisson's ratio was assumed to

be 0.2. Figure 4.1 lays out an overview of the 20-story superstructure and its mat foundation.

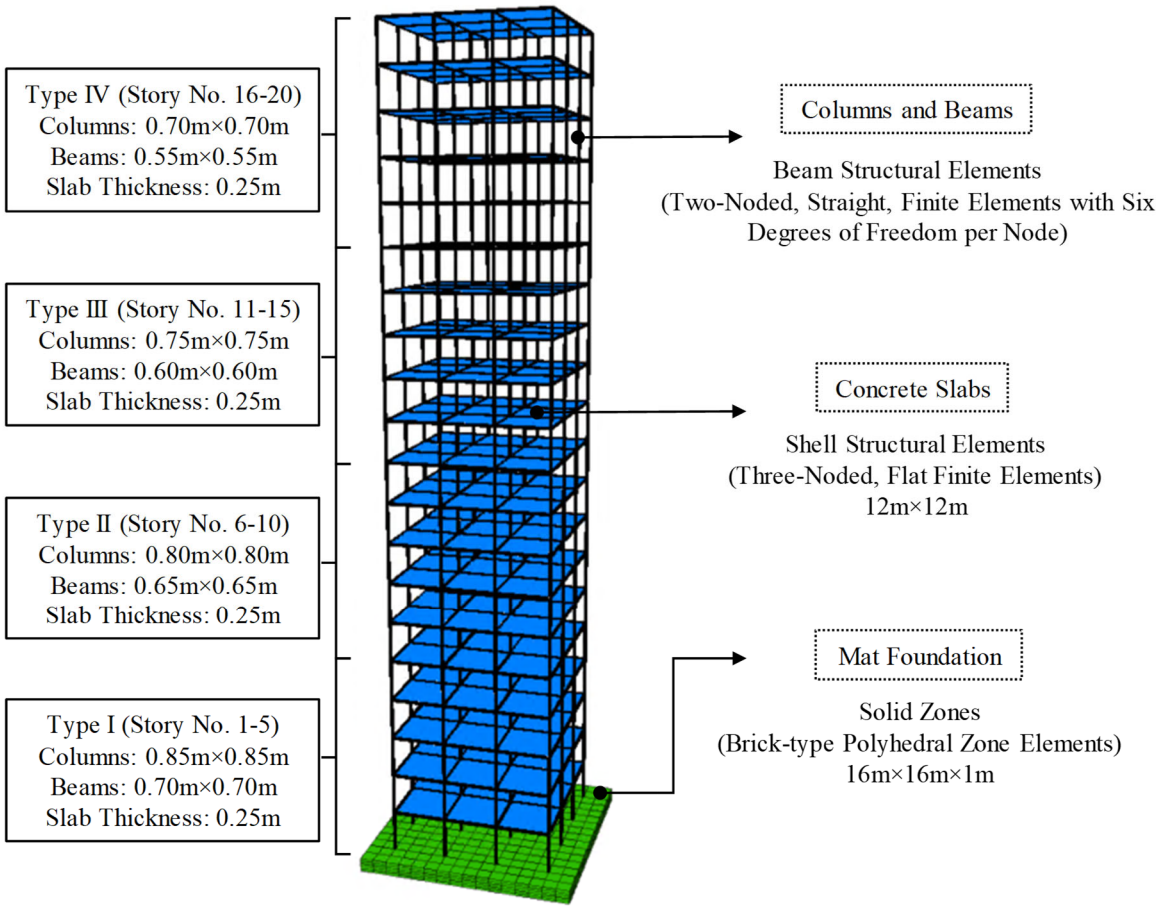

Figure 4.1 Details of designed structural sections of 20-story moment-resisting building and foundation

Following AS2870 (2011), the designed building foundation (see Figure 4.1) had a thickness of 1 m and a width of 16 m. It was modeled by the use of the solid zones with the purpose of considering its significant thickness. The bulk modulus, shear modulus, and mass density of the mat foundation were equal to 1.67×10^{10} N/m^2, 1.25×10^{10} N/m^2, and 2400 kg/m^3, respectively, for the same grade and yield stress of the concrete, explained above for the building. Moreover, the elastic-perfectly plastic model, adopted in this study, controlled any inelastic behavior, occurring in the foundation body. It should be noted that the bearing capacity of the mat foundation, subjected to the building gravity loads, satisfied the minimum required factor of safety (FOS) of 3, estimated based on the Meyerhof method (Meyerhof, 1963).

4.2.2 Description of Adopted Hyperbolic Hardening with Hysteretic Damping

The soil constitutive model, capturing the elastic-perfectly plastic response via adopting the well-established Mohr-Coulomb yield condition, popular among the practicing engineers, is oftentimes used in the seismic research studies (e.g., Arablouei et al., 2011; Isam et al., 2012). Thus, only the detailed description of the Hyperbolic Hardening with Hysteretic Damping (H2-HD) model is delivered in this section.

According to Zytynski et al. (1978), most of the natural soil deposits are overconsolidated to some degree such that their initial behavior when subjected to any loadings is quasi-elastic. In this study, the incremental expression of the Hooke's law, similar to the UBCSAND soil constitutive model, proposed by Puebla (1999), in terms of the principal stresses and strains, was adopted so as to describe a non-dissipative deformation mechanism. Referring to the Hardening Soil (HS) model (proposed by Schanz et al. (1999)) and UBC3D model (introduced by Petalas and Galavi (2013)), the shear yield function (based on the Mohr-Coulomb failure criterion) and volumetric yield function (for the sake of simplicity, a vertical line on a plot of $p' - q$, being used in the different geotechnical projects (e.g., Jenck et al., 2009; Abdelouhab et al., 2011)), referred to as f_q and f_p, are formulated in Equations (4.1) and (4.2), respectively. In addition, the volumetric (g_p) and shear (g_q) potential functions, capturing the associated flow rule and a non-associated flow rule due to the dilation, are as reported in Equations (4.2) and (4.3), consecutively.

$$f_q = \left(\frac{6sin\varphi^{mob}}{3 - sin\varphi^{mob}}\right)p' - q + \left(\frac{6cos\varphi^{mob}}{3 - sin\varphi^{mob}}\right)\left(c' \frac{cot\varphi'_f}{cot\varphi^{mob}}\right) \tag{4.1}$$

$$f_p = g_p = p' \tag{4.2}$$

$$g_q = \left(\frac{6sin\psi^{mob}}{3 - sin\psi^{mob}}\right)p' - q \tag{4.3}$$

where, φ^{mob} and ψ^{mob} are the mobilized (developed) friction and dilation angles, respectively, q is the deviatoric stress, and c' is the ultimate effective cohesion.

Referring to DiMaggio and Sandler (1971) and Liu et al. (2005), initially, the cap model was only developed for the sands and now has been resourcefully extended to the clays and rocks. In H2-HD, the soil volumetric behavior was captured by a power law, which is as Equation (4.4) (Duncan et al., 1980), in the isotropic compression condition.

$$K = \frac{dp'}{d\varepsilon_v} = K^{ref}(\frac{p'}{p^{ref}})^{\kappa_1} \tag{4.4}$$

where, K is the bulk modulus, $dp'/d\varepsilon_v$ is the loading tangent modulus, K^{ref} is the slope of the laboratory curve in an isotropic consolidation test for the mean effective stress (p') versus the volumetric strain (ε_v) at the reference mean effective stress (p^{ref}), and κ_1 is an empirical exponent, which is usually in the range of 0.5-1 and 0.9-1 for the sands and clays, consecutively, reported by Von Soos and Bohac (2002).

The cap pressure (p^{cap}) in the H2-HD soil model, defining the updated position of the cap yield surface amidst the analysis, equaled the maximum of the mean effective stress (p'), i.e., the current stress state, and the preconsolidation pressure. Since the slopes of the λ-line, i.e., the compression index, and κ-line, i.e., the recompression index, are the soil constants from a consolidation test, a constant parameter K_M was simply defined as a ratio of the elastic bulk modulus ($K_c = dp^{cap}/d\varepsilon_v^e$) to the plastic bulk modulus ($K_p = dp^{cap}/d\varepsilon_v^p$), i.e., the hardening modulus, in the isotropic compression condition. Hence, Equation (4.5) represents $K_c = K_M.dp^{cap}/d\varepsilon_v^p$, where $K_M = d\varepsilon_v^p/d\varepsilon_v^e = (\lambda/\kappa) - 1$ is named "elasto-plastic bulk multiplier". Combining Equations (4.4) and (4.5) results in the determination of p^{cap} in terms

of ε_v^p, reported in Equation (4.6), which was adopted through a coded subroutine (cptable) in this study.

$$K_c = (1 + K_M)K^{ref}(\frac{p^{cap}}{Pref})^{\kappa_1} \tag{4.5}$$

$$p^{cap} = p^{ref}[(1-n)(\frac{1+K_M}{K_M})(\frac{K^{ref}}{p^{ref}})\varepsilon_v^p]^{\frac{1}{1-\kappa_1}} \tag{4.6}$$

Considering the Rowe stress-dilatancy theory (Rowe, 1962), the relationship between the rate of the plastic volumetric strain ($\dot{\varepsilon}_v^p$) and plastic shear strain ($\dot{\varepsilon}_s^p$) would be $\dot{\varepsilon}_v^p = (sin\psi^{mob})\dot{\varepsilon}_s^p$. Referring to Schanz and Vermeer (1996) and the above-mentioned shear hardening flow rule, Equation (4.7) could be obtained.

$$sin\psi^{mob} = \frac{sin\varphi^{mob} - \frac{sin\varphi_f' - sin\psi_f}{1 - sin\varphi_f'.sin\psi_f}}{1 - sin\varphi^{mob}.\frac{sin\varphi_f' - sin\psi_f}{1 - sin\varphi_f'.sin\psi_f}} \tag{4.7}$$

where, ψ_f and φ_f' are the failure dilatancy and failure effective friction angle, respectively. In this study, the variations of the mobilized dilation angle in terms of the plastic shear strain through Equation (4.7), was coded using the relevant subroutine (i.e., dtable).

Beaty and Byrne (1998) affirmed that the elastic response, generally, is much stiffer than the plastic behavior, causing the relatively little impact on the shape of the hyperbolic shear stress-strain response. Thus, the hyperbolic hardening rule, given in Equation (4.8) (Byrne et al., 2003), inspired by the original work conducted by Duncan and Chang (1970), was used to represent the mobilized stress ratio (η^{mob}) versus the plastic shear strain (ε_s^p). Moreover, Equation (4.9), capturing the frictional hardening similar to the UBCSAND model, presented by Byrne et al. (2003), was adopted. A subroutine, named "ftable", was programmed to record the variations of the mobilized friction angle with the plastic shear strain as per the substitution

of G_m^p in Equation (4.8) by Equation (4.9). Similarly, the mobilized cohesion was correlated to the plastic shear strain using $c^{mob} = c' \frac{cot\varphi_f'}{cot\varphi^{mob}}$ via an appropriate subroutine (i.e., ctable).

$$d\eta^{mob} = d(sin\varphi^{mob}) = \frac{q}{p'} = \frac{G_m^p}{p'} d(\varepsilon_s^p) \tag{4.8}$$

$$G_m^p = \beta G_c (1 - \frac{sin\varphi^{mob}}{sin\varphi_f} R_f)^2 = \beta G_c (1 - \frac{\eta^{mob}}{\eta_f} R_f)^2 \tag{4.9}$$

In the preceding formulae, G_m^p is the mobilized plastic shear modulus. Furthermore, G_c is the elastic tangent shear modulus, whose initial value (G_{c_i}) (Figure 4.2b), in the developed numerical simulation, was calculated based on the in-situ velocity of the shear wave ($V_{s,i}$) (Figure 4.2a), propagating through the soil elements, inducing the small-strain shear modulus ($G_0 = G_{max} = \rho {V_{s,i}}^2$, where ρ is the soil mass density). It should be noted that the variations of G_c with the mean effective stress were captured in this study following Equation (4.10), consistent with the previously conducted studies by Duncan et al. (1980). Indeed, in Equation (4.10), G_c^{ref} is the elastic tangent shear modulus at the reference mean effective stress (p^{ref}). Moreover, the key factor in employing the hyperbola in the H2-HD soil model was its asymptote position, also known as "ultimate stress ratio", i.e., $\eta_{ult} = \eta_f / R_f$. The stress ratio at the failure (η_f) abided by the Mohr-Coulomb failure law, denoting the occurrence of the perfectly plastic behavior prior to reaching the said asymptote in view of the fact that R_f is the failure ratio, always smaller than 1.0, whilst a typical value, used in many cases, is 0.9, reported by Duncan et al. (1980). In Equation (4.9), β, as a user-defined dimensionless calibration factor, is called the elastic-plastic coupling coefficient. β was estimated by relating the plastic modulus at a low level of the stress ratio, i.e., $\eta \approx 0$, to the small-strain shear modulus.

$$G_c = G_c^{ref} (\frac{p'}{p^{ref}})^{\kappa_1} \tag{4.10}$$

4.2.3 Adopted Soil Parameters in Numerical Model

It is perceived that the majority of the seismic codes (e.g., AS1170.4, 2007; ASCE7-10, 2010) considered the top 30 m of the soil profile for the site classification since the amplification and/or attenuation of the earthquake waves occur in the aforesaid depth. Therefore, the three soil models, including the isotropic Elastic with Hysteretic Damping (E-HD) model, elastic-perfectly plastic Mohr-Coulomb with Hysteretic Damping (MC-HD) model, and Hyperbolic Hardening with Hysteretic Damping (H2-HD) model, were assigned to the 30 m deep clayey sand soil with the USCS symbol of SC. The soil deposit, modeled in this study, was categorized as the stiff soil, i.e., the site class D as to ASCE7-10 (2010), on the basis of the weighted average shear wave velocity, i.e., 350 m/s, estimated from Figure 4.2a. The soil properties for the adopted soil constitutive models are summarized in Table 4.1, which were extracted from the actual in-situ and laboratory tests, published by Rahvar (2006). It needs to be underlined that the H2-HD model, inspired by the UBCSAND soil constitutive model, introduced by Puebla (1999), was verified for the soil dynamics field via the centrifuge and numerical modeling plus the element testing by Beaty and Byrne (1998), Byrne et al. (2003), and Byrne et al. (2004).

The overconsolidation ratio (OCR) profile, portrayed in Figure 4.2c, was estimated as $OCR = \sigma'_{pc}/\sigma'_v$ based on the calculation of the vertical preconsolidation pressure (σ'_{pc}), suggested by Urbaitis et al. (2016), for the given geostatic initial vertical effective stress (σ'_v) and small-strain shear modulus (G_0). The in-situ stress states were captured based on the overconsolidated K_0 coefficient ($K_{0(oc)}$) in compliance with the OCR profile. It is of interest to notice that the primary position of the cap yield surface in the employed H2-HD model was based on the initial cap pressure (p_i^{cap}), equal to the initial preconsolidation pressure. The product of OCR and the mean effective stress, demonstrating the current stress state in the soil medium, resulted in the initial preconsolidation pressure. Figure 4.2d shows the adopted

undrained shear strength profile of the soil of interest.

Table 4.1 Adopted soil parameters for E-HD, MC-HD, and H2-HD soil constitutive models

Parameter	Symbol	Unit	Value or Description	
Soil Classification (USCS)	SC	---	Clayey Sand	Clayey Sand
Depth Range	---	m	0-30	0-30
Adopted Soil Constitutive Model	---	---	E-HD MC-HD	H2-HD
Soil Mass Density	ρ	kg/m^3	1900	1900
Soil Poisson's Ratio	ν	---	0.3	0.3
In-Situ Shear Wave Velocity$_{@\text{Reference Point}}$	$V_{s,i}$	m/s	250	250
Small-Strain Shear Modulus$_{@\text{Reference Point}}$	G_0	MPa	119	119
Elastic Bulk Modulus$_{@\text{Reference Point}}$	K_c	MPa	258	---
Initial Elastic Bulk Modulus$_{@\text{Reference Point}}$	K_{c_i}	MPa	---	258
Reference Mean Effective Stress$_{@\text{Reference Point}}$	p^{ref}	kPa	---	117
Overconsolidated K_0 Coefficient$_{@\text{Reference Point}}$	$K_{0(OC)}$	---	---	0.8
Overconsolidation Ratio$_{@\text{Reference Point}}$	OCR	---	---	2.5
Isotropic Tangent Bulk Modulus$_{@\text{Reference Point}}$	K^{ref}	MPa	---	56
p^{ref}-related Elastic Shear Modulus$_{@\text{Reference Point}}$	G_c^{ref}	MPa	---	160
Initial Cap Pressure$_{@\text{Reference Point}}$	p_i^{cap}	kPa	---	293
Failure Effective Friction Angle	φ_f'	°	35	35
Ultimate Effective Cohesion	c'	kPa	20	20
Failure Dilation Angle	ψ_f	°	5	5
Stress Dependency Exponent	κ_1	---	---	0.9
Failure Ratio	R_f	---	---	0.9
Failure Stress Ratio	η_f	---	---	0.57
Ultimate Stress Ratio	η_{ult}	---	---	0.64
Elastic-Plastic Coupling Coefficient	β	---	---	0.35
Compression Index	λ	---	---	0.13
Recompression Index	κ	---	---	0.021
Elasto-Plastic Bulk Multiplier	K_M	---	---	5.2
Hardening Tables	---	---	---	$ftable$ $ctable$ $dtable$
Cap Pressure Table	---	---	---	$cptable$
Calibrated Parameters for Hysteretic Damping	L_1	---	-3.20	-3.20
	L_2	---	1.05	1.05

*Reference Point: Depth of 7.3 m from ground level (see Figure 4.2).

4.2.4 Adopted Hysteretic Damping Algorithm for Soil

The hysteretic behavior of the soil, governed by the unloading-reloading response, taking into account the stiffness degradation, can capture the energy dissipation during the cyclic loading in the absence of the plastic flow. Such an energy loss, which is essentially required to be considered in SSSI, as stated by Ambrosini (2006), would be obtained by utilizing the Masing

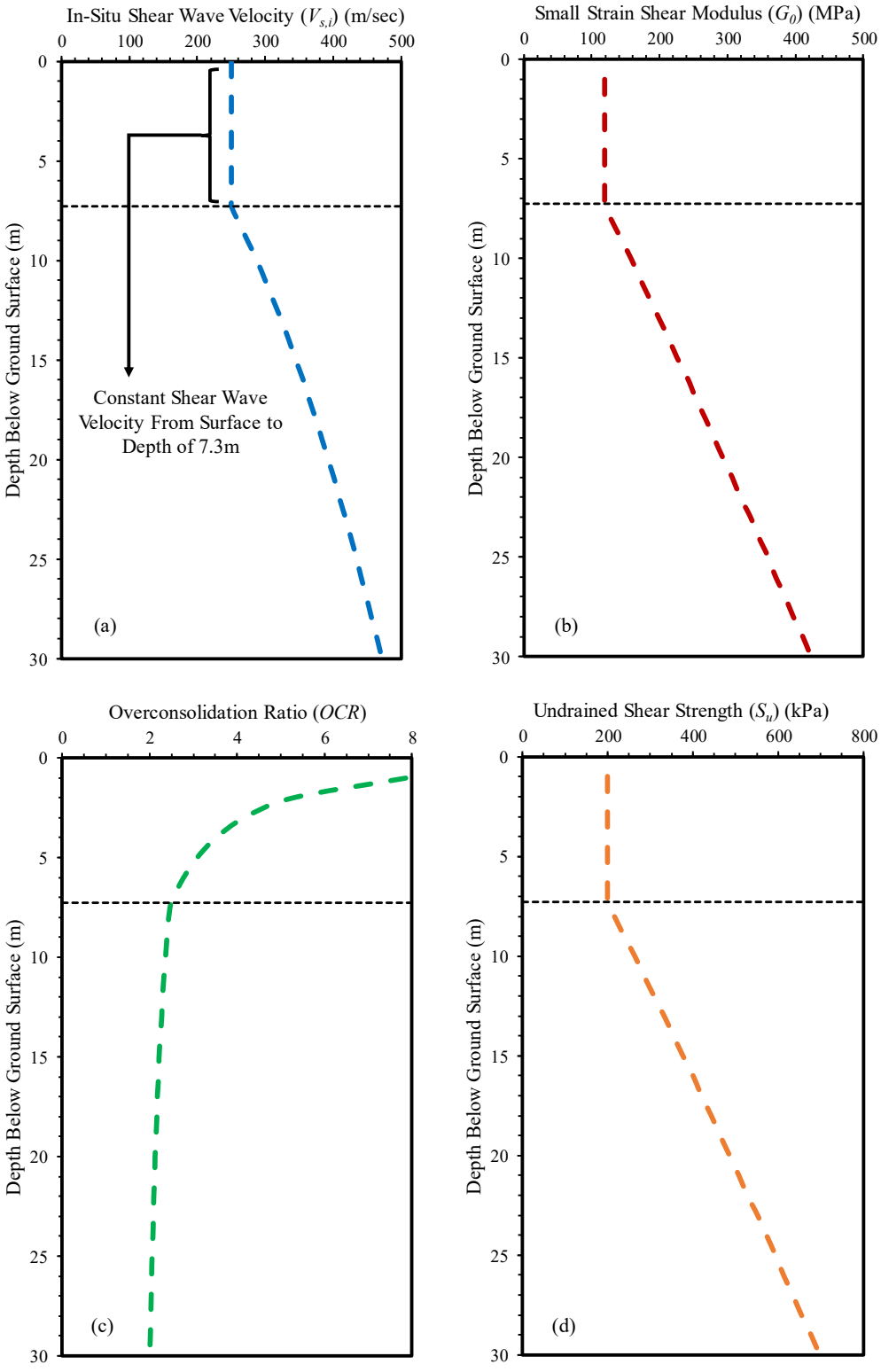

Figure 4.2 Adopted soil properties profiles: (a) in-situ shear wave velocity ($V_{s,i}$), (b) small strain shear modulus (G_0), (c) overconsolidation ratio (OCR), and (d) undrained shear strength (S_u)

rules (Masing, 1926) and a backbone curve in the stress state that no plastic flow is applicable. In this study, the soil backbone curves were adopted by $\bar{\tau}/\gamma = M_s$ and the nonlinear

incremental constitutive relation, i.e., $G_0 M_t$. Note that $\bar{\tau}$, γ, M_s, and M_t are the normalized shear stress, cyclic shear strain, normalized secant modulus reported in Equation (4.11) (Itasca, 2012), and normalized tangent modulus (Equation (4.12) (Itasca, 2012)). In Equation (4.11), used to plot the degradation curve, shown in Figure 4.3a, L_1 and L_2 are the extreme values of the logarithmic strains, i.e., the values at which the tangent slopes become zero, and L is the logarithmic strain, i.e., $L = \log_{10} \gamma$.

$$M_s = [\frac{L_2 - L}{L_2 - L_1}]^2 (3 - 2\left[\frac{L_2 - L}{L_2 - L_1}\right]) \tag{4.11}$$

$$M_t = \frac{d\bar{\tau}}{d\gamma} = M_s + \gamma \frac{dM_s}{d\gamma} \tag{4.12}$$

As can be seen in Figures 4.3a and b, the adopted S-shaped curve, represented by Equation (4.11), and its corresponding damping ratio curve were adequately congruent with the ones, proposed by Seed and Idriss (1970). The curve fitting parameters (L_1 and L_2), equal to -3.20 and 1.05, respectively, were derived through trial and error associated with analyzing a one-zone sample of the soil of interest at the several cyclic strain levels followed by comparing the obtained trends of the modulus reduction and damping ratio with the reference ones, taken from Seed and Idriss (1970). Summary of the calibrated parameters, required for the hysteretic damping model, could be also found in Table 4.1.

4.2.5 Interface Element and Boundary Conditions

The interface element, adopted in the current study, between the mat foundation and underlying soil, with the zero thickness simulating the frictional contact referring to Yu et al. (2015), was represented by the two springs and a slider. The normal stiffness (K_n) and shear stiffness (K_s), shown in Figure 4.4b, were set to ten times the equivalent stiffness of the neighboring zone in order to minimize the influence of the interface stiffness on the system compliance, as suggested by Hokmabadi and Fatahi (2016). The interface stiffnesses were

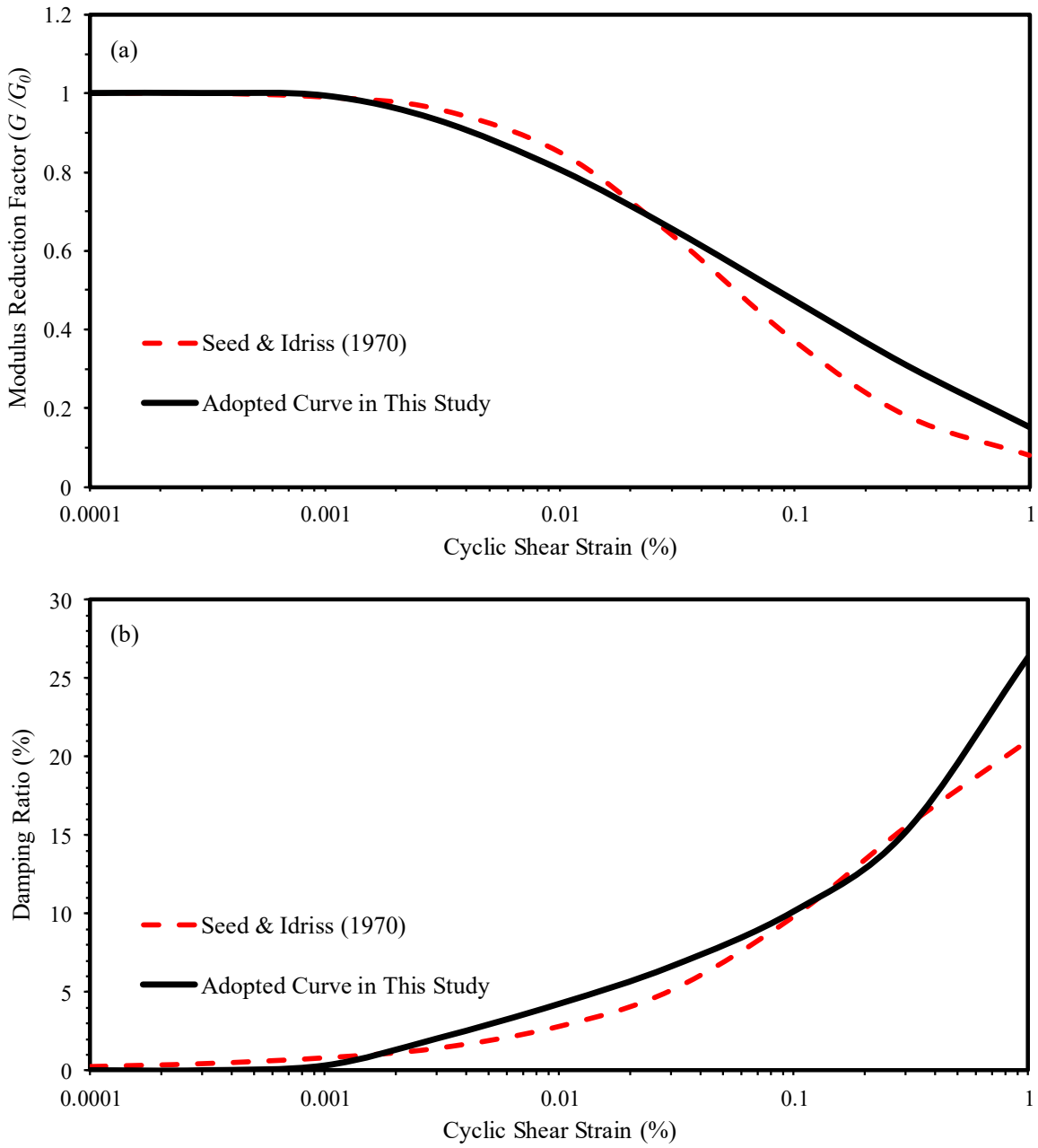

Figure 4.3 Adopted soil modulus degradation curve and corresponding damping ratio curve (data taken from Seed and Idriss (1970)): (a) relation between G/G_0 and cyclic shear strain, and (b) relation between corresponding material damping ratio and cyclic shear strain

added to the accumulated stiffnesses at the grid points on both sides of the interface, including the surfaces of the concrete foundation and soil deposit, so as to maintain the numerical stability. The shear strength of the interface was defined on the basis of the Mohr-Coulomb criterion to allow the possible foundation sliding during the analysis. It should be noted that the tensile strength of the interface was set to zero to capture any possible separation or gapping

between the foundation and surrounding soil.

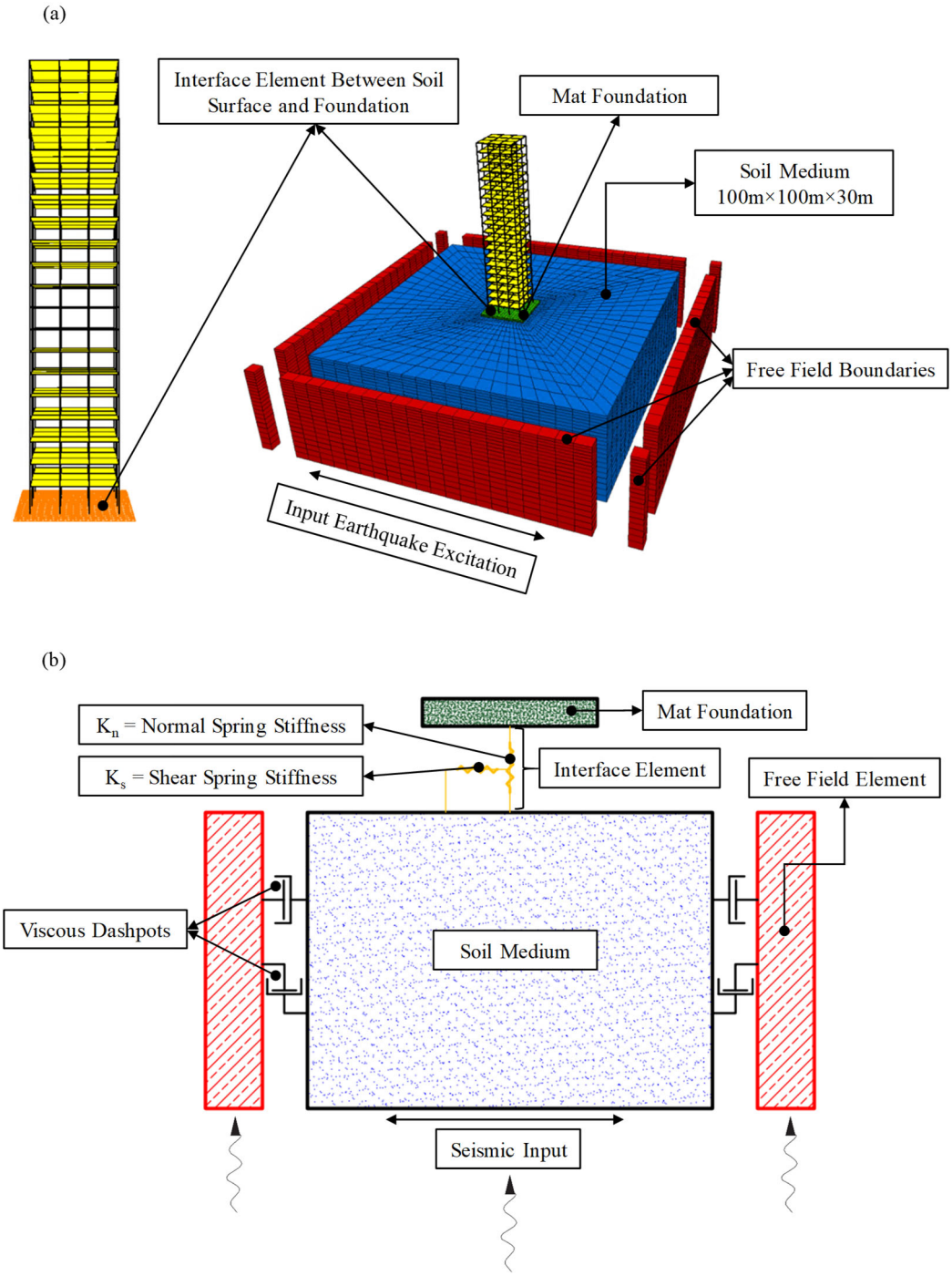

Figure 4.4 Integrated soil-foundation-superstructure interaction system foregrounding boundary conditions, interface element, numerical grids, and input earthquake motion: (a) user-visible numerical model in FLAC3D, and (b) internal facets of numerical model in FLAC3D

In the static mode of this study, in which the system was only under the gravity loads, the base of the model was fixed in all the translational directions whereas the side boundaries were fixed only in the horizontal directions. In the seismic analyses of this study, reducing the wave

reflections at the side artificial boundaries as much as possible was taken into account by imposing the resistant tractions (t_n and t_s) at every timestep on the side grid points in the main grids. The independent viscous dashpots referring to Lysmer and Kuhlemeyer (1969) as depicted in Figure 4.4b, introducing the absorbing boundary condition, in the normal and shear directions ($t_n = -\rho C_p v_n$ and $t_s = -\rho C_s v_s$, wherein ρ is the soil mass density, C_p is the p-wave velocity, C_s is the s-wave velocity, and v_n and v_s are the normal and shear components of the velocity at the lateral boundary, respectively) were employed.

As the boundary conditions at the sides of the model must account for the free field motions, underscored by Semblat (2011), the numerical model herein contained the main soil medium in combination with the vertical free field soil elements, shown in Figure 4.4b. Together with the aforementioned absorbing boundary condition, the free field soil elements provided the free field boundary condition, presented in Figure 4.4a, simulating the seismic motions, propagating along the edges of the numerical model. Karimi et al. (2018) stated that the soil column in the free field should deform primarily in shear and not in bending. Consequently, a pure shear movement was captured by constraining the free field grids and main grids on the same elevation at the lateral boundaries to move together, implying having the same degrees of freedom. In this present study, such a one-dimensional wave propagation within the free field elements, acting like an infinite boundaries, was enforced by converting the free field motion into the total boundary tractions (T_n and T_s), applied to the main soil medium according to Equations (4.13) and (4.14).

$$T_n = \sigma^{ff} - \rho C_p (v_n - v_n^{ff}) \tag{4.13}$$

$$T_s = \tau^{ff} - \rho C_s (v_s - v_s^{ff}) \tag{4.14}$$

where, v_n^{ff} and v_s^{ff} are the normal and shear components of the velocity of the grid point in the side free field, respectively, σ^{ff} is the free field normal stress, and τ^{ff} is the free field

shear stress.

The superstructure rested on a 30-m deep stiff soil of class D, presented in ASCE7-10 (2010), whose lateral boundaries were, after trial and error, placed at the distance of 100 m from the other pairs in order to minimize the wave reflection, induced by the artificial boundaries, satisfying minimum five times the width of the existing building, suggested by Rayhani and El Naggar (2008), i.e., 60 m. Beyond of that, the soil nonlinearity allowed the considerable amount of the earthquake energy to be dissipated in the adopted 3D model. Additionally, the adopted rigid boundary for simulating of the strong bedrock, demonstrating the large dynamic impedance, i.e., the low velocity sediments sitting on the high velocity bedrock, was in line with the suggestion, put forward by Hatzigeorgiou and Beskos (2010).

4.2.6 Adopted Earthquake Records

The exclusive features of the near-field earthquakes, such as the severity of the damage and cruciality of the responses, reported by Alavi and Krawinkler (2004), contributed to their suitability for assessing the seismic performance of the adopted 20-story moment-resisting superstructure on a mat foundation in the developed soil-structure interaction system under the influence of the soil plasticity. Hence, the two well-known baseline-corrected near-field earthquake accelerations, namely, the 1999 Chi-Chi (Taiwan) and 2011 Kohriyama (Japan) earthquakes, were utilized in this study. Since the lateral boundaries of the main grids were coupled to the free field grids by the viscous dashpots to absorb the outward waves, the seismic excitations were only applied to the base of the model, assuming to be representative of the seismic bedrock, as a common method in the seismic SSI numerical simulations (e.g., Castaldo and De Iuliis, 2014; Karimi et al., 2018). As a consequence, the said earthquake input motions, cherry-picked from the different sites, were scaled to a design response spectrum of a strong rock prior to being horizontally applied at the seismic bedrock.

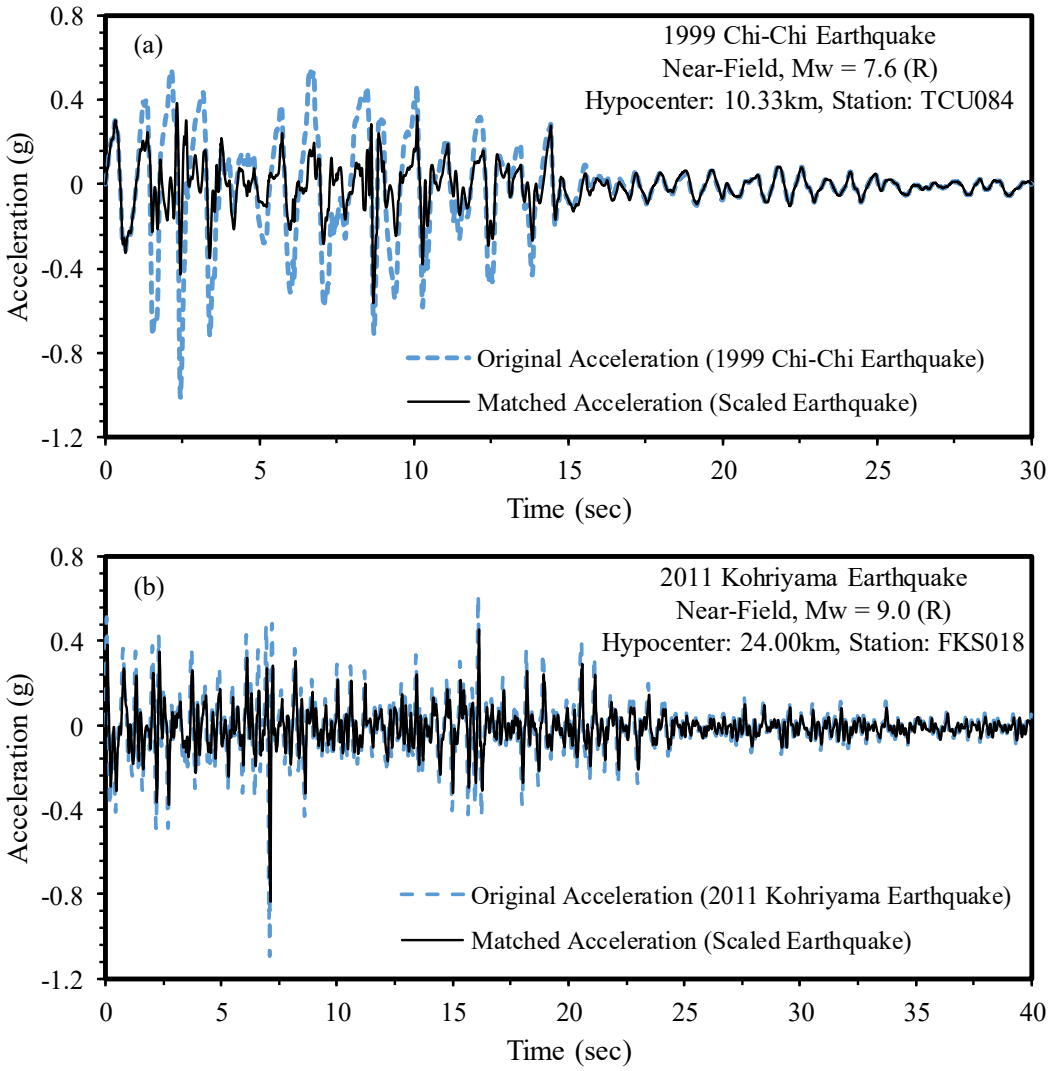

Figure 4.5 Scaled earthquake records from: (a) 1999 Chi-Chi earthquake, and (b) 2011 Kohriyama earthquake

The response spectrum matching, aka "spectral matching", which can be utilized in the framework of both the force-based and performance-based design methods, as pointed out by Katsanos et al. (2010), adjusting the frequency content of an accelerogram till its response spectrum almost matches a target response spectrum with the minimal alteration of the displacement and velocity histories of the record, was adopted in this study using SeismoMatch software (SEISMOSOFT, 2016). The design response spectrum of a strong rock, i.e., the bedrock, as the target response spectrum, had the earthquake hazard factor (Z), equal to 0.6 as the most extreme case presented in AS1170.4 (2007). Given the importance level, equaling 2, and the earthquake annual probability of the exceedance, i.e., 1:500, in accord with the

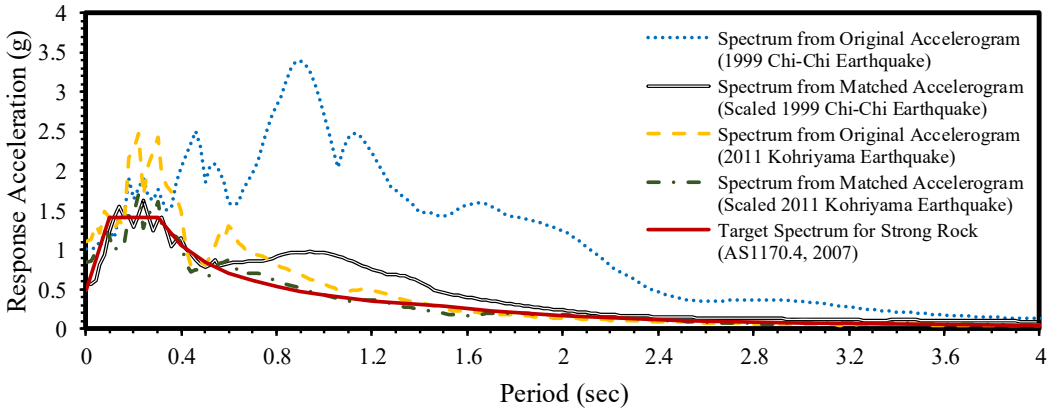

Figure 4.6 Acceleration response spectra of original and matched accelerograms plus target spectrum

prescribed building types in NCC (2016), the probability factor (k_p) was set to 1.0 according to AS1170.4 (2007). Figure 4.5 exhibits the acceleration time histories of the original (TCU084 receiving station - Taiwan) and scaled 1999 Chi-Chi earthquakes plus the original (FKS018 receiving station - Japan) and scaled 2011 Kohriyama earthquakes. As discerned in Figure 4.6, the response spectra attributed to the matched records more or less conformed to the spectrum for the strong rock according to AS1170.4 (2007).

4.3 Results and Discussions

The seismic analyses of the three-dimensional soil-structure interaction numerical models in the time domain, undergoing the scaled 1999 Chi-Chi earthquake and scaled 2011 Kohriyama excitation, were carried out using the direct integration method in FLAC3D. The results, presented and discussed in this section, brought out that the type of the soil constitutive model was a major contributor to the prediction of the seismic response of the case study, considered herein.

4.3.1 Response Spectra and Natural Frequencies

Figures 4.7a and b demonstrate the acceleration response spectra of the bedrock records and recorded ground motions at the foundation level, utilizing a system damping ratio of 5%,

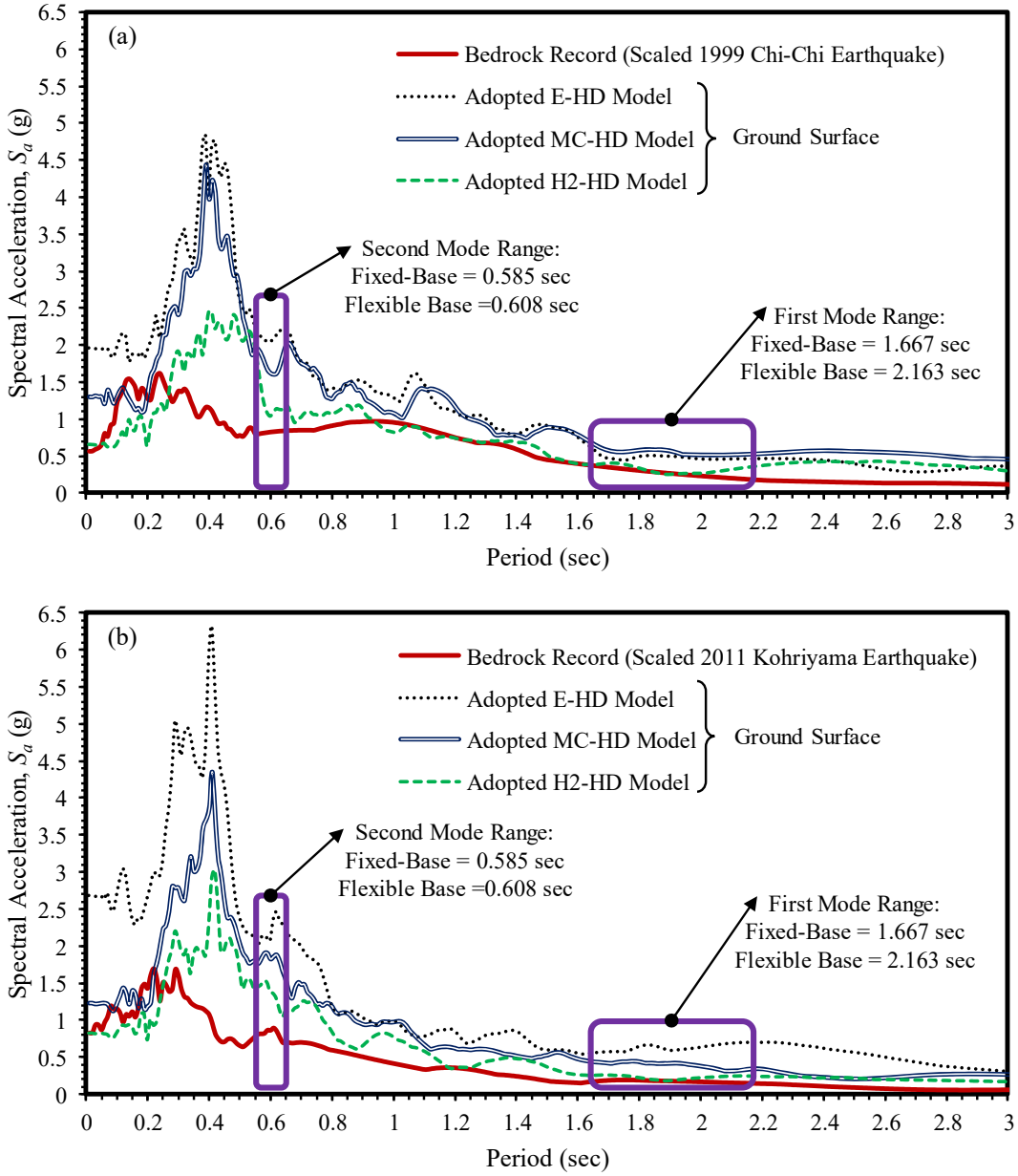

Figure 4.7 Acceleration response spectra, with 5% damping ratio for structure, associated with bedrock records and foundation level motions for adopted soil constitutive models (E-HD, MC-HD, and H2-HD) subjected to: (a) scaled 1999 Chi-Chi earthquake, and (b) scaled 2011 Kohriyama earthquake

recommended by FEMA-P-1050-1 (2015), through the Duhamel integral method. Referring to Figure 4.7, the shift in the period, corresponding to the maximum response acceleration ($S_{a_{max}}$), called "resonance peak period", took place in all the considered models herein. For instance, the resonance peak period of the scaled 1999 Chi-Chi earthquake was 0.24 s as a reading on the horizontal axis in Figure 4.7a, corresponding to 1.6g as the spectral acceleration.

The average period of 0.40 s was observed for the three recorded motions on the ground surface (i.e., 67% increase from 0.24 to 0.40 s). The observed shift in the resonance peak period was tacitly due to the local site effects, soil-structure interaction action, and soil shear stiffness degradation, resulting from the seismically-induced straining in the soil medium.

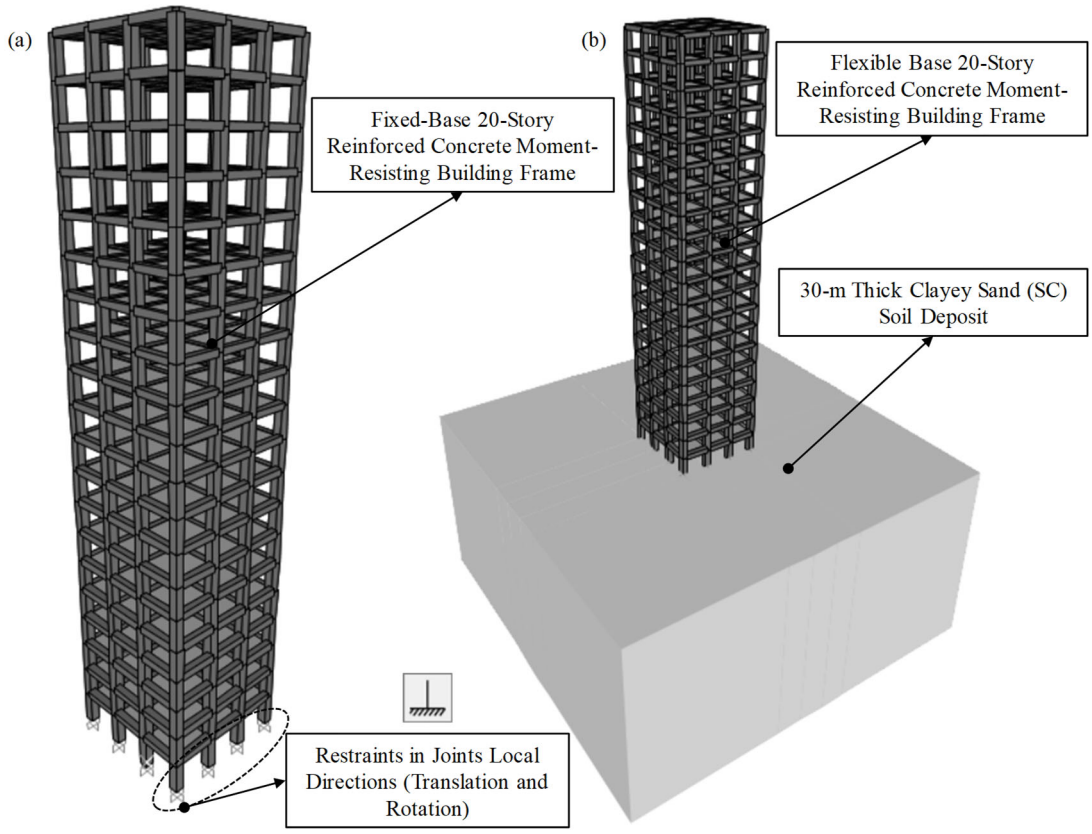

Figure 4.8 Modeling structural frame in SAP2000 for modal analysis: (a) fixed-base building, and (b) flexible base building

Since having the knowledge of the periods attributed to the first and second modes was essential for studying such derived response spectra, the fixed-base and flexible base structural frames of the investigated building were built in SAP2000 (CSI, 2016), portrayed in Figure 4.8. The caption on Figure 4.9 states the deformed shapes of the fixed-base building in its first and second modes of vibration, possessing the frequencies of 0.6 Hz and 1.709 Hz, respectively. The fundamental period of the fixed-base building, i.e., 1.667 s (see Table 4.2), was in a good agreement with the approximate fundamental period values, estimated via the suggested equations for the concrete moment-resisting frames in Eurocode 8 – Part 1 (2004)

($T = 0.075H^{3/4}$) and ASCE7-10 (2010) ($T = 0.0466H^{0.9}$), i.e., 1.617 s and 1.857 s, respectively, considering H as the building height (60 m). It was previously reported by NIST-GCR-11-917-15 (2011) that the second mode period is often bracketed by the one-quarter and one-third of the fundamental period so long as the building frame is regular. Table 4.2 demonstrates the correctness of the said period range for the second mode.

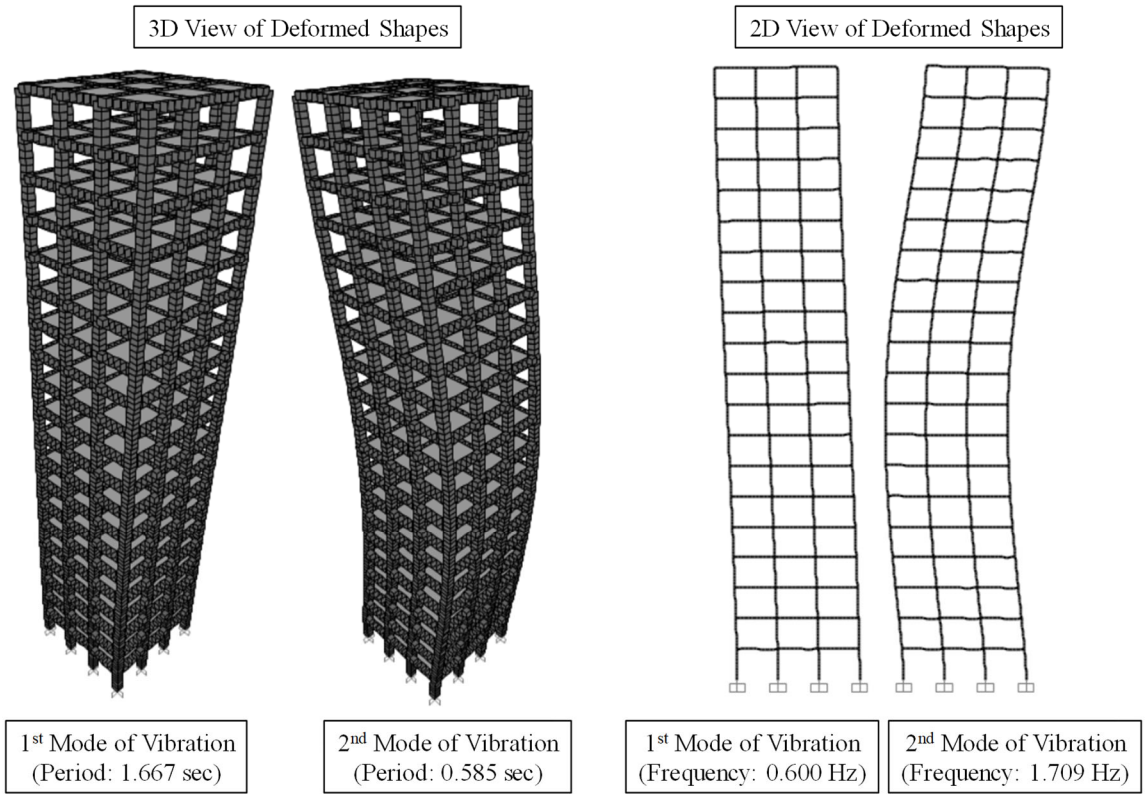

Figure 4.9 2D and 3D representations of structural deformations for first and second modes of vibration in SAP2000 from modal analysis of fixed-base building

Table 4.2 Variations of natural period and frequency of adopted 20-story moment-resisting building in fixed-base and flexible base cases

Building Base Condition	Period (sec)		Frequency (Hz)	
	1st Mode	2nd Mode	1st Mode	2nd Mode
Fixed-Base	1.667	0.585	0.600	1.709
Flexible Base	2.163	0.608	0.462	1.645

As seen in Table 4.2, the surges in the natural periods of the first and second modes from the fixed-base 20-story building to the flexible 20-story superstructure were about 30% (from 1.667 s to 2.163 s) and 4% (from 0.585 s to 0.608 s), respectively. The perceived increases were by reason of the extra degrees of freedom, induced by introducing the soil deposit in the

soil-structure interaction model. The influence of the soil-structure interaction on the fundamental period of a building could be approximated by invoking Equation (4.15), presented by ASCE7-10 (2010), for the structure, supported on the mat foundation, resting at or near the ground surface. The fundamental period of the flexible base building, i.e., 2.163 s, reported in Table 4.2, was in fine accordance with the effective period of the flexible base building ($\tilde{T}$), i.e., 2.377 s, obtained from Equation (4.15).

$$\tilde{T} = T\sqrt{1 + \left(\frac{25\bar{\alpha}r_a\bar{h}}{\bar{V}_{s,i}{}^2T^2}\right)\left(1 + \frac{1.12r_a\bar{h}^2}{\alpha_\theta r_m^3}\right)} \tag{4.15}$$

where, T ($= 0.0466H^{0.9}$) is the fundamental period of the fixed-base building (1.857 s), H is the building height (60 m), $\bar{\alpha}$ ($= \frac{\bar{W}}{\gamma_s A_f \bar{h}}$) is the relative weight density of the structure and underlying soil (0.151), $\bar{W}$ ($= 0.7W_t$) is the effective seismic weight of the building (30 MN), W_t is the total weight of the building (43 MN), γ_s is the unit weight of the soil (18633 N/m^3), A_f is the area of the load-carrying foundation (256 m^2), $\bar{h}$ ($= 0.7H$) is the effective height of the building (42 m), $\bar{V}_{s,i}$ is the weighted average shear wave velocity (350 m/s as per Figure 4.2a), r_a ($= \sqrt{\frac{A_f}{\pi}}$) and r_m ($= \sqrt[4]{\frac{4I}{\pi}}$) are the characteristic foundation lengths (9.027 m and 4.566 m, respectively), I is the static moment of inertia of the load-carrying foundation about a horizontal centroidal axis normal to the direction in which the structure is analyzed (341.3 m^4), and α_θ is the dynamic foundation stiffness modifier for the rocking (unity for $\frac{r_m}{\bar{V}_{s,i}T} < 0.05$).

As reported in Figure 4.7b, the maximum response acceleration changed from 1.7g for the scaled 2011 Kohriyama bedrock input to 6.32g, 4.35g, and 3.02g for the E-HD, MC-HD, and H2-HD models, in the order given. The reasons behind the order of the response spectra were the plasticity-induced damping and nonlinear soil behavior. Both the aforesaid factors were captured by the hyperbolic hardening with hysteretic damping soil model from the onset of the virgin loading. Consequently, the structural base shear diminishment would be expected herein

once employing the H2-HD soil model.

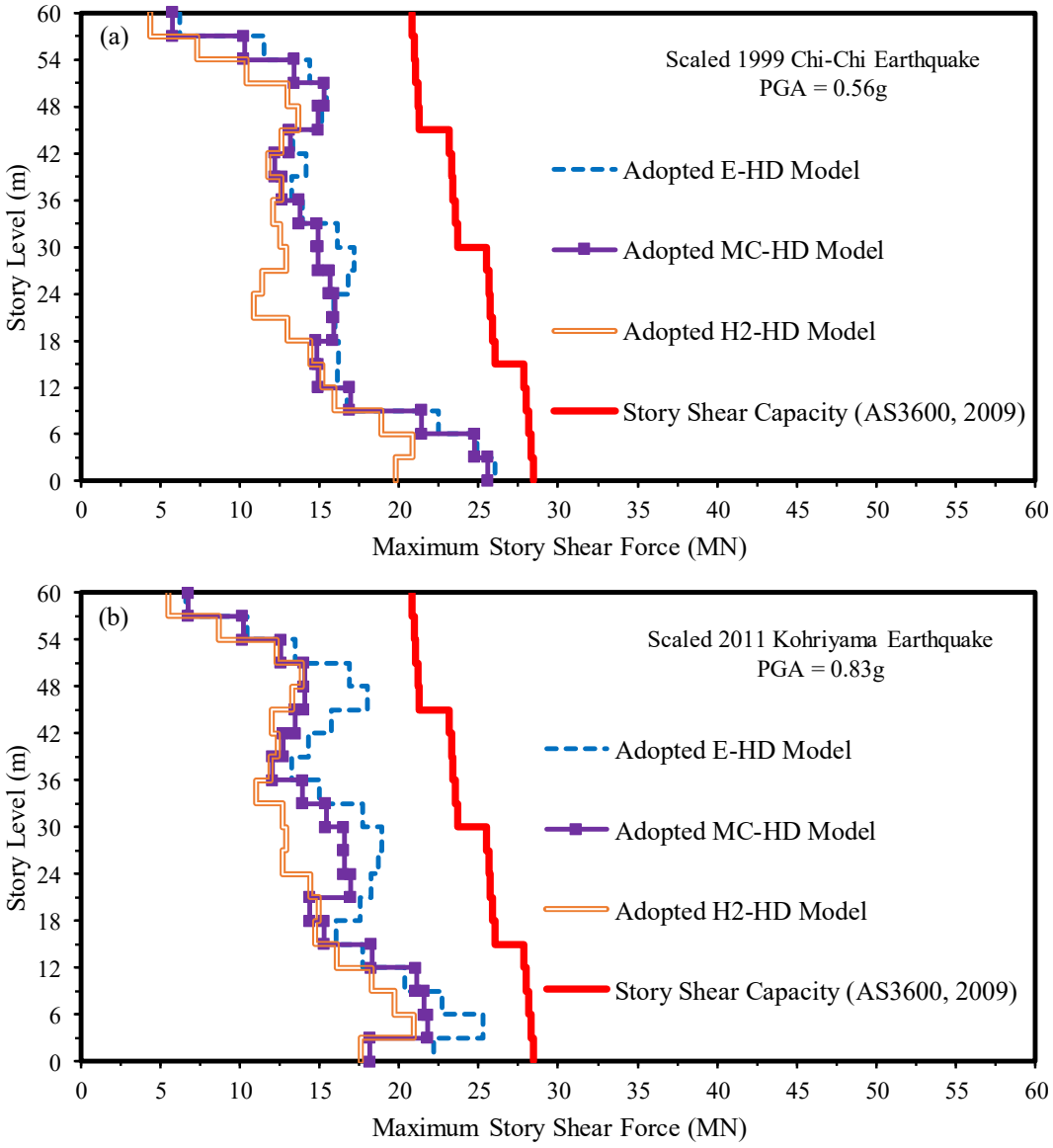

Figure 4.10 Shear force envelope distributions along structure height for adopted soil constitutive models (E-HD, MC-HD, and H2-HD) subjected to: (a) scaled 1999 Chi-Chi earthquake, and (b) scaled 2011 Kohriyama earthquake

4.3.2 Generated Shear Forces in Superstructure

As can be noted in Figures 4.10a and b, the predicted absolute maximum shear forces, while adopting the H2-HD model, were unalike to the corresponding values of the E-HD and MC-HD models. The said disparity took place in the majority of the levels, particularly between Levels 6-12, having the maximum value of about 7 MN. Indeed, not only the magnitude but

also the distribution pattern of the predicted shear force were affected by the choice of the soil model. For information, the distribution pattern of the shear force is exposed to view on Figure 4.10, known as "shear force envelope". Figure 4.11 reveals that the soil plasticity reduced the predicted structural demand under the scaled 1999 Chi-Chi and scaled 2011 Kohriyama earthquakes from the E-HD model (i.e., 26 MN and 22.15 MN, respectively) to the H2-HD model (i.e., 19.81 MN and 17.59 MN, respectively). Admittedly, looking back to Figure 4.7, the response spectra, belonging to the H2-HD soil model, underlay the other soil models trends in the whole range of periods. Indeed, a higher value of the spectral acceleration (S_a) intimated that the structural system was attracting more seismic energy at a certain natural period.

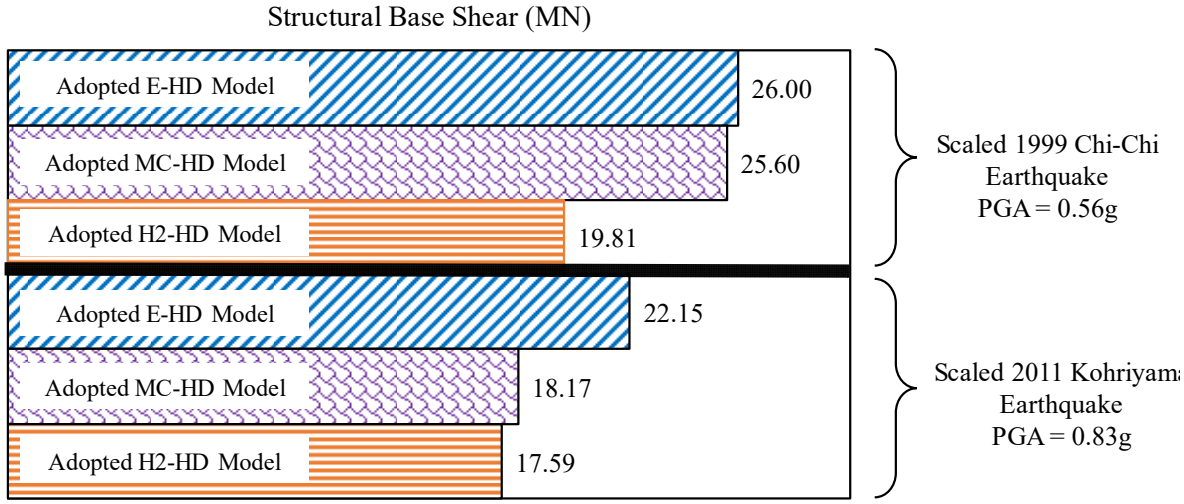

Figure 4.11 Maximum base shear forces in superstructure for adopted soil constitutive models (E-HD, MC-HD, and H2-HD) subjected to scaled 1999 Chi-Chi and scaled 2011 Kohriyama earthquakes

The base shear demand of an inelastic flexible base MDOF system (V_{MDOF}) on a mat foundation can be determined from the response spectrum for an equivalent fixed-base SDOF system using Equation (4.16), proposed by Lu et al. (2016), wherein V_{SDOF} is the base shear demand of a fixed-base SDOF system. The predicted base shear for the scaled 1999 Chi-Chi earthquake, i.e., 26 MN, reported in Figure 4.11, was bracketed by those of the inelastic flexible base MDOF system ($V_{MDOF}(T, \alpha_0, s, \mu)$ = 20-27 MN). Indeed, V_{MDOF} = 20 MN was calculated

on the basis of the first mode period (1.857 s), S_a = 0.51g from the E-HD trend in Figure 4.7a, V_{SDOF} = 22 MN based on W = 43 MN, α_0 = 0.41, s = 4.667, μ = 2, R_M = 0.526, and R_F = 2.1. The larger value, i.e., V_{MDOF} = 27 MN, was calculated on the basis of the first mode period (1.617 s), S_a = 0.69g from the E-HD trend in Fig. 7a, V_{SDOF} = 30 MN based on W = 43 MN, α_0 = 0.47, and the same values of s, μ, R_M, and R_F as before. The scaled 2011 Kohriyama earthquake led to 22.15 MN (see Figure 4.11) as the base shear for the adopted E-HD model, which was in a good agreement with the calculated range of 21 MN (T = 1.617 s, S_a = 0.53g, V_{SDOF} = 23 MN, α_0 = 0.47, s = 4.667, μ = 2, R_M = 0.526, and R_F = 2.1) to 25 MN (T = 1.857 s, S_a = 0.64g, V_{SDOF} = 28 MN, α_0 = 0.41, s = 4.667, μ = 2, R_M = 0.526, and R_F = 2.1).

$$V_{MDOF}(T, \alpha_0, s, \mu) = \frac{V_{SDOF}(T, \alpha_0 = 0, \mu = 1)}{R_M R_F} \tag{4.16}$$

where, α_0 ($= \frac{2\pi\bar{h}}{\bar{V}_S T}$) is the structure-to-soil stiffness ratio (0.47 for T = 1.617 s, and 0.41 for T = 1.857 s), $\bar{h}$ ($= 0.7H$) is the effective height of the building (42 m), H is the building height (60 m), $\bar{V}_S$ is the weighted average shear wave velocity (350 m/s as per Figure 4.2a), T ($= 0.075H^{3/4}$, suggested by Eurocode 8 – Part 1 (2004), and $= 0.0466H^{0.9}$, reported by ASCE7-10 (2010)) is the fundamental period of the fixed-base building corresponding to the first mode of vibration (1.617 s and 1.857 s, respectively), s ($= \frac{\bar{h}}{r_{eq}}$) is the slenderness ratio of the structure (4.667), r_{eq} is the radius of the equivalent circular foundation (9 m), R_M ($= \frac{1}{1+(N_S-1)Ln(c_{sd}\mu^{(0.05-N_S/1000)})}$) is the MDOF modification factor of a SSI system (0.526), N_s is the number of the stories (20), c_{sd} is a soil-dependent parameter (equal to 1.027, referring to Lu et al. (2016) for the site class D as to ASCE7-10 (2010)), μ is the ductility demand (considering 2 for the ordinary concrete moment-resisting frame according to AS1170.4 (2007)), and R_F is the SDOF strength reduction factor (equal to 2.1, as to Lu et al. (2016), for the site class D based on α_0, s, and μ).

Even though the more realistic elasto-plastic response of the soil, as captured in the H2-HD model, lessened the shear forces, the amount and trend of such a reduction were not the same on every level as observed in Figure 4.10. There was no notable difference in the values of the spectral acceleration (S_a) in the first mode period range, i.e., 1.667-2.163 s, exhibited in Figures 4.7a and b. Conversely, the E-HD trends in the aforesaid figures, under the both seismic inputs, sat atop the others in the second mode period range, i.e., 0.585-0.608 s. From such considerations, the predicted structural shear force distributions, displayed in Figure 4.10, confirmed the contribution of the different modes in the structural response. The other reason behind the difference between the shear force envelope trends of the adopted soil models could be justified by reviewing the Peak Ground Acceleration (PGA) values. The PGA values, corresponding to the bedrock and ground surface motions, were recorded at the intersections of the response spectrum trends and vertical axes in Figures 4.7a and b. PGA is related to the structural inertial forces. Looking back to Figure 4.7, the PGA values for the ground motions in the E-HD (i.e., 1.96g and 2.68g) and MC-HD (i.e., 1.29g and 1.24g) models experienced the twofold to fourfold increases compared to those corresponding to the scaled Chi-Chi and scaled Kohriyama bedrock records, respectively. Yet, the H2-HD model presented the more or less similar PGA values (i.e., 0.65g for the scaled Chi-Chi excitation and 0.82g for the scaled Kohriyama earthquake) in comparison with those of the scaled bedrock records, i.e., 0.56g and 0.83g, consecutively.

Regarding the superstructure safety control, in the first instance, the lateral sliding resistance of the foundation under the earthquake excitation must be checked. To address that, the foundation-soil interface friction angle of 26 degrees was considered. The said angle corresponded to the friction coefficient of 0.5 as recommended by FEMA273 (1997) for the clayey sands. The foundation sliding resistance was about 25 MN under the total permanent action, totaled up from the weight of the building and foundation. Therefore, the factor of safety

(FOS) against sliding, being approximately 1.5, was provided by the application of the H2-HD model referring to Figure 4.11. Contrarily, the E-HD and MC-HD soil models ended up with the overestimation of the base shear force, particularly once subjected to the scaled 1999 Chi-Chi excitation, i.e., around 26 MN. That overestimation could be suspected of imposing the unnecessary expense on the project. Next, the story shear capacity must not be breached by the story seismically-induced shear force. In the present study, the ultimate shear strength of each story in conjunction with the contribution of the shear reinforcement was determined as per AS3600 (2009), depicted in Figures 4.10a and b. None of the adopted soil constitutive models were responsible for the shear failure of the structural components in the moment-resisting building as all the predicted shear force envelope distributions were placed in the safe zone.

4.3.3 Foundation Rocking and Settlements

Figure 4.12 portrays that the soil plasticity-induced rocking was significant in this study since the H2-HD soil model resulted in the amplified foundation rocking due to the soil yielding. Contrarily, the elasticity-based model (i.e., E-HD) and elastic-perfectly plastic model (i.e., MC-HD), thoroughly dismissed the existence of the plastic strains prior to the soil failure state. Thus, referring to Figures 4.10 and 4.11, less structural shear forces were generated whilst employing the shear-volumetric hardening concept in contrast to the E-HD and MC-HD models as the earthquake energy was dissipated through the rocking-dissipation because of the soil plasticity.

Figure 4.13 is a pictorial description of the maximum and residual foundation rocking, explaining how far the structure rocked during the applied earthquakes. Taking the results of the scaled 1999 Chi-Chi excitation under scrutiny, the obtained maximum rocking enjoyed the over fivefold upsurge by transferring from the E-HD and MC-HD soil models to the H2-HD constitutive relationship. As reported in Figure 4.13 for the scaled Chi-Chi shaking input, the

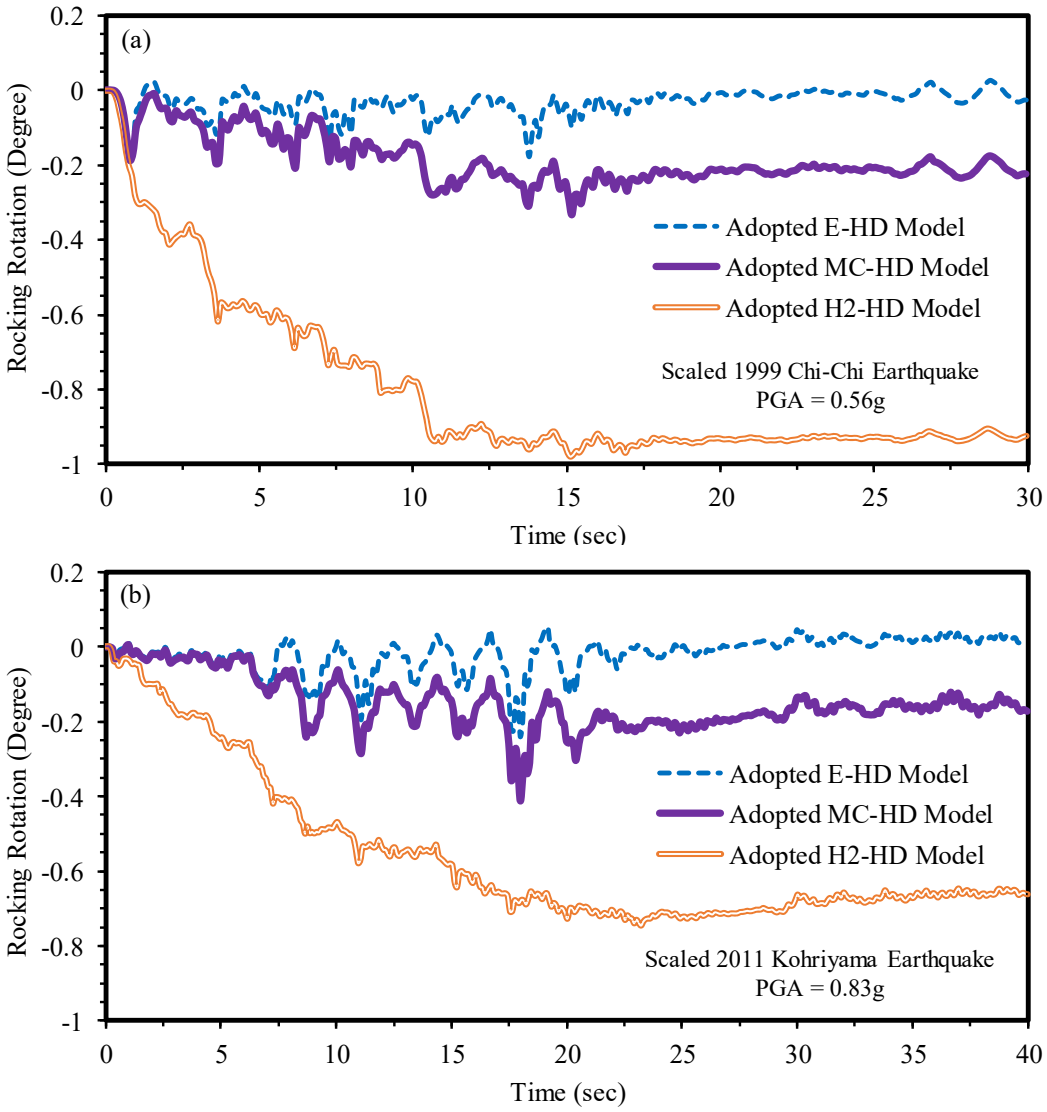

Figure 4.12 Time histories of foundation rocking for adopted soil constitutive models (E-HD, MC-HD, and H2-HD) subjected to: (a) scaled 1999 Chi-Chi earthquake, and (b) scaled 2011 Kohriyama earthquake

comparison for the residual foundation rocking exhibited a conspicuous boost, i.e., 0.224 degrees (for MC-HD) to 0.925 degrees (for H2-HD). The maximum foundation rotation was 0.747 degrees for the H2-HD model, subjected to the scaled Kohriyama earthquake, whereas the corresponding parameter in the MC-HD model was diminished by 45% to 0.411 degrees. Therefore, it is obvious that the H2-HD model would impose more influence on the prediction of the building lateral deflection than the other two soil models.

Bowles (1996) suggested that the foundation differential settlement ratio, also known as "deflection ratio", is demanded to be less than 1/300 such that the tilt is not noticeable for the

tall buildings. The differential settlement ratios in Figure 4.13 were calculated on the basis of the ratios of the maximum foundation differential settlement values, listed in Table 4.3, to the foundation width, i.e., 16 m. Considering the results of the scaled 1999 Chi-Chi earthquake in Figure 4.13, the H2-HD deflection ratio (i.e., 0.017) was about 3 times greater than that of the MC-HD model (i.e., 0.006). Quite differently, the incorrect safe state, meaning that the foundation differential settlement ratio was less than 1/300, was predicted when the E-HD model was adopted. Skempton and MacDonald (1956) suggested the upper limiting value of 75 mm for the tolerable maximum settlement of the mat foundations. According to Table 4.3, the adopted H2-HD soil model disclosed the transient foundation settlement up to 223 mm, which did not meet the criterion of interest. The values of the maximum vertical displacements at the center of the foundation from the analyses of the E-HD and MC-HD models (see Table 4.3) misled the design engineers by indicating the unrealistic safety of the superstructure. The notable differences between the predicted values of the residual settlement, plotted in Figure 4.14, could be patently interpreted as the inevitable momentousness of the soil model type in SSSI. The residual settlement, shown in Figure 4.14, was the average settlement for the center of the foundation. By way of illustration, the permanent settlement was 198 mm for the H2-HD model under the scaled 2011 Kohriyama earthquake, breaching the limiting value of 75 mm, while for the case of the MC-HD model, the corresponding settlement was declined by roughly 96% to 8 mm.

Table 4.3 Predicted maximum differential settlement and maximum foundation settlement

Foundation Settlement Type	Adopted Soil Constitutive Model	Applied Earthquake Record	
		Scaled 1999 Chi-Chi Earthquake	Scaled 2011 Kohriyama Earthquake
Maximum Differential Settlement (mm)	E-HD	50	67
	MC-HD	93	115
	H2-HD	274	209
Maximum Vertical Displacement at Center of Foundation (mm)	E-HD	13 (+)*	22 (+)*
	MC-HD	11 (+)*	14 (-)*
	H2-HD	223 (-)*	198 (-)*

*(+): Upward vertical displacement, and (-): Downward vertical displacement.

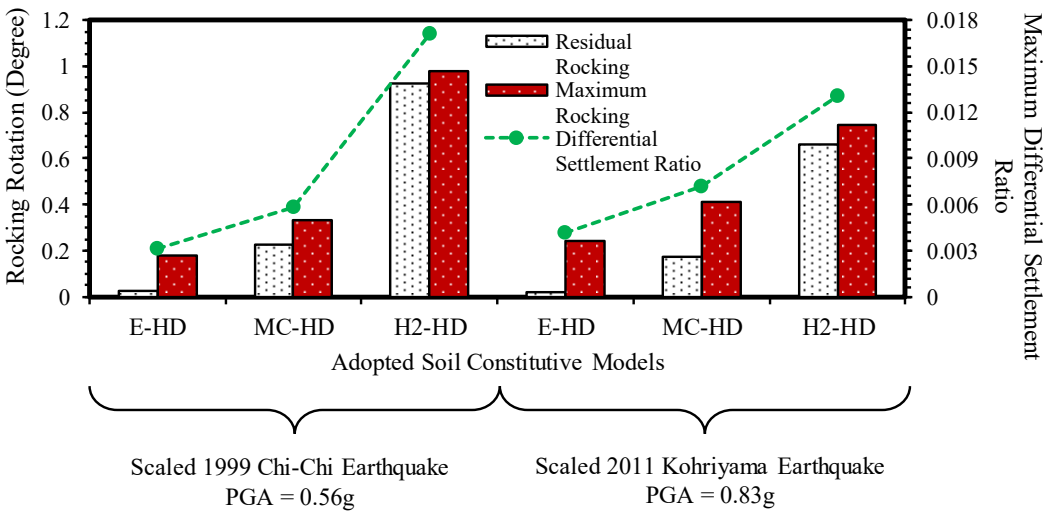

Figure 4.13 Residual and maximum foundation rocking plus maximum differential settlement ratios for adopted soil constitutive models (E-HD, MC-HD, and H2-HD) subjected to scaled 1999 Chi-Chi and scaled 2011 Kohriyama earthquakes

It is hereby asserted that saving time and cost of the numerical calculation would certainly set forth the acceptance of the infinitesimal values of the permanent foundation settlement in Figure 4.14 for the E-HD model, subjected to the scaled 1999 Chi-Chi and scaled 2011 Kohriyama earthquakes. Referring back to Figures 4.12a and b, it is evident that beyond 20 s, the foundation rocking, in what is known as “rigid body rotation”, variations were negligible. It denotes that the predicted residual outcomes in this study were representative and reliable. Indeed, the residual settlement in the E-HD model will reach zero if the analysis is up and running for the significant extra time right after the earthquake loading, giving rise to a lengthy analysis.

The upward movements of 22 mm and 11 mm, reported in Table 4.3, took place at the foundation center while utilizing the E-HD and MC-HD models, respectively. Yet, the continuous settlement in the H2-HD models under the scaled cherry-picked earthquakes was predicted, illustrated graphically in Figures 4.15 and 4.16. Such lack of consideration of the soil plasticity can obviously result in the under-prediction of the foundation post-earthquake settlement in addition to the unrealistic prediction of the earthquake energy, pinpointing the structure.

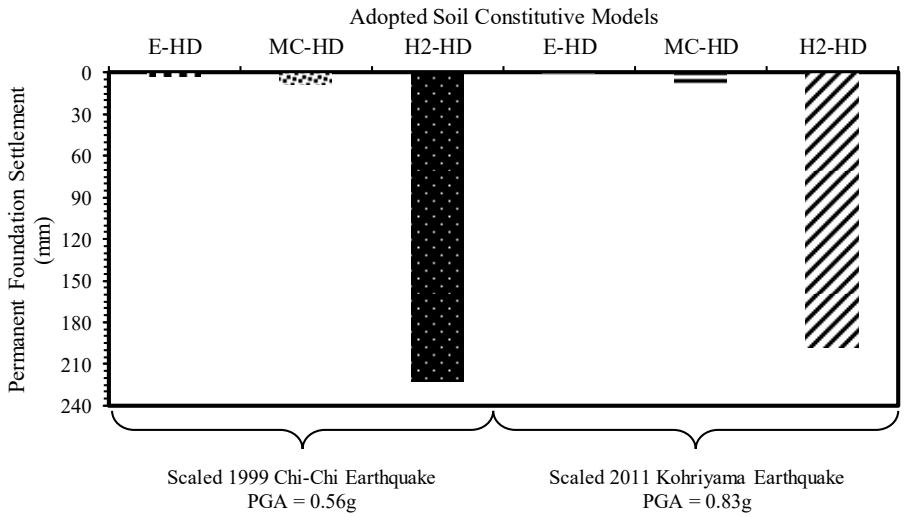

Figure 4.14 Permanent settlement at center of foundation for adopted soil constitutive models (E-HD, MC-HD, and H2-HD) subjected to scaled 1999 Chi-Chi and scaled 2011 Kohriyama earthquakes

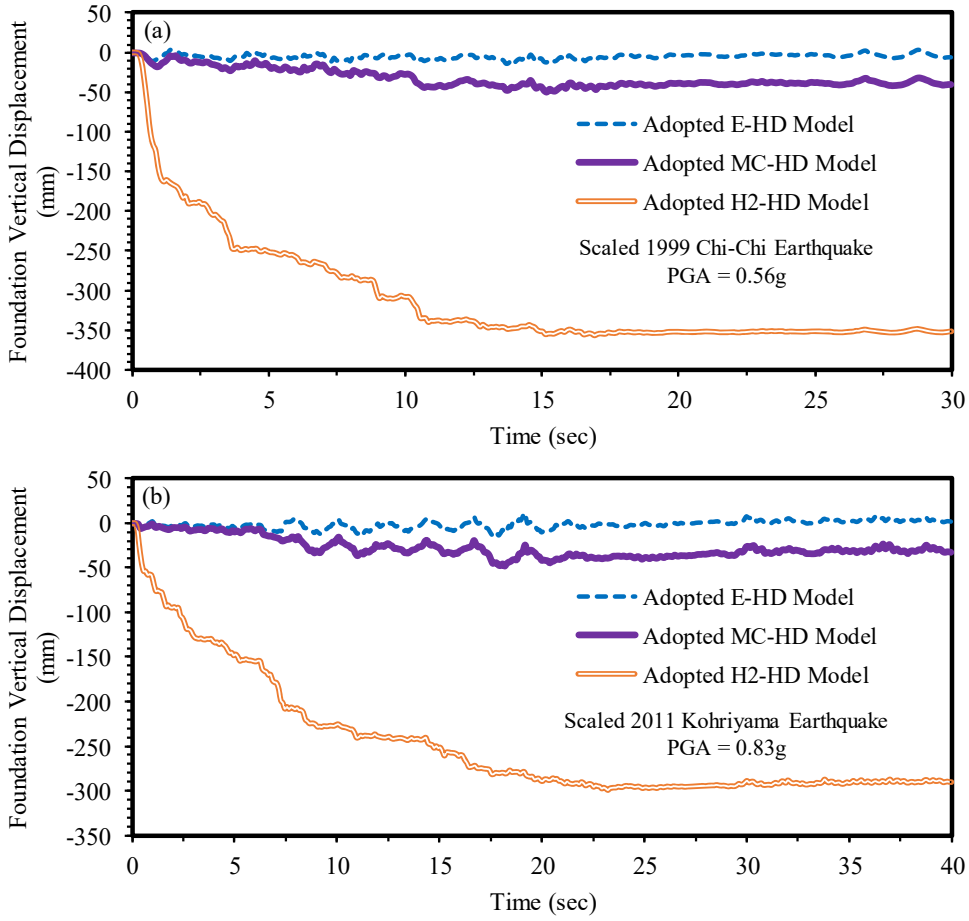

Figure 4.15 Vertical displacement histories associated with left side of foundation for adopted soil constitutive models (E-HD, MC-HD, and H2-HD) subjected to: (a) scaled 1999 Chi-Chi earthquake, and (b) scaled 2011 Kohriyama earthquake

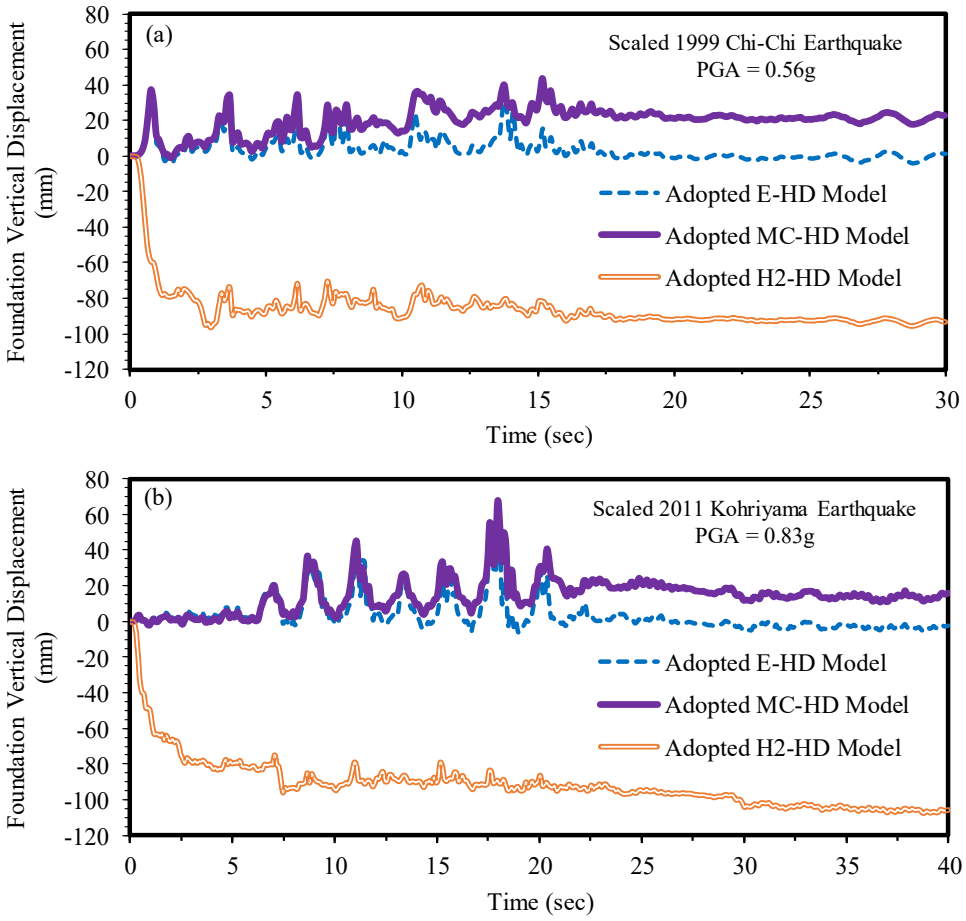

Figure 4.16 Vertical displacement histories associated with right side of foundation for adopted soil constitutive models (E-HD, MC-HD, and H2-HD) subjected to: (a) scaled 1999 Chi-Chi earthquake, and (b) scaled 2011 Kohriyama earthquake

This sector is about the verification for the obtained foundation settlements from the H2-HD model under the applied earthquakes. Richards et al. (1993) proposed a method, based on the active-passive Coulomb wedge mechanism and sliding-block approach, for the calculation of the seismic settlement of a shallow foundation, herein subjected to only one horizontal component of an earthquake (i.e., Δ in Equation (4.17)).

$$\Delta = 0.087 \left[\frac{{V_c}^2 A^3}{g {k_h^*}^4}\right] (tan\Omega) \tag{4.17}$$

where, V_c is the velocity coefficient of the earthquake, A is the acceleration coefficient of the earthquake per gravitational acceleration (g), k_h^* is the critical acceleration, and Ω is the active Coulomb wedge angle.

As listed in Table 4.4, the predicted settlements of the center of the adopted mat foundation, when employing the H2-HD soil model, under the scaled 1999 Chi-Chi and scaled 2011 Kohriyama earthquakes were 223 mm and 198 mm, respectively. Table 4.4 also expresses that the former (i.e., 223 mm) and latter (i.e., 198 mm) were bracketed by the range of 133-269 mm, as the estimated earthquake-induced settlements via Equation (4.17). In the said calculation, the effective range of period was estimated based on the predicted base shear for H2-HD, presented in Figure 4.11, and fundamental period of the flexible base building, i.e., 2.163 s. Therefore, $\bar{S}_a$ and $\bar{S}_v$, used as A and V in Equation (4.17), consecutively, were the mean spectral acceleration and corresponding mean spectral velocity in the aforesaid range, respectively. The rest of the parameters to be used in Equation (4.17) are as follows: (i) g = 9.81 m/s^2; (ii) k_h^* was determined to be 0.2 considering the unembedded mat foundation, static safety factor of 3 for the bearing capacity, foundation width of 16 m, soil failure effective friction angle (φ_f') of 35°; and (iii) $tan\Omega$ = 1.2 referring to Richards et al. (1993).

Table 4.4 Verification of seismic settlement of adopted mat foundation using H2-HD soil model

Applied Earthquake Record	A & V_c in Equation (4.17)		Numerically Predicted Maximum Settlement at Center of Foundation in This Study (mm)	Estimated Earthquake-Induced Settlement via Equation (4.17) (mm)
Scaled 1999 Chi-Chi Earthquake	$\bar{S}_a$ (g)	0.33	223	269
	$\bar{S}_v$ (m/s)	1.06		
Scaled 2011 Kohriyama Earthquake	$\bar{S}_a$ (g)	0.30	198	133
	$\bar{S}_v$ (m/s)	0.86		

The ground-movement-related building damage based on the approximate crack width in combination with the maximum differential settlement was posited by Day and Boone (1998). The damage category in such a serviceable yardstick was shifted from “Moderate” (50-80 mm) to “Severe” (80-130 mm) and “Very Severe” (>130 mm) from the E-HD model to the H2-HD model. The 274-mm differential settlement under the scaled 1999 Chi-Chi earthquake was reported in Table 4.3 for the H2-HD soil model. The predicted differential settlements were 67 mm and 115 mm in the E-HD and MC-HD models subjected to the scaled 2011 Kohriyama

excitation, respectively. Henceforth, the readers could take delivery of the following points, derived from the current study of the seismic performance of the adopted 20-story reinforced concrete moment-resisting building on a mat foundation: (i) the simulations, having the E-HD and MC-HD models, did not project the loss of the bearing in some structural elements and possible danger of the structural instability; (ii) not putting the soil plastic hardening into effect from the onset of the virgin loading caused the requirement of an extensive repair job; and (iii) the predicted seismic response of the adopted moment-resisting building in the soil-structure system was clearly affected by the type of the soil stress-strain relationship.

4.3.4 Structural Lateral Deflections

The seismic structural lateral deflection in the adopted superstructure encompassed the structural distortion, foundation rocking or differential settlement of the foundation slab, and lateral translation of the foundation. The last one could be dismissed since the other components oversaw the structural lateral deflections, relative to the base. In this project, the movements of the columns bases on the foundation level were subtracted from those of the building stories to determine the lateral deflections of the structure. Thus, all the recorded displacements, reported in Figures 4.17 and Figure 4.18, were relative to the movements of the foundation. The foundation rotation (or the rocking) and settlement of the foundation slab were comprehensively discussed in Section 4.3.3.

Figure 4.17 displays the numerical predictions of the time history of the lateral deflection at the top level (roof). A scrutiny of Figures 4.12a and b along with Figures 4.17a and b could reveal that the foundation rocking highly impacted the building lateral deflections under both the applied excitations. For example, over 70% of the predicted maximum lateral displacement of the rooftop in Figure 4.17b was governed by the predicted foundation rotation at the same occurrence time from Figure 4.12b. The above-mentioned factor was about 80% for the scaled

1999 Chi-Chi excitation. Hence, in the current study, the soil plasticity, utterly captured in the H2-HD model, intended to amplify the building lateral deflection via boosting the foundation rocking component due to the progressive soil yielding.

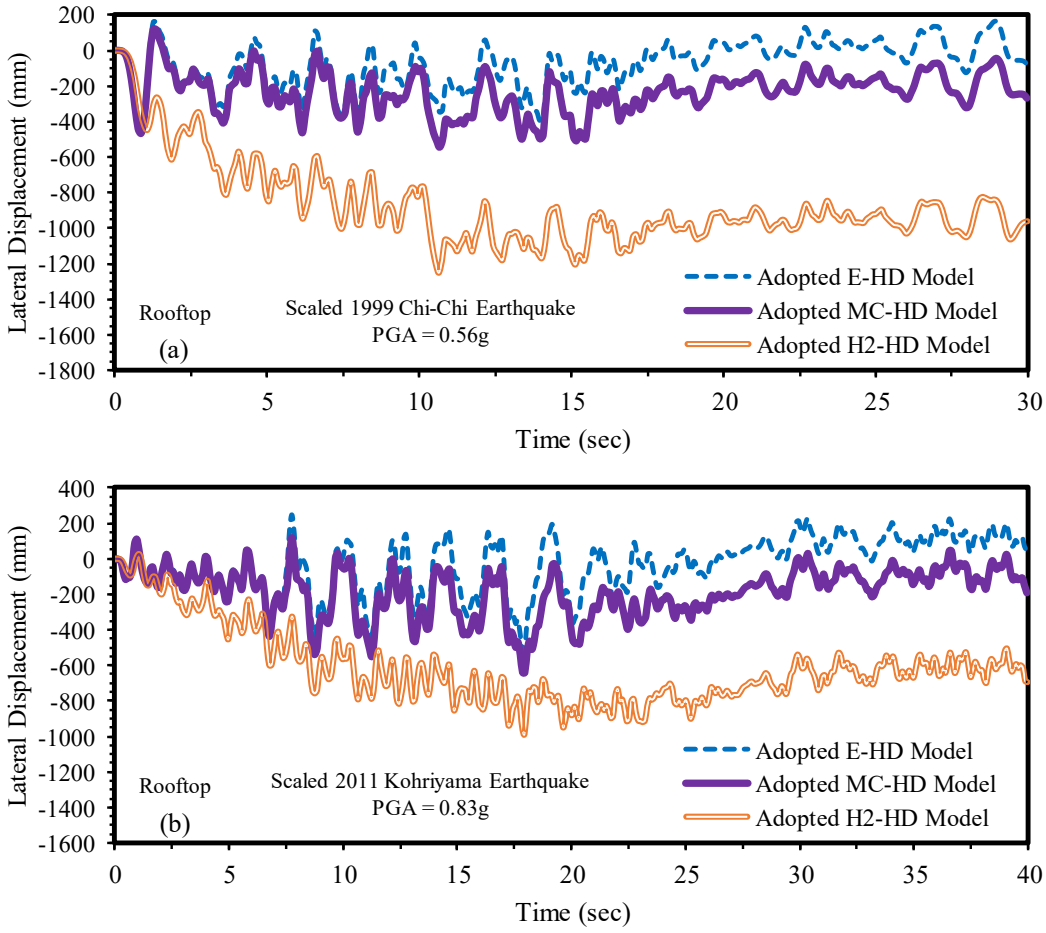

Figure 4.17 Time histories of lateral displacement of rooftop for adopted soil constitutive models (E-HD, MC-HD, and H2-HD) subjected to: (a) scaled 1999 Chi-Chi earthquake, and (b) scaled 2011 Kohriyama earthquake

It is acknowledged that the transient lateral displacements, plotted in Figures 4.18a and b, were taken when the rooftop lateral displacement reached its maxima (see Figures 4.17a and b) based on the methodology, reported by Hokmabadi et al. (2012). The maximum structural lateral displacements corresponding to the E-HD, MC-HD, and H2-HD soil models were 450 mm, 540 mm, and 1250 mm, respectively, with the corresponding occurrence times, being 0.9 s, 10.7 s, and 10.6 s, consecutively, for the scaled 1999 Chi-Chi earthquake. As reported in Figures 4.17b and 4.18b, the obtained maximum structural lateral displacements and

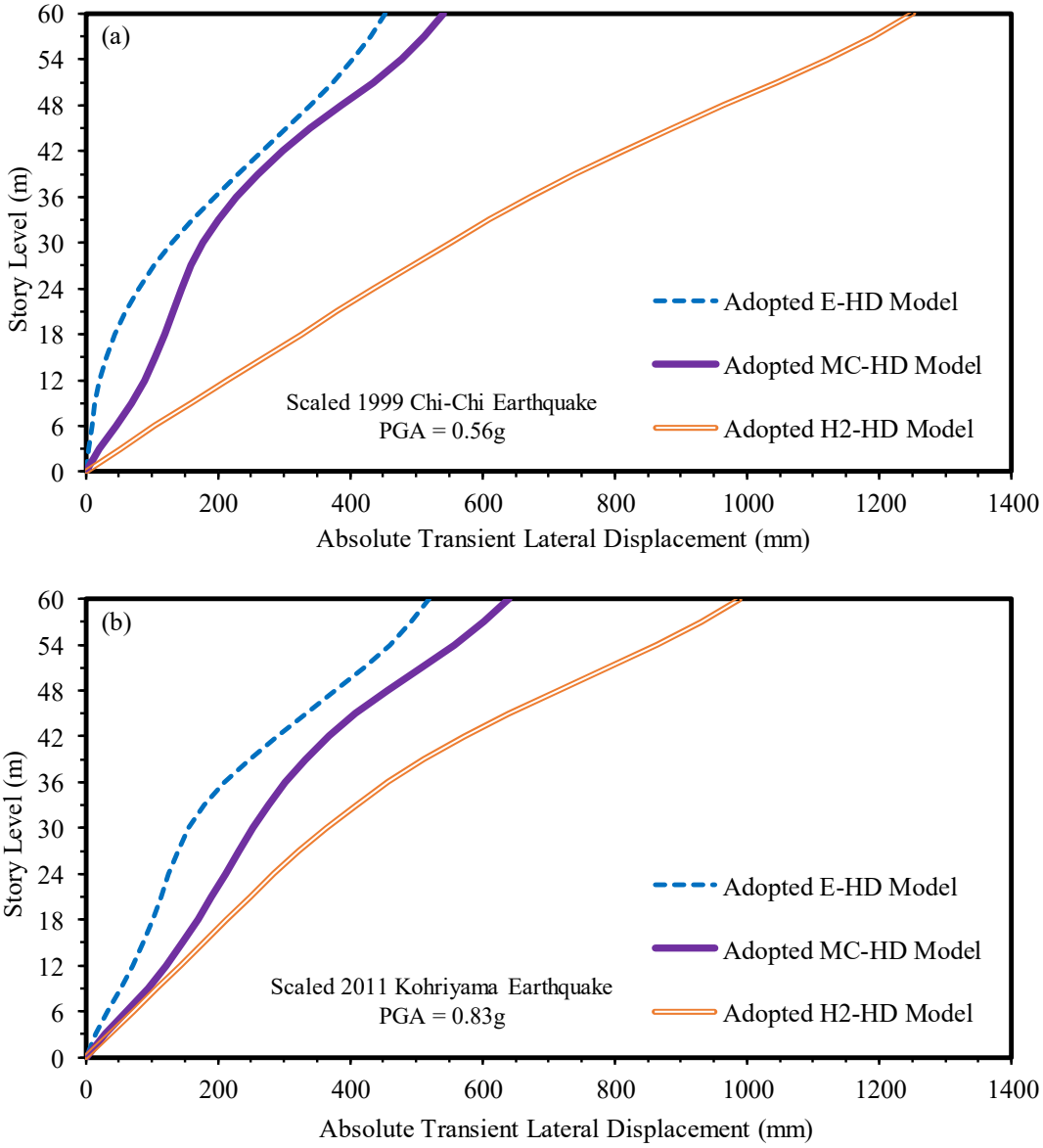

Figure 4.18 Transient lateral displacements of 20-story superstructure for adopted soil constitutive models (E-HD, MC-HD, and H2-HD) subjected to: (a) scaled 1999 Chi-Chi earthquake, and (b) scaled 2011 Kohriyama earthquake

corresponding occurrence times for the scaled 2011 Kohriyama excitation, adopting the E-HD, MC-HD, and H2-HD models, were (520 mm, 17.9 s), (640 mm, 18.0 s), and (1000 mm, 17.9 s), respectively. Indeed, the transient lateral displacements at the roof, when the nonlinear plastic soil model (H2-HD) was adopted, considerably outweighed the corresponding predictions for the E-HD and MC-HD models, by about 278% and 231% for the scaled Chi-Chi earthquake, and by about 192% and 156% under the scaled Kohriyama earthquake, respectively. From all accounts, the lateral displacement response for the H2-HD soil model

was dominated by the foundation rotation.

It is observed that the more the foundation rocking, the more the structural lateral deflection while the more seismic energy would be spent on the rigid body rotation, resulting in reducing the shear force-induced structural distortion. Referring back to Figure 4.11 for the scaled 1999 Chi-Chi earthquake, employing the H2-HD soil model reduced the predicted base shear from 26 MN to 19.81 MN, contributing to the structural distortion diminishment (see Figure 4.18a). In addition, the predicted transient lateral deflection trends from the hardening soil model, almost linear in Figures 4.18a and b by comparison with the curvy trends of the simple, conventional soil models, signified that the structural distortion played a less critical role in the variations of the structural lateral deflection once the soil pre-failure plasticity was taken into account for the soil and foundation configurations, adopted in this study.

Figure 4.19 indicates that the application of the H2-HD model gave rise to the detrimental residual lateral deflection of the adopted reinforced concrete building under the scaled 1999 Chi-Chi shaking excitation. In that respect, the superstructure underwent a maximum permanent lateral displacement of 962 mm. The said value was 1300% and 360% more than the predicted maximum residual lateral displacements that the same structure undertook while utilizing the E-HD (i.e., 74 mm) and MC-HD (i.e., 267 mm) models, respectively. Such a large prediction for the residual lateral deflection was the culprit for: (i) making the structure appear unsafe to the occupants; (ii) impairing the structural response to the aftershocks by jeopardizing the global stability of the laterally displaced building frame; and (iii) skyrocketing the cost of the post-seismic repair. In respect of the SSSI effect on the ductility, the previous studies (e.g., Lu et al., 2016) shed light on the reduction in the ductility demand courtesy of the soil-structure interaction by reason of displacing such a demand from the superstructure to the ground. Even so, the current study disclosed that such a so-called positive effect was counterbalanced by the large rotation at the foundation level in light of the required soil plasticity in SSSI, potentially

jeopardizing the seismic performance of the adopted 20-story moment-resisting superstructure, founded on a mat foundation.

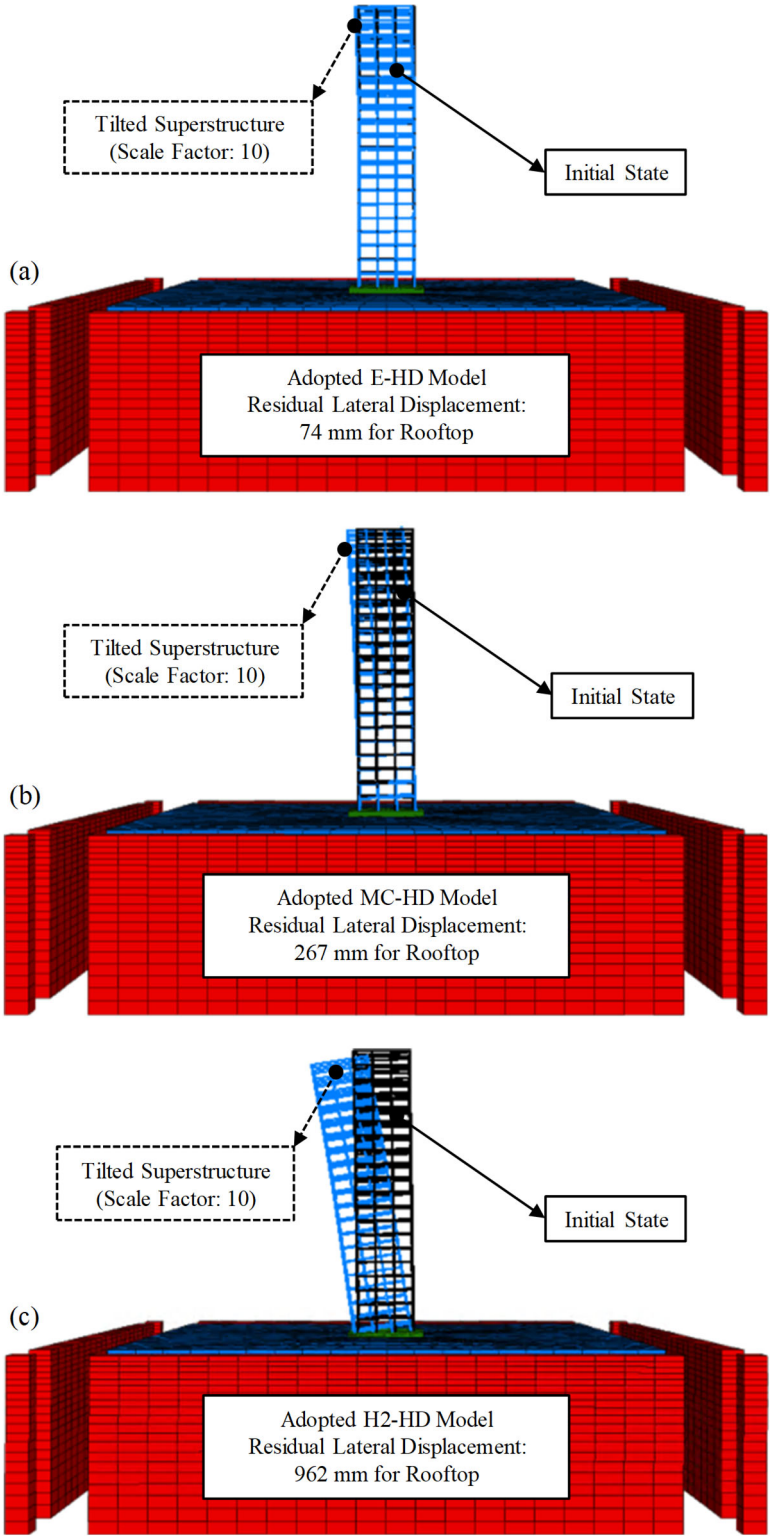

Figure 4.19 Residual lateral displacements of 20-story superstructure subsequent to scaled 1999 Chi-Chi earthquake event for adopted soil constitutive models: (a) E-HD, (b) MC-HD, and (c) H2-HD

4.3.5 Structural Inter-Story Drift Ratios

As per the performance-based seismic design code of FEMA273 (1997), the life safety seismic performance level is a combination of the seismic performance attributed to both the structural and non-structural members in a building, giving rise to the fact that the lateral displacements at the center of mass associated with the respective story must be used for the calculation of the total inter-story drift ratio as the damage parameter, reported by Ghosh and Fanella (2003). It is reasoned to conclude that the total inter-story drift ratio of the adopted building had two components: (i) distortional inter-story drift ratio, corresponding directly to the shear forces, generated in the building columns; and (ii) rocking-induced inter-story drift ratio due to the foundation tilt, i.e., the rigid body rotation.

Figure 4.20 presents the predictions of the transient total inter-story drift ratios of the reinforced concrete building amidst the applied shaking excitations for the adopted soil constitutive models. Both the scaled excitations commented on the inadequately designed superstructure when the seismic behavior of the soil mass was simulated by the H2-HD soil model courtesy of surpassing the 2% life safety drift limit, recommended by FEMA273 (1997). For instance, the maximum transient total inter-story drift ratios of 1.22% and 1.47% for the elastic model (E-HD) during the scaled 1999 Chi-Chi earthquake and scaled 2011 Kohriyama earthquake were predicted, respectively. On the contrary, the shear-volumetric hardening model (H2-HD) resulted in 2.67% (119% increase, breaching the 2% acceptable criterion) and 2.59% (76% ascent, not satisfying the 2% acceptable criterion), consecutively. By the same token, increasing the total inter-story drift ratio, emerging from the rocking component, well overseen by H2-HD in this study, accordingly augmented the $P-\Delta$ effect. In all the numerical simulations herein, the $P-\Delta$ effect was taken into consideration by activating the large-strain mode in FLAC3D. Such an effect, caused by the gravity loads acting at the center of mass of each floor on the displaced configuration of a building, was crucial since the damage of the

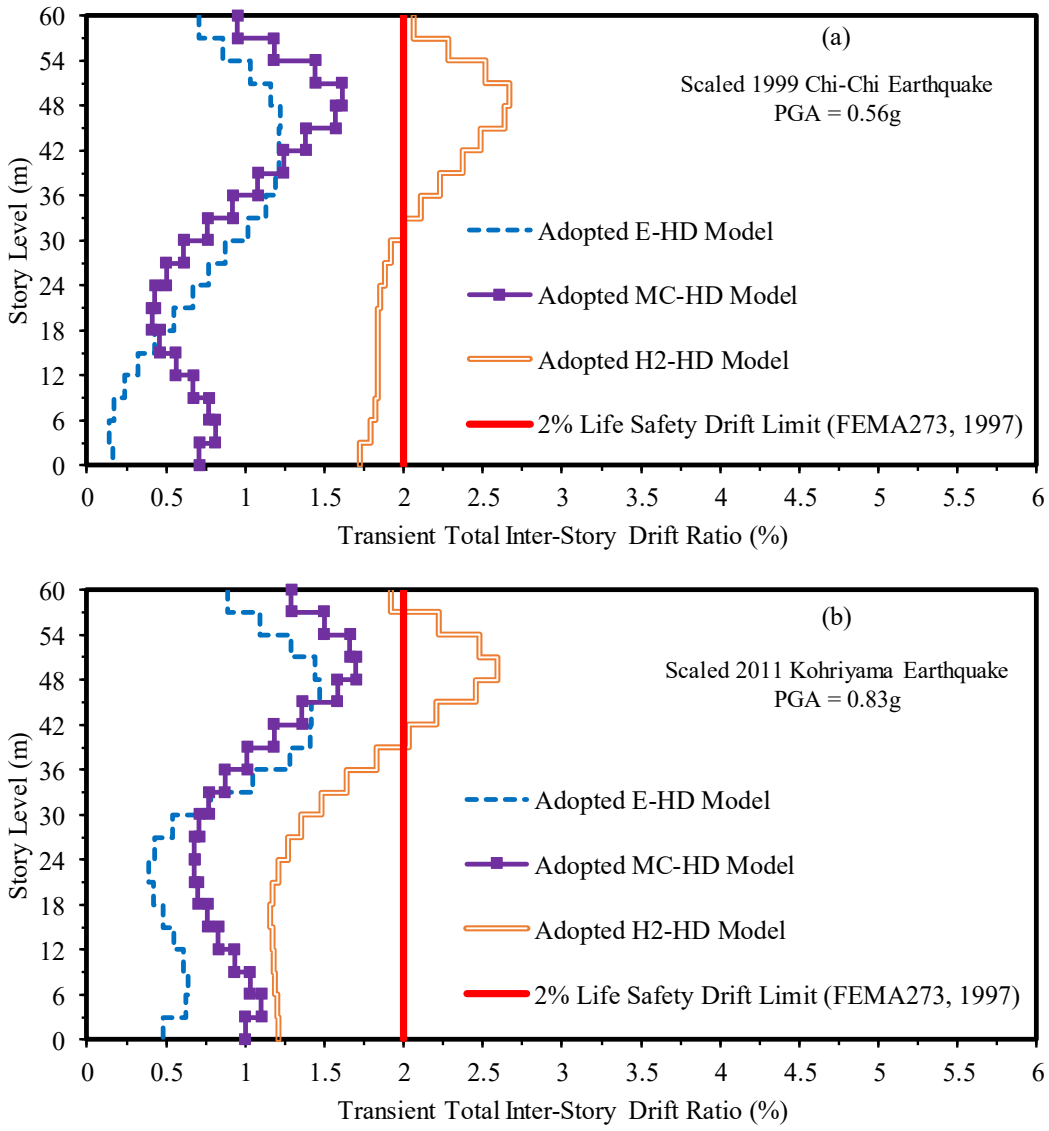

Figure 4.20 Transient total inter-story drift ratios of 20-story superstructure for adopted soil constitutive models (E-HD, MC-HD, and H2-HD) subjected to: (a) scaled 1999 Chi-Chi earthquake, and (b) scaled 2011 Kohriyama earthquake

non-structural members is directly related to the total inter-story drift ratio, as pointed out by Gelagoti et al. (2012). These results underscored that utilizing the soil hardening plasticity from the onset of the loading in SSSI dislocated the predicted performance level of the adopted moment-resisting building frame, in terms of both the structural and non-structural members responses, from the life safety state to the near collapse damage level or even the collapse state by surging the overall lateral displacement of the superstructure on a mat foundation.

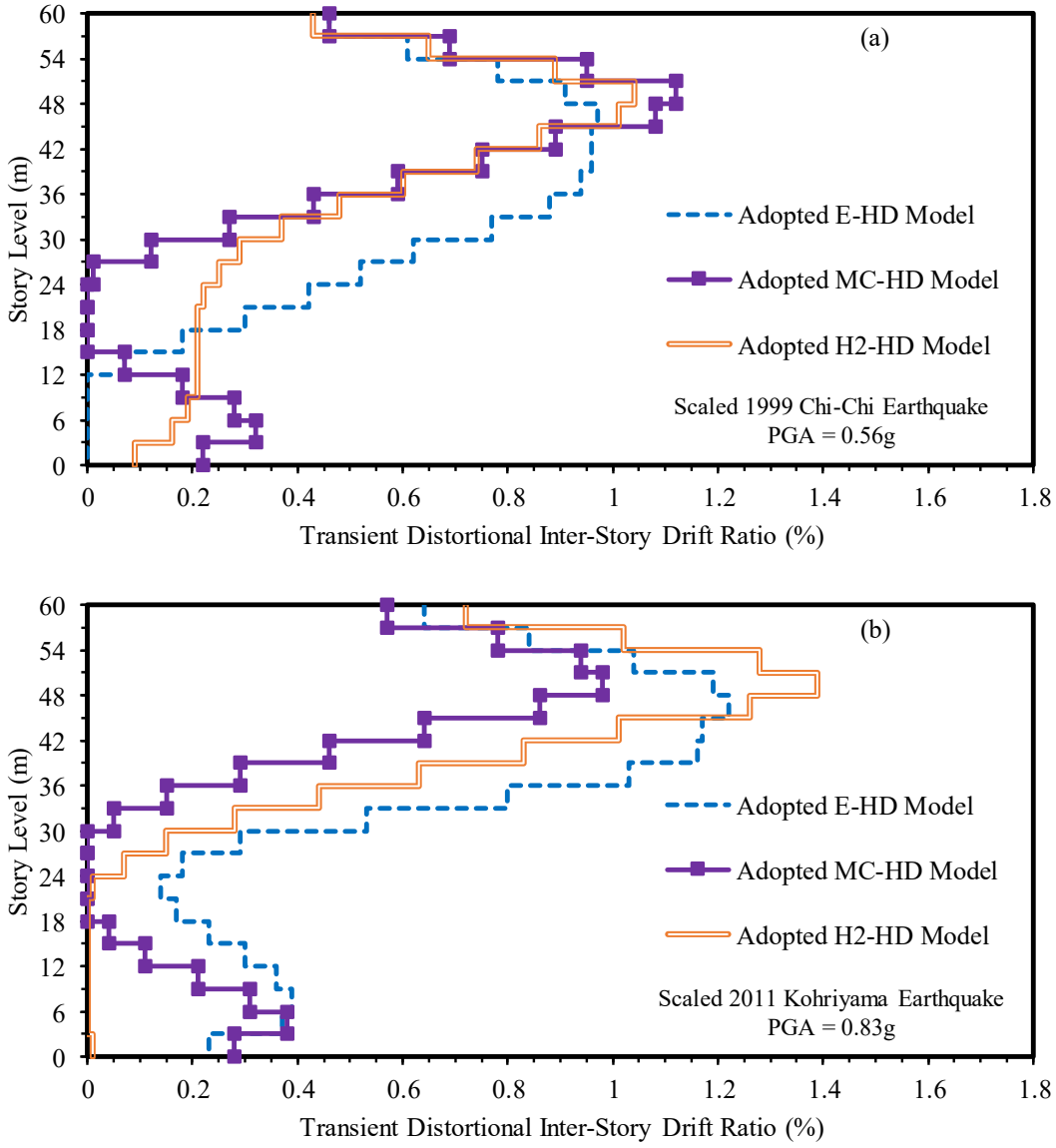

Figure 4.21 Transient distortional inter-story drift ratios of 20-story superstructure for adopted soil constitutive models (E-HD, MC-HD, and H2-HD) subjected to: (a) scaled 1999 Chi-Chi earthquake, and (b) scaled 2011 Kohriyama earthquake

The distortional inter-story drift ratio demonstrated the relative horizontal displacement, excluding the foundation rocking or the rigid body rotation, divided by the story height. Figure 4.21 displays the predicted transient shear-induced distortional inter-story drift ratios computed by subtracting the transient foundation rocking-induced inter-story drift ratios from the transient total inter-story drift ratios, displayed in Figure 4.20. The former was the predicted foundation rotation in Figure 4.12 at the same occurrence time as the maximum roof displacement happened, found from Figure 4.17. As it is discerned in Figure 4.21 by

comparison with Figure 4.20, the decrease in the distortional inter-story drift ratio was a ramification of the surge in the soil plasticity from E-HD to H2-HD by reason of reducing the shear forces along the structure height as previously reported in Figure 4.10. Conversely, the soil pre-failure plasticity amplified the rocking component as per Figure 4.12, increasing the overall lateral deflection in the superstructure (see Figure 4.18). It could be concluded that the ratio between the foundation rocking and structural distortion components, contributing to the experienced structural lateral deflection and corresponding total inter-story drift ratio, was a function of the type of plasticity in the applied soil constitutive model.

According to FEMA273 (1997), the residual total inter-story drift ratio must remain less than 1% with the intention of ending up with the minor post-earthquake damage state. In line with Figure 4.19, the predicted residual total inter-story drift ratios in Figures 4.22a and b for the E-HD and MC-HD models were in the safe zone by complying with the 1% acceptance criterion. In respect of the H2-HD constitutive model, the adopted moment resisting building experienced the exceedance of the 1% life safety drift limit, recommended by FEMA273 (1997), by reaching 1.83% under the scaled 1999 Chi-Chi earthquake. It is manifest that the introduction of the nonlinear plastic soil model threw light on the import of choosing the appropriate soil constitutive model under the dynamic loading in the SSSI analyses of the reinforced concrete moment-resisting frames. The predicted maximum residual total inter-story drift ratio of the H2-HD model (i.e., 1.51%) compared to the E-HD (i.e., 0.22%) and MC-HD (i.e., 0.55%) soil models was 686% and 275% higher, consecutively, for the Kohriyama seismic input. On the same topic, the distribution of the permanent total inter-story drift ratio for the H2-HD soil model was completely located on the right side of the 1% life safety drift limit in Figure 4.22(a). The residual total inter-story drift ratio prediction in this study was predominately governed by the considerable permanent foundation rocking, emerging from precisely capturing the soil plastic deformation before the failure envelope was violated.

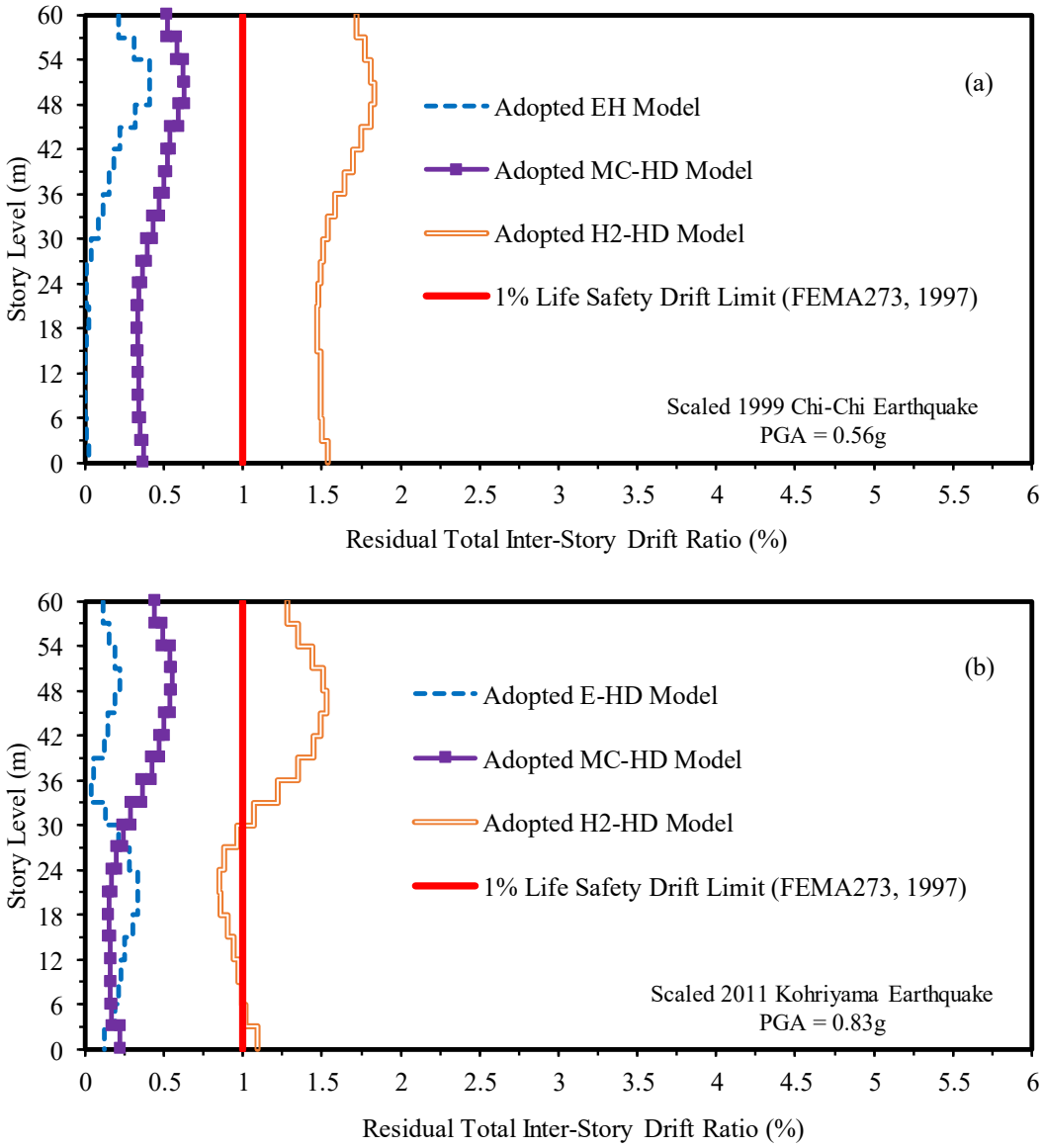

Figure 4.22 Residual total inter-story drift ratios of 20-story superstructure for adopted soil constitutive models (E-HD, MC-HD, and H2-HD) subjected to: (a) scaled 1999 Chi-Chi earthquake, and (b) scaled 2011 Kohriyama earthquake

In this study, the predicted transient and residual total inter-story drift ratios were compared with the life safety drift limits since the damage control and performance assessment of both the structural elements and non-structural components should be concurrently satisfied as asserted by Krawinkler et al. (2003). On that basis, the structure of interest for the range of earthquakes, applied in this study, did not meet the life safety drift limit not only for the predicted transient total inter-story drift ratio ($\prec$ 2%) but also for the predicted residual total inter-story drift ratio ($\prec$ 1%). It could be concluded that the paramountcy of employing the

nonlinearity, hardening, and plasticity of the soil mass in SSSI would be unquestionable when the foundation of a moment-resisting building frame experiences the significant rocking.

4.4 Summary

In spite of the fact that the number of research studies on the topics, related to the Seismic Soil-Structure Interaction (SSSI) has been on the increase, the numerical simulations of the dynamic behaviors associated with the soils are delimited by employing a group of simple, conventional soil constitutive models. Continuing on this line, the lessons, learned, from the past strong earthquake events, e.g., the 1995 Kobe (Japan), 2008 Wenchuan (China), 2010 Port-au-Prince (Haiti), and 2010 Maule (Chile) earthquakes, disclosed that not only the consideration of SSSI is per se essential in the design and analysis but also excelling the level of accuracy attributed to the numerical analyses of SSSI is extremely vital so as to ensure the safety and reliability of the structures.

The key contribution of this research work was adopting a three-dimensional finite difference approach using FLAC3D, accounting for the nonlinearity and pre-failure yielding of a realistic soil deposit, in order to bridge the existing gap, arising from bypassing the advanced concepts in the employed soil constitutive models, such as the elasto-plastic with the strain hardening, for performing the SSSI numerical simulations. The soil models, adopted in this study, were the isotropic Elastic with Hysteretic Damping (E-HD), elastic-perfectly plastic Mohr-Coulomb with Hysteretic Damping (MC-HD), and Hyperbolic Hardening with Hysteretic Damping (H2-HD) models. The salient features of the H2-HD model are recapped as follows: (i) hyperbolic stress-strain relationship during the triaxial drained compression; (ii) mobilization of the friction angle based on the plastic shear strain (shear hardening); (iii) plastic volumetric strain during the primary compression (volumetric cap hardening); (iv) shear-induced volume changes (dilation hardening); (v) stress-dependent elastic stiffness according

to a power law; (vi) different unloading-reloading behavior compared to the virgin loading; (vii) capturing the preconsolidation stress and its evolution; and (viii) Mohr-Coulomb failure yardstick.

The fulfillment was achieved in this study by providing a clear insight into the effects of harnessing the assorted soil constitutive models on the seismic performance predictions of a 20-story reinforced concrete moment-resisting building, founded on a mat foundation. For instance, the post-earthquake permanent lateral deflection of the adopted mat-supported 20-story building experienced a significant ascent (i.e., 12 times increase) when employing more appropriate and proper soil elasto-plastic behavior in the SSSI analysis. It is reasoned to state that the high cost of demolishing, retrofitting, and re-building of the damaged superstructures could be avoided throughout assigning the appropriate soil constitutive models to the soil layers, suitable for the numerical simulations of the soil-structure interaction under the dynamic loading.

CHAPTER 5

EFFECTS OF PORE WATER PRESSURE ON SEISMIC PERFORMANCE OF BUILDINGS ON SATURATED CLAYEY DEPOSIT CONSIDERING SOIL-STRUCTURE INTERACTION

5.1 General

The seismic performance of a 15-story reinforced concrete moment-resisting building, taking into account the nonlinear behavior of the soil, superstructure, and foundation, was examined through the three-dimensional coupled soil-structure analysis using the direct method in FLAC3D. The dependency of the soil shear modulus and damping ratio on the seismically-induced shear strains was captured. The interaction between the soil mass and building foundation was simulated by the use of the interface elements, mimicking the possible sliding, separation, and gapping. Three cases were set in this study so as to evaluate the extent to which the simulation of the seismically-induced excess pore water pressure could impact the performance of the adopted superstructure during the picked near-field earthquake excitations. The chosen cases were as follows: (i) drained effective stress response analysis (DES analysis case); (ii) undrained effective stress response analysis (UES analysis case); and (iii) undrained total stress response analysis (UTS analysis case). The predicted response spectra, story shear forces, foundation rocking, soil settlements, and structural lateral deflections plus the structural

inter-story drift ratios under the scaled 1999 Chi-Chi (Taiwan) and 1971 San Fernando (USA) earthquakes were scrutinized in this study. The said near-field earthquake excitations were scaled via the spectral matching. It could be concluded that dismissing the generation of the excess pore water pressure in the seismic analyses of the soil-structure systems would result in the safety-threatening design due to overlooking the severe damage, imposed on the structural members and non-structural elements of the superstructures, resting on the shallow foundations.

5.2 Numerical Simulation

A series of hysteretic three-dimensional nonlinear numerical analyses of the soil-structure system was carried out in the time domain using FLAC3D finite difference software and its powerful internal programming language, named “FISH”. The numerical model of the soil-structure system in this study consisted of the solid zones plus the shell and beam structural elements as well as the interface element and free field boundary condition. It should be noted that the three-dimensional finite difference analysis was employed by several other researchers in the various geotechnical earthquake engineering applications (e.g., Zhang et al., 2015; Khosravifar et al., 2018; Yeganeh and Fatahi, 2019). The detailed descriptions of the shallow-founded 15-story building, resting on the saturated clayey sand deposit, along with the employed seismic boundary conditions and appropriate soil-mat foundation interface are presented below.

5.2.1 Modeling of Superstructure and Mat Foundation

The 15-story reinforced concrete moment-resisting building in this study with an approximate total weight of 32 MN satisfied not only the structural and seismic design essentials as to AS/NZS1170.1 (2002), AS1170.4 (2007), and AS3600 (2009), but also the

construction norms. The structural and earthquake engineering software SAP2000 (CSI, 2016) was employed to perform the routine analysis/design procedure. Figure 5.1 presents the details of the designed structural sections of the 15-story building, adopted in this study. Note that the imposed slab action, i.e., the live load onto the floors, equaled 2 kPa as stated in AS/NZS1170.1 (2002) for the domestic and residential activities. Referring to Figure 5.2, the total height and width of the said spatial frame were 45 m and 12 m, respectively, considering the story height of 3 m and three equal bays, i.e., 4 m each, in both horizontal directions.

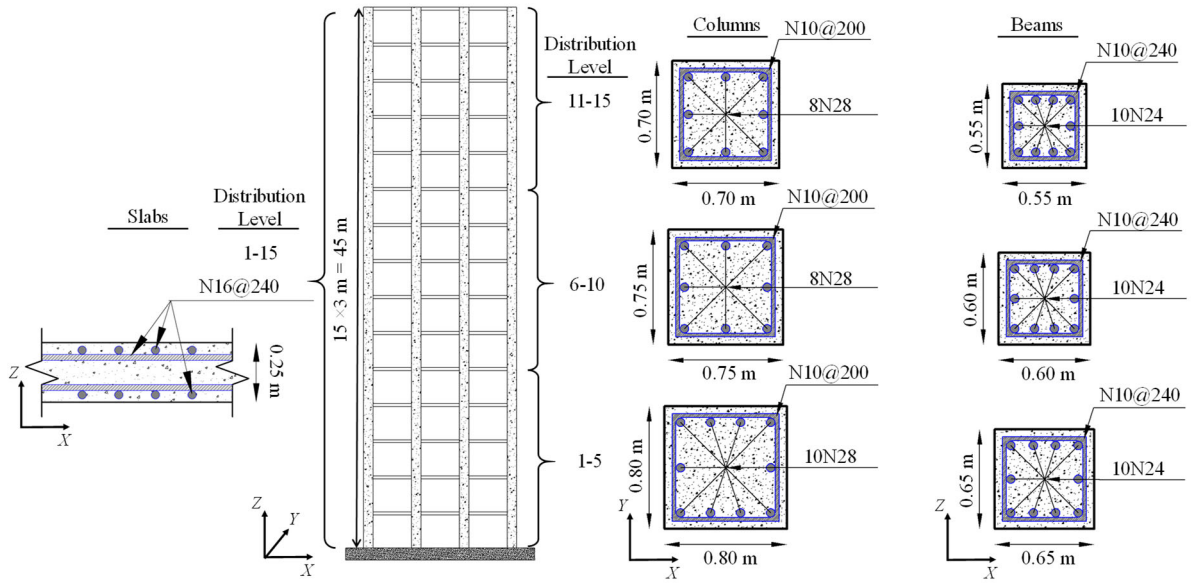

Figure 5.1 Designed structural sections and reinforcement details of columns, beams, and slabs

The columns and beams were modeled via the beam structural element, which is a two-noded, straight element. The seismic force resistance in the adopted superstructure was provided by the structural members and corresponding joints by means of the flexure. The three-noded, flat shell structural element represented the 0.25 m thick concrete slabs in the designed building. The slabs were assumed to provide the rigid planes by being rigidly attached to the surrounding beams and columns in all the six degrees of freedom. The implemented beam and shell structural elements in the numerical model of this study in FLAC3D are exhibited in Figure 5.2b. The material properties of the concrete and steel reinforcements, adopted in this study for the building and mat foundation, are listed in Table 5.1.

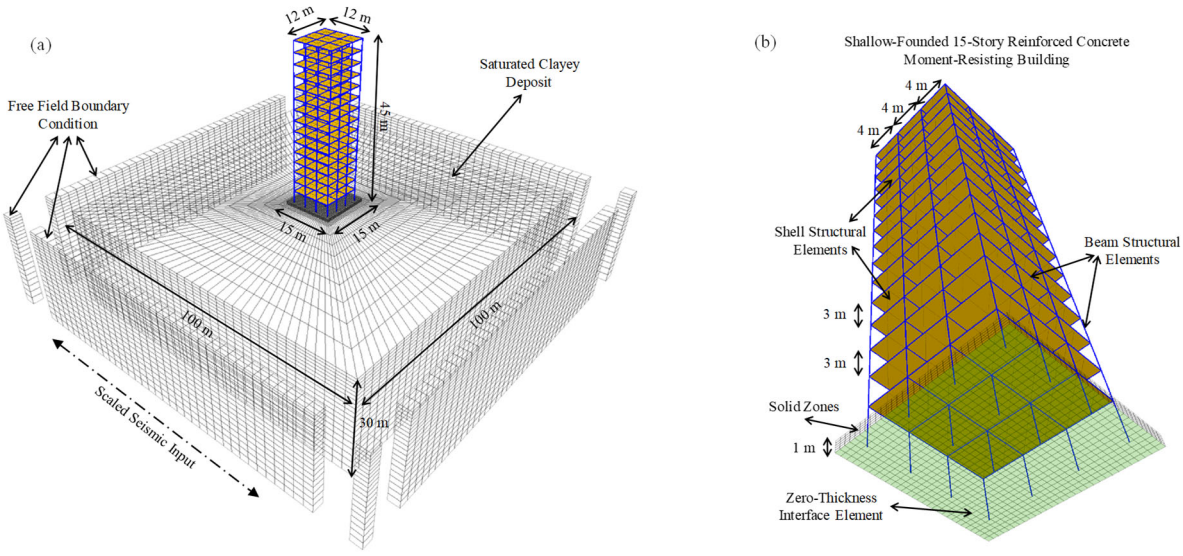

Figure 5.2 Adopted soil-structure system via direct one-step approach in FLAC3D: (a) schematic layout of soil deposit-mat foundation-building frame system, and (b) illustration of structural elements, solid zones, and interface elements

Table 5.1 Adopted properties of concrete material and steel reinforcing bars in designed building and foundation

Material	Property	Notation	Value	Unit	Reference
Concrete	Grade	---	32	---	AS3600 (2009)
	Density	ρ_c	2400	kg/m^3	
	Characteristic Compressive Strength	f_c'	32	MPa	
	Mean In-Situ Compressive Strength	f_{cmi}	35	MPa	
	Modulus of Elasticity	E_c	30.1	GPa	
	Poisson's Ratio	ν_c	0.2	---	
	Bulk Modulus	K_{cc}	16.7	GPa	
Steel Reinforcement	Grade	---	D500N	---	AS/NZS4671 (2001) & Menegon et al. (2015)
	Density	ρ_s	7850	kg/m^3	
	Strength Grade	---	500	MPa	
	Characteristic Yield Strength	f_{sy}	550	MPa	
	Ultimate Stress	f_{su}	660	MPa	
	Ultimate Strain	ε_{su}	9.5	%	
	Modulus of Elasticity	E_s	200	GPa	

To better understand the dynamic behavior of the adopted superstructure under the lateral loadings, the cracked-section flexural stiffness properties were assigned to the reinforced concrete components. Therefore, the moment of inertia of the uncracked structural sections associated with the slabs, beams, and columns underwent the 75%, 65% and 30% reductions, according to ACI318 (2014), listed in Table 5.2. Moreover, the nonlinear behavior of the superstructure was simulated via defining the plastic hinges through introducing the plastic

moment capacity ($M^p = f_c' \frac{\omega l^2}{4}$). The plastic moment capacity limits, reported in Table 5.2, were calculated based on the Grade 32 concrete characteristic compressive strength (f_c'), i.e., 32 MPa, in addition to the width and height of the structural members, denoted by ω and l, respectively, also presented in Table 5.2. It is noteworthy to mention that the elastic-perfectly plastic model supervised the possible nonlinearity in the designed building foundation. Besides, the geometric nonlinearity of the adopted superstructure, capturing the global $P-\Delta$ effect, was accommodated in this study by the use of the large-strain solution mode in FLAC3D. The global $P-\Delta$ effect in all the considered cases, i.e., the DES, UES, and UTS analysis cases, resulted from the destabilizing effect of the gravity loads on the lateral load-induced deflections. The adopted large-strain mode defined a framework wherein the grid point coordinates were updated when the computed displacements were large by comparison with the zone sizes. On that basis, the numerical grids moved when the material yielded. Note that, at each timestep of the analysis in this study, the new positions of the grid points were calculated from the current velocity. Equation (5.1) was in charge of updating each grid point location (Λ_i) with the consideration of the vector component of the velocity (V_i) over the time interval, shown by Δt. In fact, the stress and strain components in the constitutive relation were corrected accordingly during the analysis. The solution for the velocities at the grid points was employed to calculate the strains. The stress correction ($\Delta\sigma_{ij}$), defining the new value of the stress for the next calculation cycle, was computed throughout Equation (5.2). Note that $V_{i,j}$ is the partial derivative of V_i with respect to j.

$$\Lambda_i(t+\Delta t) = \Lambda_i(t) + \Delta t V_i\left(t+\frac{\Delta t}{2}\right) \tag{5.1}$$

$$\Delta\sigma_{ij} = \left[\left(\frac{V_{i,k}-V_{k,i}}{2}\right)\sigma_{kj} - \sigma_{ik}\left(\frac{V_{k,j}-V_{j,k}}{2}\right)\right]\Delta t \tag{5.2}$$

Table 5.2 Adopted plastic moment capacity and assigned cracked moment of inertia to structural elements

Member Type / Unit	Story No.	Level	Element Type	Section Dimension	Plastic Moment Capacity (M^p)	Moment of Inertia	Cracked Moment of Inertia
	---	m	---	m	MN.m	$\times 10^{-2}$ m^4	$\times 10^{-2}$ m^4
Column	11-15	30-45	Beam Structural Element	0.70×0.70	2.74	2.00	1.40
	6-10	15-30		0.75×0.75	3.38	2.64	1.85
	1-5	0-15		0.80×0.80	4.10	3.41	2.39
Beam	11-15	33-45	Beam Structural Element	0.55×0.55	1.33	0.76	0.27
	6-10	18-30		0.60×0.60	1.73	1.08	0.38
	1-5	3-15		0.65×0.65	2.20	1.49	0.52
Slab	1-15	3-45	Shell Structural Element	0.25[1]	---	0.13 pmr[2]	0.03

[1]Thickness.
[2]pmr: per meter run.

With due attention to the merits and demerits of three main damping models, namely, the local damping, hysteretic damping, and Rayleigh damping, elaborated by Mánica et al. (2014), this study implemented the local damping coefficient for the adopted 15-story building and its foundation. α ($= \frac{\Delta\varpi}{\varpi} = \pi\zeta$ as to Itasca (2012)) was the ratio of the dissipated energy ($\Delta\varpi$) per oscillation cycle to the maximum, transient strain energy (ϖ). The local damping coefficient of 0.157 in this study represented the 5% critical damping (ζ) for the building.

The building of interest was supported by a square mat foundation with a thickness of 1 m and a width of 15 m. The adopted foundation possessed the same grades of the concrete and steel reinforcing bars as the superstructure, referring back to Table 5.1. The solid zones were used to model the mat foundation's significant thickness (see Figure 5.2b), capturing its shear deformations under the applied loads, as presented by Yeganeh et al. (2015). As per the Meyerhof method (Meyerhof, 1963) with the use of the bearing capacity, shape, depth, and load inclination factors, the static bearing capacity of the mat foundation under the building gravity loadings was acceptable, fulfilling the minimum required factor of safety (FOS) of 3, suggested by Das (2015). The limiting values of 50 mm and 25 mm for the maximum and differential settlements, reported by Bowles (1996), respectively, were also met in the static

conditions. Furthermore, the seismic bearing capacity degradation stemmed from the reduction of the soil strength due to the shear stresses, transmitted to the soil mass through the soil-structure interface, in addition to the soil inertial forces. Richards et al. (1993) proposed a method for estimating the seismic bearing capacity of a shallow foundation on the soils based on the modification of the static bearing capacity factors, i.e., N_{cS}, N_{qS}, and $N_{\gamma S}$, due to the components of the soil cohesion, ground surcharge pressure, and soil unit weight, respectively. Referring to Richards et al. (1993), the ratios of the seismic to the static bearing capacity factors, i.e., $\frac{N_{cE}}{N_{cS}}$, $\frac{N_{qE}}{N_{qS}}$, and $\frac{N_{\gamma E}}{N_{\gamma S}}$, were derived to be 0.20, 0.15, and 0.10, respectively, for a given horizontal seismic coefficient k_h = 0.5 (note that the subscript E represents the seismic/earthquake). Indeed, k_h was calculated using Equation (5.3), referring to Segrestin and Bastick (1988), related to the horizontal peak base accelerations of the adopted earthquakes, symbolized by a_h. In fact, 0.65g and 0.86g were the horizontal peak base accelerations of the scaled 1999 Chi-Chi earthquake and scaled 1971 San Fernando earthquake, respectively. The seismic bearing capacity of the concrete mat foundation met the factor of safety (FOS) of 1.75, as recommended by Das (2015) under the most extreme conditions, such as the large earthquakes.

$$k_h = \left(\frac{a_h}{g}\right)\left[1.45 - \left(\frac{a_h}{g}\right)\right] \tag{5.3}$$

5.2.2 Modeling of Soil Deposit and Soil-Foundation Interface

The computational cost and efficiency as well as alleviating the boundary effects on the seismic predictions were considered in a series of hysteretic three-dimensional nonlinear numerical analyses of the adopted soil-structure system. Therefore, the optimal dimensions of the soil medium were selected as 100 m × 100 m × 30 m (long × wide × deep), illustrated in Figure 5.2a, so as to lessen the wave reflection from the boundary walls. The brick-type solid

zones constructed the 3D soil medium in this study. The vertical dimensions on the zones were reduced notably from the base of the soil deposit to the interaction domain in order to more accurately capture the larger deformation gradients in the vicinity of the superstructure. At the model base, the vertical zone dimension was 2.9 m based on the one eighth of the minimum wavelength, referring to Kuhlemeyer and Lysmer (1973). The minimum wavelength was divided by 24, suggested by Karimi and Dashti (2016), resulted in the 0.9-m size for the zones adjacent to the mat foundation. Moreover, to benefit the current research study with more reliable input data, the soil properties were taken from the geotechnical report, published by Rahvar (2006), presenting the results of some common in-situ and laboratory tests. The Unified Soil Classification System (USCS) classified the soil at the site as the clayey sand (SC).

The 15-story moment-resisting building was positioned in the plan center of the soil surface, as shown in Figure 5.2a. The plan dimensions of the soil volume, i.e., 100 m × 100 m, in the adopted numerical model were finalized after trial and error by consulting with some suggestions, e.g., the minimum five times the existing building width, suggested by Rayhani and El Naggar (2008), (i.e., 5×12 = 60 m). The soil damping and soil plasticity also reduced the boundary effects on the seismic response of the adopted building. On a separate note, the engineering-seismic bedrock depth was assumed to be at the depth of 30 m as to the standard practice for the site classification, presented in ASCE7-10 (2010), herein corresponding to the shear wave velocity of about 500 m/s, displayed in Figure 5.5b, and unconfined compressive strength, greater than 50 MPa as to NZS1170.5 (2004). The employed depth of the numerical model also satisfied the three times the equivalent radius of the foundation, reported by Ghandil and Behnamfar (2015), i.e., $3\times(1.09\times15)/2 \approx 25$ m.

The transition surface with zero thickness between the concrete mat foundation and soil medium, supervising the possible discontinuity (i.e., the sliding and/or separation) and transfer of the stresses (i.e., the shear and normal stresses), was referred to as the interface element in

this study, depicted in Figure 5.2b. The adopted interface element was a collection of the triangular zones, connecting the foundation and soil grid points together using equal degrees of freedom. The interface nodes possessed the normal and shear springs and sliders. The sliding behavior was captured when the current shear stress at the interface element (τ_{int}), calculated via Equation (5.4), surpassed the interface shear strength ($\tau_{f,int}$) from Equation (5.5), governed by the Mohr-Coulomb failure criterion. Furthermore, the current effective normal stress of the interface element ($\sigma'_{n,int}$) was calculated through Equation (5.6) on the basis of the normal spring stiffness (K_n), interface normal displacement (d_n^{int}), measured from the soil surface towards the foundation base as the target face, and pore water pressure (u).

$$\tau_{int} = K_s(d_s^{int} + \Delta d_s^{int}) \tag{5.4}$$

$$\tau_{f,int} = \sigma'_{n,int} tan\varphi'_{int} + c'_{int} \tag{5.5}$$

$$\sigma'_{n,int} = K_n d_n^{int} - u \tag{5.6}$$

where, K_s is the shear spring stiffness, d_s^{int} and Δd_s^{int} are the previous shear displacement of the interface element and incremental shear displacement between the two consecutive calculation times, respectively, and φ'_{int} and c'_{int} are the effective friction angle of the interface element (= $\tan^{-1}(2/3 \tan \varphi')$ = 25°, while φ' is the soil effective friction angle, which could be found in Table 5.4) and effective cohesion of the interface element (= $2/3\, c'$ = 13 kPa, while c' is the soil effective cohesion, reported in Table 5.4), consecutively.

The shear and normal spring stiffness values in Equations (5.4) and (5.6) were estimated as to the equivalent stiffness of the stiffest neighboring zone over all the zones adjacent to the interface. Equation (5.7), suggested by Itasca (2012), presents the apparent stiffness (K_s and K_n). Since the shear modulus near the ground surface was 118.75 MPa, displayed in Figure 5.5b, and effective Poisson's ratio (ν') was 0.3 (see Table 5.4), the apparent stiffness for the shear and normal springs at the interface element equaled 4.62 GPa.

$$K_s = K_n = 10 \times max\left[\frac{2G}{\Delta z_{min}}\left(\frac{1-\nu'}{1-2\nu'}\right)\right] \quad (5.7)$$

where, Δz_{min} is the smallest dimension of a zone, perpendicular to the interface (i.e., 0.9 m in this study).

The limiting tensile strength (T_{int}) was set to zero. As a consequence, the adopted interface element allowed the foundation to experience the separated state from the soil deposit, i.e., the uplifting/gapping, during the applied earthquake events. Note that the above-mentioned normal and shear stresses were set to zero during the conducted analyses in this study once gapping was formed. In summary, the zero tensile strength interface element, adopted in this study, considered the most influential key factors to the soil stiffness degradation, reported by Ganev et al. (1998), including: (i) nonlinear stress-strain dependence of the soil material; (ii) separation of the soil from the structure; and (iii) effects of the excess pore water pressure.

5.2.3 Seismic Boundary Conditions and Scaled Earthquake Excitations

Considering the cubic soil mass, plotted in Figure 5.2a, the lateral boundaries were only fixed in the horizontal directions under the gravity loading before the earthquake. At the model base, however, all the threefold translational movements were fixed. In the seismic analyses of this study, the rigid boundary condition was adopted at the base of the numerical model, simulating the existence of the strong bedrock. The adopted rigid boundary demonstrated the significant impedance difference between the seismic bedrock and soil deposit. Furthermore, simulating the propagation of the seismic motions along the side boundaries was established herein by assigning the free field boundary condition to the lateral edges of the numerical model. The adopted free field boundary condition, exhibited in Figure 5.2a, consisted of the vertical free field soil elements and absorbing boundaries. The latter was responsible for alleviating the wave reflections from the artificial vertical boundaries. Such an aim was fulfilled in this study by means of introducing the normal and shear independent viscous

dashpots on the side grid points in the main grids, as suggested by Lysmer and Kuhlemeyer (1969). The aforesaid dashpots were in function via the resistant tractions in the shear direction (T_s^{ab} from Equation (5.8)) and normal direction (T_n^{ab} from Equation (5.9)).

$$T_s^{ab} = -\rho C_s v_s \tag{5.8}$$

$$T_n^{ab} = -\rho C_p v_n \tag{5.9}$$

where, ρ is the total soil density (i.e., 1900 kg/m^3, reported in Table 5.4), C_s and C_p are the s-wave and p-wave velocities, respectively, whilst v_s and v_n are the shear and normal components of the velocity at the side boundaries, in the order given.

The free field soil elements at the side boundaries were in the shape of a soil column, separated from the main body of the soil deposit by the above-mentioned dashpots of the absorbing boundaries. The said elements deformed purely in shear, simulating the 1D wave propagation in the 3D infinite boundaries. To replicate the free field ground motion in line with the preceding studies (e.g., Zhang and Liu, 2017), the free field grids and main grids on the same elevations at the opposite vertical sides in the adopted soil model were forced to undergo the equal longitudinal and vertical displacements. As a result, the total boundary tractions were calculated at every timestep by adding the shear (T_s^{ff}, calculated via Equation (5.10)) and normal (T_n^{ff}, calculated via Equation (5.11)) components of the free field tractions to the corresponding resistant tractions, i.e., T_s^{ab} and T_n^{ab}, in Equations (5.8) and (5.9), respectively.

$$T_s^{ff} = \tau^{ff} + \rho C_s v_s^{ff} \tag{5.10}$$

$$T_n^{ff} = \sigma^{ff} + \rho C_p v_n^{ff} \tag{5.11}$$

where, τ^{ff} and σ^{ff} are the free field shear and normal stresses, respectively, and v_s^{ff} and v_n^{ff} are the shear and normal components of the velocity at the side free field, consecutively.

With due attention to the previous studies (e.g., Jennings, 1971; Naeim et al., 2000), the near-field excitations forced the structures to behave in the inelastic range as well as exhibiting

the high values of the inter-story drift ratios owing to the higher inertial forces. Therefore, the two well-known near-field seismic records, namely, the 1999 Chi-Chi (Taiwan) and 1971 San Fernando (USA) earthquakes, were nominated for the seismic assessment of the adopted 15-story reinforced concrete moment-resisting building, resting on a saturated soil deposit. Table 5.3 enlists the main properties of the picked earthquakes. As mentioned earlier, the viscous dashpots coupled the free field and main grids, diminishing the reflections by absorbing the waves, reaching the side boundaries. In consequence, only the seismic bedrock level hosted the aforesaid seismic shaking records, in the form of the acceleration time histories. As a result, the seismic waves were propagating upward within the soil mass from the bottom boundary. It is to be underlined that the durations of the 1999 Chi-Chi and 1971 San Fernando records were reasonably truncated to 17 s and 12 s, respectively, without significantly affecting the outcomes, similar to the previous research studies (e.g., Khaloo et al., 2016).

Table 5.3 Characteristics of cherry-picked earthquake records

Parameter	Seismic Event	
	Chi-Chi Earthquake	San Fernando Earthquake
Year of Occurrence	1999	1971
Country	Taiwan	USA
Recording Station	TCU084	Pacoima Dam
Type	Near-Field	Near-Field
Magnitude (R)	7.6	6.6
Hypocenter Distance (km)	10.33	11.90
Duration (sec)	17	12
Peak Horizontal Acceleration (g)	1.01	1.17
Time of Peak Horizontal Acceleration (sec)	2.43	5.74
Average of Spectral Accelerations (g)	1.48	0.85

Inasmuch as the chosen seismic input motions were applied horizontally at the bedrock, they ought to be scaled to the design response spectrum of such a high velocity bedrock. The response spectrum matching (spectral matching) technique was adopted in this study using the wavelets algorithm based on the improved tapered cosine adjustment function, formulated in Equation (5.12). Al Atik and Abrahamson (2010) proposed the following equation, preventing the drift in the modified velocity and displacement time series, which was adopted in this study.

$$a_j(t) = cos\left[\left(\omega_j\sqrt{1-\beta_j^2}\right)(t - t_j + \Delta t_j)e^{\left[-((t-t_j+\Delta t_j)/\gamma_j)^2\right]}\right] \quad (5.12)$$

where, $a_j(t)$ is the amplitude of the j^{th} wavelet at time t, ω_j is the circular frequency of the j^{th} wavelet, β_j is the damping level, proportion of the critical, of the j^{th} oscillator, t_j is the time of the peak response of the j^{th} oscillator under the action of the j^{th} wavelet, Δt_j is the difference between the time of the peak response (t_j) and reference origin of the wavelet, and γ_j is the frequency dependent coefficient (i.e., $\gamma(f) = 1.178/f^{0.93}$), used to adjust the duration of the adjustment function.

The site class A from NZS1170.5 (2004), representing the strong rock, defined the target response spectrum, plotted in Figure 5.3 through $C(T)$ in Equation (5.13), while the seed response spectra were presented by the picked ground-motion records. Basically, the correction of the differences in the frequency contents of the seed and target response spectra was performed in the framework of the spectral matching method within the specified period range. The minimum and maximum periods of the aforesaid range in this study were 0.3 s and 2 s to account for the higher mode effects and effect of the period elongation due to the potential plastic deformations and soil-structure interaction, respectively. The former was reported by NIST-GCR-11-917-15 (2011) to be chosen as $0.2T$. ASCE7-10 (2010) proposed Equation (5.14) for the calculation of the fundamental period (T) of the concrete moment-resisting frame in the fixed-base condition, which was equal to 1.43 s since the total height (H) of the adopted building was 45 m. The maximum value of the period range, i.e., 2 s, was estimated based on $\sqrt{\mu}T$, recommended by Miranda and Ruiz-García (2002), where μ is the ductility demand, considering 2 in this study for the ordinary concrete moment-resisting frame as to AS1170.4 (2007). Figures 5.3 and 5.4 display the comparison of the response spectra concomitant with the raw and spectrally matched seismic motions plus the time histories of the original and scaled accelerations associated with the picked seismic motions, respectively.

$$C(T) = C_h(T)ZR_p\left\{1 + (N_{max} - 1)\left[\frac{20 - D_{sd}}{18}\right]\right\} \quad (5.13)$$

$$T = 0.0466H^{0.9} \quad (5.14)$$

where, $C_h(T)$ is the spectral shape factor, which is a function of the site subsoil class and building vibration period (T), Z is the hazard factor, equal to 0.45 for an extreme case, much greater than 0.13, R_p is the return period factor, estimated to be 1.0 (i.e., $ZR = 0.45 < 0.7$) on the basis of the importance level of 2, design working life of 50 years, and annual probability of exceedance of 1/500, taken from AS/NZS1170.0 (2002), N_{max} is the maximum near-fault factor (considered to be 1.1 in this study), and D_{sd} is the shortest distance from the site to the nearest fault (assumed to be 3 km in this study).

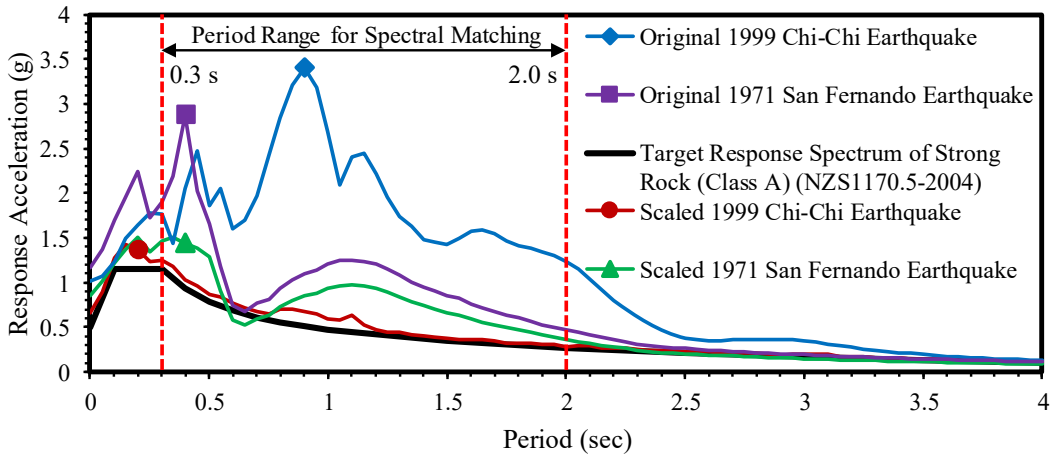

Figure 5.3 Response spectra of seeds, target, and scaled seismic motions

5.2.4 Numerical Simulation of Saturated Soil Behavior

The constitutive behavior of the adopted saturated cohesive soil, symbolized by SC, as a two-phase material, encompassing the soil solids and water in the voids, was captured by the Mohr-Coulomb shear failure envelope in conjunction with the hysteretic damping framework. The so-called elastic-perfectly plastic Mohr-Coulomb soil model with zero dilatancy in this study was a combination of the Hooke's law and Coulomb's failure criterion. The incremental expression of the Hooke's law was adopted in the form of Equation (5.15). The generalized

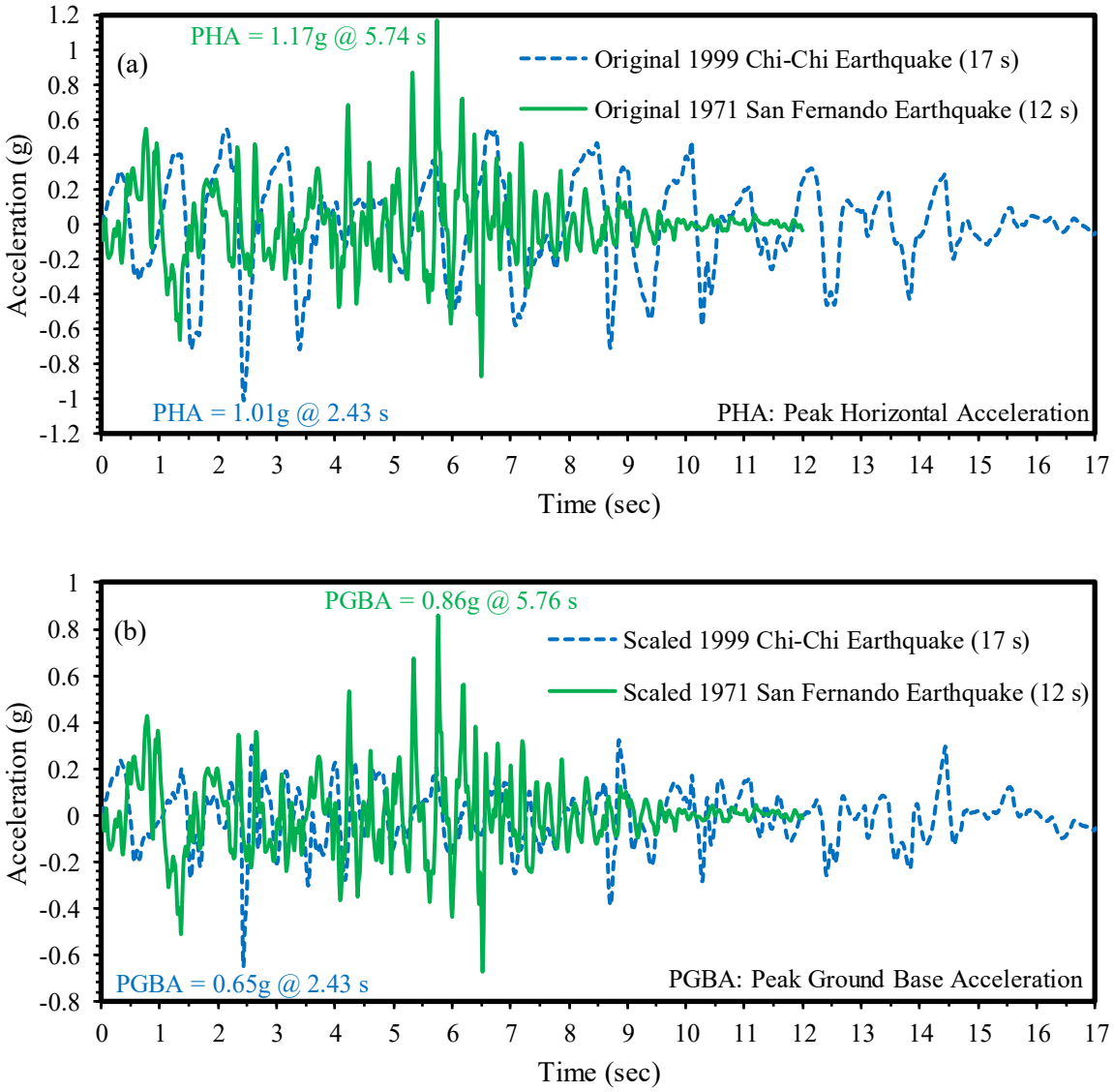

Figure 5.4 Adopted earthquake accelerograms: (a) original seismic records, and (b) matched seismic accelerations

form of the Coulomb's soil shear resistance expression was programmed such that the shear strength of the soil (τ_f) equaled $c' + p'tan\varphi'$, where c' and φ', as the effective strength parameters, are the soil effective cohesion (20 kPa), and soil effective friction angle (35°), respectively, and p' is the mean effective stress (i.e., $p' = (1/3)(\sigma_1' + \sigma_2' + \sigma_3')$). What is more, the Mohr-Coulomb yield yardstick was written in terms of the generalized shear stress ($q = \sqrt{3J_2}$, wherein J_2 is the second deviatoric stress invariant) and p' as to Equation (5.16). Table 5.4 presents the adopted soil parameters for the employed soil constitutive model.

$$\Delta\sigma_{ij} = \left(K' - \frac{2}{3}G\right)\delta_{ij}\Delta\varepsilon_{kk} + 2G\Delta\varepsilon_{ij} \tag{5.15}$$

$$f = q - (p'sin\varphi' + c'cos\varphi')\left[\frac{3}{\sqrt{3}cos\theta_l + sin\theta_l sin\varphi'}\right] \tag{5.16}$$

$$\theta_l = tan^{-1}\left\{\frac{2\sigma_3' - \sigma_1' - \sigma_2'}{\sqrt{3}(\sigma_1' - \sigma_2')}\right\} \tag{5.17}$$

where, K' is the effective bulk modulus, G is the shear modulus, δ_{ij} is the Kronecker delta, $\Delta\varepsilon$ is the strain increment, and θ_l is the Lode's angle.

Table 5.4 Adopted geotechnical properties for clayey sand in this study

Property	Notation	Value	Unit or Description	Reference
Soil Classification	SC	---	Clayey Sand (USCS)	Rahvar (2006)
Soil Thickness	H_s	30	m	
Total Density	ρ	1900	kg/m^3	
Porosity	n	0.35	---	
Plasticity Index	I_P	20	%	
Degree of Saturation	S_r	100	%	
Water Density	ρ_w	1000	kg/m^3	
Water Bulk Modulus	K_w	2	GPa	
Effective Friction Angle	φ'	35	°	
Effective Cohesion	c'	20	kPa	
Effective Poisson's Ratio	ν'	0.3	---	
Undrained Poisson's Ratio	ν_u	0.497	---	
Dilation Angle	ψ	0	°	
Stress Dependency Exponent	κ_1	0.9	---	Hardin and Drnevich (1972)
Plasticity Index-Dependent Exponent	κ_2	0.1	---	
Reference Mean Effective Stress	p^{ref}	100	kPa	Houlsby et al. (2005)
Calibrated Parameters for Hysteretic Damping	α_1	1.0	---	Curve Fitting Procedure (Data Taken From Seed and Idriss (1970))
	α_2	-0.7	---	
	α_3	-1.1	---	

The effective stress approach was utilized in both drained and undrained conditions; nonetheless, the analysis type based on the undrained total stress solution made its way to this research study in light of the popularity among the practicing engineers. Such an analysis, where the undrained shear strength of the soil (S_u) was used to represent the shear strength of the soil during the seismic analysis, was called the undrained total stress (UTS) analysis case

in this study. Wang et al. (2008) highlighted that the in-situ K_0 (i.e., the at-rest earth pressure coefficient) profile of the soil deposit impacts the undrained shear strength of the soil. In this study, K_0 for the adopted clayey deposit was estimated based on the plasticity index (I_P), as proposed by Alpan (1967), and overconsolidation ratio (OCR), as recommended by Caquot and Kerisel (1966), using Equation (5.18). The variations of adopted OCR and K_0 with depth are graphed in Figure 5.5a. Accordingly, the undrained shear strength (S_u) of the soil of interest was computed via Equation (5.19), taken from Hara et al. (1974), where σ'_v is the in-situ effective overburden stress. The variation of the estimated undrained shear strength versus the depth below the ground surface is illustrated graphically in Figure 5.6.

$$K_0 = [0.19 + 0.233 \log I_P(\%)]\sqrt{OCR} \tag{5.18}$$

$$S_u = \sqrt{\left\{\left[\frac{1+K_0}{2}\sigma'_v sin\varphi' + c'cos\varphi'\right]^2 - \left[\frac{1-K_0}{2}\sigma'_v\right]^2\right\}} \tag{5.19}$$

In this study, the dependency of the soil stiffness on the mean effective stress was considered under the seismic loads. In this regard, the adopted stress-dependent shear modulus was expressed as Equation (5.20), recommended by Viggiani and Atkinson (1995), where G_0 is the small-strain shear modulus, displayed in Figure 5.5b, p^{ref} is the reference mean effective stress, conveniently taken as the atmospheric pressure, i.e., 100 kPa (referring to Houlsby et al. (2005)), OCR is the overconsolidation ratio, as plotted in Figure 5.5a, κ_1 is the stress dependency exponent, whose value was 0.9, as suggested by Hardin and Drnevich (1972), and κ_2 is the plasticity index-dependent exponent, equal to 0.1 in this study, based on Hardin and Drnevich (1972) and corresponding to the adopted soil plasticity index of 20%.

$$G = G_0 \left(\frac{p'}{p^{ref}}\right)^{\kappa_1} OCR^{\kappa_2} \tag{5.20}$$

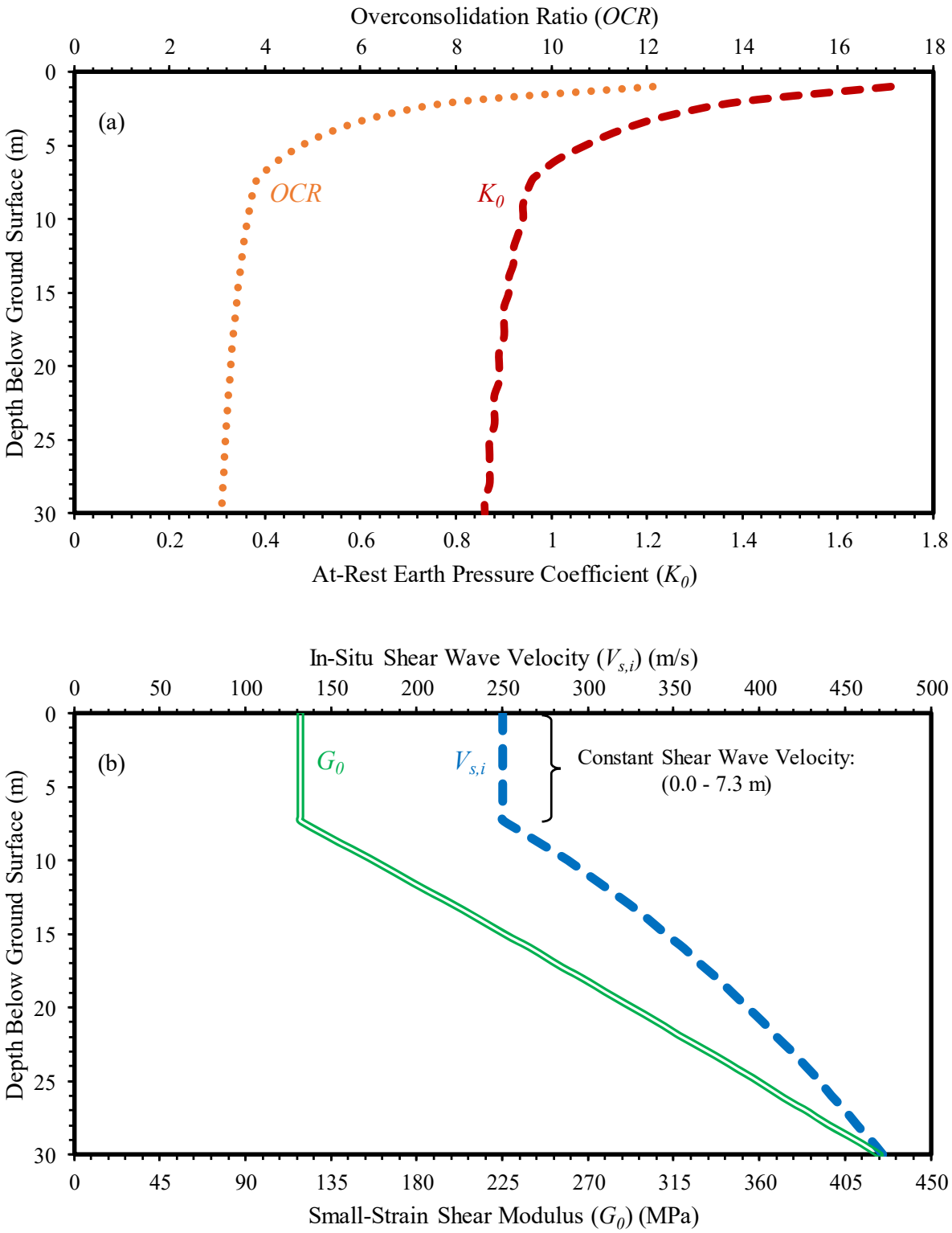

Figure 5.5 Adopted profiles of geotechnical properties for investigated soil: (a) overconsolidation ratio (OCR) and at-rest earth pressure coefficient (K_0), and (b) in-situ shear wave velocity ($V_{s,i}$) and small-strain shear modulus (G_0)

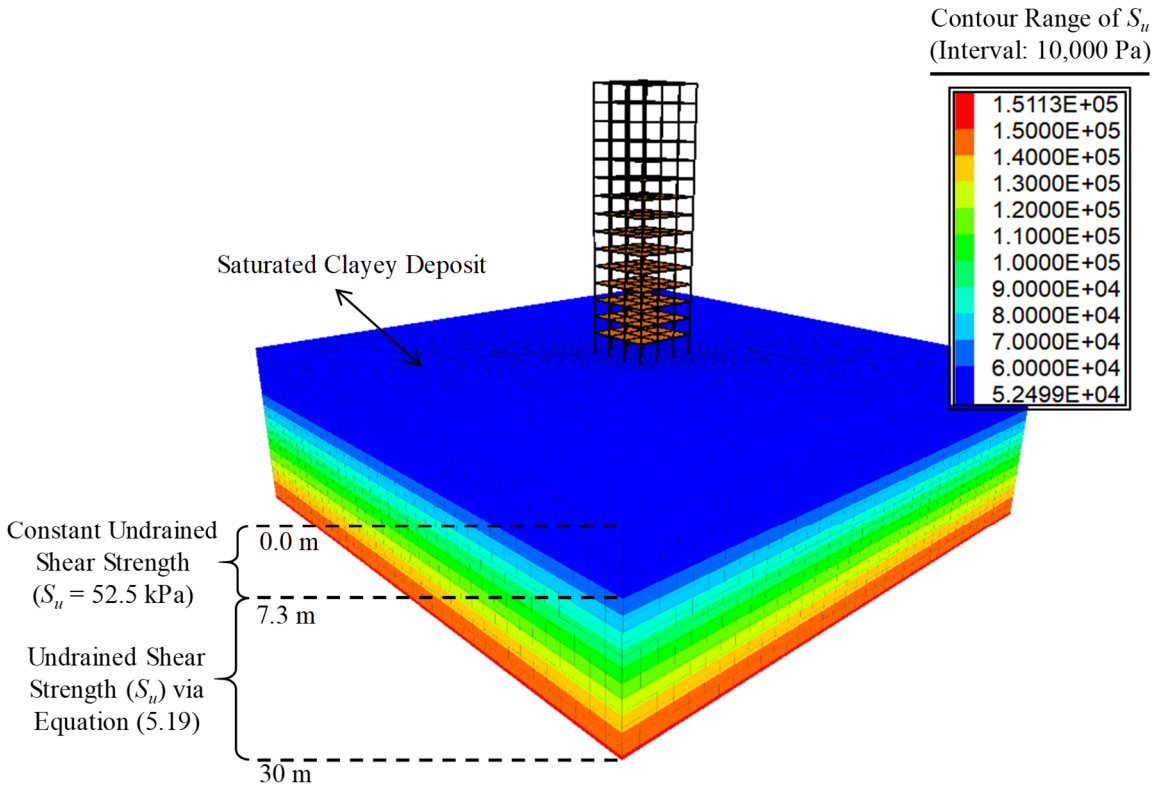

Figure 5.6 Contours of adopted undrained shear strength (S_u) for saturated clayey deposit

The effective bulk modulus under the drained condition, imposed in the DES analysis case, was computed as to the shear modulus (i.e., $K' = (2G)\left[(1+\nu')/\left(3(1-2\nu')\right)\right]$, where ν' = 0.3 is the effective Poisson's ratio. In the UES analysis case, the undrained bulk modulus (K_u) was obtained from Equation (5.21), wherein, K_w is the water bulk modulus, and n is the soil porosity, which were 2×10^9 Pa and 0.35, respectively, reported in Table 5.4. The adopted undrained Poisson's ratio (ν_u) of 0.497, in line with the research work of Stümpel et al. (1984), was relevant to the UTS analysis case wherein the given soil was assumed to be incompressible.

$$K_u = K' + (K_w/n) \tag{5.21}$$

The energy dissipation characteristics of the adopted clayey soil deposit during the cyclically-induced unloading/reloading excursions in this study, stemmed from the hysteretic behavior. Such a behavior could strongly influence the nature and distribution of the earthquake damage, as emphasized by Kramer (1996). The Masing rule (Masing, 1926), implemented in the hysteretic damping algorithm of this study, captured such unloading/reloading responses as

well as the dissipation of the energy in line with the recommendation from Newmark and Rosenblueth (1971). The adopted algorithm also simulated the variations of the shear modulus and corresponding damping ratio with the generated cyclic shear strain in the soil under the scaled earthquake excitations. In that regard, Equation (5.22) was programmed to define the normalized shear modulus reduction curve (i.e., $\frac{G}{G_0} - \gamma$). It needs to be underlined that the implemented hysteretic damping algorithm simulated the nonlinear stress-strain behavior of the adopted soil up to the point of the first reversal and also between the consecutive reversals in the absence of the plastic flow using Equation (5.23), illustrating the soil backbone or skeleton curves.

$$\frac{G}{G_0} = \frac{\alpha_1}{1 + e^{(\alpha_3 - \log\gamma)/\alpha_2}} \tag{5.22}$$

$$\Gamma_{tm} = \frac{G}{G_0} + \gamma \frac{d\left(\frac{G}{G_0}\right)}{d\gamma} \tag{5.23}$$

where, G_0 is the small-strain shear modulus, Γ_{tm} is the normalized tangent modulus, and γ is the cyclic shear strain, whilst α_1, α_2, and α_3 are the calibrated factors, estimated from the curve fitting process.

The variations of G_0 ($= \rho {V_{s,i}}^2$) and in-situ shear wave velocity ($V_{s,i}$) with the depth below the ground surface could be found in Figure 5.5b. In this study, ρ was the total soil density (i.e., 1900 kg/m^3), presumed to be equal to the effective density. The reason was owing to the negligible relative motion between the pore fluid and soil particles, as explained by Qiu et al. (2015), when the shear wave propagated through the adopted saturated soil. The calibrated factors (α_1 = 1.0, α_2 = -0.7, and α_3 = -1.1), also reported in Table 5.4, were estimated by subjecting the soil of interest to the several cyclic shear strains through a one-zone soil sample analysis. Such a trial and error procedure ended when their generated shear modulus reduction

and damping ratio curves, as portrayed in Figure 5.7, were in a good agreement with the corresponding trends, recommended by Seed and Idriss (1970).

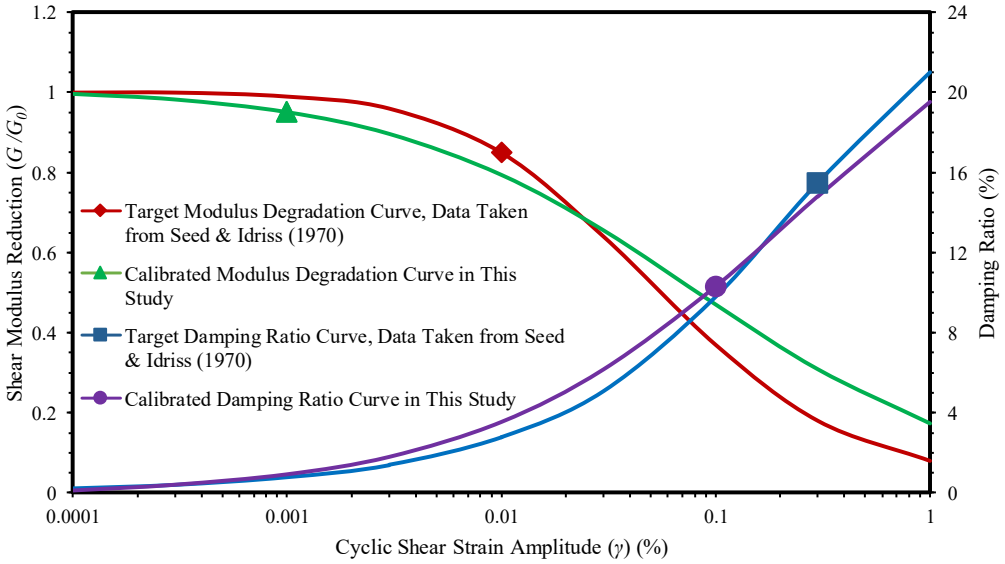

Figure 5.7 Adopted normalized shear modulus reduction and corresponding damping ratio curves via programmed hysteretic damping framework in this study

5.3 Results and Discussions

Following the framework, described in the previous sections, the effects of the seismically-induced excess pore water pressure on the seismic response of a 15-story reinforced concrete moment-resisting building with a mat foundation incorporating the soil-structure interaction are presented and discussed in this section. Comparing the predictions of the drained effective stress response analysis (DES analysis case), undrained effective stress response analysis (UES analysis case), and undrained total stress response analysis (UTS analysis case) formed the core of this research study.

5.3.1 Earthquake Response Spectra

Figure 5.8 displays the response spectra of the motions at the bedrock and ground surface through the Duhamel integral method for a damping value of 5%, suggested by FEMA-P-1050-1 (2015). In line with the previous research studies (e.g., Basu et al., 2019), the amplification

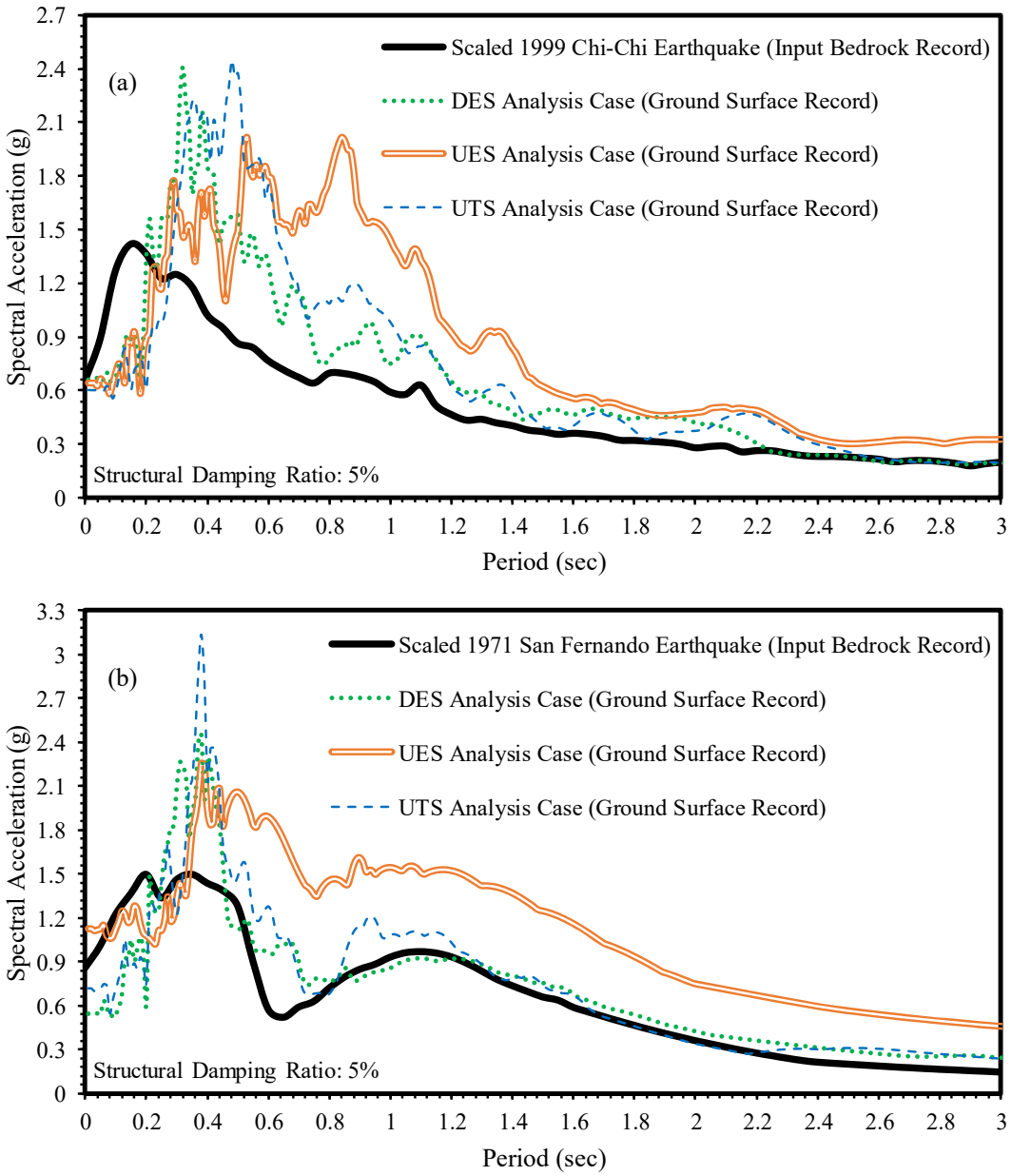

Figure 5.8 Response spectra of bedrock records and ground motions in DES, UES, and UTS analysis cases under excitations of: (a) scaled 1999 Chi-Chi earthquake, and (b) scaled 1971 San Fernando earthquake

of the long-period spectral accelerations, happening in the UES analysis case, as discerned in Figures 5.8a and b, was due to the occurrence of the shear wave velocity reduction. Such a reduction was captured in this study by means of the adopted strain-compatible shear modulus feature through the hysteretic damping framework, referring back to Figure 5.7. The predominant period, wherein the Fourier amplitude spectrum of the bedrock record reached its maximum, presented in Figure 5.9, was determined to be 1 s. The amplification values under

the scaled 1999 Chi-Chi earthquake at the aforesaid period (i.e., 1 s) were 1.26, 2.43, and 1.65, in the DES, UES, and UTS analysis cases, respectively. Considering the scaled 1971 San Fernando earthquake from Figure 5.8b, the amplifications were 1.65 (for the UES analysis case) and 1.16 (for the UTS analysis case) whereas the deamplification factor of around 0.9 was only observed under the drained behavior in the DES analysis case at the known predominant period. Such an underestimation of the amplification on the low frequencies, could be highly prejudicial for the flexible superstructures in the event of the insignificant higher mode effects.

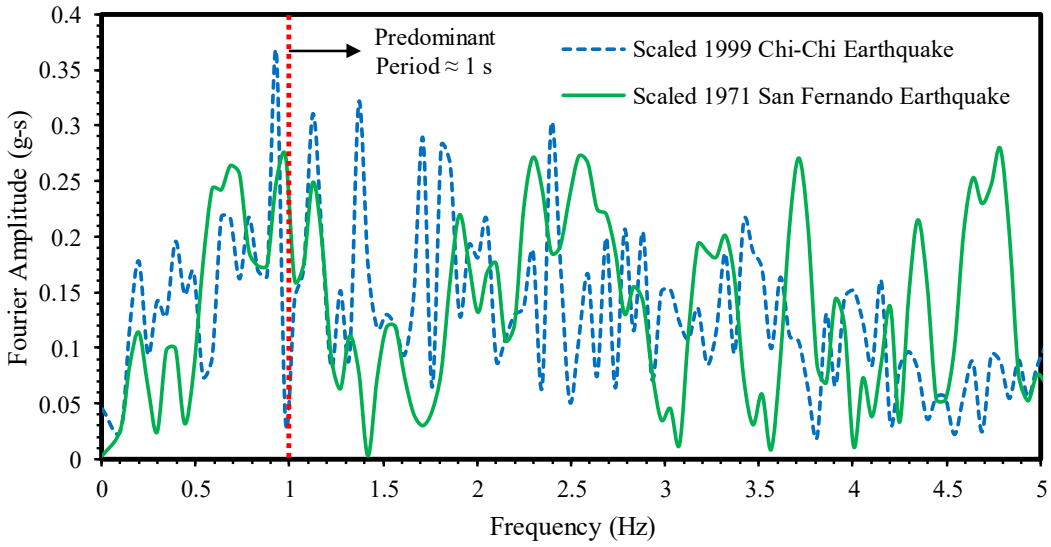

Figure 5.9 Quantitative representation of energy distributions associated with scaled 1999 Chi-Chi and scaled 1971 San Fernando acceleration records over frequency range

Since the excess pore water pressure freely dissipated in the drained condition (i.e., the DES analysis case), the soil stiffness was on the increase due to the overall ascending of the mean effective stress. To back up the last statement, the changes in the mean effective stresses at the depth of 0.5 m beneath the center of the mat foundation were portrayed in Figures 5.10a and b. The maximum difference between the predicted mean effective stresses of the DES and UES analysis cases was 193 kPa, subjected to the scaled 1971 San Fernando earthquake (see Figure 5.10b). The mean effective stress in the UES analysis case reached the minimum value of 42 kPa at the time of 7.76 s, as displayed in Figure 5.10a, whereas the peak mean effective stress

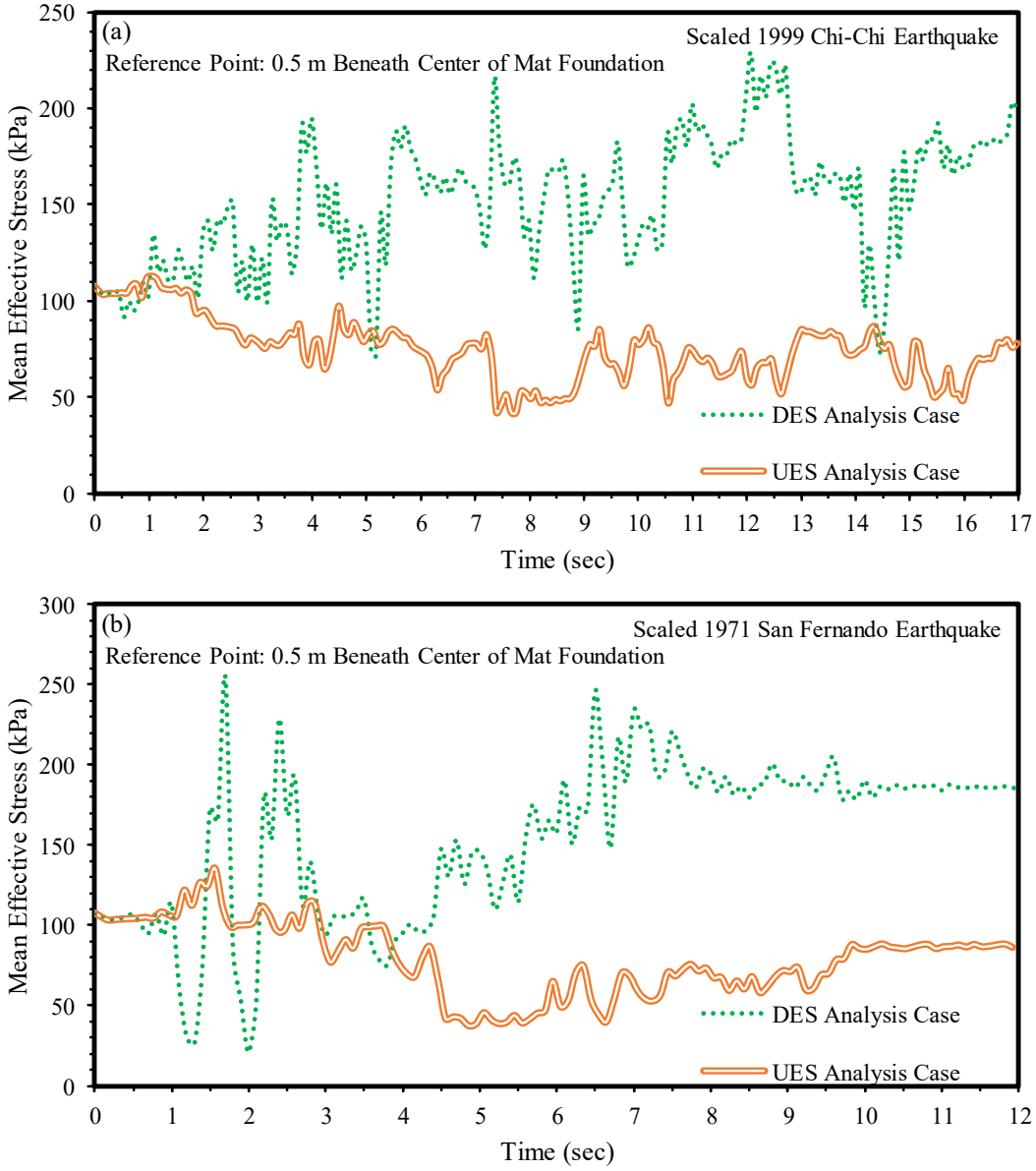

Figure 5.10 Changes in mean effective stress at 0.5 m below foundation center in DES and UES analysis cases under excitations of: (a) scaled 1999 Chi-Chi earthquake, and (b) scaled 1971 San Fernando earthquake

and corresponding time under the scaled 1999 Chi-Chi earthquake, experienced in the DES analysis case, were 229 kPa and 12.07 s, respectively. It is of note that the stress redistribution, which happened in the UES analysis case, resulted in decreasing the mean effective stress and increasing the excess pore water pressure. More importantly, Figure 5.10 clearly showed that the level of the mean effective stresses in the DES analysis case was well more than that of the UES analysis case. Therefore, the soil in the DES case became stiffer according to the stress-

dependent soil stiffness. However, the UES analysis case undertook the increase of the excess pore water pressure instead of the increase in the effective stresses (which took place in the DES analysis case) due to the undrained nature of the problem.

The crucial difference between the UTS case, and the other two cases (i.e., DES and UES) was the locations of the failure planes, causing the possible variations in the soil strength. To say more precisely, the $\varphi_u = 0$ analysis (i.e., the UTS analysis case) had a failure plane at 45° whereas the actual failure took place at an angle of $45 + \varphi'/2$ (i.e., 62.5°). Such a condition delayed the yielding of the soil in the UTS analysis case in comparison with the DES and UES analysis cases. Therefore, the smaller soil deformations and higher seismic lateral forces on the building were expected in the UTS analysis case.

5.3.2 Shear Forces Developed in Superstructure

Figure 5.11 illustrates the shear force distributions along the building height when the summation of all the columns shear forces on a same level reached the utmost amidst the applied excitations. In respect to the superstructure safety control, all the analyzed cases in this study obeyed the shear capacity distribution, plotted in Figures 5.11a and b. The story shear capacity (V_u) was estimated according to AS3600 (2009) based on the ultimate shear strength of the story and contribution of the shear reinforcement via Equation (5.24).

$$V_u = \frac{1.1 n_c}{14 \times 10^3 A_g}\left(14A_g + F_a\right)(1600 - d_0)\sqrt[3]{\omega^2 {d_0}^2 A_t f_c'} + \frac{A_s d_o}{S_s} f_{sy} \tag{5.24}$$

where, n_c is the number of the columns at the story of interest, A_g is the gross cross-sectional area, F_a is the axial compressive force on a cross-section, d_0 is the distance from the extreme compressive fibre of a cross-section to the centroid of the outermost layer of the tensile reinforcement, ω is the width of a cross-section, A_t is the cross-sectional area of the longitudinal tensile reinforcement, f_c' is the concrete characteristic compressive strength, A_s is

the cross-sectional area of the shear reinforcement, S_s is the center-to-center spacing of the shear reinforcement, and f_{sy} is the characteristic yield strength of the reinforcement.

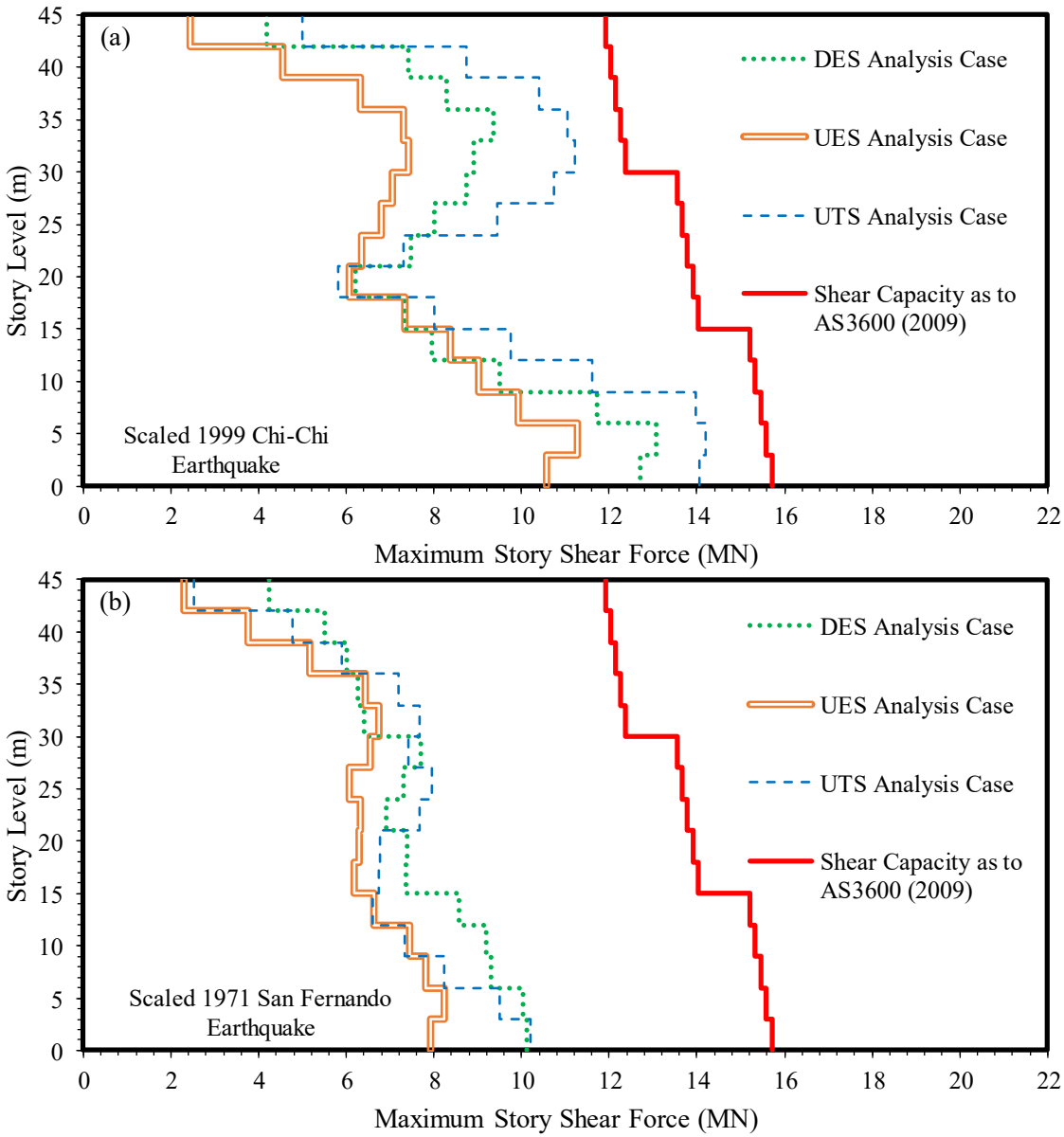

Figure 5.11 Developed shear forces over height of building in DES, UES, and UTS analysis cases under excitations of: (a) scaled 1999 Chi-Chi earthquake, and (b) scaled 1971 San Fernando earthquake

The range of the effective periods attributed to the adopted system of the soil mass and long-period superstructure from the second mode to the first mode, aka “fundamental mode”, was determined to be 0.48-1.89 s using SAP2000 software. The reported second mode period was bracketed by the one-quarter (i.e., 0.47 s) and one-third (i.e., 0.63 s) of the fundamental

period (i.e., 1.89 s) as to NIST-GCR-11-917-15 (2011). The estimated period for the first mode, i.e., 1.89 s, was validated by the effective period for the shallow-founded structure with the consideration of the soil flexibility (i.e., $\tilde{T}_{eff}$). The effective period of the flexible base building ($\tilde{T}_{eff}$ = 1.93 s) was calculated via Equation (5.25), presented in ASCE7-10 (2010), benefiting from the proposed equation of the fundamental period of the fixed-base building in AS1170.4 (2007).

$$\tilde{T}_{eff} = \left\{(0.094H^{0.75})^2 + \left(\frac{17.5W_t}{\pi^{0.5}\gamma_s {A_f}^{0.5}\bar{V}_{s,i}^2}\right)\left(1 + \frac{0.194\pi^{0.25}{A_f}^{0.5}H^2}{I^{0.75}}\right)\right\}^{0.5} \quad (5.25)$$

where, H is the building height (45 m), W_t is the total weight of the building (32 MN), γ_s is the soil unit weight (18,633 N/m^3), A_f is the foundation area (225 m^2), $\bar{V}_{s,i}$ is the weighted average shear wave velocity of the soil profile (350 m/s according to Figure 5.5b), and I is the static moment of inertia of the foundation about a horizontal centroidal axis, normal to the direction in which the structure was analyzed (281.25 m^4).

Figure 5.8 shows that the response spectra of the undrained effective stress model, subjected to the both applied seismic loadings, sat atop those of the DES and UTS analysis cases in the above-mentioned effective period range, i.e., 0.48-1.89 s. Nonetheless, investigating the trends in Figure 5.11 disclosed the extent to which the higher mode effects affected the generated shear forces in the adopted building frame. Taking the results of the scaled 1999 Chi-Chi excitation under scrutiny from Figure 5.8a, the predicted spectral accelerations, corresponding to the first mode, in the DES and UTS analysis cases, i.e., 0.45g and 0.36g, respectively, were in the vicinity of that of the UES analysis case (i.e., 0.46g). Nevertheless, 1.36g, as the second-mode spectral acceleration of the UES analysis case in the same figure, was greatly outnumbered by those of the DES (i.e., 1.57g) and UTS (i.e., 2.44g) analysis cases. In turn, the structural shear force distributions of the DES and UTS analysis cases exceeded the distribution of the structural shear forces in the UES analysis case, presented in Figure 5.11a. Likewise, in

Figure 5.8b, the second-mode spectral acceleration in the UTS analysis case was enlarged by 77% to 1.47g from the first-mode spectral acceleration of the UES analysis case (i.e., 0.83g) under the influence of the scaled 1971 San Fernando earthquake.

Table 5.5 reveals that the shear strains during the picked scaled earthquakes were significant in the shallow depths such as 0.5 m and 1.5 m, where the soil behavior was highly nonlinear owing to the rocking of the superstructure and its foundation, in comparison to the deep depth of 15 m. Considering the results of the scaled 1999 Chi-Chi earthquake from Table 5.5, the cyclic shear strain enjoyed the twofold upsurge by transferring from the UTS analysis case (i.e., 1.40%) to the UES analysis case (i.e., 2.81%) at the depth of 0.5 m beneath the foundation. On that basis, the DES and UTS analysis cases possessed the lowest hysteretic damping, responsible for elevating the predicted base shear from 10.6 MN in the UES analysis case to 14 MN in the UTS analysis case (referring back to Figure 5.11a). The scaled 1971 San Fernando earthquake brought forth the almost 30% surge in the maximum base shear (i.e., 10.21 MN) when disregarding the excess pore water pressure build-up by comparison with the case, wherein the excess pore water pressure was captured (i.e., 7.93 MN in the UES analysis case, shown in Figure 5.11b).

Table 5.5 Seismically-induced shear strains beneath center of mat foundation

Depth (m)	Seismically-Induced Shear Strains Below Foundation					
	Scaled 1999 Chi-Chi Earthquake			Scaled 1971 San Fernando Earthquake		
	DES Analysis Case	UES Analysis Case	UTS Analysis Case	DES Analysis Case	UES Analysis Case	UTS Analysis Case
0.5	1.72%	2.81%	1.40%	1.72%	4.96%	1.28%
1.5	1.78%	1.94%	1.77%	1.14%	3.82%	0.85%
15	0.50%	0.83%	0.39%	0.50%	0.51%	0.19%

The base shear validation exercise was conducted in this study using a set of equations, proposed by NZS1170.5 (2004) and ASCE/SEI-7 (2010), for the estimation of the flexible base structure's base shear. While Equation (5.26) (presented in ASCE/SEI-7 (2010)) aims to determine the base shear, adjusted for the soil-structure interaction phenomenon, shown by $\tilde{V}$,

Equation (5.27) (presented in NZS1170.5 (2004)) calculates the fixed-base structure's base shear (V). Note that Z, R_p, N_{max}, and D_{sd}, equal to 0.45, 1.0, 1.1, and 3 km, respectively, were introduced previously in Equation (5.13). In Equation (5.26), $\tilde{\beta}$ is the fraction of the critical damping for the structure-foundation system, estimated by means of Equation (5.28), suggested by ASCE/SEI-7 (2010), including the foundation damping factor (β_f, considered to be 0.01 in this study).

$$\tilde{V} = V - \left[\frac{\overline{W}}{2} Z R_p \left\{1 + (N_{max} - 1)\left[\frac{20 - D_{sd}}{18}\right]\right\}\left(C_h(T) - C_h\left(\tilde{T}_{eff}\right)\left(\frac{0.05}{\tilde{\beta}}\right)^{0.4}\right)\right] \quad (5.26)$$

$$V = W_t \left(0.5 C_h(T) Z R_p \left\{1 + (N_{max} - 1)\left[\frac{20 - D_{sd}}{18}\right]\right\}\right) \quad (5.27)$$

$$\tilde{\beta} = \beta_f + \frac{0.05}{\left(\frac{\tilde{T}_{eff}}{T}\right)^3} \quad (5.28)$$

$$T = 0.094 H^{0.75} \quad (5.29)$$

where, $\overline{W}$ is the effective seismic weight of the building ($\overline{W} = 0.7 W_t = 2.4$ MN, wherein W_t is the total weight of the adopted moment-resisting building (i.e., 32 MN)), $C_h(T)$ is the spectral shape factor, and $C_h\left(\tilde{T}_{eff}\right)$ is the effective spectral shape factor.

$C_h(T)$ was a function of the site subsoil class and fundamental period (T). The two site classes C (for the shallow soil sites) and D (for the soft soil sites), according to NZS1170.5 (2004), relevant to the adopted soil medium in this study, were considered. In addition, 1.43 s and 1.63 s were the estimated fundamental periods of the fixed-base 15-story reinforced concrete moment-resisting building as per Equations (5.14) and (5.29), proposed by ASCE/SEI-7 (2010) and AS1170.4 (2007), respectively. The effective spectral shape factor ($C_h\left(\tilde{T}_{eff}\right)$) was determined by the effective period of the flexible base building ($\tilde{T}_{eff}$, equal to 1.93 s from Equation (5.25)). Table 5.6 expresses the adopted values of $C_h(T)$ and $C_h\left(\tilde{T}_{eff}\right)$.

Referring to Table 5.6, invoking Equation (5.26) resulted in the range of 6.09 MN to 11.08 MN for the flexible base structure's base shear ($\tilde{V}$). Note that ASCE/SEI-7 (2010) limited the lowest value of $\tilde{V}$ to 70% of the fixed-base structure's base shear (V), which was met in this verification approach as exhibited in Table 5.6. As presented in Figure 5.12, the predicted base shears by the UES analysis case, subjected to the scaled 1999 Chi-Chi (i.e., 10.56 MN) and 1971 San Fernando earthquakes (i.e., 7.93 MN), were reasonably bracketed by the aforesaid code-based flexible base structure's base shears.

Table 5.6 Estimation of code-based flexible base structure's seismic base shear ($\tilde{V}$)

T (sec)	Site Class (NZS1170.5 (2004))	$C_h(T)$	$\tilde{T}_{eff}$ (sec)	$C_h(\tilde{T}_{eff})$	V (MN)	$\tilde{V}$ (MN)	$\tilde{V}_{min} = 0.7V$ (MN)
Equation (5.14): 1.43	C	0.92	1.93	0.69	7.27	6.83	5.09
	D	1.50	1.93	1.12	11.80	11.08	8.26
Equation (5.29): 1.63	C	0.82	1.93	0.69	6.49	6.09	4.54
	D	1.34	1.93	1.12	10.54	9.89	7.38

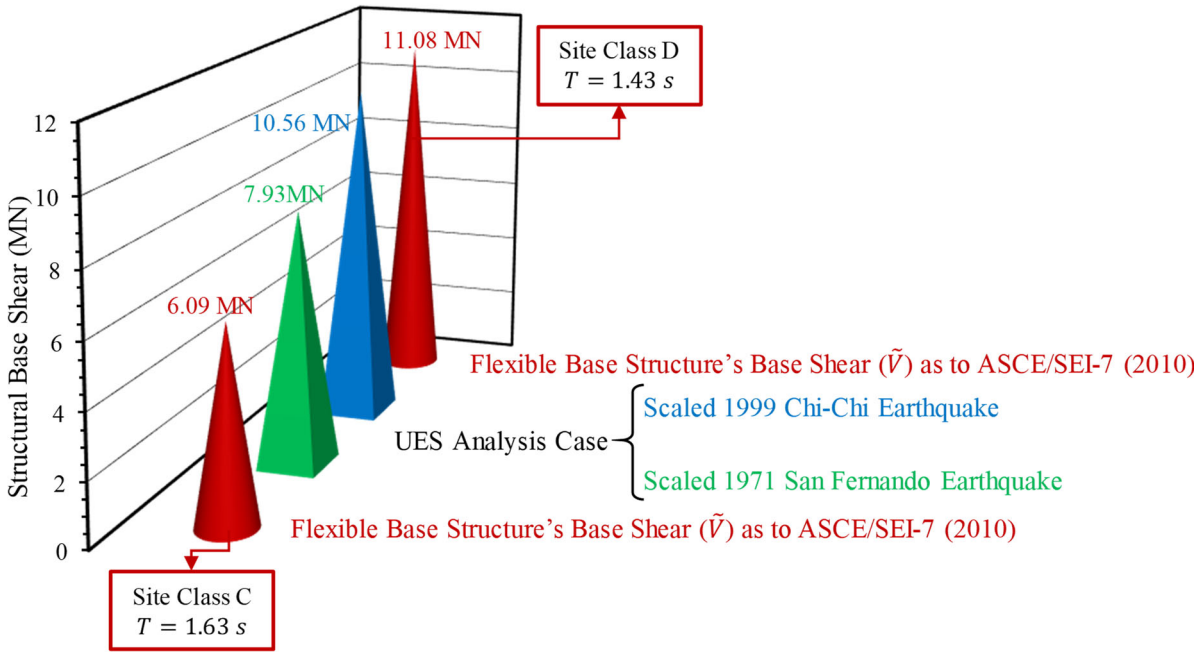

Figure 5.12 Verification of predicted structural base shears in UES analysis case under excitations of scaled 1999 Chi-Chi and scaled 1971 San Fernando earthquakes

Moreover, as stated by Ghaboussi and Dikmen (1984), the higher the PGSA/PGBA ratio, the more hysteretic damping and higher excess pore water pressure build-up. The current

research study also revealed that more hysteretic damping was hosted in the UES analysis case compared to the DES and UTS analysis cases thanks to holding the highest PGSA/PGBA ratio. For instance, the PGSA/PGBA ratios under the scaled 1971 San Fernando earthquake, calculated from Figure 5.8b, were 0.63, 1.31, and 0.83 in the DES, UES, and UTS analysis cases, in the order given. Looking back to Figure 5.8, the Peak Ground Base Acceleration (PGBA) and Peak Ground Surface Acceleration (PGSA) values were at the intersections of the response spectrum trends and vertical axes, titled "spectral acceleration".

5.3.3 Foundation Rocking and Earthquake-Induced Settlements

The histories of the rocking rotations in degrees, plotted in Figure 5.13, were calculated based on the differences in the deformations of the right and left sides of the mat foundation at the same time, divided by the foundation slab width, i.e., 15 m. The predicted amplifications in the long-period spectra, observed in the UES analysis case in Figures 5.8a and b, were believed to produce the large displacements and corresponding significant foundation rocking. Such considerable deformations in the soil foundation, also observed by Torabi and Rayhani (2014), resulted in further rocking-induced excess pore water pressure (referring back to Section 5.3.1) as well as extra reduction in the cyclic shear strain-dependent shear modulus (i.e., the notable soil nonlinearity). The obtained residual foundation rotations (Figure 5.13a), and maximum cyclic shear strains in the vicinage of the concrete foundation (Table 5.5), for the DES, UES, and UTS analysis cases were: (0.49 degrees, 1.72%), (0.99 degrees, 2.81%), and (0.14 degrees, 1.40%), respectively, for the scaled 1999 Chi-Chi earthquake. The higher generated cyclic shear strains in the UES analysis case resulted in the considerable permanent foundation rocking, i.e., 0.99 degrees. Taking the scaled 1971 San Fernando seismic event as an example, the permanent foundation rocking was on the decrease from the UES analysis case to the UTS analysis case due to the captured shear strain decrement. The residual rocking

rotations, corresponding to the UES, DES, and UTS analysis cases, were 1.09 degrees, 0.41 degrees, and 0.25 degrees, taken from Figure 5.13b, consecutively, with the corresponding maximum cyclic shear strains, being 3.82%, 1.14%, and 0.85%, as Table 5.5 presents for the depth of 1.5 m below the foundation center, respectively.

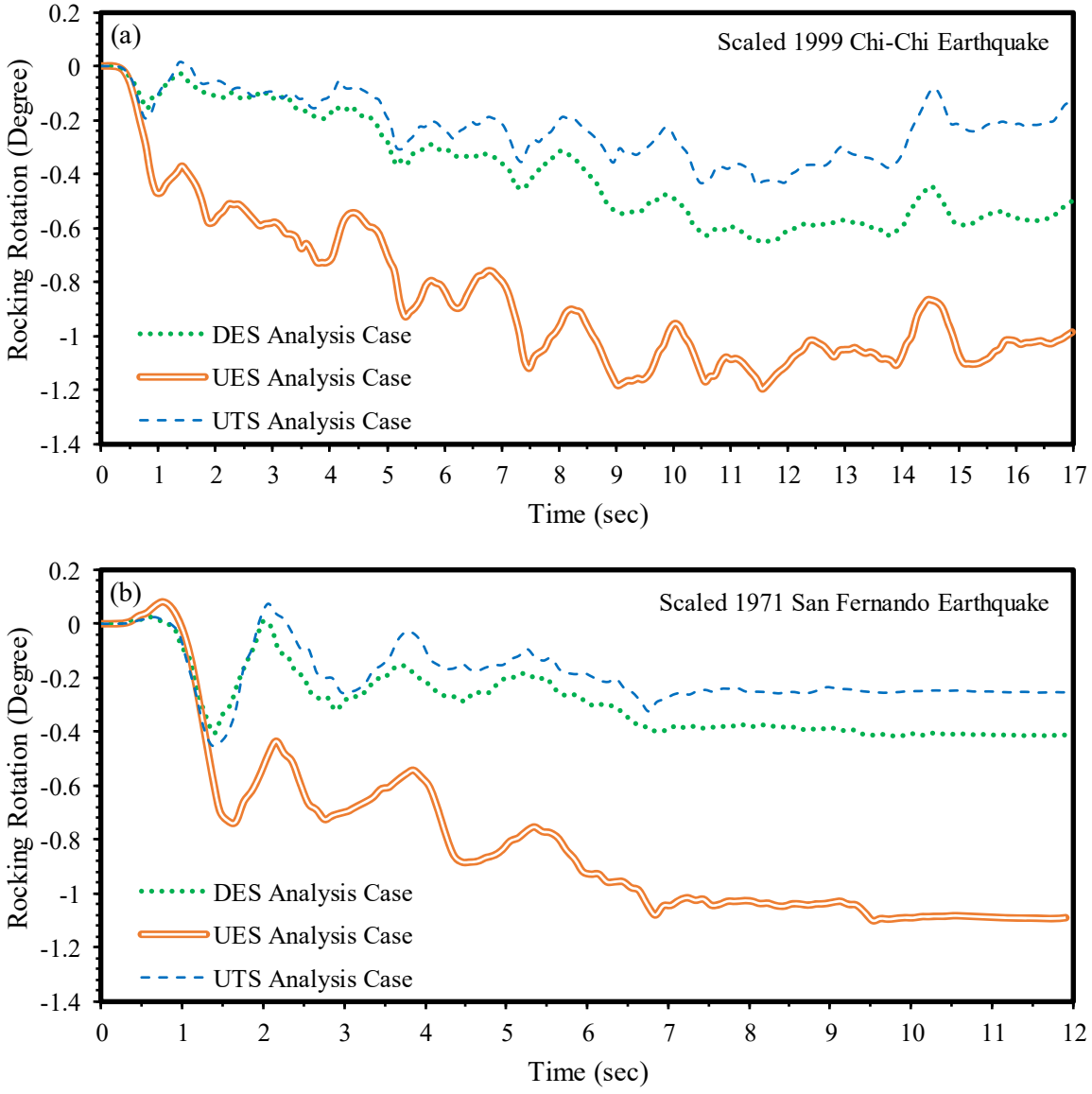

Figure 5.13 Foundation rotation histories in DES, UES, and UTS analysis cases under excitations of: (a) scaled 1999 Chi-Chi earthquake, and (b) scaled 1971 San Fernando earthquake

As mentioned earlier, the component of the excess pore water pressure build-up due to the foundation rocking caused the reduction in the mean effective stresses in the UES analysis case, illustrated in Figure 5.10. On that basis, Figures 5.13a and b consequentially portray the

detrimental effects of the excess pore water pressure generation because of the significant diminishment in the stress-dependent soil stiffness of the UES case in line with Equation (5.20). According to Figure 5.13a, the scaled 1999 Chi-Chi earthquake led to the maximum rocking rotations of 0.66, 1.20, and 0.44 degrees in the DES, UES, and UTS analysis cases, respectively. As can be seen in Figure 5.13b for the scaled 1971 San Fernando earthquake, the predicted maximum rocking rotation and its occurrence time in the UES analysis case were 1.1 degrees and 9.6 s, in the order given. Under the aforesaid excitation, the superstructure and its mat foundation in the DES analysis case (with the rocking angle of 0.42 degrees) and UTS analysis case (with the rocking angle of 0.45 degrees) roughly experienced one third of the maximum rocking rotation in the UES analysis case (i.e., 1.1 degrees). Additionally, referring to Figure 5.11, the reduced lateral forces for the 15-story building in the UES analysis case compared with the DES and UTS analysis cases, could be concluded. Such an observation was a consequence of the considerable foundation rocking-induced damping, happening in the UES analysis case in this study. Previously, Kim et al. (2015) reported that ascending the soil inelastic strain could be the reason behind such significant damping in the event of the marked rocking rotation.

The vertical displacements at the center of the mat foundation, recorded during the applications of the scaled 1999 Chi-Chi and scaled 1971 San Fernando bedrock inputs, were graphically illustrated in Figure 5.14 in conjunction with the corresponding differential settlements. In order to quantitatively evaluate the performance of the designed mat foundation in the adopted soil-structure system, the allowable settlement, ranged between 50 to 125 mm, reported by Bowles (1996), was harnessed for the adopted clayey sand. As evident in Figure 5.14b, the predicted maximum vertical displacements at the center of the foundation in the DES (i.e., 83 mm) and UTS (i.e., 39 mm) analysis cases under the scaled 1971 San Fernando excitation were bracketed by the 50 to 125 mm range. In contrast, the foundation in

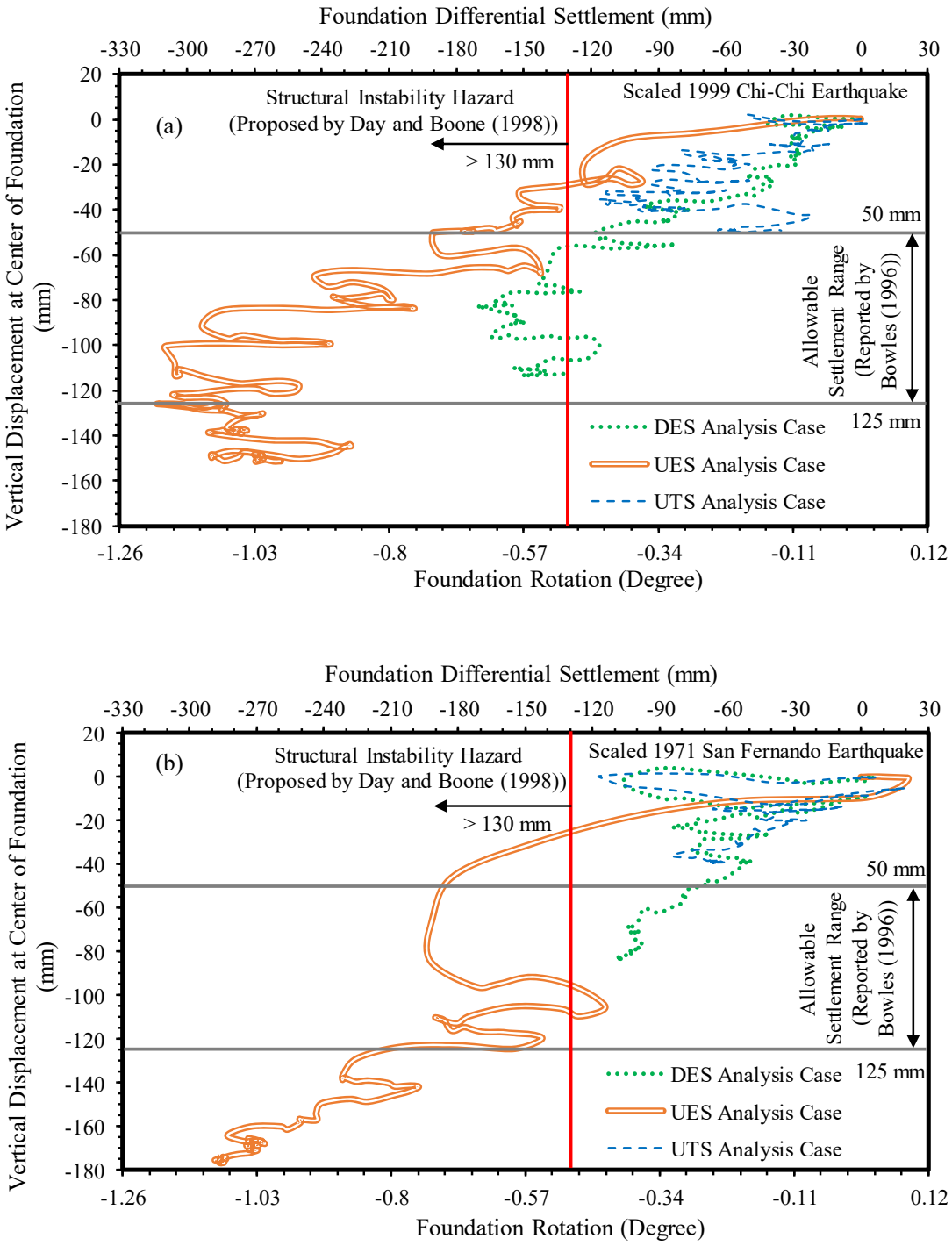

Figure 5.14 Vertical displacements at center of foundation, differential settlements, and foundation rotations in DES, UES, and UTS analysis cases during excitations of: (a) scaled 1999 Chi-Chi earthquake, and (b) scaled 1971 San Fernando earthquake

the UES analysis case settled around 177 mm, as Figure 5.14b shows, which well exceeded the allowable settlement, owing to the observed soil nonlinearity and rocking-induced excess pore water pressure. The same story line could be stated based on the results of the DES (114 mm $\in$ [50, 125]), UES (151 mm $\notin$ [50, 125]), and UTS (50 mm $\in$ [50, 125]) analysis cases,

subjected to the scaled 1999 Chi-Chi seismic event (see Figure 5.14a). Indeed, misleading the design engineers emerged from indicating the unrealistic safety of the superstructure once ignoring the simulation of the excess pore water pressure in the seismic analysis.

The maximum differential settlement in the UES analysis case was 313 mm when the scaled 1999 Chi-Chi earthquake shook the soil-structure system. Such a pronounced transient differential settlement along with the 258 mm residual differential settlement in the UES analysis case, as can be seen in Figure 5.14a, breached the 130 mm limit, proposed by Day and Boone (1998). Indeed, "Very Severe" is the descriptive name of that damage category, corresponding to the 130 mm differential settlement in the realm of the ground-movement-related building damage assessment. A major repair job, involving the partial or complete rebuilding, and the danger of the structural instability throughout the loss of the bearing in some of the structural elements could be accordingly expected. Likewise, Figure 5.14b discloses that the predicted transient differential settlements of the DES (i.e., 109 mm) and UTS (i.e., 117 mm) analysis cases, were elevated by 164% and 146%, respectively, to 288 mm ($\prec$ 130 mm, well exceeding the very severe damage limit), corresponding to the UES analysis case, subjected to the scaled 1971 San Fernando seismic event. Additionally, Figure 5.15 portrays the 2D contours of the residual vertical displacements at the cross section, passing from the center of the mat foundation, directly derived from the conducted numerical simulations. The presented results in Figures 5.15a to c (for the scaled 1999 Chi-Chi earthquake) and Figures 5.15d to f (for the scaled 1971 San Fernando earthquake) also demonstrated the hazardous soil deformations, predicted in the UES analysis case.

According to Teachavorasinskun et al. (2001), the shear modulus is dominated much more by the shear strains than by the effective stress changes. In the current study, the seismically-induced shear strains, presented in Table 5.5, were higher in the DES analysis case than the UTS analysis case. As a result, the foundation rocking (see Figure 5.13) as well as the total and

differential settlements (see Figure 5.14) for the DES analysis case outweighed their counterparts in the UTS analysis case.

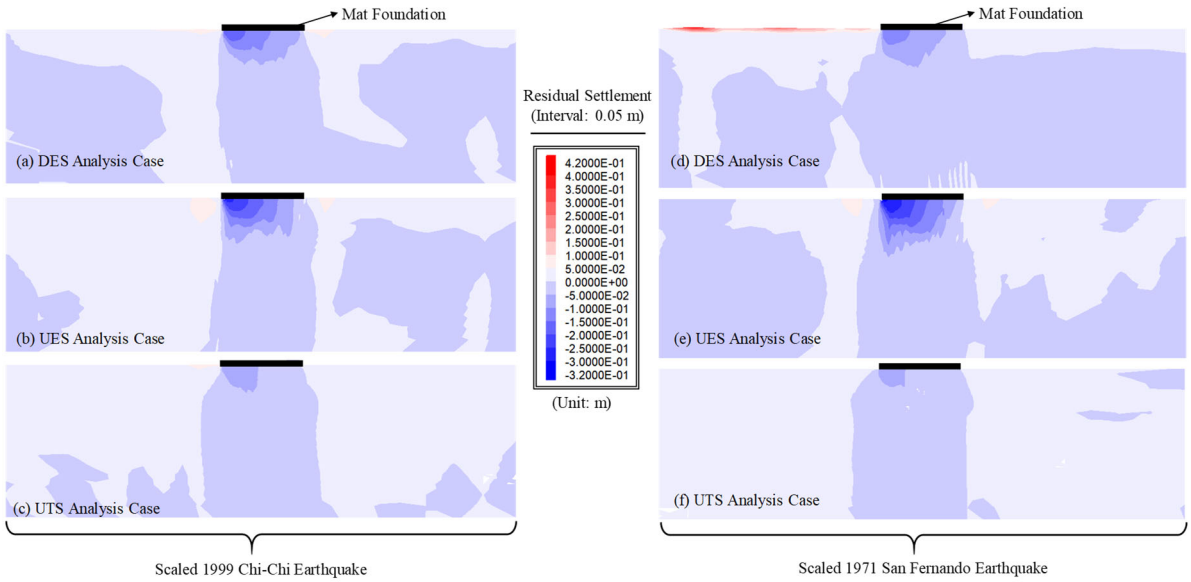

Figure 5.15 Contours of residual vertical displacements at cross section passing from center of foundation in DES, UES, and UTS analysis cases subsequent to scaled 1999 Chi-Chi earthquake (a, b, and c) and scaled 1971 San Fernando earthquake (d, e, and f)

5.3.4 Structural Lateral Deflections

Figure 5.16 exhibits the transient lateral displacements of the 15-story building when the rooftop lateral displacements were observed to be maximum. For instance, the predicted transient lateral displacements at the rooftop were 460 mm and 497 mm (Table 5.7), due to the scaled 1971 San Fernando earthquake in the DES and UTS analysis cases, respectively. However, the UES analysis case predicted the 953 mm lateral displacement (Figure 5.16b), at the rooftop for the aforesaid earthquake. Considering the results of the scaled 1999 Chi-Chi seismic record in Figure 5.16a, the maximum transient lateral displacement of the rooftop in the UES analysis case (1051 mm) was 66% and 126% more than the corresponding values in the DES (i.e., 635 mm) and UTS (i.e., 466 mm) analysis cases, consecutively. It could be inferred that the seismic assessment of the shallow-founded structures on a saturated deposit had better be done throughout the undrained effective stress approach.

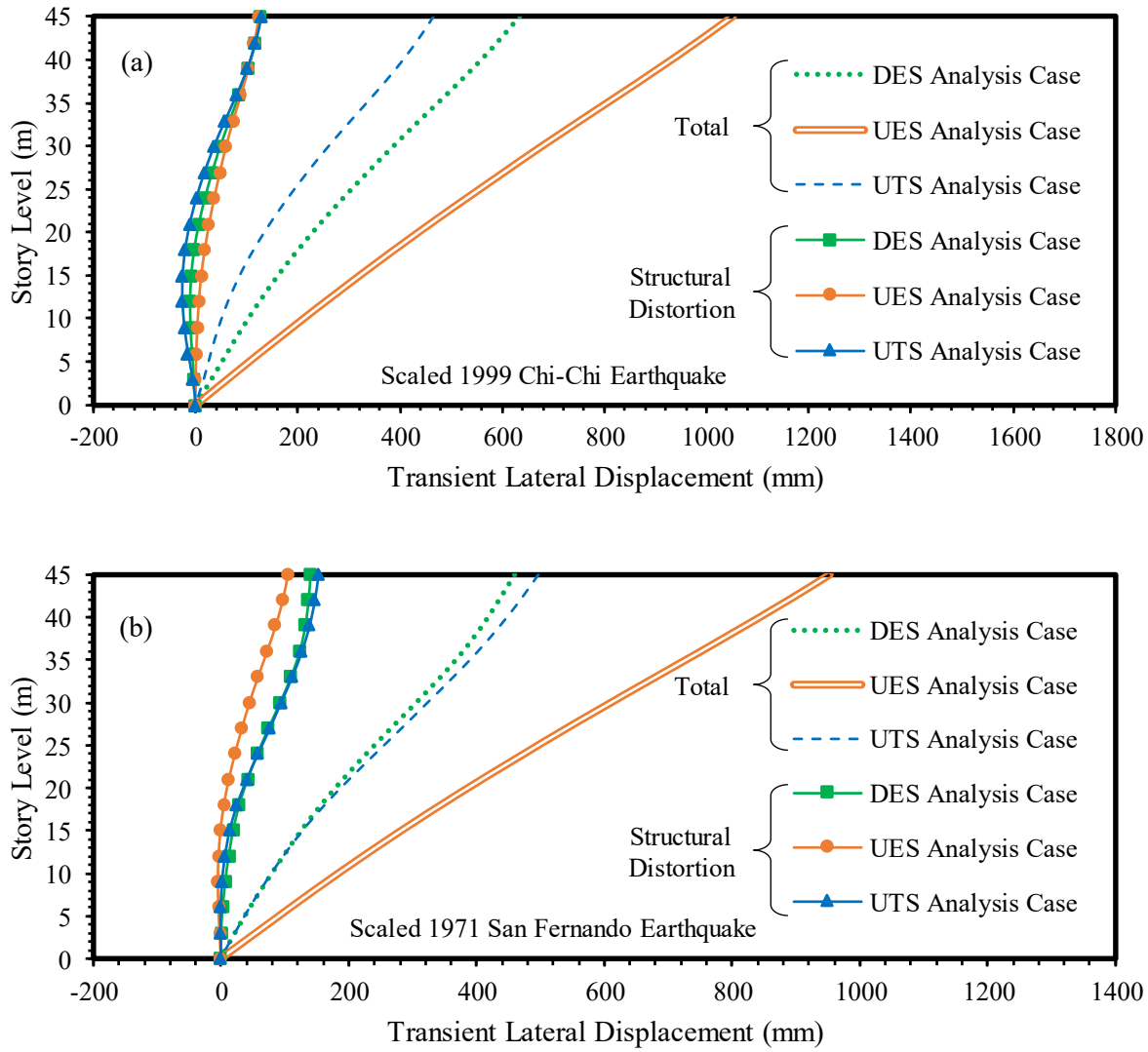

Figure 5.16 Transient total and structural distortion-induced lateral displacements of 15-story superstructure in DES, UES, and UTS analysis cases under excitations of: (a) scaled 1999 Chi-Chi earthquake, and (b) scaled 1971 San Fernando earthquake

Table 5.7 Predicted transient total lateral displacements plus foundation rocking and structural distortion components of 15-story superstructure at rooftop

Applied Excitation	Analysis Case	Transient Total Lateral Displacement (mm)	Foundation Rocking Component (mm)	Structural Distortion Component (mm)
Scaled 1999 Chi-Chi Earthquake	DES	635	508	127
	UES	1051	928	123
	UTS	466	338	128
Scaled 1971 San Fernando Earthquake	DES	460	321	139
	UES	953	849	104
	UTS	497	345	152

Note that the lateral translations of the mat foundation, having the negligible effects on the system frequency changes, as mentioned by Jennings and Bielak (1973), were deducted from

the lateral movements of the building stories prior to sketching out Figure 5.16. As a result, the foundation rocking and story structural distortion constructed the seismic structural lateral displacements, measured at the center of mass at each story level, as illustrated by Zeevaert (1991). The structural distortion components of the lateral deflections, also presented in Figure 5.16, directly corresponded to the shear forces, generated in the building columns. Comparing the trends of the transient structural distortion-induced lateral displacements and transient total lateral displacements for all the considered cases revealed that the story structural distortion played a less critical role in the variations of the structural lateral deflection. For instance, nearly 90% of the rooftop's transient total lateral displacement in the UES analysis case (i.e., 1051 mm) under the scaled 1999 Chi-Chi earthquake was governed by the foundation rotation (i.e., 928 mm), reported in Table 5.7. A scrutiny of Figure 5.16b and Table 5.7 for the scaled 1971 San Fernando earthquake set forth that the predicted ratio of the transient structural distortion-induced lateral displacement to the transient total lateral displacement at the rooftop was lessened from 30% in the DES and UTS analysis cases to 10% in the UES analysis case. Such a change could be due to the effects of the higher structural vibration modes as the structural distortion was directly related to the generated shear forces in the superstructure. As explained in Section 5.3.2, the higher mode effects were activated in the analyzed soil-structure system when disregarding the excess pore water pressure build-up in the adopted saturated clayey sand deposit. The said higher mode effects elevated the shear forces along the building height in the DES and UTS analysis cases (see Figure 5.11), signifying the increase in the structural distortions. As mentioned in the previous sections, the cyclic shear strains, generated in the UES analysis case, listed in Table 5.5, lowered the strain-compatible shear modulus and increased the corresponding damping ratio. The latter was the reason for the reduced story shear forces in the UES analysis case as compared to the DES and UTS analysis cases, referring back to Figure 5.11. The more the soil shear modulus reduced, the more the foundation rocked

during the applied earthquakes, illustrated in Figure 5.13. The numerical predictions of the time history of the excess pore water pressure in the UES analysis case, subjected to the 1999 Chi-Chi earthquake, are presented in Figure 5.17 for the different depths within the saturated soil medium. As exemplified in Figure 5.17, the amount of the excess pore water pressure was on the decrease as the depth of the reference point increased.

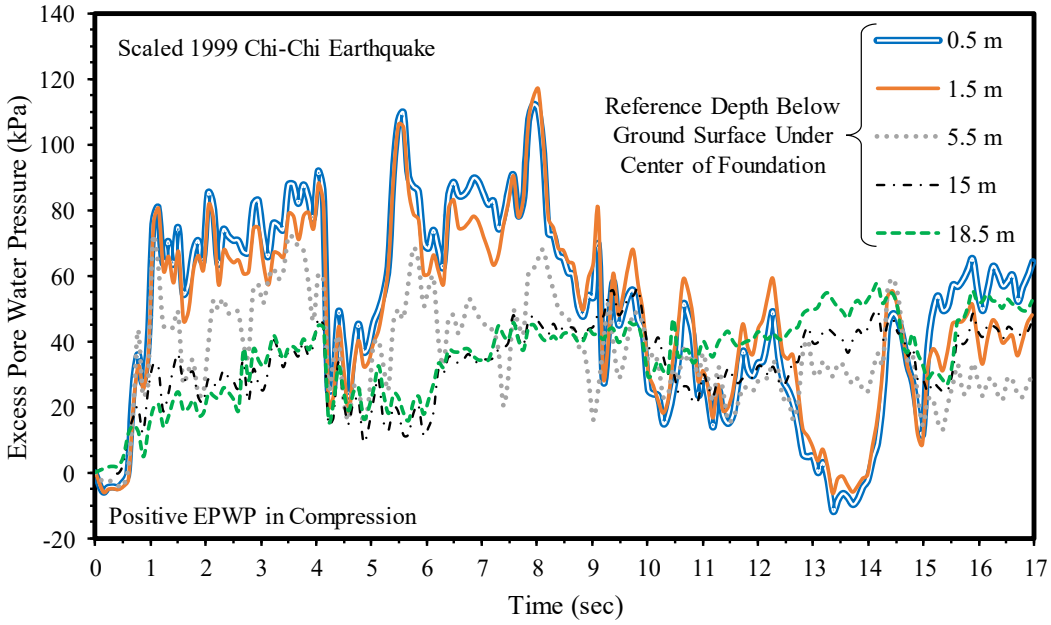

Figure 5.17 Excess pore water pressure histories of reference depths beneath foundation center in UES case subjected to scaled 1999 Chi-Chi earthquake

According to Priestley (1993) and Bojórquez and Ruiz-García (2013), the residual lateral displacement demand could have the irreparable consequences on the seismic performance of a superstructure given the difficulty of straightening a bent building after an earthquake excitation. Referring to Figure 5.18, displaying the permanent lateral deflections of the superstructure under both applied earthquakes, the maximum residual lateral displacements occurred at the rooftop in the DES, UES, and UTS analysis cases. The application of the UES analysis case predicted 775 mm and 857 mm as the maximum residual lateral displacements under the scaled 1999 Chi-Chi and scaled 1971 San Fernando bedrock inputs, respectively. The said values surpassed 410 mm as the allowable residual lateral displacement with due attention to 45 m as the height of the 15-story building. The said limiting value was based on the

reparability limit of the overall residual deflection angle, i.e., 1/110, suggested by Iwata et al. (2006). Quite differently, the DES and UTS analysis cases misleadingly met the aforesaid yardstick (i.e., 410 mm) by wrongly predicting the acceptable post-earthquake states. Looking back to Figure 5.18b, the rooftop residual lateral displacement in the DES analysis case, subjected to the scaled 1971 San Fernando earthquake, was diminished by 62% to 325 mm compared to 857 mm of the UES analysis case. Additionally, the adopted building frame exhibited only 106 mm of the residual lateral displacement at the rooftop in the UTS analysis case under the influence of the scaled 1999 Chi-Chi earthquake, as reported in Figure 5.18a. Therefore, the detrimental consequences of ignoring the excess pore water pressure in the seismic simulations of a saturated soil deposit could be summarized as follows: (i) partial or the total loss of the structural elements; (ii) increased cost of replacement/repair of the non-structural components; (iii) impaired response of the building to a subsequent earthquake due to its post-earthquake tilted geometry; (iv) inhabitability and nonfunctionality of the building; and (v) psychological and physiological discomfort, imposed on the occupants.

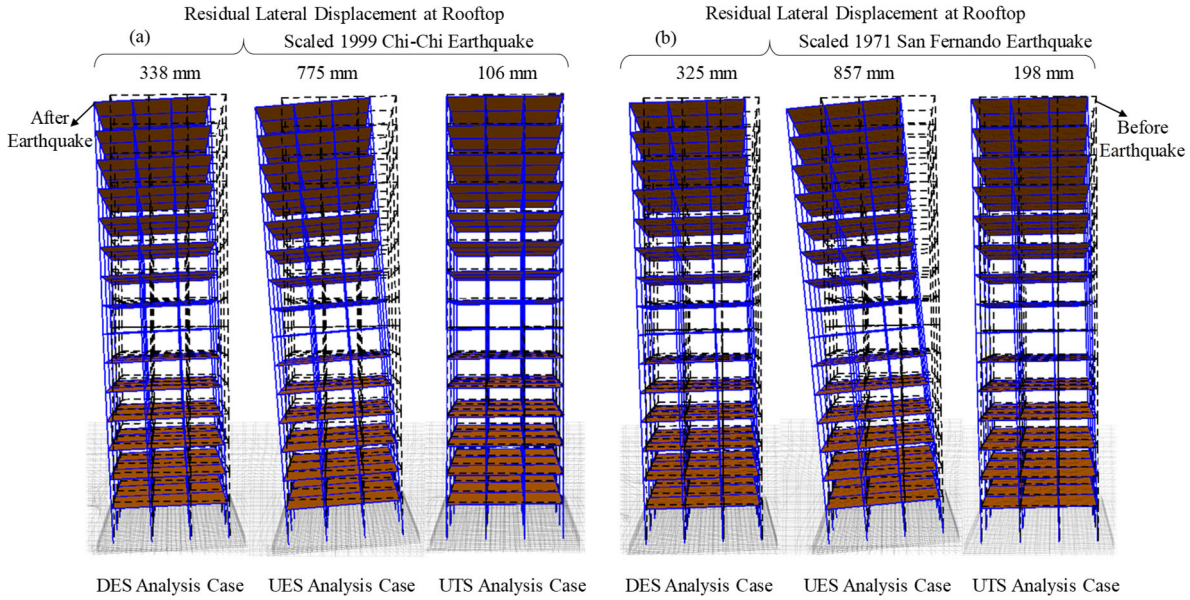

Figure 5.18 Predicted residual lateral deflections of 15-story superstructure in DES, UES, and UTS analysis cases under excitations of: (a) scaled 1999 Chi-Chi earthquake, and (b) scaled 1971 San Fernando earthquake

5.3.5 Structural Inter-Story Drift Ratios

The caption on Figure 5.19 states the transient total inter-story drift ratios of the building, determined as to AS1170.4 (2007) using Equation (5.30). The UES analysis case, subjected to the scaled 1999 Chi-Chi (presented in Figure 5.19a) and scaled 1971 San Fernando (displayed in Figure 5.19b) earthquakes, ended up with the highest transient total inter-story drift ratios, surpassing the 2% acceptable criterion, required by FEMA273 (1997). Indeed, FEMA273 (1997), as a performance-based seismic design code, proposed the 2% life safety drift ratio limit, implying the potentially significant and costly damage, occurring to the structural members and non-structural components during an earthquake. Moreover, the 45% and 70% increases in the maximum transient total inter-story drift ratios from the DES (i.e., 1.76%) and UTS (i.e., 1.51%) analysis cases to the UES analysis case (i.e., 2.56%), consecutively, were observed in Figure 5.19a. Breaching the above-mentioned 2% acceptable criterion took place on the majority of the building stories above the 5th level during the scaled 1971 San Fernando earthquake in the UES analysis case, exhibited in Figure 5.19b. In that regard, the scaled 1971 San Fernando earthquake triggered the maximum transient total inter-story drift ratio of 2.35% in the UES analysis case, mainly induced by the foundation rocking. Conversely, the cases, ignoring the excess pore water pressure simulation (i.e., the DES analysis case (with the 1.30% drift ratio) and UTS analysis case (with the 1.38% drift ratio)), shown in Figure 5.19b, were deceitfully placed in the safe zone on the basis of complying with the 2% life safety drift ratio limit.

$$DR_{tt} = \frac{d_{i+1} - d_i}{h} \tag{5.30}$$

where, DR_{tt} is the total inter-story drift ratio, d_i and d_{i+1} are the deflections at the $(i)^{th}$ and $(i+1)^{th}$ levels, respectively, and h is the story height (i.e., 3 m in this study).

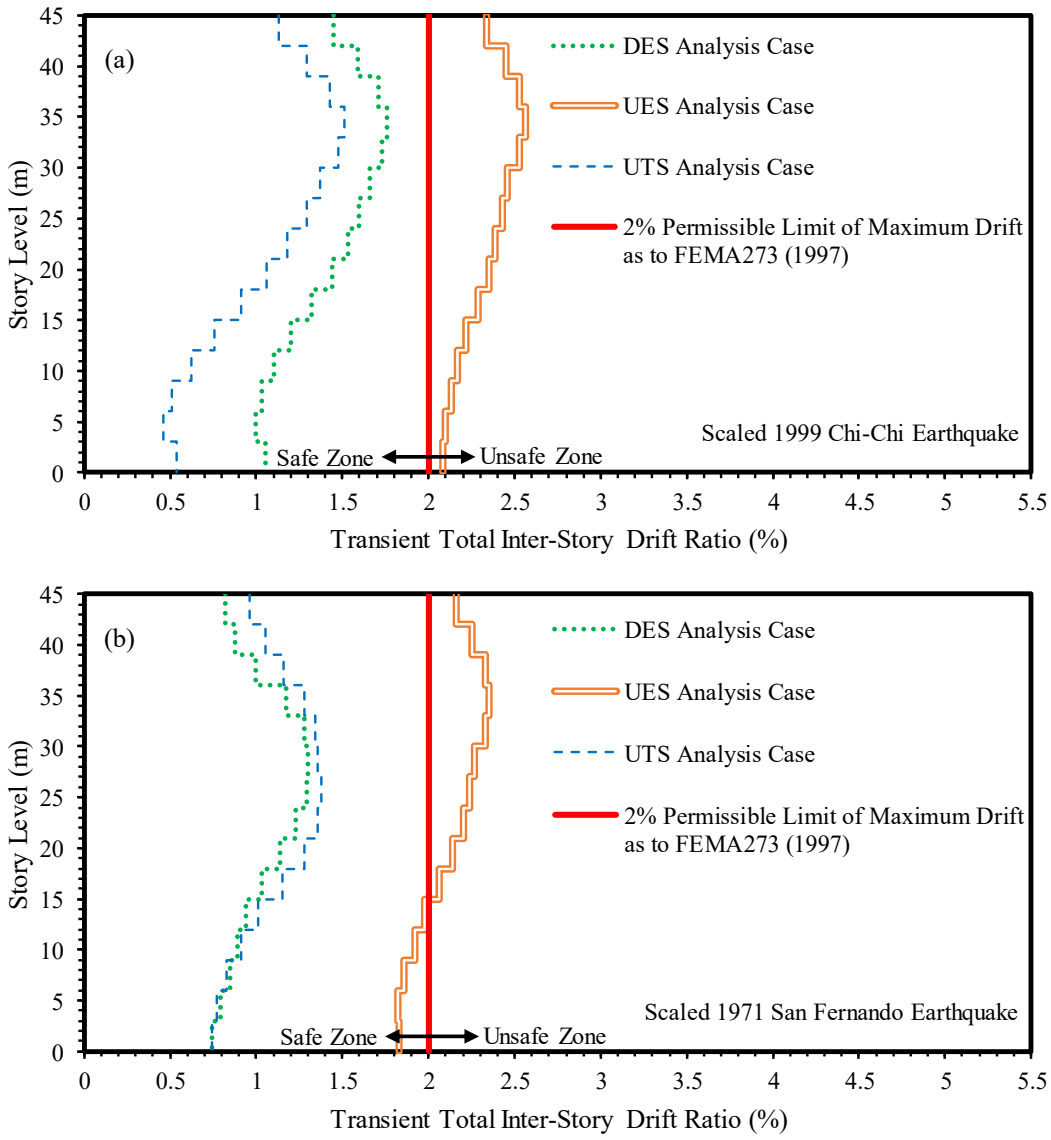

Figure 5.19 Transient total inter-story drift ratios of 15-story superstructure in DES, UES, and UTS analysis cases under excitations of: (a) scaled 1999 Chi-Chi earthquake, and (b) scaled 1971 San Fernando earthquake

Similar to the total lateral displacement, reported in the previous section, the distortional and foundation rocking-induced inter-story drift ratios formed the total inter-story drift ratio of the adopted superstructure. The former was due to the seismically-induced shear forces in the building columns whilst the latter resulted from the rigid body rotation of the mat foundation under the seismic loading. The predicted transient shear-induced distortional inter-story drift ratios, exhibited in Figure 5.20, were computed by subtracting the transient foundation rocking-induced inter-story drift ratios from the transient total inter-story drift ratios, displayed in

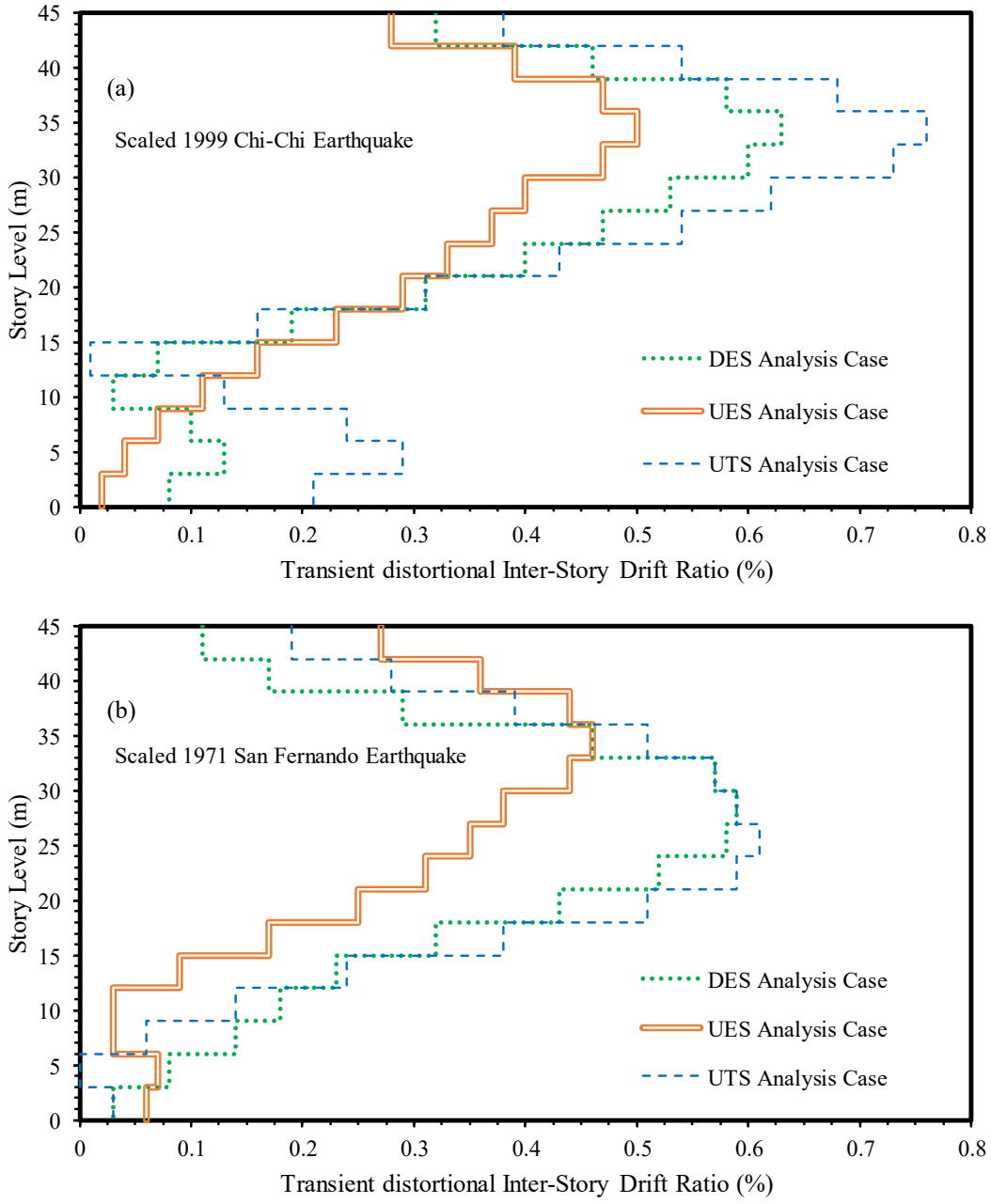

Figure 5.20 Transient distortional inter-story drift ratios of 15-story superstructure in DES, UES, and UTS analysis cases under excitations of: (a) scaled 1999 Chi-Chi earthquake, and (b) scaled 1971 San Fernando earthquake

Figure 5.19. In line with the reduction in the shear forces along the building height when comparing the DES, UES, and UTS analysis cases, demonstrated in Figure 5.11a under the scaled 1999 Chi-Chi earthquake, the lowest values for the transient distortional inter-story drift ratio belonged to in the UES analysis case, as evident in Figure 5.20a. Furthermore, the simulation of the excess pore water pressure in the UES analysis case caused the significant

foundation rocking under the influence of the scaled 1971 San Fernando earthquake, looking back to Figure 5.13b. That was the reason that the distortional drift ratios in the UES case were surpassed by those of the DES and UTS analysis cases in Figure 5.20.

According to Sözen (1981), the expected percentage of the structural damage ($Damage\ \%$) in an earthquake-resisting structural system can be assessed using Equation (5.31), wherein DR_{tt} is the total inter-story drift ratio of the story level of interest in percentage. As it is discerned in Figure 5.21a for the scaled 1999 Chi-Chi seismic event, the estimated structural damage index in the UES analysis case was 92% owing to the significant transient total inter-story drift ratio for the rooftop (i.e., 2.34%). That damage index (i.e., 92%) was rather two times and three times greater than the expected damage indices in the DES (i.e., 47.5%) and UTS (i.e., 31.5%) analysis cases, respectively. Moreover, the previous research studies cast light on the growth of the ductility demand, consequent to the soil-structure interaction (e.g., Esteva, 1987; Jarernprasert et al., 2013). The results of the current study for the adopted 15-story moment-resisting superstructure called attention to a breakthrough in the essential consideration of the excess pore water pressure build-up in the seismic soil-structure interaction analyses due to the extra surge in the ductility demand. To set that out, the total inter-story drift ratio predictions of the 8th level are illustrated in Figure 5.21b for the scaled 1971 San Fernando seismic input. That figure shows that the average anticipated structural damage index on the 8th story was 40% for the DES and UTS analysis cases. On the contrary, in the UES analysis case under the scaled 1971 San Fernando earthquake, jeopardizing the seismic performance of the adopted superstructure was on the line. In that regard, the 2.22%, as the transient total inter-story drift ratio of the 8th story, hazardously produced the structural damage index of 86% in the UES analysis case. Such an incident forewarned the practicing engineers as regards the possibility of the collapse damage level occurrence if the excess pore water pressure generation is not considered in analyzing the seismic behavior of the saturated soils.

$$Damage\ \% = \left(\frac{DR_{tt}}{2} - \frac{1}{4}\right) \times 100 \tag{5.31}$$

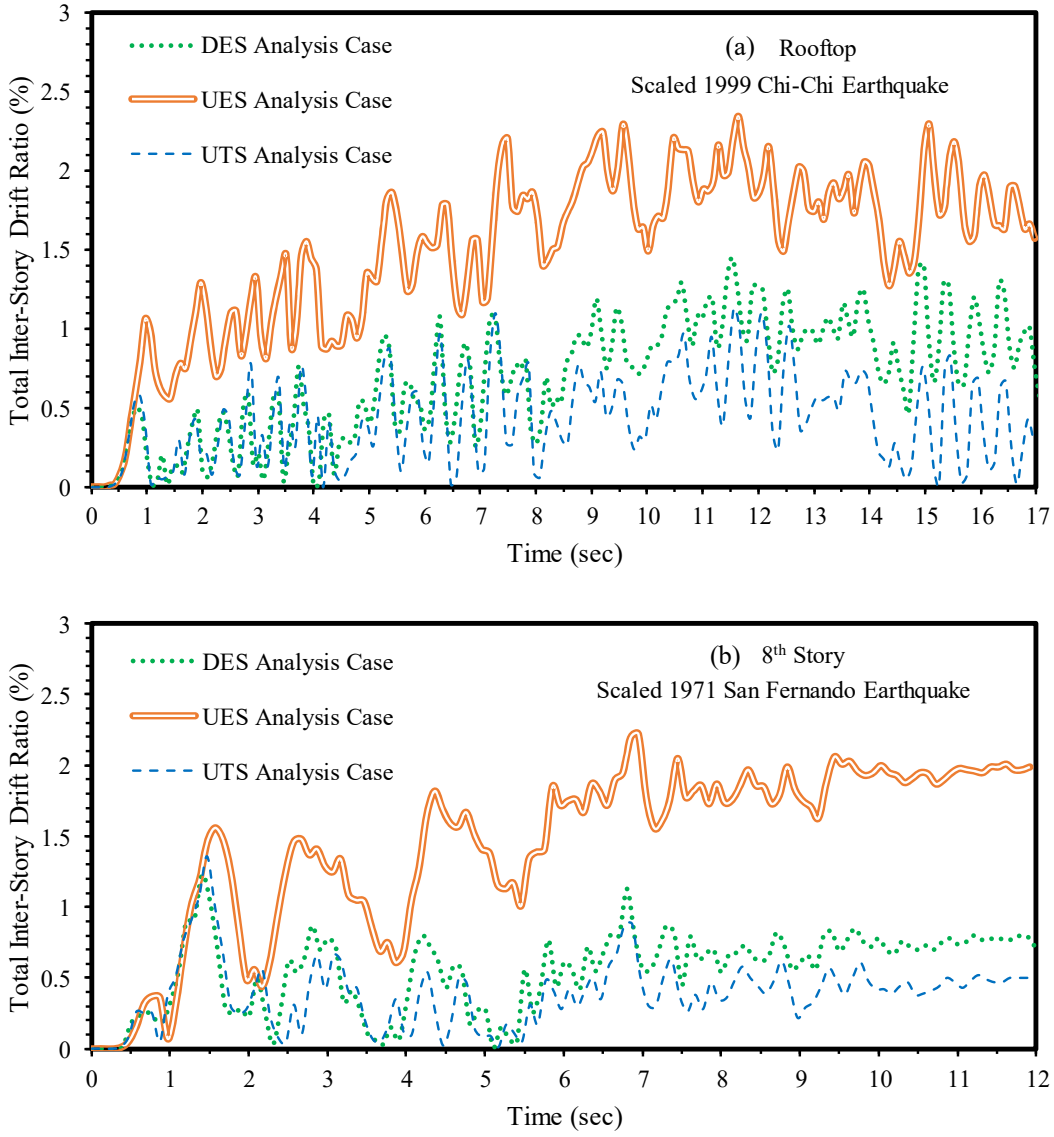

Figure 5.21 Time histories of total inter-story drift ratios in DES, UES, and UTS analysis cases under excitations of: (a) scaled 1999 Chi-Chi earthquake for rooftop, and (b) scaled 1971 San Fernando earthquake for 8th story

Christopoulos et al. (2003) elucidated the paramountcy of the residual deformation of a building frame from the post-earthquake performance assessment standpoint. Figure 5.22 is the pictorial description of the total inter-story drift ratios, permanently imposed on the adopted shallow-founded 15-story superstructure for the range of applied earthquakes. The 1% life safety drift ratio limit, recommended by FEMA273 (1997), was not met in the UES analysis

case courtesy of encountering 1.72% and 1.90% as the predicted residual total inter-story drift ratios under the scaled 1999 Chi-Chi and scaled 1971 San Fernando earthquakes, respectively. Contrarily, the maximum residual total inter-story drift ratios of 0.86% and 0.44% were predicted by the DES and UTS analysis cases, respectively, misleadingly located in the safe zone of Figure 5.22. Thus, assessing the seismic performance of the saturated clayey soil-structure interaction requires capturing the shaking-induced excess pore water pressure, which could endanger the building integrity and safety owing to overlooking the excessive post-earthquake deformations.

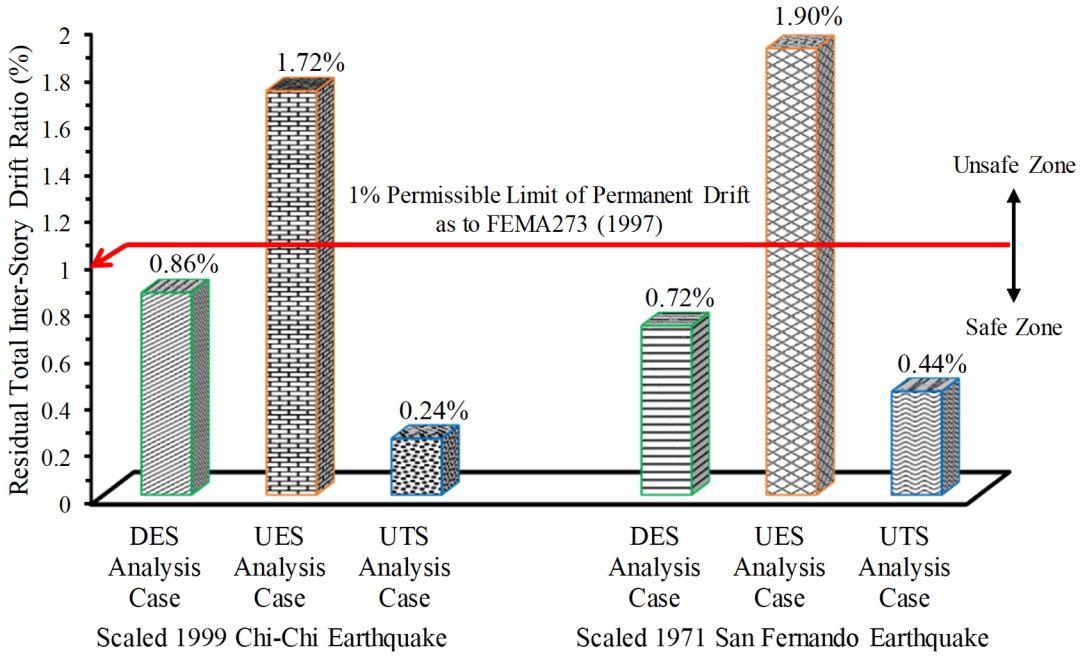

Figure 5.22 Residual total inter-story drift ratios in DES, UES, and UTS analysis cases under excitations of scaled 1999 Chi-Chi and scaled 1971 San Fernando earthquakes

5.4 Summary

The current study aimed to provide a comprehensive insight to the design and practicing engineers by elaborating the possible and potentially detrimental effects of the excess pore water pressure generation on the seismic performance of the reinforced concrete moment-resisting buildings, excluding the liquefaction occurrence. This research work adopted the

direct one-step approach, whereby the entire system was analyzed in one attempt during an applied earthquake. In all the elasto-plastic-based 3D coupled soil-structure interaction numerical simulations using FLAC3D (Itasca Consulting Group, 2012), the hysteretic damping and soil stiffness degradation with the shear strain were invoked. Note that the hyperbolic relation between the shear stresses and shear strains for the virgin loading phase, i.e., the skeleton curve, under either the drained or undrained loading conditions was responsible for capturing the soil hysteretic damping feature.

In this research study, three different approaches, viz, the drained effective stress response analysis, undrained effective stress response analysis, and undrained total stress response analysis, hereinafter called “DES analysis case”, “UES analysis case”, and “UTS analysis case”, respectively, were employed. In the DES analysis, the soil yielding, controlled by the effective stress state, was induced by the elastic-perfectly plastic Mohr-Coulomb soil constitutive model. The soil, however, was modeled as a one phase equivalent solid with the total stresses in the UTS analysis. Quite differently, the UES calculation mode was capable of directly giving a prediction of the earthquake-induced excess pore water pressure.

The results herein vividly exhibited the pronounced effects of the excess pore water pressure on the seismic responses of the soil-structure systems, signifying that the seismic safety of the superstructures, resting on the non-liquefiable saturated soils, could be still put in serious jeopardy. In that respect, the component of the excess pore water pressure build-up due to the foundation rocking caused the reduction in the mean effective stresses, predicted in the UES analysis case. The said condition imposed the significant damage on the adopted 15-story superstructure. The damage index (i.e., 92%), when capturing the generation of the excess pore water pressure, was rather two times and three times greater than the expected damage indices in the DES (i.e., 47.5%) and UTS (i.e., 31.5%) analysis cases, respectively. This study also showed that the UTS analysis case, which is commonly utilized for the undrained analyses by

the design and practicing engineers, cannot deal with the effects of the seismically-induced excess pore water pressure. It is reasoned to proclaim that the seismic performance of the buildings on the non-liquefiable soils in the earthquake-prone zones would be significantly weakened by neglecting the excess pore water pressure generation, giving rise to imposing the detrimental consequences on the society.

CHAPTER 6

CONCLUSIONS AND RECOMMENDATIONS

6.1 Conclusions

In the contemporary era, a growing demand of the high rise buildings, characterizing the skyline of a typical modern megacity, in the urban areas is evident. The current research project made use of the direct method by employing FLAC3D, as a finite difference software program. FLAC3D, used in the engineering mechanics computation, provides the wide-ranging facilities for modeling and analyzing the soil-structure interaction problems as compared to the other geotechnical and structural software programs. A series of hysteretic three-dimensional fully coupled nonlinear numerical analyses of the soil-structure system was carried out in the time domain using FLAC3D and its powerful internal programming language, named "FISH". The code-conforming 15-story and 20-story reinforced concrete moment-resisting buildings, as an example of the typical high rise buildings in the relatively high-risk earthquake-prone zones, were adopted. The material and geometric nonlinearities (i.e., the uplifting, gapping, and $P-\Delta$ effect) were accommodated in the said analyses. The programmed hysteretic damping algorithm was in charge of simulating the variations of the soil shear modulus and corresponding damping against the seismically-induced shear strain. The 1% and 2% life safety drift limits should be met by the residual and transient total inter-story drift ratios, respectively, in the PBSD framework, as recommended by FEMA273 (1997). On turning the pages of this thesis, the following conclusions could be delivered:

6.1.1 Effects of Shear Wave Velocity Profile of Soil on Seismic Performance of High Rise Buildings

- Shear wave velocity is a valuable indicator of the dynamic properties of the soils on account of its direct relation with the small-strain shear modulus.
- Mohr-Coulomb with the hysteretic damping feature acted as the adopted soil constitutive model in the numerical SSI simulations herein.
- Case A was the in-situ non-uniform profile of the shear wave velocity and Case B represented the equivalent uniform profile as to the weighted average shear wave velocity.
- Maximum of the 60%-difference was observed in the story shear forces between Case A and Case B.
- Higher mode effects resulted in the difference, observed on the patterns of the shear force distributions associated with Case A and Case B.
- Response spectrum of Case A sat above that of Case B in the shorter period range (i.e., less than the second mode period range), signifying the possible critical state for the shorter building frames compared to the adopted 20-story building in this study.
- Small-strain shear modulus in the vicinity of the mat foundation in Case B was approximately three times greater than that of Case A, denoting the overestimation of the soil stiffness in the interaction domain.
- Case B misled the design and practicing engineers as the predicted transient inter-story drift ratios satisfied the 2% life safety drift limit as to FEMA273 (1997).
- Maximum transient inter-story drift ratio in Case A reached 2.5% ($\precnsim$ 2% as to FEMA273 (1997)).

- Field-based profile of the soil shear wave velocity, introduced in Case A, triggered the severely damaged structural elements and non-structural components.
- Maximum lateral displacement of the rooftop in Case A was 1111 mm, which was 21% greater than that of Case B.
- Utilizing the weighted average shear wave velocity in lieu of the field-based profile would lead to the unsafe design of the buildings, resting on the mat foundations, subjected to the strong earthquakes.
- Actual shear wave velocity profile, resulting from the field/lab measurements, ought to be directly employed in the seismic analysis of SSI.

6.1.2 Effects of Degree of Saturation on Seismic Performance of High Rise Buildings Considering Soil-Structure Interaction

- Variations in the degree of saturation due to the climate change, seasonal variations, and loading-unloading situations during the buildings' service life, could effectuate the field shear wave velocity measurement in the effective vadose zone.
- Zone of influence was assumed to be 4 m in this study with due attention to the recommended values for the effective vadose zone by AS2870 (2011).
- Mohr-Coulomb with the hysteretic damping feature acted as the adopted soil constitutive model in the numerical SSI simulations.
- Four values of the degree of saturation (S_r), including 5%, 17.5%, 60%, and 100%, were assigned to the top 4 m of the soil profile, whose corresponding shear wave velocities were 230, 270, 190, and 170 m/s, consecutively.
- Shear force envelope distribution of the S_r = 17.5% case surpassed the others due to the higher mode effects.

- Concerning the seismic base shear, there was a 10%-increase from the S_r = 100% case to the S_r = 17.5% case.
- The lesser the degree of saturation, the higher the seismic energy, reaching the superstructures, occurring in or after a prolonged drought.
- Rocking of the mat foundations could be boosted by the overturning moments, induced by the seismic shear forces in the superstructures, higher for the drier vadose zone in the vicinity of the ground surface.
- Significant foundation rocking, predicted for the S_r = 5% case, was the reason for the observed considerable transient lateral deflection of the adopted building, e.g., 1336 mm at the rooftop.
- Lowest shear modulus, reported for the S_r = 100% case, would have had an adverse effect on the amount of the foundation rocking in this study by elevating the total settlement of the mat foundation whilst reducing the differential settlement due to the highest soil self-weight in the effective vadose zone.
- Maximum transient inter-story drift ratios of 1.98% and 2.26% in the S_r = 17.5% and S_r = 5% cases triggered the partial or total loss of the structural and non-structural elements and gave rise to skyrocketing the cost of replacement and repair of the said elements as exceeding the 2% life safety drift limit as to FEMA273 (1997).
- Necessitousness of utilizing the soil properties, such as the shear wave velocity in accordance with the degree of saturation in the effective vadose zone was shown in this study.
- Buildings would suffer worse damage from the earthquakes in the dry rather than the wet seasons referring to Figure 6.1.

- The damp soil is basically softer and so absorbs more energy than the dry, stiff soil. After a dry season, during a seismic event, the selected building in this study will experience more load, will move more, will crack more and ultimately will be unsafe whether it remains standing or collapses.
- Implementations of the presented results herein would help the governments and emergency agencies react to the earthquake events more effectively, depending on the time of the year and weather experienced.

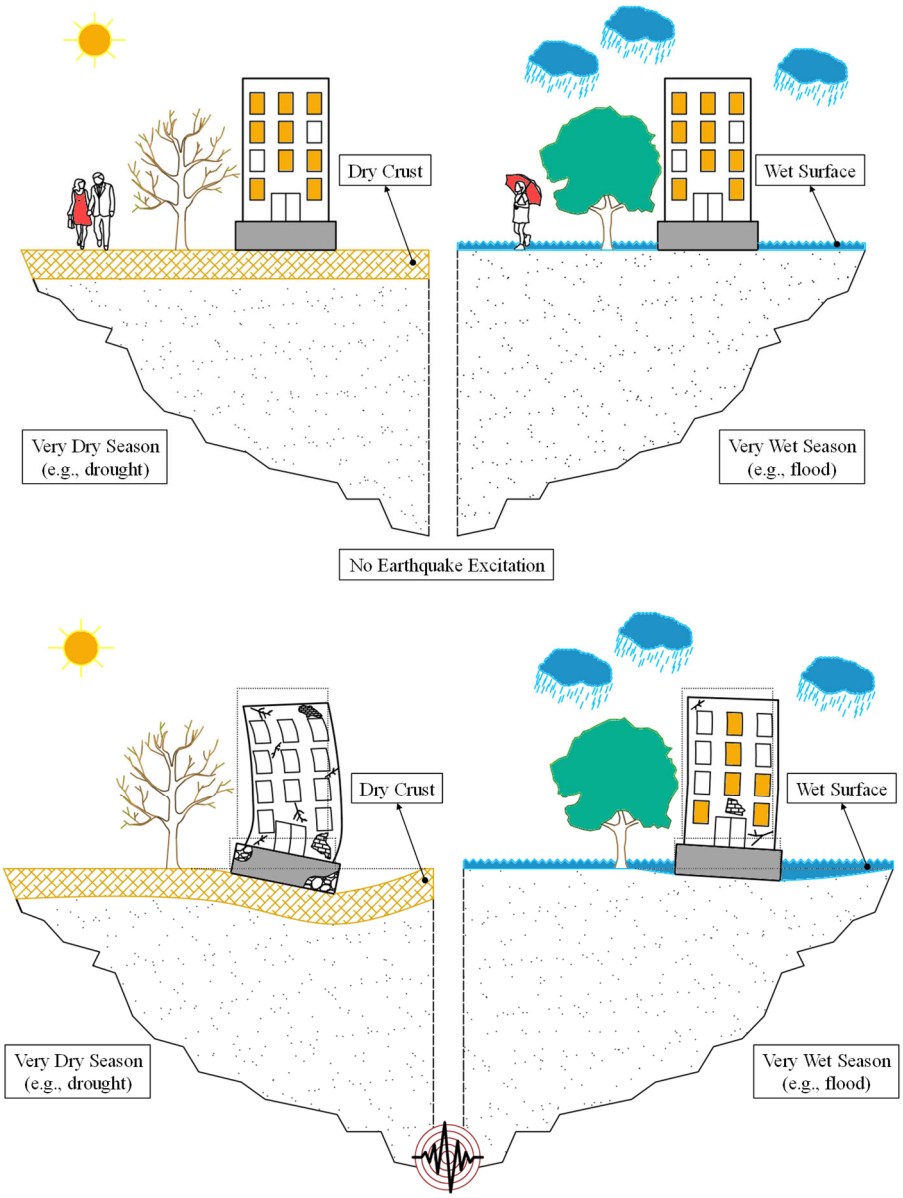

Figure 6.1 Damp soils absorb more energy from seismic events, meaning less damage

6.1.3 Effects of Hyperbolic Hardening Parameters on Seismic Performance of High Rise Buildings Considering Soil-Structure Interaction

- Hyperbolic Hardening with Hysteretic Damping (H2-HD) model was chosen among the advanced hardening plasticity-based soil constitutive models.
- Investigation of the extent to which the choice of the hyperbolic hardening parameters would be capable of impacting the seismic response of the reinforced concrete moment-resisting buildings with a mat foundation considering SSI was conducted in this study.
- Plastic strain hardening rule was affected by the failure ratio (R_f, whose values were 0.7, 0.8, and 0.9) and elastic-plastic coupling coefficient (β, whose values were 0.1, 0.2, 0.35).
- Case I (R_f = 0.70, β = 0.35), Case II (R_f = 0.80, β = 0.35), Case III (R_f = 0.90, β = 0.35), Case IV (R_f = 0.70, β = 0.20), and Case V (R_f = 0.70, β = 0.10) were considered in this study.
- Hardening plasticity-induced damping in conjunction with the perfect plasticity-induced damping and hysteretic damping resulted in some level of deamplification, observed via the response spectra.
- Hardening plasticity-induced damping and hysteretic damping were on the decrease as R_f decreased and/or β increased, augmenting the inertial forces, generated in the superstructure during the earthquake.
- Observing about 30% diminishment in the story shear force on the 6th story from Case I to Case V.
- Effect of β on the structural demand outweighed that of R_f.

- Reducing the elastic-plastic coupling coefficient, whilst keeping R_f constant (i.e., comparing Cases I, IV, and V), induced the 15% reduction in the base shear, whereas the corresponding drop due to the changes in R_f was about 4% (i.e., comparing Cases I, II, and III).
- Lower the R_f value (e.g., Case I), the more contribution of the brittle manner to the soil behavior. The foundation rocking rotations were ascended owing to the soil perfect plasticity status at the low plastic shear strains.
- Permanent rotation of the foundation slab was 0.50 degrees for Case I whereas the corresponding value in Case V was declined by over 50% to 0.24 degrees.
- 750 mm at the rooftop, as the largest lateral displacement, was predicted for Case I.
- Right selection of the parameters in the shear-volumetric hardening H2-HD model (e.g., via the calibration of the model parameters to the laboratory test data, such as the triaxial test results) could result in the safer or even more cost-effective design of the superstructures, subjected to the strong earthquakes.
- Initial and decremental slopes of the plastic form of the hyperbola in combination with how soon violating the shear failure envelope could be the culprit of the unsafe design in some cases considering SSI.
- Laboratory tests must be conducted so as to obtain the parameters associated with the chosen advanced hardening plasticity-based soil models.
- Inaccurate selection of the model parameters based on some general recommendations in the literature could result in the unreliable predictions, jeopardizing the safety or resulting in the significantly overdesigned or expensive construction.

6.1.4 Effects of Choice of Soil Constitutive Model on Seismic Performance of Moment-Resisting Frames Experiencing Foundation Rocking Subjected to Near-Field Earthquakes

- Investigation of the extent to which the choice of the soil constitutive models can impact the seismic performance of the reinforced concrete moment-resisting buildings with a mat foundation considering SSI was carried out in this study.
- Adopted soil constitutive models in this study were the isotropic Elastic with Hysteretic Damping (E-HD) model, elastic-perfectly plastic Mohr-Coulomb with Hysteretic Damping (MC-HD) model, and Hyperbolic Hardening with Hysteretic Damping (H2-HD) model.
- Elasticity-based model (i.e., E-HD) and elastic-perfectly plastic model (i.e., MC-HD), dismissed the existence of the plastic strains prior to the soil failure state.
- Hardening plasticity-induced damping and nonlinear soil behavior were captured by the hyperbolic hardening with hysteretic damping soil model from the onset of the virgin loading.
- Response spectra, belonging to the H2-HD soil model, underlay the other soil models' trends in the whole range of periods.
- Not only the magnitudes but also the distribution patterns of the predicted shear forces were affected by the choice of the soil constitutive model.
- Soil plasticity reduced the predicted structural demand from the E-HD model (i.e., 26 MN) to the H2-HD model (i.e., 17.59 MN).
- Even though the more realistic elasto-plastic response of the soil, as captured in the H2-HD model, lessened the shear forces, the amount and trend of such a reduction were not the same on every level.

- Soil plasticity-induced rocking was significant in this study since the H2-HD soil model resulted in the amplified foundation rocking due to the soil yielding.
- Obtained maximum rocking enjoyed the over fivefold upsurge by transferring from the E-HD and MC-HD soil models to the H2-HD constitutive relationship.
- Based on the maximum vertical displacements at the center of the foundation, the E-HD and MC-HD models misled the design engineers by indicating the unrealistic safety of the superstructure.
- Post-earthquake permanent lateral deflection of the adopted mat-supported 20-story building experienced a significant ascent (i.e., 12 times increase) when employing more appropriate and proper soil elasto-plastic behavior in the seismic SSI analysis.
- Predicted transient total inter-story drift ratios of the H2-HD soil model exceeded the 2% life safety drift limit (proposed by FEMA273 (1997)) by reaching 2.7% whilst the non-plastic pre-failure soil models (i.e., E-HD and MC-HD) misleadingly met the said yardstick.
- 1% acceptance criterion, according to FEMA273 (1997), for the residual total inter-story drift ratio was satisfied only by the E-HD and MC-HD models, engendering the non-conservative, safety-threatening design.
- Dismissal of the hardening plasticity could cause the loss of the bearing in the structural elements and possible danger of the structural instability.
- Not putting the soil plastic hardening into effect from the onset of the virgin loading would trigger the requirement of an extensive repair job.
- Lack of consideration of the soil plasticity would result in the under-prediction of the foundations' post-earthquake settlements in addition to the unrealistic predictions of the earthquake energy, pinpointing the structures.

- Predicted seismic response of the moment-resisting buildings in the soil-structure system could be affected by the type of the soil stress-strain relationship.

6.1.5 Effects of Pore Water Pressure on Seismic Performance of Buildings on Saturated Clayey Deposit Considering Soil-Structure Interaction

- Seismically-induced excess pore water pressure will be generated in almost all types of the saturated soils to the different levels in contrast with the seismic liquefaction.
- Studies cases in this research work were as follows: (i) Drained Effective Stress response analysis (DES analysis case); (ii) Undrained Effective Stress response analysis (UES analysis case); and (iii) Undrained Total Stress response analysis (UTS analysis case).
- Smaller soil deformations and higher seismic lateral forces on the building in the UTS analysis case is expected due to the delay in the yielding of the soil in the UTS analysis case compared to the DES and UES analysis cases, stemming from the locations of the failure planes.
- Soil hysteretic damping algorithm, capturing the nonlinear variations of the soil stiffness and damping ratio with the seismically-induced shear strains, was adopted while the Mohr-Coulomb failure criterion was introduced in this study to capture the perfect plasticity-induced damping.
- Cyclic shear strain enjoyed the twofold upsurge by transferring from the UTS analysis case (i.e., 1.40%) to the UES analysis case (i.e., 2.81%) at the depth of 0.5 m beneath the mat foundation.
- DES and UTS analysis cases possessed the lowest hysteretic damping based on the generated cyclic shear strains and PGSA/PGBA ratio. PGBA and PGSA stand for

the peak ground base acceleration and peak ground surface acceleration, respectively.

- Considerable reduction of the shear wave velocity, captured by the strain-compatible shear modulus feature through the hysteretic damping framework, resulted in the amplification of the long-period spectral accelerations in the UES analysis case (i.e., around 2.43).
- Underestimation of the amplification on the low frequencies, observed in the DES and UTS analysis cases, could be highly prejudicial for the flexible superstructures in the event of the insignificant higher mode effects.
- Higher mode effects were activated in the soil-structure system when disregarding the excess pore water pressure build-up.
- 30% surge in the maximum base shear was predicted when disregarding the excess pore water pressure build-up.
- lower soil shear modulus in the UES analysis case of this study due to the higher generated cyclic shear strains (related to the shear modulus reduction feature) as well as the reduced mean effective stresses (related to the stress-dependent shear modulus feature) induced the pronounced foundation rocking as compared to the DES and UTS analysis cases.
- Residual rocking rotations, corresponding to the UES, DES, and UTS analysis cases, were 1.09 degrees, 0.41 degrees, and 0.25 degrees, respectively.
- Significant rocking gave rise to the considerable structural lateral deflections and inter-story drift ratios, hazardously breaching the reparability limit of the allowable residual lateral displacement, as well as the 1% and 2% permissible limits of the transient and residual inter-story drift ratios (as per FEMA273 (1997)), respectively.
- Total settlement and differential settlement undertook up to the four times increase

compared to the DES and UTS analysis cases in view of the generation of the excess pore water pressure.

- Predicted structural damage index of the adopted 15-story reinforced concrete moment-resisting superstructure in the undrained effective stress response analysis was around 90%.
- Dismissing the generation of the excess pore water pressure in the seismic SSI analysis might contribute to ratcheting up the lateral deformations of the buildings, the loss of the lateral resistance, economic loss, and high cost of repair.
- Ensuring the seismic safety of the superstructures, resting on the non-liquefiable saturated soils, would necessitate taking the seismically-induced pore water pressure into consideration when carrying out the numerical simulations of the soil-structure interaction.

6.2 Recommendations for Future Work

The current study was an effort to comprehensively scrutinize the extent to which the seismic performance of the mat-supported reinforced concrete moment-resisting buildings would be affected by the soil hardening plasticity and excess pore water pressure build-up based on the dynamic soil-structure interaction analysis, incorporating the performance-based seismic design concept. Additionally, the foundation rocking isolation technique was assessed throughout investigating the above-mentioned factors for the high rise buildings, experiencing the significant rocking under the severe earthquake events. Continuing on this line, this thesis recommended utilizing the in-situ shear wave velocity profile directly in conjunction with the consideration associated with the changes in the degree of saturation for the estimation of the small-strain shear modulus, required by the dynamic analyses. From all accounts, the further numerical studies and also experimental tests in order to verify the derived numerical

simulation results are recommended for the future studies in the realm of the seismic soil-structure interaction. Developing the new design approaches is also highly needed. The future research work might be carried out on the seismic performance of the superstructures by putting the ideas and outcomes of this thesis into practice in the following areas:

- Consideration of the irregular superstructures, also covering a wide range of lateral force resisting systems, e.g., the shear wall braced moment-resisting frames.
- Consideration of the embedded shallow foundations, including the active and passive pressures of the surrounding soils.
- Consideration of the deep foundations, including the vertical and possibly inclined piles as well as optimizing the pile group configurations.
- Investigation of the seismic pounding between the adjacent superstructures with the same and different total and story heights.
- Consideration of the layered soil profiles, combining the clays, and sands, or rocks.
- Inclusion of the number of cycles in the soil plasticity-based soil constitutive models under the dynamic loading.
- Consideration of the undrained dilation and consolidation of the saturated sediments.
- Investigation of the seismic interaction between the liquefiable soils and superstructures.
- Consideration of the vertical components of the earthquakes along with their horizontal components.
- Inclusion of the aftershocks in the assessment of the seismic performance of the superstructures.

Finally, it could be hereby asserted that the results of this study and other existing research studies could be employed so as to develop the new elaborative design guidelines for the evaluation of the seismic performance of the superstructures under the soil-foundation-structure interaction, fulfilling the current gap in the existing design procedures and available codes and regulations.

BIBLIOGRAPHY

Abate, G., Massimino, M., Maugeri, M. & Wood, D.M. 2010, 'Numerical modelling of a shaking table test for soil-foundation-superstructure interaction by means of a soil constitutive model implemented in a FEM code', *Geotechnical and Geological Engineering*, vol. 28, no. 1, pp. 37-59.

Abdelouhab, A., Dias, D. & Freitag, N. 2011, 'Numerical analysis of the behaviour of mechanically stabilized earth walls reinforced with different types of strips', *Geotextiles and Geomembranes*, vol. 29, no. 2, pp. 116-29.

ACI318 2014, *Building code requirements for structural concrete and commentary*, American Concrete Institute, Farmington Hills.

Aki, K. 1993, 'Local site effects on weak and strong ground motion', *Tectonophysics*, vol. 218, no. 1-3, pp. 93-111.

Al Atik, L. & Abrahamson, N. 2010, 'An improved method for nonstationary spectral matching', *Earthquake Spectra*, vol. 26, no. 3, pp. 601-17.

Alavi, B. & Krawinkler, H. 2004, 'Behavior of moment-resisting frame structures subjected to near-fault ground motions', *Earthquake Engineering & Structural Dynamics*, vol. 33, no. 6, pp. 687-706.

Aldea, A., Iiba, M., Demetriu, S. & Kashima, T. 2007, 'Evidence of soil-structure interaction from earthquake records at a high-rise building site in Bucharest', *4th International Conference on Earthquake Geotechnical Engineering*, pp. 25-8.

Allotey, N. & El Naggar, M. 2005, 'Soil–structure interaction in performance-based design—a review', *Proceedings of the 11th International Conference on Computational Methods and Advanced in Geomechanics, Torino, Italy*, pp. 19-24.

Allotey, N. & El Naggar, M.H. 2008, 'Generalized dynamic Winkler model for nonlinear soil–structure interaction analysis', *Canadian Geotechnical Journal*, vol. 45, no. 4, pp. 560-73.

Alpan, I. 1967, 'The empirical evaluation of the coefficient K_0 and K_{0R}', *Soils and Foundations*, vol. 7, no. 1, pp. 31-40.

Ambraseys, N. 1977, 'Long-period effects in the Romanian earthquake of March 1977', *Nature*, vol. 268, no. 5618, pp. 324-5.

Ambrosini, R.D. 2006, 'Material damping vs. radiation damping in soil–structure interaction analysis', *Computers and Geotechnics*, vol. 33, no. 2, pp. 86-92.

Amorosi, A., Boldini, D. & Di Lernia, A. 2017, 'Dynamic soil-structure interaction: a three-dimensional numerical approach and its application to the Lotung case study', *Computers and Geotechnics*, vol. 90, pp. 34-54.

Anastasopoulos, I. 2010, 'Beyond conventional capacity design: towards a new design philosophy', *Soil–foundation–structure interaction. New York: CRC Press, Taylor & Francis Group*, pp. 213-20.

Anastasopoulos, I., Gazetas, G., Loli, M., Apostolou, M. & Gerolymos, N. 2010, 'Soil failure can be used for seismic protection of structures', *Bulletin of Earthquake Engineering*, vol. 8, no. 2, pp. 309-26.

Anastasopoulos, I., Loli, M., Georgarakos, T. & Drosos, V. 2013, 'Shaking table testing of rocking—isolated bridge pier on sand', *Journal of Earthquake Engineering*, vol. 17, no. 1, pp. 1-32.

Andersen, K.H. 2015, 'Cyclic soil parameters for offshore foundation design', *Frontiers in offshore geotechnics III*, vol. 5, Taylor & Francis Group.

Ansal, A.M. & Erken, A. 1989, 'Undrained behavior of clay under cyclic shear stresses', *Journal of Geotechnical Engineering*, vol. 115, no. 7, pp. 968-83.

Arablouei, A., Gharabaghi, A., Ghalandarzadeh, A., Abedi, K. & Ishibashi, I. 2011, 'Effects of seawater–structure–soil interaction on seismic performance of caisson-type quay wall', *Computers and Structures*, vol. 89, no. 23-24, pp. 2439-59.

AS1170.4 2007, *Structural design actions - Part 4: Earthquake actions in Australia*, Standards Australia, Sydney.

AS2870 2011, *Residential slabs and footings*, Standards Australia, Sydney.

AS3600 2009, *Concrete structures*, Standards Australia, Sydney.

AS/NZS1170.0 2002, *Structural design action - Part 0: General principals*, Standards Australia/Standards New Zealand, Sydney.

AS/NZS1170.1 2002, *Structural design actions - Part 1: permanent, imposed and other actions*, Standards Australia/Standards New Zealand, Sydney.

AS/NZS4671 2001, *Steel Reinforcing Materials*, Standards Australia/Standards New Zealand, Sydney.

ASCE7-10 2010, *Minimum design loads and associated criteria for buildings and other structures,* American Society of Civil Engineering & Structural Engineering Institute, Virginia.

ASCE7-16 2016, *Minimum design loads and associated criteria for buildings and other structures*, American Society of Civil Engineering & Structural Engineering Institute, Virginia.

ASCE-41-17 2017, *Seismic evaluation and retrofit of existing buildings*, American Society of Civil Engineering & Structural Engineering Institute, Virginia.

ASEP 2010, *National structural code of the Philippines*, Association of Structural Engineers of the Philippines, Quezon City.

Ashour, M. & Ardalan, H. 2011, 'Piles in fully liquefied soils with lateral spread', *Computers and Geotechnics*, vol. 38, no. 6, pp. 821-33.

Assimaki, D. 1999, 'Frequency-and pressure-dependent dynamic soil properties for seismic analysis of deep sites', PhD thesis, Massachusetts Institute of Technology.

ATC3-06 1978, *Tentative provisions for the development of seismic regulations for buildings: a cooperative effort with the design professions, building code interests, and the research community*, Applied Technology Council, Redwood City.

ATC-40 1996, Seismic evaluation and retrofit of concrete buildings, Applied Technology Council, Redwood City.

Atkinson, J. 2000, 'Non-linear soil stiffness in routine design', *Géotechnique*, vol. 50, no. 5, pp. 487-508.

Atkinson, J., Richardson, D. & Stallebrass, S. 1990, 'Effect of recent stress history on the stiffness of overconsolidated soil', *Géotechnique*, vol. 40, no. 4, pp. 531-40.

Attalla, M.R., Paret, T. & Freeman, S.A. 1998, 'Near-source behavior of buildings under pulse-type earthquakes', *Proceedings of the sixth US National Conference on Earthquake Engineering*.

Auersch, L. & Schmid, G. 1990, 'A simple boundary element formulation and its application to wavefield excited soil-structure interaction', *Earthquake Engineering and Structural Dynamics*, vol. 19, no. 7, pp. 931-47.

Avilés, J. & Pérez-Rocha, L.E. 2003, 'Soil–structure interaction in yielding systems', *Earthquake Engineering and Structural Dynamics*, vol. 32, no. 11, pp. 1749-71.

Bagheri, M., Jamkhaneh, M.E. & Samali, B. 2018, 'Effect of Seismic Soil–Pile–Structure Interaction on Mid-and High-Rise Steel Buildings Resting on a Group of Pile Foundations', *International Journal of Geomechanics*, vol. 18, no. 9, p. 04018103.

Bai, Y. & Xu, Z.-D. 2019, *Structural Dynamics*, John Wiley & Sons.

Baladi, G. & Rohani, B. 1979, 'Elastic-plastic model for saturated sand', *Journal of Geotechnical and Geoenvironmental Engineering*, vol. 105, no. ASCE 14510.

Balkaya, C., Yuksel, S.B. & Derinoz, O. 2012, 'Soil-structure interaction effects on the fundamental periods of the shear-wall dominant buildings', *The Structural Design of Tall and Special Buildings*, vol. 21, no. 6, pp. 416-30.

Barcena, A. & Esteva, L. 2007, 'Influence of dynamic soil–structure interaction on the nonlinear response and seismic reliability of multistorey systems', *Earthquake Engineering & Structural Dynamics*, vol. 36, no. 3, pp. 327-46.

Bardet, J.-P. 1987, 'Bounding surface modeling of cyclic sand behavior', *Proceedings of the Workshop on Constitutive Laws for the Analysis of Fill Retention Structures. Edited by E. Evgin, Ottawa*, pp. 1-19.

Bartlett, P. 1976, 'Foundation rocking on clay soil', PhD thesis, Department of Civil Engineering, University of Auckland.

Basu, D., Boga, M. & Dey, A. 2019, 'A time-domain nonlinear effective-stress non-Masing approach of ground response analysis of Guwahati city, India', *Earthquake Engineering and Engineering Vibration*, vol. 18, no. 1, pp. 61-75.

Bazant, Z.P. 1985, *Mechanics of Geomaterials; Rocks, Concretes, Soil*, John Wiley and Sons, Inc., New York.

Beaty, M. & Byrne, P. 2011, *UBCSAND Constitutive Model: Version 904aR.* , Documentation Report: UBCSAND Constitutive Model on Itasca UDM Web Site, UCD/CGM-10/01.

Beaty, M. & Byrne, P.M. 1998, 'An Effective Stress Model for Pedicting Liquefaction Behaviour of Sand', *Geotechnical Earthquake Engineering and Soil Dynamics III*, ASCE, pp. 766-77.

Beresnev, I.A., Field, E.H., Van Den Abeele, K. & Johnson, P.A. 1998, 'Magnitude of nonlinear sediment response in Los Angeles basin during the 1994 Northridge, California, earthquake', *Bulletin of the Seismological Society of America*, vol. 88, no. 4, pp. 1079-84.

Bertero, R.D., Bertero, V.V. & Teran-Gilmore, A. 1996, 'Performance-based earthquake-resistant design based on comprehensive design philosophy and energy concepts', *Proceedings of 11th World Conference on Earthquake Engineering*.

Bery, G., Bolt, B., Sozen, M. & Rojahm, C. 1980, *Earthquake in Romania, March 4, 1977: an engineering report*, National Academies.

Bhattacharya, K. & Dutta, S.C. 2004, 'Assessing lateral period of building frames incorporating soil-flexibility', *Journal of Sound and Vibration*, vol. 269, no. 3-5, pp. 795-821.

Bielak, J. 1976, 'Modal analysis for building-soil interaction', *Journal of the Engineering Mechanics Division*, vol. 102, no. 5, pp. 771-86.

Bielak, J. & Christiano, P. 1984, 'On the effective seismic input for non-linear soil-structure interaction systems', *Earthquake Engineering & Structural Dynamics*, vol. 12, no. 1, pp. 107-19.

Bird, J.F. & Bommer, J.J. 2004, 'Earthquake losses due to ground failure', *Engineering Geology*, vol. 75, no. 2, pp. 147-79.

Bojórquez, E. & Ruiz-García, J. 2013, 'Residual drift demands in moment-resisting steel frames subjected to narrow-band earthquake ground motions', *Earthquake Engineering & Structural Dynamics*, vol. 42, no. 11, pp. 1583-98.

Borcherdt, R.D. 1970, 'Effects of local geology on ground motion near San Francisco Bay', *Bulletin of the Seismological Society of America*, vol. 60, no. 1, pp. 29-61.

Boulanger, R. & Ziotopoulou, K. 2013, 'Formulation of a sand plasticity plane-strain model for earthquake engineering applications', *Soil Dynamics and Earthquake Engineering*, vol. 53, pp. 254-67.

Bowles, L. 1996, *Foundation analysis and design*, 5th edn, McGraw-hill, New York.

BSLJ 2013, *Building Standard Law of Japan*, Building Center of Japan, Tokyo.

Budhu, M. 2010, *Soil Mechanics and Foundations*, 3rd edn, John Wiley & Sons, New York.

Bullen, K.E. & Bolt, B.A. 1985, *An introduction to the theory of seismology*, Cambridge University Press.

Bungale, S. 2016, *Tall building design steel, concrete, and composite systems*, CRC Press-Taylor & Francis Group, Boca Raton.

Byrne, P., Park, S. & Beaty, M. 2003, 'Seismic liquefaction: Centrifuge and numerical modelling', *FLAC and Numerical Modelling in Geomechanics-2003*, pp. 321-31.

Byrne, P.M., Park, S.-S., Beaty, M., Sharp, M., Gonzalez, L. & Abdoun, T. 2004, 'Numerical modeling of liquefaction and comparison with centrifuge tests', *Canadian Geotechnical Journal*, vol. 41, no. 2, pp. 193-211.

Caquot, A. & Kerisel, J. 1966, *Traité de mécanique des sols*, 4th edn, Gauthier-Villars, Paris.

Carr, A. 2008, 'Soil-structure interaction', *Advanced Nonlinear Seismic Structural Analysis Notes*, Pavia, Italy.

Carr, V.J., Lewin, T.J., Webster, R., Hazell, P., Kenardy, J. & Carter, G.L. 1995, 'Psychosocial sequelae of the 1989 Newcastle earthquake: I. Community disaster experiences and psychological morbidity 6 months post-disaster', *Psychological Medicine*, vol. 25, no. 3, pp. 539-55.

Castaldo, P. & De Iuliis, M. 2014, 'Effects of deep excavation on seismic vulnerability of existing reinforced concrete framed structures', *Soil Dynamics and Earthquake Engineering*, vol. 64, pp. 102-12.

Celebi, E., Göktepe, F. & Karahan, N. 2012, 'Non-linear finite element analysis for prediction of seismic response of buildings considering soil-structure interaction', *Natural Hazards and Earth System Sciences*, vol. 12, no. 11, pp. 3495-505.

Celebi, M. 1998, 'Turkish earthquakes: two reports. Lessons from the Adana-Ceyhan quake and the Dinar aftershock', *EERI Newsletter*, vol. 32, no. 9, p. 8.

Celebi, M. & Şafak, E. 1991, 'Seismic response of Transamerica building. I: Data and preliminary analysis', *Journal of Structural Engineering*, vol. 117, no. 8, pp. 2389-404.

Chakrabortty, P. & Popescu, R. 2012, 'Numerical simulation of centrifuge tests on homogeneous and heterogeneous soil models', *Computers and Geotechnics*, vol. 41, pp. 95-105.

Chang, B., Raychowdhury, P., Hutchinson, T., Thomas, J., Gajan, S. & Kutter, B. 2007, 'Evaluation of the seismic performance of combined frame-wall-foundation structural systems through centrifuge testing', *Proceedings of the 4th International Conference on Earthquake Geotechnical Engineering*.

Chang, B.J., Raychowdhury, P., Hutchinson, T.C., Thomas, J., Gajan, S. & Kutter, B. 2006, 'Centrifuge testing of combined frame-wall-foundation structural systems', *Proceedings of the 8th US National Conference on Earthquake Engineering*.

Chen, Y.F. & Krauthammer, T. 1989, 'A combined ADINA finite difference approach with substructuring for solving seismically induced nonlinear soil-structure interaction problems', *Computers and Structures*, vol. 32, no. 3-4, pp. 779-85.

Chitas, P. 2008, 'Site-effect assessment using acceleration time series. Application to São Sebastião volcanic crater', PhD thesis.

Choinière, M., Paultre, P. & Léger, P. 2019, 'Influence of soil-structure interaction on seismic demands in shear wall building gravity load frames', *Engineering Structures*, vol. 198, p. 109259.

Choobbasti, A.J., Rezaei, S., Farrokhzad, F. & Azar, P.H. 2014, 'Evaluation of site response characteristic using nonlinear method (Case study: Babol, Iran)', *Frontiers of Structural and Civil Engineering*, vol. 8, no. 1, pp. 69-82.

Christopoulos, C., Pampanin, S. & Nigel Priestley, M. 2003, 'Performance-based seismic response of frame structures including residual deformations part I: single-degree of freedom systems', *Journal of Earthquake Engineering*, vol. 7, no. 01, pp. 97-118.

Chu, D. 2006, 'Three-dimensional nonlinear dynamic analysis of soil-pile-structure interaction', PhD thesis, Washington University.

Clough, R. & Penzien, J. 1975, 'Dynamics of Structures, McGraw-Hill Book Co', *Inc., New York, NY*.

Coleman, J.L., Bolisetti, C. & Whittaker, A.S. 2016, 'Time-domain soil-structure interaction analysis of nuclear facilities', *Nuclear Engineering and Design*, vol. 298, pp. 264-70.

Comartin, C., Keaton, J., Grant, P., Martin, G. & Power, M. 1996, 'Transitions in seismic analysis and design procedures for buildings and their foundations', *Proceedings of the 6th Workshop on the Improvement of Structural Design and Construction Practice in the US and Japan*, pp. 15-5.

Conacher, A. & Murray, I. 1969, 'The meckering earthquake, Western Australia, 14 october 1968', *Australian Geographer*, vol. 11, no. 2, pp. 179-84.

Conniff, D.E. & Kiousis, P.D. 2007, 'Elastoplastic medium for foundation settlements and monotonic soil–structure interaction under combined loadings', *International Journal for Numerical and Analytical Methods in Geomechanics*, vol. 31, no. 6, pp. 789-807.

Cruse, T.A. & Rizzo, F.J. 1968, 'A direct formulation and numerical solution of the general transient elastodynamic problem. I', *Journal of Mathematical Analysis and Applications*, vol. 22, no. 1, pp. 244-59.

CSI 2016, *SAP2000: Integrated solution for structural analysis and design, version 19.0*, Computers and Structures Inc., Berkley.

Cundall, P. 1976, 'Explicit finite differnce method in geomechanics', *Second Int. Conf. Numerical Methods in Geomechanics, Blacksburg, 1976*, vol. 1, pp. 132-50.

Dafalias, Y.F. 1986, 'Bounding surface plasticity. I: Mathematical foundation and hypoplasticity', *Journal of Engineering Mechanics*, vol. 112, no. 9, pp. 966-87.

Darve, F. 1990, 'Incrementally non-linear constitutive relationships', *Geomaterials: Constitutive Equations and Modelling*, CRC Press, pp. 229-54.

Das, B.M. 2015, *Principles of foundation engineering*, Cengage learning.

Das, B.M. & Ramana, G. 2011, *Principles of Soil Dynamics*, Second Edition edn, Cengage Learning, USA.

Datta, T.K. 2010, *Seismic analysis of structures*, John Wiley & Sons.

David, M. & Zdravkovic, L. 1999, *Finite element analysis in geotechnical engineering: theory*, Thomas Telford.

Day, R.W. & Boone, S.J. 1998, 'Discussion and Closure: Ground-Movement-Related Building Damage', *Journal of Geotechnical and Geoenvironmental Engineering*, vol. 124, no. 5, pp. 462-5.

Di Julio, R.M. 2001, 'Linear static seismic lateral force procedures', *The Seismic Design Handbook*, Springer, pp. 247-73.

Díaz-Rodríguez, J. & López-Molina, J. 2008, 'Strain thresholds in soil dynamics', *The 14th World Conference on Earthquake Engineering*, pp. 12-7.

DiMaggio, F.L. & Sandler, I.S. 1971, 'Material model for granular soils', *Journal of Engineering Mechanics*.

Dobry, R. 2014, 'Simplified methods in soil dynamics', *Soil Dynamics and Earthquake Engineering*, vol. 61, pp. 246-68.

Dobry, R., Ladd, R., Yokel, F.Y., Chung, R.M. & Powell, D. 1982, *Prediction of pore water pressure buildup and liquefaction of sands during earthquakes by the cyclic strain method*, vol. 138, National Bureau of Standards Gaithersburg, MD.

Dobry, R. & Vucetic, M. 1987, *Dynamic properties and seismic response of soft clay deposits*, Department of Civil Engineering, Rensselaer Polytechnic Institute.

Dominguez, J. & Roesset, J. 1978, *Dynamic stiffness of rectangular foundations*, vol. 79, Massachusetts Institute of Technology, Department of Civil Engineering, Constructed Facilities Division.

Dong, Y. & Lu, N. 2016, 'Dependencies of shear wave velocity and shear modulus of soil on saturation', *Journal of Engineering Mechanics*, vol. 142, no. 11, p. 04016083.

Doroudian, M. & Vucetic, M. 1995, 'A direct simple shear device for measuring small-strain behavior', *Geotechnical Testing Journal*, vol. 18, no. 1, pp. 69-85.

Drosos, V., Georgarakos, T., Loli, M., Anastasopoulos, I., Zarzouras, O. & Gazetas, G. 2012, 'Soil-foundation-structure interaction with mobilization of bearing capacity: Experimental study on sand', *Journal of Geotechnical and Geoenvironmental Engineering*, vol. 138, no. 11, pp. 1369-86.

Duncan, J., Byrne, P., Wong, K.S. & Mabry, P. 1980, *Strength, stress–strain and bulk modulus parameters for finite element analysis of stresses and movements in soil mass. Rep. No*, UCB/GT/80-01, University of California, Berkeley, Calif.

Duncan, J.M. & Chang, C.-Y. 1970, 'Nonlinear analysis of stress and strain in soils', *Journal of Soil Mechanics & Foundations Div*.

Dutta, S.C., Bhattacharya, K. & Roy, R. 2004, 'Response of low-rise buildings under seismic ground excitation incorporating soil–structure interaction', *Soil Dynamics and Earthquake Engineering*, vol. 24, no. 12, pp. 893-914.

Dutta, S.C. & Roy, R. 2002, 'A critical review on idealization and modeling for interaction among soil–foundation–structure system', *Computers and Structures*, vol. 80, no. 20-21, pp. 1579-94.

Eguchi, R.T., Goltz, J.D., Taylor, C.E., Chang, S.E., Flores, P.J., Johnson, L.A., Seligson, H.A. & Blais, N.C. 1998, 'Direct economic losses in the Northridge earthquake: A three-year post-event perspective', *Earthquake Spectra*, vol. 14, no. 2, pp. 245-64.

El Ganainy, H. & El Naggar, M. 2009, 'Seismic performance of three-dimensional frame structures with underground stories', *Soil Dynamics and Earthquake Engineering*, vol. 29, no. 9, pp. 1249-61.

El Naggar, M. 2012, 'Bridging the Gap Between Structural and Geotechnical Engineers in SSI for Performance-Based Design', *Special Topics in Earthquake Geotechnical Engineering*, Springer, pp. 315-51.

Esteva, L. 1987, 'Earthquake engineering research and practice in Mexico after the 1985 earthquakes', *Bulletin of the New Zealand Society for Earthquake Engineering*, vol. 20, no. 3, pp. 159-200.

Eurocode 8 – Part 1 2004, *Design of structures for earthquake resistance. Part 1: General rules, seismic actions and rules for buildings*. European Committee for Standardization, Brussels.

Eurocode 8 – Part 5 2004, *Design of structures for earthquake resistance, Part 5: Foundations, retaining structures and geotechnical aspects*. European Committee for Standardization, Brussels.

Fajfar, P. 2018, 'Analysis in seismic provisions for buildings: past, present and future', *European Conference on Earthquake Engineering Thessaloniki, Greece*, Springer, pp. 1-49.

Far, H. 2019, 'Advanced computation methods for soil-structure interaction analysis of structures resting on soft soils', *International Journal of Geotechnical Engineering*, vol. 13, no. 4, pp. 352-9.

Fatahi, B., Huang, B., Yeganeh, N., Terzaghi, S. & Banerjee, S. 2020, 'Three-Dimensional Simulation of Seismic Slope–Foundation–Structure Interaction for Buildings Near Shallow Slopes', *International Journal of Geomechanics*, vol. 20, no. 1, p. 04019140.

Fatahi, B., Van Nguyen, Q., Xu, R. & Sun, W.-j. 2018, 'Three-dimensional response of neighboring buildings sitting on pile foundations to seismic pounding', *International Journal of Geomechanics*, vol. 18, no. 4, p. 04018007.

FEMA273 1997, *NEHRP guidelines for the seismic rehabilitation of buildings*, Applied Technology Council, Redwood City.

FEMA356 2000, *Prestandard and commentary for the seismic rehabilitation of buildings*, American Society of Civil Engineers, Reston.

FEMA440 2005, *Improvement of nonlinear static seismic analysis procedures*, Applied Technology Council, Redwood City.

FEMA283 1996, *Performance based seismic design of buildings: An action plan for future studies*, Federal Emergency Management Agency, Washington, D.C.

FEMA450 – Part 2 2003, *NEHRP Recommended provisions for seismic regulations for new buildings and other structures—part 2: commentary*. Building Seismic Safety Council, Washington, D.C.

FEMA-P-750 2009, *NEHRP Recommended seismic provisions for new buildings and other structures*, National Institute of Building Sciences, Washington, DC.

FEMA-P-1050-1 2015, *NEHRP Recommended seismic provisions: Design examples*, Building Seismic Safety Council,, Washington DC.

Finn, W., Ledbetter, R. & Beratan, L. 1986, 'Seismic soil-structure interaction: Analysis and centrifuge model studies', *Nuclear Engineering and Design*, vol. 94, no. 1, pp. 53-66.

Finn, W.L. 2005, 'A study of piles during earthquakes: issues of design and analysis', *Bulletin of Earthquake Engineering*, vol. 3, no. 2, p. 141.

Frangopol, D.M. & Curley, J.P. 1987, 'Effects of damage and redundancy on structural reliability', *Journal of Structural Engineering*, vol. 113, no. 7, pp. 1533-49.

Franke, K.W., Lingwall, B.N., Youd, T.L., Blonquist, J. & Liang, J.H. 2019, 'Overestimation of liquefaction hazard in areas of low to moderate seismicity due to improper characterization of probabilistic seismic loading', *Soil Dynamics and Earthquake Engineering*, vol. 116, pp. 681-91.

Gajan, S., Hutchinson, T.C., Kutter, B.L., Raychowdhury, P., Ugalde, J.A. & Stewart, J.P. 2008, *Numerical models for analysis and performance-based design of shallow foundations subjected to seismic loading*, Pacific Earthquake Engineering Research Center.

Galal, K. & Naimi, M. 2008, 'Effect of soil conditions on the response of reinforced concrete tall structures to near-fault earthquakes', *The Structural Design of Tall and Special Buildings*, vol. 17, no. 3, pp. 541-62.

Ganev, T., Yamazaki, F., Ishizaki, H. & Kitazawa, M. 1998, 'Response analysis of the Higashi–Kobe Bridge and surrounding soil in the 1995 Hyogoken–Nanbu Earthquake', *Earthquake Engineering and Structural Dynamics*, vol. 27, no. 6, pp. 557-76.

Ganev, T., Yamazaki, F., Katayama, T. & Ueshima, T. 1997, 'Soil-structure interaction analysis of the Hualien containment model', *Soil Dynamics and Earthquake Engineering*, vol. 16, no. 7-8, pp. 459-70.

Gazetas, G. 1991a, 'Displacement and soil-structure interaction under dynamic and cyclic loading', *Proc. 10th European Conf. on SMFE*, vol. 3, pp. 1091-104.

Gazetas, G. 1991b, 'Formulas and charts for impedances of surface and embedded foundations', *Journal of Geotechnical Engineering*, vol. 117, no. 9, pp. 1363-81.

Gazetas, G. 2015, '4th Ishihara lecture: Soil–foundation–structure systems beyond conventional seismic failure thresholds', *Soil Dynamics and Earthquake Engineering*, vol. 68, pp. 23-39.

Gazetas, G., Anastasopoulos, I., Adamidis, O. & Kontoroupi, T. 2013, 'Nonlinear rocking stiffness of foundations', *Soil Dynamics and Earthquake Engineering*, vol. 47, pp. 83-91.

Gazetas, G. & Apostolou, M. 2004, 'Nonlinear soil–structure interaction: foundation uplifting and soil yielding', *Proceedings Third UJNR Workshop on Soil-Structure Interaction*, pp. 29-30.

Gazetas, G., Garini, E. & Zafeirakos, A. 2016, 'Seismic analysis of tall anchored sheet-pile walls', *Soil Dynamics and Earthquake Engineering*, vol. 91, pp. 209-21.

Gazetas, G. & Mylonakis, G. 1998, 'Seismic soil-structure interaction: New evidence and emerging issues State of the Art Paper', *Geotechnical Earthquake Engineering and Soil Dynamics Geo-Institute ASCE Conference*, eds P. Dakoulas, E.K. Yegian & R. D. Holtz, vol. II, pp. 1119-74.

GB50011 2010, *Code for seismic design of buildings*, China Building Industry Press, Beijing.

Gelagoti, F., Kourkoulis, R., Anastasopoulos, I. & Gazetas, G. 2012a, 'Rocking-isolated frame structures: Margins of safety against toppling collapse and simplified design approach', *Soil Dynamics and Earthquake Engineering*, vol. 32, no. 1, pp. 87-102.

Gelagoti, F., Kourkoulis, R., Anastasopoulos, I. & Gazetas, G. 2012b, 'Rocking isolation of low-rise frame structures founded on isolated footings', *Earthquake Engineering and Structural Dynamics*, vol. 41, no. 7, pp. 1177-97.

Genes, M.C. & Kocak, S. 2005, 'Dynamic soil–structure interaction analysis of layered unbounded media via a coupled finite element/boundary element/scaled boundary finite element model', *International Journal for Numerical Methods in Engineering*, vol. 62, no. 6, pp. 798-823.

Georgescu, E.-S. & Pomonis, A. 2008, 'The Romanian earthquake of March 4, 1977 revisited: New insights into its territorial, economic and social impacts and their bearing on the preparedness for the future', *Proceedings of the 14th World Conference on Earthquake Engineering, Beijing, China*, pp. 12-7.

Georgiannou, V. 1991, 'Static and dynamic measurements of undrained stiffness on natural overconsolidated clays', *Proc. 10th Eur. Conf. Soil Mech. and Fnd Engng*, vol. 1, pp. 91-5.

Ghaboussi, J. & Dikmen, S.U. 1984, 'Effective stress analysis of seismic response and liquefaction: case studies', *Journal of Geotechnical Engineering*, vol. 110, no. 5, pp. 645-58.

Ghalibafian, H., Foschi, R.O. & Ventura, C.E. 2008, 'Performance-based assessment of the effects of soil-structure interaction on the seismic demands of bridge piers: A proposed methodology', *Fourteenth World Conference on Earthquake Engineering*.

Ghandil, M. & Behnamfar, F. 2015, 'The near-field method for dynamic analysis of structures on soft soils including inelastic soil–structure interaction', *Soil Dynamics and Earthquake Engineering*, vol. 75, pp. 1-17.

Ghannad, M. & Ahmadnia, A. 2006, 'The effect of soil-structure interaction on inelastic structural demands', *European Earthquake Engineering*, vol. 20, no. 1, p. 23.

Ghiocel, D.M. & Ghanem, R.G. 2002, 'Stochastic finite-element analysis of seismic soil–structure interaction', *Journal of Engineering Mechanics*, vol. 128, no. 1, pp. 66-77.

Ghobarah, A. 2001, 'Performance-based design in earthquake engineering: state of development', *Engineering Structures*, vol. 23, no. 8, pp. 878-84.

Ghosh, S.K. & Fanella, D.A. 2003, *Seismic and Wind Design of Concrete Buildings:(2000 IBC, ASCE 7-98, ACI 318-99)*, Kaplan AEC Engineering.

Ghrib, F. & Mamedov, H. 2004, 'Period formulas of shear wall buildings with flexible bases', *Earthquake Engineering and Structural Dynamics*, vol. 33, no. 3, pp. 295-314.

Goel, R.K. & Chopra, A.K. 1998, 'Period formulas for concrete shear wall buildings', *Journal of Structural Engineering*, vol. 124, no. 4, pp. 426-33.

Goel, S.C. & Leelataviwat, S. 1998, 'Seismic design by plastic method', *Engineering Structures*, vol. 20, no. 4-6, pp. 465-71.

Groholski, D. 2012, 'Seismic site response analysis and extraction of dynamic soil behavior and pore pressure response from downhole array measurements', PhD thesis, University of Illinois at Urbana-Champaign.

Gundersen, A.S. & Josefsen, J.-M. 2016, 'Modelling of Undrained Clay Subjected to Cyclic Loading-Semi-Explicit Material Model', Masters thesis, NTNU.

Gutierrez, J.A. & Chopra, A.K. 1978, 'A substructure method for earthquake analysis of structures including structure-soil interaction', *Earthquake Engineering & Structural Dynamics*, vol. 6, no. 1, pp. 51-69.

Hadjian, A., Luco, J. & Tsai, N. 1974, 'Soil-structure interaction: continuum or finite element?', *Nuclear Engineering and Design*, vol. 31, no. 2, pp. 151-67.

Hakhamaneshi, M., Kutter, B., Deng, L., Hutchinson, T. & Liu, W. 2012, 'New findings from centrifuge modeling of rocking shallow foundations in clayey ground', *GeoCongress 2012: State of the Art and Practice in Geotechnical Engineering*, pp. 195-204.

Halabian, A.M. & El Naggar, M.H. 2002, 'Effect of non-linear soil–structure interaction on seismic response of tall slender structures', *Soil Dynamics and Earthquake Engineering*, vol. 22, no. 8, pp. 639-58.

Hamburger, R. 1996, 'Implementing performance-based seismic design in structural engineering practice', *Proceedings of 11th World Conference on Earthquake Engineering, Acapulco, Mexico. Paper*.

Han, D. & Chen, W.-F. 1985, 'A nonuniform hardening plasticity model for concrete materials', *Mechanics of Materials*, vol. 4, no. 3-4, pp. 283-302.

Hara, A., Ohta, T., Niwa, M., Tanaka, S. & Banno, T. 1974, 'Shear modulus and shear strength of cohesive soils', *Soils and Foundations*, vol. 14, no. 3, pp. 1-12.

Hardin, B.O. & Black, W.L. 1968, 'Vibration modulus of normally consolidated clay', *Journal of Soil Mechanics & Foundations Div*.

Hardin, B.O. & Drnevich, V.P. 1972a, 'Shear modulus and damping in soils: design equations and curves', *Journal of Soil Mechanics & Foundations Div*, vol. 98, no. sm7.

Hardin, B.O. & Drnevich, V.P. 1972b, 'Shear modulus and damping in soils: measurement and parameter effects', *Journal of Soil Mechanics & Foundations Div*, vol. 98, no. sm6.

Hartzell, S. 1979, 'Analysis of the Bucharest strong ground motion record for the March 4, 1977 Romanian earthquake', *Bulletin of the Seismological Society of America*, vol. 69, no. 2, pp. 513-30.

Hatzigeorgiou, G.D. & Beskos, D.E. 2010, 'Soil–structure interaction effects on seismic inelastic analysis of 3-D tunnels', *Soil Dynamics and Earthquake Engineering*, vol. 30, no. 9, pp. 851-61.

Hazirbaba, K. & Rathje, E.M. 2009, 'Pore pressure generation of silty sands due to induced cyclic shear strains', *Journal of Geotechnical and Geoenvironmental Engineering*, vol. 135, no. 12, pp. 1892-905.

Head, K. 1986, 'Manual of Laboratory Testing. Volume 3: Effective Stress Tests, ELE International Ltd', Pentech Press, London.

Hokmabadi, A.S. & Fatahi, B. 2016, 'Influence of foundation type on seismic performance of buildings considering soil–structure interaction', *International Journal of Structural Stability and Dynamics*, vol. 16, no. 08, p. 1550043.

Hokmabadi, A.S., Fatahi, B. & Samali, B. 2012, 'Recording inter-storey drifts of structures in time-history approach for seismic design of building frames', *Australian Journal of Structural Engineering*, vol. 13, no. 2, pp. 175-9.

Hokmabadi, A.S., Fatahi, B. & Samali, B. 2014a, 'Assessment of soil–pile–structure interaction influencing seismic response of mid-rise buildings sitting on floating pile foundations', *Computers and Geotechnics*, vol. 55, pp. 172-86.

Hokmabadi, A.S., Fatahi, B. & Samali, B. 2014b, 'Physical modeling of seismic soil-pile-structure interaction for buildings on soft soils', *International Journal of Geomechanics*, vol. 15, no. 2, p. 04014046.

Houlsby, G., Amorosi, A. & Rojas, E. 2005, 'Elastic moduli of soils dependent on pressure: a hyperelastic formulation', *Géotechnique*, vol. 55, no. 5, pp. 383-92.

Housner, G.W. 1963, 'The behavior of inverted pendulum structures during earthquakes', *Bulletin of the Seismological Society of America*, vol. 53, no. 2, pp. 403-17.

Housner, G.W. 1986, 'Overview of Factors Involved in the Mexico Earthquakes', *The Mexico Earthquakes—1985: Factors Involved and Lessons Learned*, ASCE, pp. 1-6.

Hsu, C.-C. & Vucetic, M. 2006, 'Threshold shear strain for cyclic pore-water pressure in cohesive soils', *Journal of Geotechnical and Geoenvironmental Engineering*, vol. 132, no. 10, pp. 1325-35.

Hueckel, T. & Nova, R. 1979, 'Some hysteresis effects of the behaviour of geologic media', *International Journal of Solids and Structures*, vol. 15, no. 8, pp. 625-42.

Hung, H.H., Liu, K.Y., Ho, T.H. & Chang, K.C. 2011, 'An experimental study on the rocking response of bridge piers with spread footing foundations', *Earthquake Engineering and Structural Dynamics*, vol. 40, no. 7, pp. 749-69.

Hutchinson, T.C., Raychowdhury, P. & Chang, B. 2006, 'Nonlinear structure and foundation response during seismic loading: dual lateral load resisting systems', *Proceedings of the 8th US National Conference on Earthquake Engineering*.

Idriss, I. & Sun, J. 1992, *User's Manual for SHAKE91: Center for Geotechnical Modeling*, Department of Civil and Environmental Engineering, University of California, Davis, CA.

Iranian Standard 2800 2017, *Iranian code of practice for seismic resistance design of buildings*, Building and Housing Research Centre, Tehran.

IS-1893 2002, *Indian standard criteria for earthquake resistant design of structures, Part 1: General provision and buildings*, Bureau of Indian Standards, New Delhi.

Isam, S., Hassan, A. & Mhamed, S. 2012, '3D elastoplastic analysis of the seismic performance of inclined micropiles', *Computers and Geotechnics*, vol. 39, pp. 1-7.

Ishibashi, I. 1992, 'Discussion of "Effect of Soil Plasticity on Cyclic Response" by Mladen Vucetic and Ricardo Dobry (January, 1991, Vol. 117, No. 1)', *Journal of Geotechnical Engineering*, vol. 118, no. 5, pp. 830-2.

Ishibashi, I. & Zhang, X. 1993, 'Unified dynamic shear moduli and damping ratios of sand and clay', *Soils and Foundations*, vol. 33, no. 1, pp. 182-91.

Ishihara, K. 1996, *Soil behaviour in earthquake geotechnics*, Oxford University Press.

Ishihara, K. & Yoshimine, M. 1992, 'Evaluation of settlements in sand deposits following liquefaction during earthquakes', *Soils and Foundations*, vol. 32, no. 1, pp. 173-88.

Ishiyama, Y. 2011, *Intorduction to earthquake engineering and seismic codes in the world*, Hokkaido University, Hokkaido, Japan.

Itasca 2012, *User's Manual FLAC3D: Fast lagrangian analysis of continua in 3 dimensions, version 5.0*, Itasca International Inc., Minneapolis.

Iwata, Y., Sugimoto, H. & Kuguamura, H. 2006, 'Reparability limit of steel structural buildings based on the actual data of the Hyogoken-Nanbu earthquake', *Proceedings of the 38th Joint Panel. Wind and Seismic effects. NIST Special Publication*, vol. 1057, pp. 23-32.

Jangid, R. 2007, 'Optimum lead–rubber isolation bearings for near-fault motions', *Engineering Structures*, vol. 29, no. 10, pp. 2503-13.

Jangid, R. & Londhe, Y. 1998, 'Effectiveness of elliptical rolling rods for base isolation', *Journal of Structural Engineering*, vol. 124, no. 4, pp. 469-72.

Jarernprasert, S., Bazan-Zurita, E. & Bielak, J. 2013, 'Seismic soil-structure interaction response of inelastic structures', *Soil Dynamics and Earthquake Engineering*, vol. 47, pp. 132-43.

Jayalekshmi, B. & Chinmayi, H. 2016, 'Effect of soil stiffness on seismic response of reinforced concrete buildings with shear walls', *Innovative Infrastructure Solutions*, vol. 1, no. 1, p. 2.

Jenck, O., Dias, D. & Kastner, R. 2009, 'Three-dimensional numerical modeling of a piled embankment', *International Journal of Geomechanics*, vol. 9, no. 3, pp. 102-12.

Jennings, P.C. 1971, *Engineering features of the San Fernando earthquake of February 9, 1971*, Earthquake Engineering Research Laboratory.

Jennings, P.C. & Bielak, J. 1973, 'Dynamics of building-soil interaction', *Bulletin of the Seismological Society of America*, vol. 63, no. 1, pp. 9-48.

Jia, J. 2018, 'Dynamic and Cyclic Properties of Soils', *Soil Dynamics and Foundation Modeling*, Springer, pp. 75-108.

Jiang, X. & Yan, Z. 1998, 'Earthquake response analysis of building-foundation-building interaction system', *Journal of Vibration Engineering*, vol. 11, no. 1, pp. 31-7.

Johnston, J. & White, S. 2018, *Understanding the Meckering earthquake: Western Australia, 14 October 1968*, Geological Survey of Western Australia.

Karimi, Z. & Dashti, S. 2016, 'Seismic performance of shallow founded structures on liquefiable ground: validation of numerical simulations using centrifuge experiments', *Journal of Geotechnical and Geoenvironmental Engineering*, vol. 142, no. 6, p. 04016011.

Karimi, Z., Dashti, S., Bullock, Z., Porter, K. & Liel, A. 2018, 'Key predictors of structure settlement on liquefiable ground: a numerical parametric study', *Soil Dynamics and Earthquake Engineering*, vol. 113, pp. 286-308.

Katsanos, E.I., Sextos, A.G. & Manolis, G.D. 2010, 'Selection of earthquake ground motion records: A state-of-the-art review from a structural engineering perspective', *Soil Dynamics and Earthquake Engineering*, vol. 30, no. 4, pp. 157-69.

Kausel, E. 2010, 'Early history of soil–structure interaction', *Soil Dynamics and Earthquake Engineering*, vol. 30, no. 9, pp. 822-32.

Kavitha, P., Beena, K. & Narayanan, K. 2016, 'A review on soil–structure interaction analysis of laterally loaded piles', *Innovative Infrastructure Solutions*, vol. 1, no. 1, p. 14.

KBC 2009, *Korean building code-structural*, Architectural Institute of Korea, Seoul.

Khalil, L., Sadek, M. & Shahrour, I. 2007, 'Influence of the soil–structure interaction on the fundamental period of buildings', *Earthquake Engineering & Structural Dynamics*, vol. 36, no. 15, pp. 2445-53.

Khaloo, A., Nozhati, S., Masoomi, H. & Faghihmaleki, H. 2016, 'Influence of earthquake record truncation on fragility curves of RC frames with different damage indices', *Journal of Building Engineering*, vol. 7, pp. 23-30.

Khosravifar, A., Elgamal, A., Lu, J. & Li, J. 2018, 'A 3D model for earthquake-induced liquefaction triggering and post-liquefaction response', *Soil Dynamics and Earthquake Engineering*, vol. 110, pp. 43-52.

Khouri, N.Q. 1984, 'Dynamic properties of soils', PhD thesis, Syracuse University.

Kim, D.-K., Lee, S.-H., Kim, D.-S., Choo, Y.W. & Park, H.-G. 2015, 'Rocking effect of a mat foundation on the earthquake response of structures', *Journal of Geotechnical and Geoenvironmental Engineering*, vol. 141, no. 1, p. 04014085.

King, A. & Shelton, R. 2004, 'New Zealand advances in performance-based seismic design', *13th World Conference on Earthquake Engineering, Vancouver, BC, Canada*.

Kishida, T., Boulanger, R.W., Abrahamson, N.A., Wehling, T.M. & Driller, M.W. 2009, 'Regression models for dynamic properties of highly organic soils', *Journal of Geotechnical and Geoenvironmental Engineering*, vol. 135, no. 4, pp. 533-43.

Klemencic, R., Li, G.-Q. & Fry, J.A. 2012, 'Performance-Based Seismic Design - State of Practice', *CTBUH-2012: 9th Word Conference*, Shanghai.

Kokusho, T. 1980, 'Cyclic triaxial test of dynamic soil properties for wide strain range', *Soils and Foundations*, vol. 20, no. 2, pp. 45-60.

Kokusho, T., Yoshida, Y. & Esashi, Y. 1982, 'Dynamic properties of soft clay for wide strain range', *Soils and Foundations*, vol. 22, no. 4, pp. 1-18.

Kondnor, R.L. & Zelasko, J.S. 1963, 'A hyperbolic stress-strain folnzulatiort of sands', *Proceedings 2nd Pan American Conference on Soil Mechanics and Foundation Engineering*, pp. 289-324.

Kourkoulis, R., Gelagoti, F. & Anastasopoulos, I. 2012, 'Rocking isolation of frames on isolated footings: design insights and limitations', *Journal of Earthquake Engineering*, vol. 16, no. 3, pp. 374-400.

Koutsoftas, D. 1978, 'Effect of cyclic loads on undrained strength of two marine clays', *Journal of Geotechnical and Geoenvironmental Engineering*, vol. 104, no. ASCE 13751.

Kramer, S. 1996, 'Geotechnical Earthquake Engineering', *Pren-tice Hall, New Jersey*.

Kramer, S.L. 2008, 'Performance-based earthquake engineering: opportunities and implications for geotechnical engineering practice', *Geotechnical Earthquake Engineering and Soil Dynamics IV*, pp. 1-32.

Kraus, I. & Džakić, D. 2013, 'Soil-structure interaction effects on seismic behaviour of reinforced concrete frames', *50 years Skopje Earthquake-50 years European Earthquake Engineering*.

Krawinkler, H., Medina, R. & Alavi, B. 2003, 'Seismic drift and ductility demands and their dependence on ground motions', *Engineering Structures*, vol. 25, no. 5, pp. 637-53.

Krishna, A.M., Dey, A. & Sreedeep, S. 2018, *Geotechnics for Natural and Engineered Sustainable Technologies: GeoNEst*, Springer.

Kuhlemeyer, R.L. & Lysmer, J. 1973, 'Finite element method accuracy for wave propagation problems', *Journal of Soil Mechanics & Foundations Div*, vol. 99, no. Tech Rpt.

Kumar, K. 2008, *Basic Geotechnical Earthquake Engineering, New Age International Publishers, 2008: Basic Geotechnical Earthquake Engineering*, vol. 1, Bukupedia.

Ladd, R.S., Dobry, R., Dutko, P., Yokel, F. & Chung, R. 1989, 'Pore-water pressure buildup in clean sands because of cyclic straining', *Geotechnical Testing Journal*, vol. 12, no. 1, pp. 77-86.

Lade, P.V. 2005, 'Overview of constitutive models for soils', *Soil constitutive models: Evaluation, selection, and calibration*, vol. 128, ASCE Geotechnical Special Publication, pp. 1-34.

Lamb, H. 1904, 'I. On the propagation of tremors over the surface of an elastic solid', *Philosophical Transactions of the Royal Society of London. Series A, Containing Papers of a Mathematical or Physical Character*, vol. 203, no. 359-371, pp. 1-42.

Leelataviwat, S., Goel, S.C. & Stojadinović, B. 1999, 'Toward performance-based seismic design of structures', *Earthquake Spectra*, vol. 15, no. 3, pp. 435-61.

Lin, H.T., Roesset, J. & Tassoulas, J.L. 1987, 'Dynamic interaction between adjacent foundations', *Earthquake Engineering and Structural Dynamics*, vol. 15, no. 3, pp. 323-43.

Lin, M.-L., Huang, T.-H. & You, J.-C. 1996, 'The effects of frequency on damping properties of sand', *Soil Dynamics and Earthquake Engineering*, vol. 15, no. 4, pp. 269-78.

Liu, M., Burns, S.A. & Wen, Y. 2005, 'Multiobjective optimization for performance-based seismic design of steel moment frame structures', *Earthquake Engineering and Structural Dynamics*, vol. 34, no. 3, pp. 289-306.

Liu, W. 2014, 'Balancing the beneficial contributions of foundation rocking and structural yielding in moment-frame and frame-wall building systems', PhD thesis, UC San Diego.

Liu, X., Cheng, X., Scarpas, A. & Blaauwendraad, J. 2005, 'Numerical modelling of nonlinear response of soil. Part 1: Constitutive model', *International Journal of Solids and Structures*, vol. 42, no. 7, pp. 1849-81.

Lopez-Caballero, F. & Farahmand-Razavi, A.M. 2008, 'Numerical simulation of liquefaction effects on seismic SSI', *Soil Dynamics and Earthquake Engineering*, vol. 28, no. 2, pp. 85-98.

Lou, M., Wang, H., Chen, X. & Zhai, Y. 2011, 'Structure–soil–structure interaction: Literature review', *Soil Dynamics and Earthquake Engineering*, vol. 31, no. 12, pp. 1724-31.

Lu, Y., Hajirasouliha, I. & Marshall, A.M. 2016, 'Performance-based seismic design of flexible-base multi-storey buildings considering soil–structure interaction', *Engineering Structures*, vol. 108, pp. 90-103.

Lysmer, J. & Kuhlemeyer, R.L. 1969, 'Finite dynamic model for infinite media', *Journal of the Engineering Mechanics Division*, vol. 95, no. 4, pp. 859-78.

Lysmer, J. & Richart, F.E. 1966, 'Dynamic response of footings to vertical loading', *Journal of Soil Mechanics & Foundations Div*, vol. 92(1), no. 65-91.

Ma, X., Cheng, Y., Au, S., Cai, Y. & Xu, C. 2009, 'Rocking vibration of a rigid strip footing on saturated soil', *Computers and Geotechnics*, vol. 36, no. 6, pp. 928-33.

Maheshwari, B.K., Truman, K.Z., El Naggar, M.H. & Gould, P.L. 2004, 'Three-dimensional nonlinear analysis for seismic soil–pile-structure interaction', *Soil Dynamics and Earthquake Engineering*, vol. 24, no. 4, pp. 343-56.

Maheswari, R.U., Boominathan, A. & Dodagoudar, G.R. 2010, 'Seismic site classification and site period mapping of Chennai City using geophysical and geotechnical data', *Journal of Applied Geophysics*, vol. 72, no. 3, pp. 152-68.

Mahin, S.A. & Bertero, V.V. 1981, 'An evaluation of inelastic seismic design spectra', *Journal of the Structural Division*, vol. 107, no. 9, pp. 1777-95.

Makris, N. 2014, 'A half-century of rocking isolation', *Earthquakes and Structures*, vol. 7, no. 6, pp. 1187-221.

Mánica, M., Ovando, E. & Botero, E. 2014, 'Assessment of damping models in FLAC', *Computers and Geotechnics*, vol. 59, pp. 12-20.

Mansur, W.J. 1983, 'A time-stepping technique to solve wave propagation problems using the boundary element method', PhD thesis, University of Southampton.

Masaeli, H., Khoshnoudian, F. & Ziaei, R. 2015, 'Rocking soil-structure systems subjected to near-fault pulses', *Journal of Earthquake Engineering*, vol. 19, no. 3, pp. 461-79.

Masing, G. 1926, 'Eigenspannungen und Verfestigung beim Messing [Fundamental stresses and strengthening with brass]', *Proceedings of the 2nd International Congress of Applied Mechanics*, pp. 12-7.

Matešić, L. & Vucetic, M. 2003, 'Strain-rate effect on soil secant shear modulus at small cyclic strains', *Journal of Geotechnical and Geoenvironmental Engineering*, vol. 129, no. 6, pp. 536-49.

Maugeri, M., Musumeci, G., Novità, D. & Taylor, C. 2000, 'Shaking table test of failure of a shallow foundation subjected to an eccentric load', *Soil Dynamics and Earthquake Engineering*, vol. 20, no. 5-8, pp. 435-44.

Mccue, K., Gregson, P., Sinadinovski, C. & Hodgson, L. 2001, *Australian Seismological Report 1997*, AGSO - Geoscience Australia, Canberra.

Meek, J.W. 1975, 'Effects of foundation tipping on dynamic response', *Journal of the Structural Division*, vol. 101.

Mendoza, C.E., Colmenares, J.E. & Merchan, V.E. 2005, 'Stiffness of an unsaturated compacted clayey soil at very small strains', *Proceedings of the International Symposium on Advanced Experimental Unsaturated Soil Mechanics*, pp. 199-204.

Menegon, S.J., Tsang, H.H., Wilson, J.L. & Lam, N.T.K. 2015, 'Displacement-based seismic design of limited ductile rectangular RC walls: from the design engineers perspective', *Second International Conference on Performance-based and Life-cycle Structural Engineering*, Brisbane, Australia.

Menq, F.Y. 2003, 'Dynamic properties of sandy and gravelly soils', PhD thesis, University of Texas.

Mergos, P.E. & Kawashima, K. 2005, 'Rocking isolation of a typical bridge pier on spread foundation', *Journal of Earthquake Engineering*, vol. 9, no. sup2, pp. 395-414.

Meyerhof, G.G. 1963, 'Some recent research on the bearing capacity of foundations', *Canadian Geotechnical Journal*, vol. 1, no. 1, pp. 16-26.

Meymand, P.J. 1998, 'Shaking table scale model tests of nonlinear soil-pile-superstructure interaction in soft clay', PhD thesis, University of California, Berkeley.

Michalowski, R.L. 1998, 'Soil reinforcement for seismic design of geotechnical structures', *Computers and Geotechnics*, vol. 23, no. 1-2, pp. 1-17.

Midorikawa, M., Okawa, I., Iiba, M. & Teshigawara, M. 2004, 'Performance-based seismic design provisions newly introduced to the building standard law of Japan', *Journal of Japan Association for Earthquake Engineering*, vol. 4, no. 3, pp. 162-73.

Mindlin, R.D. 1936, 'Force at a point in the interior of a semi-infinite solid', *Physics*, vol. 7, no. 5, pp. 195-202.

Miranda, E. & Ruiz-García, J. 2002, 'Evaluation of approximate methods to estimate maximum inelastic displacement demands', *Earthquake Engineering and Structural Dynamics*, vol. 31, no. 3, pp. 539-60.

Mirhabibi, A. & Soroush, A. 2013, 'Effects of building three-dimensional modeling type on twin tunneling-induced ground settlement', *Tunnelling and Underground Space Technology*, vol. 38, pp. 224-34.

Miwa, S., Ikeda, T. & Sato, T. 2006, 'Damage process of pile foundation in liquefied ground during strong ground motion', *Soil Dynamics and Earthquake Engineering*, vol. 26, no. 2-4, pp. 325-36.

Moehle, J. & Deierlein, G.G. 2004, 'A framework methodology for performance-based earthquake engineering', *13th World Conference on Earthquake Engineering*, vol. 679.

Moroni, M.O., Sarrazin, M. & Soto, P. 2012, 'Behavior of instrumented base-isolated structures during the 27 February 2010 Chile earthquake', *Earthquake Spectra*, vol. 28, no. S1, pp. S407-S24.

Mroueh, H. & Shahrour, I. 2003, 'A full 3-D finite element analysis of tunneling–adjacent structures interaction', *Computers and Geotechnics*, vol. 30, no. 3, pp. 245-53.

Muravskii, G. & Frydman, S. 1998, 'Site response analysis using a non-linear hysteretic model', *Soil Dynamics and Earthquake Engineering*, vol. 17, no. 4, pp. 227-38.

Muto, K., Takahasi, R., Aida, I., Ando, N., Hisada, T., Nakagawa, K., Omemura, H. & Osawa, Y. 1960, 'Nonlinear response analyzers and application to earthquake resistant design', *Proceedings of the Second World Conference on Earthquake Engineering*, pp. 649-68.

Mylonakis, G. & Gazetas, G. 2000, 'Seismic soil-structure interaction: beneficial or detrimental?', *Journal of Earthquake Engineering*, vol. 4, no. 3, pp. 277-301.

Naeim, F., Lew, M., Huang, S.C., Lam, H.K. & Carpenter, L.D. 2000, 'The performance of Tall buildings during the 21 September 1999 Chi-Chi earthquake, Taiwan', *The Structural Design of Tall Buildings*, vol. 9, no. 2, pp. 137-60.

Naesgaard, E. 2011, 'A hybrid effective stress–total stress procedure for analyzing soil embankments subjected to potential liquefaction and flow', PhD thesis, University of British Columbia.

Nagarajaiah, S. & Sun, X. 2001, 'Base-isolated FCC building: Impact response in Northridge earthquake', *Journal of Structural Engineering*, vol. 127, no. 9, pp. 1063-75.

Nakhaei, M. & Ghannad, M.A. 2008, 'The effect of soil–structure interaction on damage index of buildings', *Engineering Structures*, vol. 30, no. 6, pp. 1491-9.

NCC 2016, *National construction code: Volume one*, Australian Building Codes Board, Canberra.

NCh433.Of96 1996, *Earthquake resistance design of buildings*, Instituto Nacional de Normalizacion, Santiago.

Negro, P., Paolucci, R., Pedretti, S. & Faccioli, E. 2000, 'Large-scale soil-structure interaction experiments on sand under cyclic loading', *Proceedings of the 12th World Conference on Earthquake Engineering*, p. 1191.

Newmark, N. & Rosenblueth, E. 1971, *Fundamentals of earthquake engineering*, Prentice Hall. Inc., Englewood Cliffs.

Ngoc, T.P., Li, D., Fatahi, B. & Khabbaz, H. 2017, 'A review on the influence of degree of saturation on small strain shear modulus of unsaturated soils', *ICSMGE 2017-19th International Conference on Soil Mechanics and Geotechnical Engineering*.

NIST-GCR-11-917-15 2011, *Selecting and scaling earthquake ground motions for performing response-history analyses.*, NEHRP Consultants Joint Venture, Redwood City.

NZS1170.5 2004, *Structural design action - Part 5: Earthquake actions – New Zealand*, Standards New Zealand, Wellington.

O'Reilly, M.P. & Brown, S.F. 1991, *Cyclic loading of soils: from theory to design*, Blackie Glasgow, UK.

Ohara, S. & Matsuda, H. 1988, 'Study on the settlement of saturated clay layer induced by cyclic shear', *Soils and Foundations*, vol. 28, no. 3, pp. 103-13.

Otani, S. 2004, 'Japanese seismic design of high-rise reinforced concrete buildings: An example of performance based design code and state of practices', *13th World Conference on Earthquake Engineering*.

Palmeri, A. & Makris, N. 2008, 'Response analysis of rigid structures rocking on viscoelastic foundation', *Earthquake Engineering and Structural Dynamics*, vol. 37, no. 7, pp. 1039-63.

Paolucci, R., Shirato, M. & Yilmaz, M.T. 2008, 'Seismic behaviour of shallow foundations: Shaking table experiments vs numerical modelling', *Earthquake Engineering and Structural Dynamics*, vol. 37, no. 4, pp. 577-95.

Park, D. & Hashash, Y.M.A. 2004, 'Soil damping formulation in nonlinear time domain site response analysis', *Journal of Earthquake Engineering*, vol. 8, no. 02, pp. 249-74.

Park, D. & Hashash, Y.M.A. 2008, 'Rate-dependent soil behavior in seismic site response analysis', *Canadian Geotechnical Journal*, vol. 45, no. 4, pp. 454-69.

Pecker, A. 2008, *Advanced earthquake engineering analysis*, vol. 494, Springer Science & Business Media.

PEER-TBI 2017, *Guidelines for performance-based seismic design of tall buildings*, Pacific Earthquake Engineering Center, Berkeley.

Pelekis, I., Madabhushi, G.S.P. & DeJong, M.J. 2017, 'A centrifuge investigation of two different soil-structure systems with rocking and sliding on dense sand', *6th ECCOMAS Thematic Conference on Computational Methods in Structural Dynamics and Earthquake Engineering*, Rhodes Island, Greece.

Pestana, J.M. & Biscontin, G. 2000, *A simplified model describing the cyclic behavior of lightly overconsolidated clays in simple shear*, Geotechnical Engineering Report No UCB/GT/2000-03, University of California, Department of Civil Engineering.

Petalas, A. & Galavi, V. 2013, 'Plaxis Liquefaction Model UBC3DPLM', *Plaxis Report*.

Polcari, M., Albano, M., Atzori, S., Bignami, C. & Stramondo, S. 2018, 'The causative fault of the 2016 M_{wp} 6.1 Petermann ranges intraplate earthquake (Central Australia) retrieved by C-and L-band InSAR data', *Remote Sensing*, vol. 10, no. 8, p. 1311.

Popescu, R., Prevost, J.H., Deodatis, G. & Chakrabortty, P. 2006, 'Dynamics of nonlinear porous media with applications to soil liquefaction', *Soil Dynamics and Earthquake Engineering*, vol. 26, no. 6-7, pp. 648-65.

Potts, D. & Axelsson, K. 2002, *Guidelines for the use of advanced numerical analysis*, Thomas Telford.

Prakash, S. 1981, *Soil dynamics*, McGraw-Hill Companies.

Prevost, J.H. & Popescu, R. 1996, 'Constitutive relations for soil materials', *Electronic Journal of Geotechnical Engineering*, vol. 1.

Priestley, M.J.N. 1993, 'Myths and fallacies in earthquake engineering', *Bulletin of the New Zealand Society for Earthquake Engineering*, vol. 26, no. 3, pp. 329-41.

Priestley, M.J.N. 2000, 'Performance based seismic design', *Bulletin of the New Zealand Society for Earthquake Engineering*, vol. 33, no. 3, pp. 325-46.

Puebla, H. 1999, 'A constitutive model for sand and the analysis of the CanLex Embankments', PhD thesis, University of British Columbia.

Puzrin, A. 2012, *Constitutive modelling in geomechanics: Introduction*, Springer Science & Business Media.

Pyke, R.M. 1979, 'Nonlinear soil models for irregular cyclic loadings', *Journal of Geotechnical and Geoenvironmental Engineering*, vol. 105.

Qiu, T. & Fox, P.J. 2008, 'Effective soil density for propagation of small strain shear waves in saturated soil', *Journal of Geotechnical and Geoenvironmental Engineering*, vol. 134, no. 12, pp. 1815-9.

Qiu, T., Huang, Y., Guadalupe-Torres, Y., Baxter, C.D.P. & Fox, P.J. 2015, 'Effective soil density for small-strain shear waves in saturated granular materials', *Journal of Geotechnical and Geoenvironmental Engineering*, vol. 141, no. 9, p. 04015036.

Rahvar 2006, *Geotechnical, geophysical investigations and foundation design report of Kooh-e-Noor commercial complex*, Final Report, Pazhoohesh Omran Rahvar Engineering Company, Tehran.

Raj, D., Singh, Y. & Kaynia, A.M. 2018, 'Behavior of slopes under multiple adjacent footings and buildings', *International Journal of Geomechanics*, vol. 18, no. 7, p. 04018062.

Ramadan, O.M.O., Mehanny, S.S.F. & Kotb, A.A.M. 2020, 'Assessment of seismic vulnerability of continuous bridges considering soil-structure interaction and wave passage effects', *Engineering Structures*, vol. 206, p. 110161.

Ramberg, W. & Osgood, W.R. 1943, *Description of stress-strain curves by three parameters*, Technical Note No. 902, National Advisory Committee for Aeronautics.

Ramirez, C.M. & Miranda, E. 2012, 'Significance of residual drifts in building earthquake loss estimation', *Earthquake Engineering and Structural Dynamics*, vol. 41, no. 11, pp. 1477-93.

Raviola, G., Severe, J., Therosme, T., Oswald, C., Belkin, G. & Eustache, F.E. 2013, 'The 2010 Haiti earthquake response', *Psychiatric Clinics*, vol. 36, no. 3, pp. 431-50.

Raychowdhury, P. 2011, 'Seismic response of low-rise steel moment-resisting frame (SMRF) buildings incorporating nonlinear soil–structure interaction (SSI)', *Engineering Structures*, vol. 33, no. 3, pp. 958-67.

Rayhani, M.H. & El Naggar, M.H. 2008, 'Seismic response of sands in centrifuge tests', *Canadian Geotechnical Journal*, vol. 45, no. 4, pp. 470-83.

Rayhani, M.T. & El Naggar, M. 2012, 'Physical and numerical modeling of seismic soil-structure interaction in layered soils', *Geotechnical and Geological Engineering*, vol. 30, no. 2, pp. 331-42.

Reissner, E. 1936, 'Stationäre, axialsymmetrische, durch eine schüttelnde Masse erregte Schwingungen eines homogenen elastischen Halbraumes', *Ingenieur-Archiv*, vol. 7, no. 6, pp. 381-96.

Renzi, S., Madiai, C. & Vannucchi, G. 2013, 'A simplified empirical method for assessing seismic soil-structure interaction effects on ordinary shear-type buildings', *Soil Dynamics and Earthquake Engineering*, vol. 55, pp. 100-7.

Reséndiz, D. & Roesset, J.M. 1985, 'Soil-structure interaction in Mexico City during the 1985 earthquakes', *The Mexico Earthquakes—1985: Factors Involved and Lessons Learned*, ASCE, pp. 193-203.

Richards, R.J., Elms, D.G. & Budhu, M. 1993, 'Seismic bearing capacity and settlements of foundations', *Journal of Geotechnical Engineering*, vol. 119, no. 4, pp. 662-74.

Rodriguez, M.E. & Montes, R. 2000, 'Seismic response and damage analysis of buildings supported on flexible soils', *Earthquake Engineering and Structural Dynamics*, vol. 29, no. 5, pp. 647-65.

Romo, M.P. 1995, 'Clay behavior, ground response and soil-structure interaction studies in Mexico City', *Third International Conference on Recent Advances in Geotechnical Earthquake Engineering and Soil Dynamics*, St. Louis, Missouri.

Roscoe, K.H. & Burland, J.B. 1968, 'On the generalized stress-strain behaviour of wet clay', in J. Heyman & F.A. Leckie (eds), *Engineering Plasticity*, Cambridge University Press.

Rosenblueth, E. & Meli, R. 1986, 'The 1985 Mexico earthquake', *Concrete International*, vol. 8, no. 5, pp. 23-34.

Rowe, P.W. 1962, 'The stress-dilatancy relation for static equilibrium of an assembly of particles in contact', *Proceedings of the Royal Society of London. Series A. Mathematical and Physical Sciences*, vol. 269, no. 1339, pp. 500-27.

Ruiz-Garcia, J. & Miranda, E. 2005, *Perfomance-based assessment of existing structures accounting for residual displacements*, Report No. 153, Stanford University, Stanford, CA.

Rynn, J., Brennan, E., Hughes, P., Pedersen, I. & Stuart, H. 1992, 'The 1989 Newcastle, Australia, earthquake', *Bulletin of the New Zealand Society for Earthquake Engineering*, vol. 25, no. 2, pp. 77-144.

Saad, A., Sanders, D.H. & Buckle, I. 2012, 'Impact of rocking foundations on horizontally curved bridge systems subjected to seismic loading', *Structures Congress 2012*, pp. 625-35.

Sadat, M.R., Huang, J., Bin-Shafique, S. & Rezaeimalek, S. 2018, 'Study of the behavior of mechanically stabilized earth (MSE) walls subjected to differential settlements', *Geotextiles and Geomembranes*, vol. 46, no. 1, pp. 77-90.

Sáez, E., Lopez-Caballero, F. & Modaressi-Farahmand-Razavi, A. 2013, 'Inelastic dynamic soil–structure interaction effects on moment-resisting frame buildings', *Engineering Structures*, vol. 51, pp. 166-77.

Santamarina, J.C. 2003, 'Soil behavior at the microscale: Particle forces', *Proceedings of a Symposium on Soil Behavior and Soft Ground Construction*, Massachusetts, United States.

Santamarina, J.C., Klein, A. & Fam, M.A. 2001, 'Soils and waves: Particulate materials behavior, characterization and process monitoring', *Journal of Soils and Sediments*, vol. 1, no. 2.

Scarfone, R., Morigi, M. & Conti, R. 2020, 'Assessment of dynamic soil-structure interaction effects for tall buildings: A 3D numerical approach', *Soil Dynamics and Earthquake Engineering*, vol. 128, p. 105864.

Schanz, T. & Vermeer, P.A. 1996, 'Angles of friction and dilatancy of sand', *Geotechnique*, vol. 46, no. 1, pp. 145-51.

Schanz, T., Vermeer, P.A. & Bonnier, P.G. 1999, 'The hardening soil model: formulation and verification', *Beyond 2000 in computational geotechnics*, pp. 281-96.

Schnabel, P.B., Lysmer, J. & Seed, H.B. 1972, *SHAKE: A computer program for earthquake response analysis of horizontally layered sites,* , EERC Report No. 72-12, University of California, Berkeley.

Schofield, A. & Wroth, P. 1968, *Critical state soil mechanics*, vol. 310, McGraw-Hill, London.

SEAOC 1959, *Recommended lateral force requirements and commentary (SEAOC Blue Book)*, Structural Engineers Association of California, Sacramento.

SEAOC 1995, *Vision 2000 – Performance based seismic engineering of buildings*, Structural Engineers Association of California, Sacramento.

Seed, H.B. & Idriss, I.M. 1970, *Soil moduli and damping factors for dynamic response analysis*, Report No. EERC 70-10, University of California, Berkeley.

Seed, H.B., Murarka, R., Lysmer, J. & Idriss, I.M. 1976, 'Relationships of maximum acceleration, maximum velocity, distance from source, and local site conditions for moderately strong earthquakes', *Bulletin of the Seismological Society of America*, vol. 66, no. 4, pp. 1323-42.

Segrestin, P. & Bastick, M.J. 1988, 'Seismic design of reinforced earth retaining walls-The contribution of finite elements analysis', *International Geotechnical Symposium on Theory and Practice of Earth Reinforcement*, Kyushu, pp. 577-82.

Seidalinov, G. 2018, 'Constitutive and numerical modeling of clay subjected to cyclic loading', PhD thesis, University of British Columbia.

SEISMOSOFT 2016, *SeismoMatch: A computer program for adjusting earthquake records to match a specific target response spectrum*, Seismosoft Ltd, Pavia.

Semblat, J.F. 2011, 'Modeling seismic wave propagation and amplification in 1D/2D/3D linear and nonlinear unbounded media', *International Journal of Geomechanics*, vol. 11, no. 6, pp. 440-8.

Shearer, P.M. & Orcutt, J.A. 1987, 'Surface and near-surface effects on seismic waves—theory and borehole seismometer results', *Bulletin of the Seismological Society of America*, vol. 77, no. 4, pp. 1168-96.

Sherif, M.A., Ishibashi, I. & Gaddah, A.H. 1977, 'Damping ratio for dry sands', *Journal of Geotechnical and Geoenvironmental Engineering*, vol. 103, no. ASCE 13050.

Shibuya, S., Mitachi, T., Fukuda, F. & Degoshi, T. 1995, 'Strain rate effects on shear modulus and damping of normally consolidated clay', *Geotechnical Testing Journal*, vol. 18, no. 3, pp. 365-75.

Shirato, M., Kouno, T., Asai, R., Nakatani, S., Fukui, J. & Paolucci, R. 2008, 'Large-scale experiments on nonlinear behavior of shallow foundations subjected to strong earthquakes', *Soils and Foundations*, vol. 48, no. 5, pp. 673-92.

Skempton, A.W. & MacDonald, D.H. 1956, 'The allowable settlements of buildings', *Proceedings of the Institution of Civil Engineers*, vol. 5, no. 6, pp. 727-68.

Snieder, R. & Safak, E. 2006, 'Extracting the building response using seismic interferometry: Theory and application to the Millikan Library in Pasadena, California', *Bulletin of the Seismological Society of America*, vol. 96, no. 2, pp. 586-98.

Soós, M. & Vigh, L.G. 2012, 'On the Eurocode 8 limited damage criteria for non-structural elements–Analysis and requirements', *15th World Conference on Earthquake Engineering. Lisbon, Portugal*.

Sözen, M.A. 1981, 'Review of earthquake response of reinforced concrete buildings with a view to drift control', in O. Ergunay & M. Erdik (eds), *State-of-the-art in earthquake engineering*, Ankara, pp. 383-418.

Srbulov, M. 2011, *Practical soil dynamics: case studies in earthquake and geotechnical engineering*, vol. 20, Springer Science & Business Media.

Stafford, P.J. & Bommer, J.J. 2009, 'Empirical equations for the prediction of the equivalent number of cycles of earthquake ground motion', *Soil Dynamics and Earthquake Engineering*, vol. 29, no. 11-12, pp. 1425-36.

Stevens, D.J. & Krauthammer, T. 1988, 'A finite difference/finite element approach to dynamic soil-structure interaction modelling', *Computers and structures*, vol. 29, no. 2, pp. 199-205.

Stewart, J.P., Fenves, G.L. & Seed, R.B. 1999, 'Seismic soil-structure interaction in buildings. I: Analytical methods', *Journal of Geotechnical and Geoenvironmental Engineering*, vol. 125, no. 1, pp. 26-37.

Stewart, J.P., Kim, S., Bielak, J., Dobry, R. & Power, M.S. 2003, 'Revisions to soil-structure interaction procedures in NEHRP design provisions', *Earthquake Spectra*, vol. 19, no. 3, pp. 677-96.

Stümpel, H., Kähler, S., Meissner, R. & Milkereit, B. 1984, 'The use of seismic shear waves and compressional waves for lithological problems of shallow sediments', *Geophysical Prospecting*, vol. 32, no. 4, pp. 662-75.

Tabatabaiefar, H.R. & Fatahi, B. 2014, 'Idealisation of soil–structure system to determine inelastic seismic response of mid-rise building frames', *Soil Dynamics and Earthquake Engineering*, vol. 66, pp. 339-51.

Tabatabaiefar, H.R., Fatahi, B. & Samali, B. 2012, 'Seismic behavior of building frames considering dynamic soil-structure interaction', *International Journal of Geomechanics*, vol. 13, no. 4, pp. 409-20.

Tabatabaiefar, H.R., Fatahi, B. & Samali, B. 2013a, 'Lateral seismic response of building frames considering dynamic soil-structure interaction effects', *Structural Engineering and Mechanics*, vol. 45, no. 3, pp. 311-21.

Tabatabaiefar, H.R., Fatahi, B. & Samali, B. 2014, 'An empirical relationship to determine lateral seismic response of mid-rise building frames under influence of soil–structure interaction', *The Structural Design of Tall and Special Buildings*, vol. 23, no. 7, pp. 526-48.

Tabatabaiefar, S.H.R., Fatahi, B. & Samali, B. 2013b, 'Seismic behavior of building frames considering dynamic soil-structure interaction', *International Journal of Geomechanics*, vol. 13, no. 4, pp. 409-20.

Taha, A., El Naggar, M.H. & Turan, A. 2015, 'Numerical modeling of the dynamic lateral behavior of geosynthetics-reinforced pile foundation system', *Soil Dynamics and Earthquake Engineering*, vol. 77, pp. 254-66.

Taiebat, M., Shahir, H. & Pak, A. 2007, 'Study of pore pressure variation during liquefaction using two constitutive models for sand', *Soil Dynamics and Earthquake Engineering*, vol. 27, no. 1, pp. 60-72.

Tatsuoka, F., Iwasaki, T. & Takagi, Y. 1978, 'Hysteretic damping of sands under cyclic loading and its relation to shear modulus', *Soils and Foundations*, vol. 18, no. 2, pp. 25-40.

Teachavorasinskun, S., Thongchim, P. & Lukkunaprasit, P. 2001, 'Shear modulus and damping ratio of a clay during undrained cyclic loading', *Geotechnique*, vol. 51, no. 5, pp. 467-70.

TEC 2007, *Specifications for buildings to be built in seismic areas*, Ministry of Public Works and Settlement, Ankara.

Torabi, H. & Rayhani, M.T. 2014, 'Three dimensional finite element modeling of seismic soil–structure interaction in soft soil', *Computers and Geotechnics*, vol. 60, pp. 9-19.

Trifunac, M.D., Ivanović, S.S. & Todorovska, M.I. 2001, 'Apparent periods of a building. II: Time-frequency analysis', *Journal of Structural Engineering*, vol. 127, no. 5, pp. 527-37.

Trombetta, N.W., Mason, H.B., Chen, Z., Hutchinson, T.C., Bray, J.D. & Kutter, B.L. 2013, 'Nonlinear dynamic foundation and frame structure response observed in geotechnical centrifuge experiments', *Soil Dynamics and Earthquake Engineering*, vol. 50, pp. 117-33.

Tropeano, G., Chiaradonna, A., d'Onofrio, A. & Silvestri, F. 2019, 'A numerical model for non-linear coupled analysis of the seismic response of liquefiable soils', *Computers and Geotechnics*, vol. 105, pp. 211-27.

Tsai, C.C. & Hashash, Y.M. 2008, 'A novel framework integrating downhole array data and site response analysis to extract dynamic soil behavior', *Soil Dynamics and Earthquake Engineering*, vol. 28, no. 3, pp. 181-97.

Turan, A., Hinchberger, S.D. & El Naggar, M.H. 2013, 'Seismic soil–structure interaction in buildings on stiff clay with embedded basement stories', *Canadian Geotechnical Journal*, vol. 50, no. 8, pp. 858-73.

UBC 1997, *Uniform building code*, International Conference of Building Officials, Whittier.

Urbaitis, D., Lekstutyte, I. & Gribulis, D. 2016, 'Overconsolidation ratio determination of cohesive soil', *Proceedings of 13th Baltic Sea Geotechnical Conference Geotechnical Problems in Baltic Sea Region*, pp. 108-13.

Valanis, K.C. 1971, 'A theory of visco-plasticity without a yield surface, Part I: General theory', *Archives of Mechanics*, vol. 23, pp. 517-51.

Van Nguyen, Q., Fatahi, B. & Hokmabadi, A.S. 2016, 'The effects of foundation size on the seismic performance of buildings considering the soil-foundation-structure interaction', *Structural Engineering and Mechanics*.

Van Nguyen, Q., Fatahi, B. & Hokmabadi, A.S. 2017, 'Influence of size and load-bearing mechanism of piles on seismic performance of buildings considering soil–pile–

structure interaction', *International Journal of Geomechanics*, vol. 17, no. 7, p. 04017007.

Veletsos, A.S. 1977, 'Dynamics of structure-foundation systems', *Structural and Geotechnical Mechanics*, pp. 333-61.

Veletsos, A.S. & Meek, J.W. 1974, 'Dynamic behaviour of building-foundation systems', *Earthquake Engineering and Structural Dynamics*, vol. 3, no. 2, pp. 121-38.

Veletsos, A.S. & Nair, V.V. 1975, 'Seismic interaction of structures on hysteretic foundations', *Journal of the Structural Division*, vol. 101, no. 1, pp. 109-29.

Viggiani, G. & Atkinson, J.H. 1995, 'Stiffness of fine-grained soil at very small strains', *Géotechnique*, vol. 45, no. 2, pp. 249-65.

von Estorff, O. & Kausel, E. 1989, 'Coupling of boundary and finite elements for soil-structure interaction problems', *Earthquake Engineering and Structural Dynamics*, vol. 18, no. 7, pp. 1065-75.

Von Soos, P. & Bohac, J. 2002, 'Properties of soils and rocks and their laboratory determination', *Geotechnical Engineering Handbook*, vol. 1, pp. 119-206.

Vucetic, M. 1994, 'Cyclic threshold shear strains in soils', *Journal of Geotechnical engineering*, vol. 120, no. 12, pp. 2208-28.

Vucetic, M. & Dobry, R. 1991, 'Effect of soil plasticity on cyclic response', *Journal of Geotechnical Engineering*, vol. 117, no. 1, pp. 89-107.

Walton, H.J., Davids, W.G., Landon, M.E. & Clapp, J.D. 2016, 'Simulation of buried arch bridge response to backfilling and live loading', *Journal of Bridge Engineering*, vol. 21, no. 9, p. 04016052.

Wang, H.F., Lou, M.L., Chen, X. & Zhai, Y.M. 2013, 'Structure–soil–structure interaction between underground structure and ground structure', *Soil Dynamics and Earthquake Engineering*, vol. 54, pp. 31-8.

Wang, L.Z., Shen, K.L. & Ye, S.H. 2008, 'Undrained shear strength of K_0 consolidated soft soils', *International Journal of Geomechanics*, vol. 8, no. 2, pp. 105-13.

Whitman, R.V. & Liao, S. 1988, 'Fifty years of soil dynamics', *Fifteenth Nabor Carrillo Lecture. Delivered during the XX National Meeting of Soil Mechanics*, Oaxaca, Mexico.

Whittaker, A., Atkinson, G., Baker, J., Bray, J., Grant, D., Hamburger, R., Haselton, C. & Somerville, P. 2011, *Selecting and scaling earthquake ground motions for performing response-history analyses*, No. Grant/Contract Reports (NISTGCR)-11-917-15.

Wichtmann, T. 2005, 'Explicit accumulation model for non-cohesive soils under cyclic loading', PhD thesis, Inst. für Grundbau und Bodenmechanik Braunschweig, Germany.

Wichtmann, T., Niemunis, A. & Triantafyllidis, T. 2005, 'Strain accumulation in sand due to cyclic loading: drained triaxial tests', *Soil Dynamics and Earthquake Engineering*, vol. 25, no. 12, pp. 967-79.

Wiessing, P.R. & Taylor, P.W. 1979, 'Foundation rocking on sand', University of Auckland.

Wilson, J. & Lam, N.T.K.L. 2006, 'Earthquake design of buildings in Australia using velocity and displacement principles', *Australian Journal of Structural Engineering*, vol. 6, no. 2, pp. 103-18.

Winkler, E. 1867, *Theory of elasticity and strength*, Dominicus, Prague.

Wolf, J.P. 1985, *Soil-structure interaction*, Prentice Hall Inc., Englewood Cliffs, New Jersey.

Wolf, J.P. & Darbre, G.R. 1986, 'Non-linear soil–structure interaction analysis based on the boundary-element method in time domain with application to embedded foundation', *Earthquake Engineering and Structural Dynamics*, vol. 14, no. 1, pp. 83-101.

Wolf, J.P. & Deeks, A.J. 2004, *Foundation vibration analysis: A strength of materials approach*, Elsevier.

Wolf, J.P. & Obernhuber, P. 1985, 'Non-linear soil-structure-interaction analysis using dynamic stiffness or flexibility of soil in the time domain', *Earthquake Engineering and Structural Dynamics*, vol. 13, no. 2, pp. 195-212.

Wolf, J.P. & Song, C. 2002, 'Some cornerstones of dynamic soil–structure interaction', *Engineering Structures*, vol. 24, no. 1, pp. 13-28.

Wong, F.S. 1984, 'Uncertainties in dynamic soil-structure interaction', *Journal of Engineering Mechanics*, vol. 110, no. 2, pp. 308-24.

Wong, K.S. & Broms, B.B. 1989, 'Lateral wall deflections of braced excavations in clay', *Journal of Geotechnical Engineering*, vol. 115, no. 6, pp. 853-70.

Wu, H.C. & Sheu, J.C. 1983, 'Endochronic modeling for shear hysteresis of sand', *Journal of Geotechnical Engineering*, vol. 109, no. 12, pp. 1539-50.

Wu, S., Gray, D.H. & Richart Jr, F.E. 1984, 'Capillary effects on dynamic modulus of sands and silts', *Journal of Geotechnical Engineering*, vol. 110, no. 9, pp. 1188-203.

Wu, W. & Kolymbas, D. 1990, 'Numerical testing of the stability criterion for hypoplastic constitutive equations', *Mechanics of Materials*, vol. 9, no. 3, pp. 245-53.

Xia, J., Miller, R.D. & Park, C.B. 1999, 'Estimation of near-surface shear-wave velocity by inversion of Rayleigh waves', *Geophysics*, vol. 64, no. 3, pp. 691-700.

Xu, R. & Fatahi, B. 2018, 'Influence of geotextile arrangement on seismic performance of mid-rise buildings subjected to MCE shaking', *Geotextiles and Geomembranes*, vol. 46, no. 4, pp. 511-28.

Xu, R. & Fatahi, B. 2019, 'Novel application of geosynthetics to reduce residual drifts of mid-rise buildings after earthquakes', *Soil Dynamics and Earthquake Engineering*, vol. 116, pp. 331-44.

Yamahara, H. 1970, 'Ground motions during earthquakes and the input loss of earthquake power to an excitation of buildings', *Soils and Foundations*, vol. 10, no. 2, pp. 145-61.

Yang, M., Seidalinov, G. & Taiebat, M. 2019, 'Multidirectional cyclic shearing of clays and sands: Evaluation of two bounding surface plasticity models', *Soil Dynamics and Earthquake Engineering*, vol. 124, pp. 230-58.

Yazdchi, M., Khalili, N. & Valliappan, S. 1999, 'Dynamic soil–structure interaction analysis via coupled finite-element–boundary-element method', *Soil Dynamics and Earthquake Engineering*, vol. 18, no. 7, pp. 499-517.

Yeganeh, N., Bazaz, J.B. & Akhtarpour, A. 2015, 'Seismic analysis of the soil–structure interaction for a high rise building adjacent to deep excavation', *Soil Dynamics and Earthquake Engineering*, vol. 79, pp. 149-70.

Yeganeh, N. & Fatahi, B. 2019, 'Effects of choice of soil constitutive model on seismic performance of moment-resisting frames experiencing foundation rocking subjected to near-field earthquakes', *Soil Dynamics and Earthquake Engineering*, vol. 121, pp. 442-59.

Yegian, M.K., Chang, C.Y., Mullen, C.L. & Mylonakis, G. 2001, 'Soil-structure Interaction under dynamic loading for both shallow and deep foundations', *Proceedings of Fourth International Conference on Recent Advances in Geotechnical Earthquake Engineering and Soil Dynamics and Symposium in Honor of Professor WD Liam Finn*, pp. 26-31.

Yılmaz, M.T., Pekcan, O. & Bakır, B.S. 2004, 'Undrained cyclic shear and deformation behavior of silt–clay mixtures of Adapazarı, Turkey', *Soil Dynamics and Earthquake Engineering*, vol. 24, no. 7, pp. 497-507.

Yim, C.S., Chopra, A.K. & Penzien, J. 1980, 'Rocking response of rigid blocks to earthquakes', *Earthquake Engineering and Structural Dynamics*, vol. 8, no. 6, pp. 565-87.

Yniesta, S. & Brandenberg, S.J. 2017, 'Stress-ratio-based interpretation of modulus reduction and damping curves', *Journal of Geotechnical and Geoenvironmental Engineering*, vol. 143, no. 1, p. 06016021.

Yu, H. & Zeng, X. 2013, 'Seismic behavior of offshore wind turbine with gravity foundation', *Journal of Geological Resource and Engineering*, vol. 1, pp. 46-54.

Yu, Y., Damians, I.P. & Bathurst, R.J. 2015, 'Influence of choice of FLAC and PLAXIS interface models on reinforced soil–structure interactions', *Computers and Geotechnics*, vol. 65, pp. 164-74.

Zeevaert, L. 1991, 'Seismosoil dynamics of foundations in Mexico City earthquake, September 19, 1985', *Journal of Geotechnical Engineering*, vol. 117, no. 3, pp. 376-428.

Zeng, X. & Steedma, R.S. 1998, 'Bearing capacity failure of shallow foundations in earthquakes', *Geotechnique*, vol. 48, no. 2, pp. 235-56.

Zhang, J., Andrus, R.D. & Juang, C.H. 2005, 'Normalized shear modulus and material damping ratio relationships', *Journal of Geotechnical and Geoenvironmental Engineering*, vol. 131, no. 4, pp. 453-64.

Zhang, L. & Liu, H. 2017, 'Seismic response of clay-pile-raft-superstructure systems subjected to far-field ground motions', *Soil Dynamics and Earthquake Engineering*, vol. 101, pp. 209-24.

Zhang, Y., Zhang, J., Chen, G., Zheng, L. & Li, Y. 2015, 'Effects of vertical seismic force on initiation of the Daguangbao landslide induced by the 2008 Wenchuan earthquake', *Soil Dynamics and Earthquake Engineering*, vol. 73, pp. 91-102.

Zienkiewicz, O.C., Chan, A.H.C., Pastor, M., Schrefler, B.A. & Shiomi, T. 1999, *Computational geomechanics*, vol. 613, Wiley, Chichester.

Zolghadr Zadeh Jahromi, H. 2009, 'Partitioned analysis of nonlinear soil-structure interaction', PhD thesis, Imperial College London.

Zytynski, M., Randolph, M., Nova, R. & Wroth, C. 1978, 'On modelling the unloading-reloading behaviour of soils', *International Journal for Numerical and Analytical Methods in Geomechanics*, vol. 2, no. 1, pp. 87-93.